

Cellular-level mechanisms of polarity and their role in plant growth

Katie Abley

PhD Thesis

University of East Anglia

John Innes Centre

Submitted September 2014

This copy of the thesis has been supplied on condition that anyone who consults it is understood to recognise that its copyright rests with the author and that use of any information derived there from must be in accordance with current UK Copyright Law. In addition, any quotation or extract must include full attribution.

Abstract

Coordinated cell polarity fields are essential for plant and animal development. Several models have been proposed for how these cell polarity fields are established. However, it remains unclear how different models are related to each other and how coordinated cell polarity fields are generated. Here, I present a hypothesis that both plant and animal cell polarity fields are based on a common intracellular partitioning (IP) mechanism that spontaneously generates cell polarity independently from pre-established asymmetries. I show how plant polarity fields may be accounted for through an auxin-mediated indirect cell-cell coupling mechanism that coordinates polarities established by IP, and provides an explicit molecular hypothesis that is consistent with current experimental data. I show that this model behaves similarly to a flux-based model of plant polarity in several scenarios, and that these models make testable predictions that differ from those of published up-the-gradient models. To test the different plant models, I use *kanadi1kanadi2* (*kan1kan2*) mutant *Arabidopsis* leaves, which develop ectopic outgrowths, as a simple system to study the dynamics of polarity reorientations. I compare contrasting model predictions with observed polarity changes and patterns of auxin-related gene expression preceding the development of ectopic outgrowths. Together with an analysis of wild-type leaves, this reveals that indirect cell-cell coupling and flux-based models are more compatible than the up-the-gradient model with patterns of auxin biosynthesis and import in leaves. I next show that the *CUC2* transcription factor is essential for *kan1kan2* outgrowth development. Through modelling and experiments, I show that *CUC2*-regulation of auxin biosynthesis most-likely plays an important role in polarity reorientations. Finally, I present models for how epidermal and sub-epidermal PIN polarity patterns may be coordinated and lead to changes in growth. This work reveals the value of comparing different computational models with experimental data when investigating mechanisms of polarity generation.

Contents

Abstract.....	2
Contents.....	3
List of Figures	12
List of tables	19
List of accompanying information	20
Author contributions to results chapters	21
Personal acknowledgements	22
1. General Introduction.....	24
1.1 Overview	24
1.2 Cell polarity	24
1.3 Tissue cell polarity.....	25
1.4 Computational models of polarity	29
1.4.1 Models of animal planar cell polarity	29
1.4.2 Models of auxin-regulated PIN polarity	30
1.5 Gene expression patterns and polarity.....	32
2 An intracellular partitioning-based framework for tissue cell polarity in plants and animals .	35
2.1 Introduction	35

2.2	Results.....	38
2.2.1	Intracellular partitioning.....	38
2.2.2	Cell-cell coupling.....	40
2.2.3	Organising polarity across a tissue	46
2.2.4	Effects of Cell Geometry	58
2.2.5	Summary of theoretical analysis	60
2.3	Canonical examples from plants and animals	61
2.3.1	PCP in <i>Drosophila</i>	61
2.3.2	PIN localisation in plants.....	68
2.3.3	Concluding remarks	72
2.4	Model descriptions	73
2.4.1	Intracellular partitioning.....	73
2.4.2	Direct cell-cell coupling.....	81
2.4.3	Tissue gradients	85
2.4.4	Indirect cell-cell coupling.....	91
3	Comparison of models of auxin-regulated polarity.....	100
3.1	Introduction.....	100
3.2	Assumptions of the flux and up-the-gradient models.....	101

3.2.1	Flux-based model.....	101
3.2.2	Up-the-gradient model	102
3.3	Results.....	103
3.3.1	Testing intracellular partitioning behaviour	103
3.3.2	Behaviours of groups of cells in the absence of tissue-wide biases	111
3.3.3	Generation of centres of polarity convergence in indirect cell-cell coupling and flux-based models	122
3.3.4	Generation of coordinated polarity across tissues	124
3.4	Discussion.....	128
3.4.1	Classification of models	128
3.4.2	Tandem coupling models make different predictions about the precise mechanism of polarisation	133
3.4.3	Feedback between orienting signals and polarity	134
3.4.4	Conclusions	136
3.5	Model descriptions	137
3.5.1	Indirect cell-cell coupling simulation details.....	137
3.5.2	Tissue representation for up-the-gradient and flux-based models.....	137
3.5.3	Up-the-gradient model	139

3.5.4	Flux-based model.....	144
4	Mechanisms underlying the generation of centres of polarity convergence	154
4.1	Introduction.....	154
4.2	Results.....	157
4.2.1	PIN1 polarity patterns in WT and <i>kan1kan2</i> leaves	157
4.2.2	Ectopic auxin-activity maxima precede outgrowths	166
4.2.3	Models for the generation of centres of PIN1 polarity convergence.....	169
4.2.4	Patterns of auxin importer expression in WT and <i>kan1kan2</i> leaves.....	181
4.2.5	Loss of <i>AUX/LAX</i> auxin importers causes a loss of ectopic outgrowths.....	186
4.2.6	The pattern of auxin importer expression is compatible with up-the-gradient model 189	
4.2.7	Patterns of auxin biosynthesis enzyme expression in WT and <i>kan1kan2</i> leaves...	194
4.2.8	The pattern of auxin biosynthesis in WT and <i>kan1kan2</i> leaves in inconsistent with the up-the-gradient model.....	197
4.3	Discussion	201
4.3.1	Models make different predictions about patterns of auxin biosynthesis, which can be used to distinguish them experimentally.....	201
4.3.2	Predictions of the indirect cell-cell coupling model	204

4.3.3	Relevance of <i>kan1kan2</i> outgrowth development for the formation of organs in the shoot apical meristem.....	207
4.3.4	Polarity reorientations are a common feature of outgrowth development	208
4.4	Methods.....	209
4.4.1	<i>A.thaliana</i> mutant and transgenic lines.....	209
4.4.2	Genotyping.....	213
4.4.3	Plant growth conditions.....	214
4.4.4	Confocal imaging of fluorescent markers	214
4.4.5	GUS staining	215
4.4.6	Propidium iodide (PI) staining of <i>kan1kan2</i> leaves.....	217
4.4.7	OPT imaging	218
4.4.8	Computational models.....	218
5	The role of <i>CUC2</i> in polarity reorientations	228
5.1	Introduction	228
5.2	Results.....	230
5.2.1	<i>CUC2</i> is required for the development of <i>kan1kan2</i> outgrowths and ectopic centres of PIN1 polarity convergence.....	230
5.2.2	<i>CUC2::RFP</i> is initially expressed in the proximal half of the leaf and then its expression becomes more restricted.	233

5.2.3	Centres of PIN1 polarity convergence form within the proximal domain of <i>CUC2::RFP</i> expression.....	235
5.2.4	<i>CUC2::RFP</i> expression is restricted to the base of WT leaves.....	238
5.2.5	<i>kan1kan2</i> leaves that do not generate centres of PIN1 convergence have elevated expression of <i>CUC2::RFP</i> in proximal regions of the lamina.....	240
5.2.6	Models of positioning centres of PIN1 polarity convergence	242
5.2.7	<i>CUC2</i> is required for ectopic expression of <i>YUC1</i> in <i>kan1kan2</i> leaves	261
5.2.8	<i>CUC2</i> and <i>YUC</i> genes are required for the generation of ectopic sites of <i>LAX1::GUS</i> expression.....	262
5.3	Discussion	264
5.3.1	<i>CUC2</i> promotes outgrowth formation by up-regulating <i>YUC1</i> -mediated auxin synthesis	264
5.3.2	Distinguishing between up-the-gradient and indirect cell-cell coupling models...	265
5.3.3	The role of <i>CUC2</i> as a boundary gene	267
5.3.4	CUC-regulated polarity and adaxial-abaxial juxtaposition	268
5.3.5	<i>kan1kan2</i> outgrowths and serration development.....	271
5.4	Methods.....	272
5.4.1	Imaging procedures	272
5.4.2	<i>A.thaliana</i> mutant and transgenic lines	272

5.4.3	Model descriptions	274
6	Integration of polarity in the epidermis and sub-epidermis through indirect cell-cell coupling	
	282	
6.1	Introduction	282
6.2	Results.....	287
6.2.1	In <i>kan1kan2</i> leaves, new epidermal centres of convergence are coupled with sub-epidermal PIN1 strands.....	287
6.2.2	Forwards propagation of PIN strands in indirect cell-cell coupling and flux-based models	289
6.2.3	Backwards propagation of PIN strands in indirect cell-cell coupling and flux-based models.	296
6.2.4	Connecting forward and backward propagating PIN strands.....	299
6.2.5	Integrating epidermal and sub-epidermal polarity patterns in <i>kan1kan2</i> leaves ..	302
6.3	Discussion.....	311
6.3.1	An indirect cell-cell coupling model for epidermal centres of convergence and sub-epidermal PIN strands.....	311
6.3.2	Mechanisms of PIN strand formation differ between flux and indirect cell-cell coupling models.....	314
6.3.3	The indirect cell-cell coupling and flux-based models make testable predictions about the formation of sub-epidermal PIN strands.....	316

6.4	Methods.....	318
6.4.1	Immuno-localisation of PIN1	318
6.4.2	Model Descriptions.....	319
7	Hypothesis for the role of polarity fields in the generation of new 3D outgrowths.....	331
7.1	Introduction	331
7.2	Results.....	333
7.2.1	Role of an outer-inner polarity field in the growth of the transverse cross-sectional plane of the leaf.....	333
7.2.2	Quantification of growth of the <i>kan1kan2</i> abaxial epidermis.....	339
7.3	Discussion	345
7.3.1	Coordination of growth between orthogonal planes of the leaf	345
7.3.2	Candidate molecules involved in the outer-inner polarity field.....	347
7.3.3	Roles of adaxial- abaxial juxtaposition for anisotropic growth of the leaf.....	348
7.3.4	A system for investigating the role of CUC in regulating growth rates	349
7.4	Methods.....	350
7.4.1	Growth analysis	350
7.4.2	Computational models of growth.....	350
8	General Discussion.....	353

8.1	A new indirect cell-cell coupling model for plant polarity.....	353
8.2	Tandem coupling models are most compatible with locations of auxin biosynthesis ...	354
8.3	Auxin import has an important role in tandem coupling models.....	356
8.4	Evidence for organisers of polarity	358
8.5	An indirect cell-cell coupling-based hypothesis for phyllotaxis.....	359
8.6	Future work to further evaluate models	360
8.6.1	Growth and indirect cell-cell coupling	360
8.6.2	Testing candidate intracellular partitioning components.....	361
8.6.3	Testing the behaviours of cells in the absence of neighbours or pre-established asymmetries.....	364
8.6.4	The role of mechanical signals in polarity and growth	366
8.7	Concluding remarks	369
9	References	370

List of figures

Fig. 1.1 Proximo-distal polarity fields in the <i>D.melanogaster</i> wing and <i>A.thaliana</i> leaf epidermis.	26
Fig. 1.2 Schematic of polarity patterns in the longitudinal cross-sectional planes of <i>A.thaliana</i> leaves and roots.....	27
Fig. 2.1 Polarity coordination.....	36
Fig. 2.2 System for intracellular partitioning.	38
Fig. 2.3 Polarity pattern generated through intracellular partitioning.	39
Fig. 2.4 Direct cell-cell coupling.	42
Fig. 2.5 Indirect cell-cell coupling.	45
Fig. 2.6 Organisation of polarity through direct modulation of polarity components.....	49
Fig. 2.7 Two aspects of a concentration gradient.....	50
Fig. 2.8 Organisation of polarity through cellular gradients.....	53
Fig. 2.9 Organisation of polarity through intercellular gradients.....	55
Fig. 2.10 Organisation of polarity by modulation of auxin levels.....	57
Fig. 2.11 Cell-cell coupling on grids of square or irregular cells.	59
Fig. 2.12 Localisation of core planar cell polarity components at cell-cell interfaces in the <i>D.melanogaster</i> wing.....	62
Fig. 2.13. Mechanisms contributing to tissue cell polarity in models of <i>Drosophila</i> planar cell polarity.....	64

Fig. 2.14 The intracellular partitioning graph.	75
Fig. 2.15. The extracellular space graph.	86
Fig. 2.16. The cell wall graph.	92
Fig. 3.1 Intracellular partitioning in the indirect cell-cell coupling model.	105
Fig. 3.2 Intracellular partitioning in the up-the-gradient model.	106
Fig. 3.3 Intracellular partitioning in the flux-based model.	108
Fig. 3.4 Generation of locally coordinated polarities in an indirect cell-cell coupling model.	113
Fig. 3.5 Up-the-gradient model for tissues with no pre-established asymmetries in auxin concentration.	115
Fig. 3.6 Formation of a polarity convergence in an up-the-gradient model.	117
Fig. 3.7 Flux based model for tissues with no pre-established asymmetries in auxin concentration.	119
Fig. 3.8 Emergence of coordinated polarity orientations in the flux-based model.	121
Fig. 3.9 Generation of centres of polarity convergence in flux-based and indirect cell-cell coupling models.	123
Fig. 3.10 Coordination of polarity across a 2D array of cells for the up-the-gradient model.	126
Fig. 3.11 Coordination of polarity across a 2D array of cells for the flux-based model.	127
Fig. 3.12 Classification of polarity models.	129

Fig. 3.13 Differences between animal and plant models for the generation of cell polarity fields.....	135
Fig. 3.14 Graph used to represent the tissue for up-the-gradient and flux-based models.....	138
Fig. 4.1. Ectopic outgrowths in <i>kan1kan2</i> mutant leaves.....	156
Fig. 4.2 Inferring cellular PIN1 distributions from confocal images of leaves expressing <i>PIN1::PIN1:GFP</i>	160
Fig.4.3. Two examples of the <i>PIN1:GFP</i> polarity pattern preceding <i>kan1kan2</i> outgrowth development.....	163
Fig. 4.4 <i>PIN1:GFP</i> polarity pattern in an early <i>kan1kan2</i> leaf primordium.	163
Fig. 4.5. <i>PIN1::PIN1:GFP</i> expression in a WT leaf primordium.	165
Fig. 4.6 <i>PIN1:GFP</i> signal in a <i>kan1kan2</i> leaf that did not generate an ectopic outgrowth.....	166
Fig 4.7 <i>DR5::GFP</i> expression in a <i>kan1kan2</i> leaf during outgrowth development.....	168
Fig. 4.8 <i>DR5::GFP</i> expression pattern in a <i>kan1kan2</i> leaf that did not generate an ectopic outgrowth.....	169
Fig 4.9 Generation of a proximo-distal polarity field in an up-the-gradient model.....	171
Fig 4.10 Formation of centres of polarity convergence in an up-the-gradient model.....	175
Fig. 4.11 Generation of a proximo-distal polarity field in an indirect cell-cell coupling model with an explicit representation of PIN.....	177
Fig. 4.12 Formation of centres of polarity convergence in an indirect cell-cell coupling model. ..	181

Fig. 4.13 . Expression of <i>LAX1::GUS</i> in WT and <i>kan1kan2</i> leaves.	183
Fig. 4.14 Expression of <i>AUX1::AUX1:YFP</i> in WT and <i>kan1kan2</i> leaves.	185
Fig 4.15 Numbers of outgrowths in <i>kan1kan2 aux/lax</i> mutants.	189
Fig. 4.16. Generation of a proximo-distal polarity field in an up-the-gradient model with elevated auxin import in the distal minus organiser.	191
Fig. 4.17 Generation of centres of convergence in an up-the-gradient model with elevated auxin import in minus organisers	194
Fig. 4.18 Expression pattern of <i>YUCCA1::GUS</i> in WT and <i>kan1kan2</i> leaves.	197
Fig. 4.19 The effect of auxin production in proximal regions of tissue in an up-the-gradient model.	198
Fig. 4.20 The effect of a band of cells with elevated auxin synthesis distal to a cell with elevated import in indirect cell-cell coupling and up-the-gradient models.	200
Fig. 5.1 Loss of ectopic outgrowths in a <i>kan1kan2cuc2</i> background.....	230
Fig. 5.2 <i>PIN1::PIN1:GFP</i> in leaf one of the <i>kan1kan2cuc2</i> mutant.....	232
Fig. 5.3 Expression of <i>CUC2::RFP</i> and <i>PIN1::PIN1:GFP</i> in <i>kan1kan2</i> leaves during the development of ectopic centres of polarity convergence.	234
Fig. 5.4 Formation of a centre of PIN1 polarity convergence in relation to expression of <i>CUC2::RFP</i>	237
Fig. 5.5 Expression patterns of <i>CUC2::RFP</i> and <i>PIN1::PIN1:GFP</i> in WT leaves.....	240

Fig. 5.6 Expression of <i>PIN1::PIN1:GFP</i> and <i>CUC2::RFP</i> in a <i>kan1kan2</i> leaf that did not develop an ectopic outgrowth.....	242
Fig.5.7 Positioning of centres of convergence in an up-the-gradient model with CUC2.....	246
Fig 5.8 Positioning centres of convergence in the proximal half of the lamina in an up-the-gradient model with CUC2.....	248
Fig. 5.9 An up-the-gradient CUC2-plasticity model for positioning centres of convergence in <i>kan1kan2</i> leaves.....	251
Fig. 5.10 Consequence of CUC2-independent polarity reorientation in the up-the-gradient CUC2 plasticity model.....	253
Fig. 5.11 Effect of a proximal domain with elevated auxin production rates on the intracellular auxin concentration profile in an indirect cell-cell coupling model.....	256
Fig. 5.12 Positioning centres of convergence in an indirect cell-cell coupling model where CUC2 promotes auxin biosynthesis.....	259
Fig. 5.13 Expression of <i>YUC1::GUS</i> in <i>kan1kan2</i> and <i>kan1kan2cuc2</i> leaf primordia.....	262
Fig. 5.14 Expression of <i>LAX1::GUS</i> in <i>kan1kan2yuc1yuc4</i> , <i>kan1kan2</i> and <i>kan1kan2cuc2</i> backgrounds.....	263
Fig. 6.1 Forwards and backwards propagation of sub-epidermal PIN1 strands.....	283
Fig. 6.2 PIN1 immuno-localisation in transverse cross-sections of <i>kan1kan2</i> leaves.	288
Fig. 6.3 Forwards propagation of a PIN strand from an auxin source in the flux-based model....	290

Fig. 6.4 Forwards propagation of a PIN strand in an indirect cell-cell coupling system with auxin promotion of PIN.	292
Fig. 6.5 PIN strand formation by forwards propagation in an indirect cell-cell coupling system with altered assumptions about auxin movement.....	294
Fig. 6.6 Forwards propagation of a PIN strand in an indirect cell-cell coupling system where high auxin promotes auxin import and PIN.....	296
Fig. 6.7 Backwards propagation of a strand with elevated PIN from a sink cell in a flux-based model.	297
Fig. 6.8 Backwards propagation of a PIN strand in an indirect cell-cell coupling model where low extracellular auxin promotes auxin import and PIN.....	299
Fig. 6.9 Connection of PIN strands propagating forwards from a point source and backwards from a point sink in a flux-based model.	300
Fig. 6.10 Combination of forwards and backwards strand propagation rules in an indirect cell-cell coupling model.	301
Fig. 6.11 Schematics of the polarity patterns in the longitudinal cross-sectional plane of <i>kan1kan2</i> leaves.	303
Fig. 6.12 Generation of the PIN1 polarity pattern in the longitudinal cross-sectional plane of the leaf through a pre-pattern of auxin production, degradation and import.....	307
Fig. 6.13 Indirect cell-cell coupling model for the formation of a coupled epidermal centre of convergence and sub-epidermal PIN strand.....	310
Fig. 7.1. Growth within two orthogonal planes during the generation of a 3D outgrowth.	332

Fig. 7.2 Model for the growth of the transverse cross-sectional plane of the WT leaf.....	335
Fig. 7.3 A polarity reorientation-based model for growth of the transverse cross-sectional plane of the <i>kan1kan2</i> leaf.....	338
Fig. 7.4 PIN1 expression marks a middle plane identity region in WT leaf primordia.	339
Fig. 7.5 Principle directions of growth in <i>kan1kan2</i> leaves prior to outgrowth development	342
Fig. 7.6 Growth rates of <i>kan1kan2</i> leaves prior to outgrowth development.....	345

List of tables

Table 2.1. Parameter values used for simulations.....	99
Table 3.1. Parameter values used in up-the-gradient simulations.....	143
Table 3.2 Parameter values used in simulations of the flux-based model.....	153
Table 4.1. Summary of the compatibilities of up-the-gradient and indirect cell-cell coupling models with different aspects of data obtained for WT and <i>kan1kan2</i> leaves.....	203
Table 4.2. Primers used to detect the presence of WT and mutant alleles of <i>LAX1</i> , <i>LAX2</i> and <i>LAX3</i>	212
Table 4.3 PIN-related parameter values used in the indirect cell-cell coupling model.....	222
Table 4.4. Parameter values used in up-the-gradient simulations.....	225
Table 5.1. Parameter values used in up-the-gradient simulations.....	278
Table 6.1 Parameter values used in flux-based simulations.....	321

List of accompanying information

Attached is a CD containing:

- A Microsoft Word file containing all figures in the thesis in high resolution.
- VVE models that were used to perform all simulations shown in figures.
- A copy of the VVE modelling environment (implemented in L-studio) which can be used by windows users to run all the models. To run the models, after unzipping the L-studio folder, enter the sub-folder entitled “bin”, then run the Lstudio.exe file. To open a model, drag its folder (which is labelled with a figure number) into the L-studio window. Click “VVE”, then “Run” to run the model. L-studio requires Microsoft Visual Studio, which can be downloaded from http://download.cnet.com/Microsoft-Visual-Studio-2010-Ultimate/3000-2383_4-75450998.html. For Mac and Linux users, the models can be run by installing the vlab modelling environment from http://algorithmicbotany.org/virtual_laboratory/
- A GFtbox growth model used in chapter 7, which can be run by installing the GFtbox matlab package from <http://sourceforge.net/projects/gftbox/>

Author contributions to results chapters

Chapter 2

The work presented in chapter 2 is based on the following publication:

Abley, K.[‡], De Reuille, P.B.[‡], Strutt, D., Bangham, A., Prusinkiewicz, P., Marée, A.F., Grieneisen, V.A., and Coen, E. (2013). An intracellular partitioning-based framework for tissue cell polarity in plants and animals. *Development* 140, 2061-2074.

[‡]These authors contributed equally to the work

Pierre Barbier de Reuille, Enrico Coen, Verônica Grieneisen, Athanasius Marée, Andrew Bangham and I conceived of the models. David Strutt provided advice on *Drosophila* planar cell polarity. Pierre Barbier de Reuille and Przemysław Prusinkiewicz developed the VVe modelling environment used to implement the models and Pierre Barbier de Reuille implemented preliminary versions of some of the models. I implemented all the final versions of the models and ran all simulations. Enrico Coen and I wrote the paper.

Chapter 3- Chapter 6

The indirect cell-cell coupling models presented in these chapters were based on those originally implemented by Pierre Barbier de Reuille, but modified by me. I implemented all final versions of the models, performed all simulations, and did all experimental work.

Chapter 7

OPT images of the transverse cross-sectional plane of the WT leaf were generated by Karen Lee. I did all other experimental and modelling work.

Personal acknowledgements

Many thanks to:

Enrico Coen, for having the good ideas that underlie this work and for lots of interesting discussions. Thanks for all your support and for everything you've taught me during my PhD. Also, thanks for providing a great environment to work in.

Stan Marée and Verônica Grieneisen, for lots of ideas and interesting discussions and for taking time to answer detailed questions about models.

Pierre Barbier de Reuille, for teaching me how to use VVE and for implementing the original models.

Xana Rebocho, for always being extremely supportive and encouraging. Many thanks for lots of useful and interesting discussions and for help in the lab (particularly for excellent tuition on how to do immuno-localisations and RNA -in situ!).

Susana Sauret Gueto, for lots of support and advice. Thanks for teaching me how to do cloning and use the confocal and for lots of great discussions about our projects. Also, thanks for your work on polarity which led the way to this project.

Jordi Chan, for helping me to get good time-lapse confocal images and for lots of discussions about micro-tubules!

Sam Fox, for teaching me how to use the Point Tracker software, for advice on confocal imaging and image processing, and for always being encouraging.

Karen Lee, for lots of help and advice on OPT imaging, and for always being really supportive and great fun to sit next to!

Hugo Tavares, for being interested in the details of my project and for always seeming to understand what I'm talking about. Thanks for reading my thesis really carefully and for helping me to improve it.

Desmond Bradley, for always being around to answer questions, for asking me lots of difficult questions about my project, and for making the lab a really happy place to work.

Andrew Bangham, for lots of interesting discussions, for always following my lab meetings after I'd sent most people to sleep, and for always being extremely encouraging.

David Strutt, for hosting me in his lab and helping me to do experiments on single cell polarisation in *Drosophila*. Also thanks to Helen Strutt for preparing fly lines and to Samantha Warrington for help with fly work and live imaging.

My thesis examiners, Martin Howard and Jan Traas, for an interesting discussion and for useful suggestions of improvements.

The John Innes horticultural services team, particularly Lelsey Phillips and Timothy Wells, for looking after my plants.

Cindy Cooper for supporting the lab, and thanks to Roy Dunford for making it an organised and efficient place to work.

The Gatsby plant science organisation for funding my PhD. Also, thanks to the Gatsby advisors Ottoline Leyser, Jane Langdale, Liam Dolan and Nick Talbot (and to David Hanke) for providing useful training and advice throughout my PhD.

1. General Introduction

1.1 Overview

Most cells are polarised. This includes single celled organisms, such as bacteria and yeast, and cells that exist in a multicellular context, as part of plant and animal tissues (Macara and Mili, 2008; Shapiro et al., 2002; Wedlich-Soldner and Li, 2003; Goodrich and Strutt, 2011; Petrášek and Friml, 2009). The establishment of cell polarity is often one of the first events during plant and animal embryogenesis, and as development proceeds, the establishment of coordinated cell polarities in developing tissues is essential for their growth and differentiation (Petrášek and Friml, 2009; Goodrich and Strutt, 2011; Wedlich-Soldner and Li, 2003). However, the mechanisms underlying plant and animal cell polarity fields are still unclear. Despite several models for polarity generation being proposed, it remains unclear how principles underlying cell polarities in plants may be related to those in animals and in isolated cells. Also, which of the proposed models are most compatible with current experimental data, and most able to make accurate predictions, is uncertain.

1.2 Cell polarity

Cell polarity is an asymmetry in a cell, such that certain molecules or structures are located preferentially towards a particular cell end. Polarity is observed in many prokaryotic and eukaryotic single celled organisms (Drubin and Nelson, 1996; Macara and Mili, 2008; Shapiro et al., 2002; Wedlich-Soldner and Li, 2003). Two striking examples are the positioning of flagella at one end of *Vibrio cholerae* bacterial cells and the generation of bud-shaped protrusions that precede cell division in budding yeast. Isolated cells of multi-cellular organisms, such as neutrophils, also show polarity in the organisation of their cytoskeleton and plasma membrane (Gardiner et al., 2002; Ridley and Hall, 1992). Polarity of single cells is important for processes

such as cell migration, where cells must acquire a distinct front and back in order to move in a particular direction (Etienne-Manneville, 2008; Ridley et al., 2003), and in asymmetric cell division, where contents of a mother cell are divided asymmetrically during division into daughters (Long et al., 1997; Macara and Mili, 2008).

In many instances of single cell polarisation, a self organising intrinsic polarity system underlies the generation of polarity. External gradients that provide information about the surroundings, or cell-intrinsic cues which provide information about past polarisation events, then influence the orientation of cell polarity (Wedlich-Soldner and Li, 2003). For example, in the slime-mould *Dictyostelium discoideum*, cells usually migrate along gradients of chemoattractants, but in the presence of uniform concentrations of chemoattractants, cells still migrate (and are therefore polarised), but in random orientations (Devreotes and Zigmond, 1988). Also, in budding yeast, the orientation of asymmetric division is usually influenced by the bud scar, which provides information about the orientation of the previous division (Wedlich-Soldner and Li, 2003). When this bud scar is removed, cells still divide asymmetrically, but in a random orientation (Chant and Herskowitz, 1991).

1.3 Tissue cell polarity

In many tissues within plants and animals, individual cells are polarised and polarities of neighbouring cells are coordinated between neighbours, and with respect to overall tissue axes (Petrášek and Friml, 2009; Wang and Nathans, 2007). I refer to these coordinated cell polarity fields as tissue cell polarity. In animals, epithelial cells are polarised along their apical basal (outside-inside) axis. This apical-basal polarity involves the asymmetric distribution of membrane domains and is essential to maintain the integrity of epithelia (Tepass, 2012). Many epithelia are also polarised with respect to a second tissue axis. For example, the *Drosophila melanogaster*

(*D.melanogaster*) wing consists of two juxtaposed sheets of cells, in which cells are polarised along their apical basal axis, and along the proximo-distal axis of the wing (Goodrich and Strutt, 2011) (Fig. 1.1 A, B). The proximo-distal polarity of cells is established as an asymmetric distribution of proteins early in wing development and culminates in the development of a trichome from a site towards the distal end of each cell (Strutt, 2001, 2002).

Similar to the polarity field in the *D.melanogaster* wing, a proximo-distal polarity pattern is seen in the distribution of the PIN1 protein in the epidermis of the *Arabidopsis thaliana* (*A.thaliana*) leaf, which is a major focus of this work. In this context, PIN1 is localised towards the distal end of each cell (Scarpella et al., 2006; Wenzel et al., 2007) (Fig. 1.1 C), and the planar polarity field marked by PIN1 has been hypothesised to be responsible for specifying principle orientations of leaf growth (Kuchen et al., 2012).

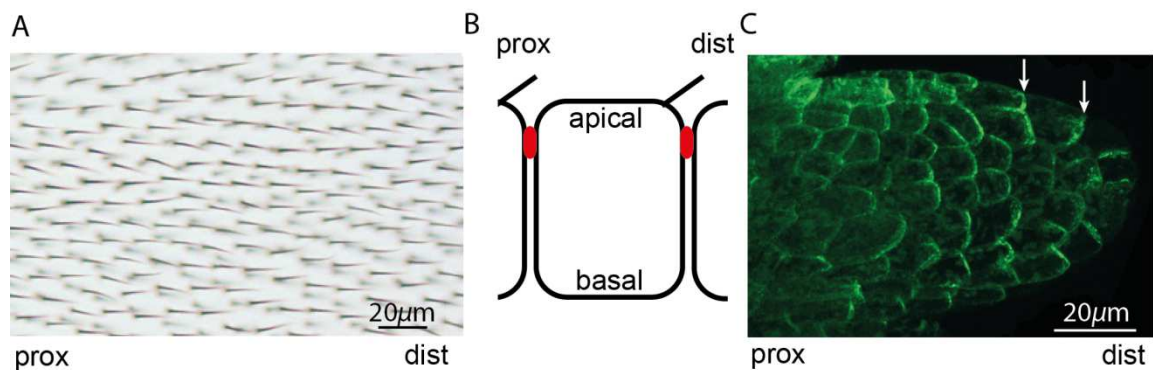


Fig. 1.1 Proximo-distal polarity fields in the *D.melanogaster* wing and *A.thaliana* leaf epidermis. **A)** Hairs on a *D.melanogaster* wing point from proximal (prox) to distal (dist) positions in a coordinated manner. Image provided by David Strutt. **B)** Schematic of an epithelial cell from the *D.melanogaster* wing, showing apical-basal and proximo-distal polarities. Red indicates tight junctions which form at the apical side of epithelial cells and diagonal lines indicate trichomes, which develop from distal cell ends. **C)** In a developing leaf primordium, the auxin efflux carrier PINFORMED1 (PIN1, visualised using a *pPIN1::PIN1:GFP* reporter (Heisler et al., 2005)) is localised towards the distal end of each cell (white arrows). Image provided by Erika Kuchen. Polarisation of plant epithelial cells along the outside-inside axis is not as well characterised as in animals and is therefore not shown.

More complex multi-cellular polarity patterns are seen when plant organs are viewed in 3D. For example, in the young *A.thaliana* leaf, distally oriented PIN1 polarities in the epidermis are combined with proximally oriented polarities in sub-epidermal cells of the developing midvein (Scarpella et al., 2006; Wenzel et al., 2007) (Fig. 1.2 A). The polarity patterns of new leaves are established in the shoot apical meristem during phyllotaxis. This involves a continual process of growth and PIN polarity reorientations, which position new shoot-derived organs at the maximum distance from existing organs (Heisler et al., 2005; Reinhardt et al., 2003). Roots also have a complex polarity pattern, with a number of different PIN proteins contributing to polarities oriented towards the root tip in central-most tissue, towards the shoot in outer-most cells, and inwardly in cells in between (Blilou et al., 2005) (Fig. 1.2 B).

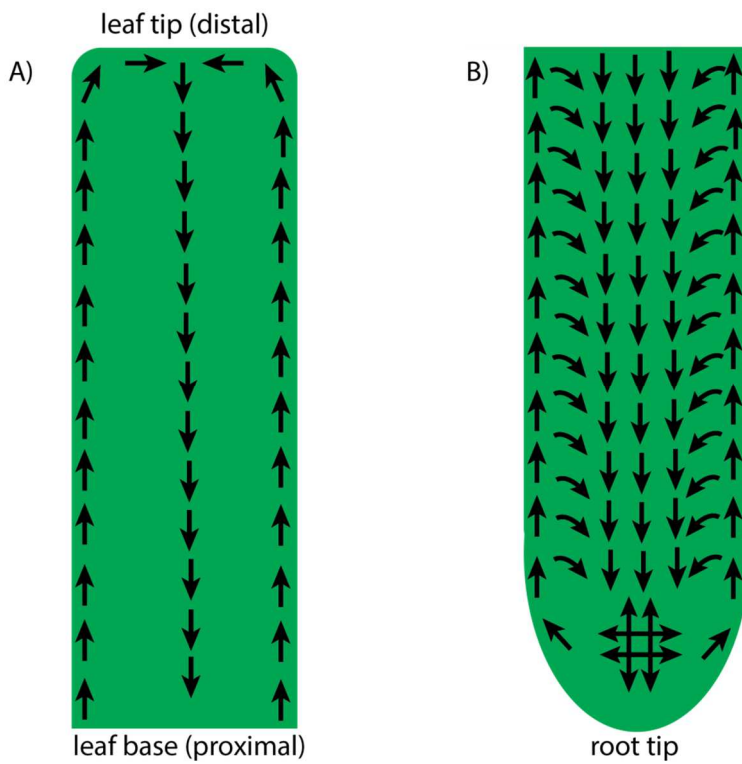


Fig. 1.2 Schematic of polarity patterns in the longitudinal cross-sectional planes of *A.thaliana* leaves and roots.

A) PIN1 polarity pattern in the longitudinal cross-sectional plane of an *A.thaliana* leaf. In the epidermis, polarities are oriented distally, towards the leaf tip. In sub-epidermal tissue, cells that express PIN1 and will later differentiate into the midvein have proximally oriented PIN1 polarities,

pointing towards the leaf base (Scarpella et al., 2006). **B)** A simple representation of the combined polarity patterns of PIN1, PIN2, PIN3, PIN4 and PIN7 seen in the root, based on schematics in Blilou et al., 2005 and Petrášek and Friml, 2009. In outer-most cell files, polarities are oriented away from the root tip, and in inner most files, polarities are oriented towards the tip. Oblique orientations are seen in cells between those with apical or basal polarity. At the root tip, PIN proteins are localised to all cell membranes (double-headed arrows).

PIN proteins export the plant hormone auxin, and their polar distribution in cells allows the polarised transport of auxin (Gälweiler et al., 1998; Vieten et al., 2007; Wisniewska et al., 2006). The effectiveness of PIN proteins in determining the direction of auxin transport is related to the properties of auxin itself. Auxin is a weak acid, and in the extracellular space, where the pH is relatively low, a large fraction of auxin is in a protonated (non-charged) form, which can passively enter cells (Rubery and Sheldrake, 1974). However, in the cytoplasm, where the pH is higher, a large fraction of auxin becomes ionised, and therefore can only leave cell through active transport, which can be mediated by polarly localised PIN proteins (Vieten et al., 2007). Polarity patterns in the embryo, leaf, meristem and root therefore influence auxin distribution patterns in these tissue contexts (Benkova et al., 2003; Blilou et al., 2005; de Reuille et al., 2006; Petrášek and Friml, 2009; Reinhardt et al., 2003). Auxin accumulates at the tips of leaves and roots, and at a maximum distance from existing primordia in meristems. In all these contexts, the auxin distribution plays an important role in regulating cell fate and growth (Overvoorde et al., 2010; Reinhardt et al., 2000; Scarpella et al., 2006). The pattern of polarised PIN proteins is therefore essential for plant morphogenesis.

1.4 Computational models of polarity

Computational modelling has been widely used to help generate hypotheses for how patterns of tissue cell polarity in plants and animals are generated (Abley et al., 2013; Garnett et al., 2010; Grieneisen and Scheres, 2009; Reeves et al., 2006; van Berkel et al., 2013). A computational

approach is useful to predict the effect of local rules or molecular interactions at higher scales of organisation, for example at the cell, tissue, or organ levels. Modelling can therefore be used to test the sufficiency of a hypothesis to account for a particular phenomenon, and can be used to generate new, and often counter-intuitive predictions, which arise from particular hypotheses. Experimental tests of these predictions can then be used to assess the validity of the hypotheses that have been modelled.

1.4.1 Models of animal planar cell polarity

A number of models have been proposed for how a group of proteins, called core planar cell polarity components, becomes asymmetrically localised within the plane of animal epithelia prior to the emergence of polarised structures, such as trichomes. Two models explicitly represent all six components of the core planar cell polarity pathway that were identified based on their mutant phenotypes (which involve apolar localisation of trichomes) and localise either to proximal or distal cell ends (Amonlirdviman et al., 2005; Le Garrec et al., 2006; Strutt and Strutt, 2009). These models include interactions between polarity components both within individual cells and between neighbouring cells, as well as their interactions with external biasing cues. Although these models can capture a number of experimental observations in 2D tissues, their behaviour is a consequence of many molecular interactions, and it is difficult to extract the key principles involved in polarity generation and coordination from the models. Another, simpler, model has been proposed which uses just two membrane bound polarity components to represent all six of the core planar cell polarity proteins (Burak and Shraiman, 2009). With this model, interactions between the two polarity components, both between and within cells, lead to the establishment of locally coordinated cell polarities where each cell has the two polarity components localised to opposite cell ends. However, to coordinate polarities across the entire tissue, tissue-wide biases are required. How this simple model relates to the more detailed

molecular models is unclear. It is also unclear how the principles of these models are related to mechanisms of polarisation in single cells, or in plants.

1.4.2 Models of auxin-regulated PIN polarity

A number of lines of evidence suggest that auxin influences patterns of PIN polarisation and therefore the directionality of its own transport (Bennett et al., 2014). Ectopic application of auxin to some tissues, such as wounded stems, causes the development of narrow strands of PIN1 expression, in which PIN1 is polarised away from the auxin source (Sauer et al., 2006). These strands differentiate into narrow vascular strands, which transport auxin away from the applied source (Jacobs, 1952). In the shoot apical meristem, a different response to auxin application is reported: in this context, PIN polarities were observed to become oriented towards regions of applied auxin (Bayer et al., 2009).

In line with these observations, two main types of model were proposed for PIN polarisation, both involving feedback between auxin and PIN allocation to the plasma-membrane. In the up-the-gradient model, each cell allocates PIN proteins preferentially to its neighbour with the highest auxin concentration (Jönsson et al., 2006; Smith et al., 2006). This leads to the formation of centres of PIN1 polarity convergence with high auxin at their centre, and when applied to a growing tissue, can account for the dynamic patterns of PIN polarisation and auxin distributions that drive phyllotactic patterning. In the flux-based model, each cell allocates PIN to membrane regions in proportion to the rate of auxin efflux across the membrane (Rolland-Lagan and Prusinkiewicz, 2005; Stoma et al., 2008). This model can account for the formation of vascular strands such as those seen in sub-epidermal tissues of leaves (Rolland-Lagan and Prusinkiewicz, 2005), and, with some additional assumptions, can also account for phyllotactic patterning (Stoma et al., 2008). A problem with up-the-gradient and flux-based models is that it is unclear how cells

could compare the auxin concentrations of their neighbours or measure the rate of net auxin efflux across the plasma membrane (Bennett et al., 2014).

However, more recently, models have been proposed that provide more explicit molecular hypotheses for the generation of plant tissue cell polarity. One model assumes that PIN proteins are allocated preferentially to membranes adjacent to cell walls under the most stress (Heisler et al., 2010). This model generates behaviours similar to the up-the-gradient model. This is because auxin is assumed to promote cell wall loosening. It is assumed that the cell wall at the interface between two neighbouring cells is divided into two compartments, with each wall compartment only being loosened by intracellular auxin in the closest cell. An elevated auxin concentration in a neighbour of a given cell therefore causes loosening of the neighbour's cell wall and an increased stress in the adjacent cell wall compartment of the given cell. This promotes allocation of PIN towards the stressed cell wall, and towards the neighbour with elevated auxin. One problem with this model is that it is unclear whether auxin in a cell can influence the mechanical properties of only part of the surrounding wall. It is also unclear whether cells can measure stress differences in their cell walls.

A number of experimental observations were incorporated into a model of auxin-regulated PIN polarity that gives rise to behaviours similar to both flux-based and up-the-gradient models (Wabnik et al., 2010, 2013). The model includes PIN transcription, which is regulated by intracellular auxin (Vieten et al., 2005), and the constitutive endocytic recycling of PIN to and from the plasma membrane (Geldner et al., 2001). The model incorporates the experimental finding that extracellular auxin inhibits the endocytosis of PIN, thus promoting its presence in adjacent plasma-membrane regions (Robert et al., 2010). In the model, this is assumed to be mediated through auxin binding to a diffusible extracellular receptor. The cell wall is divided into two compartments and each compartment may have a different concentration of auxin and receptor

bound auxin. Auxin binding to the receptor in a given cell wall compartment slows the diffusion of the receptor and causes an inhibition of PIN endocytosis in the adjacent membrane compartment. Juxtaposed membrane regions thus compete for receptor-auxin complexes. Whichever membrane initially has higher PIN, will tend to have a higher concentration of auxin-receptor complexes at its side of the cell wall, and hence recruit more PIN to the membrane. Although some assumptions of this model are well supported experimentally, whether gradients in extracellular auxin can exist in the cell wall, given the fast diffusion rate of auxin (Kramer et al., 2007), the thinness of the cell wall, and the rates of auxin export and import into cells, is unclear. Also, it is unknown whether the extracellular auxin receptor candidate, ABP1, has the required diffusibility in the cell wall.

Thus, in summary, there are a number of models of auxin-regulated tissue cell polarity, which are able to capture patterns of PIN polarity in a number of developmental contexts. All of the models hypothesise cellular or molecular behaviours which have not yet been verified experimentally. To distinguish between models, it is necessary to highlight differences in their behaviours, and in their molecular assumptions, which may then be tested experimentally.

1.5 Gene expression patterns and polarity

One way that the validity of different models may be assessed is by testing their ability to account for patterns of polarity, given experimentally observed expression patterns of genes known to influence the polarity system in specific ways. Most models of auxin-regulated tissue cell polarity have been assessed for their ability to capture PIN and auxin distributions (Rolland-Lagan et al., 2005; Stoma et al., 2008). However, which models are most compatible with expression patterns of genes known to influence auxin and PIN, for example those that regulate PIN polarity, promote auxin biosynthesis, or regulate rates of auxin import into cells, has not yet been investigated. The

wall-gradient based model of Wabnik et al., 2010, was shown to be compatible with the expression patterns of auxin biosynthetic enzymes during *A.thaliana* embryogenesis (Wabnik et al., 2013). However, it is unclear whether other models are also compatible with this experimental data.

Another study investigated interactions between polarity generated through an up-the-gradient mechanism and expression of the *CUC2* transcription factor (Bilsborough et al., 2011). *CUC2* is required for PIN polarity reorientations that specify sites of new serrations in the margin of the *A.thaliana* leaf. A proposed model suggests that *CUC2* is required for the plasticity of cells to reorient their polarity according to an up-the-gradient mechanism (Bilsborough et al., 2011). However, exactly how *CUC2* may promote cellular plasticity, and whether its down stream functions and expression pattern are also compatible with other polarity models has not been investigated.

Here, I show that both plant and animal tissue cell polarity may be based upon a spontaneous, cell-intrinsic polarity generating system, such as that found in single cells. Combining this cellular polarity system with mechanisms that couple polarities of neighbouring cells, using planar cell polarity components in the case of animals, and auxin in the case of plants, leads to locally coordinated cell polarities. Modulation of the polarity systems at tissue boundaries may then cause coordination of polarity across entire tissues. This work leads to the development of a new indirect cell-cell coupling model of plant polarity based on explicit molecular interactions that are compatible with experimental data. I show how the behaviour of this new model is related to those of other published models. I then present new experimental data related to the mechanisms underlying PIN1 polarity patterns in wild-type and *kanadi1kanandi2* (*kan1kan2*)

mutant leaves of *A. thaliana* (the latter of which develop ectopic outgrowths). This includes characterisation of dynamic patterns of expression of auxin biosynthesis enzymes, auxin importers, and the *CUC2* transcription factor, and new evidence regarding the role of these factors in epidermal PIN1 polarity reorientations. The ability of different models to account for this data is compared, allowing models to be evaluated. I also show how the new indirect cell-cell coupling model can account for the simultaneous changes in polarity that occur in epidermal and sub-epidermal tissue during the development of a new outgrowth. Finally, I present a new model for how changes in PIN1 polarity in the cross-sectional plane of *kan1kan2* leaves may be related to changes in growth in this plane.

2 An intracellular partitioning-based framework for tissue cell polarity in plants and animals

2.1 Introduction

To understand the mechanisms underlying tissue cell polarity (the coordinated orientation of cell polarities across a tissue), it helps to define two basic types of coordination: lateral and longitudinal. These types of coordination can be illustrated for a single file of cells, in which polarities are aligned head-to-tail (longitudinal coordination, Fig. 2.1 A), or aligned lateral to the direction of polarity (lateral coordination, Fig. 2.1 B). Both types of coordination can occur together within a sheet of cells, as polarity of each cell in the plane may be aligned with both its flanking cells (lateral coordination) and those ahead or behind it (longitudinal coordination) (Fig. 2.1 C). Similar considerations apply to a 3D block of cells, except that lateral coordination can be extended to a further dimension (Fig. 2.1 D). A key problem is to understand how such patterns of lateral and longitudinal coordination may be established over extended domains.

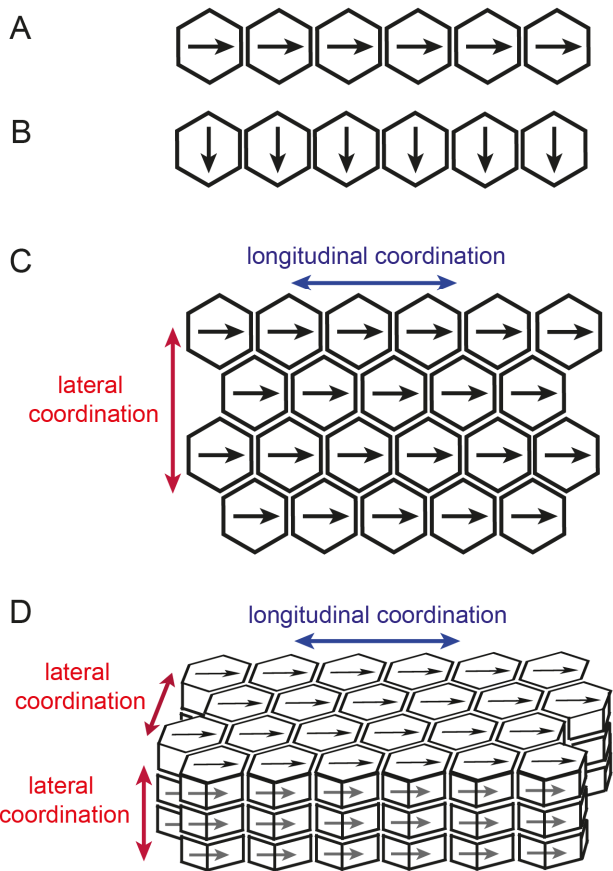


Fig. 2.1 Polarity coordination.

(A) Longitudinal coordination occurs in a single file of cells with polarities (indicated by arrows) aligned head-to-tail. **(B)** Lateral co-ordination occurs in a single file of cells with polarities aligned lateral to the direction of polarity. **(C)** Longitudinal and lateral co-ordination can both occur together in a sheet of cells. **(D)** For a 3D block of cells, lateral coordination of polarity may be extended to a further dimension.

One type of model, proposed for both plants and animals, assumes that neighbouring cells have the ability to compare concentrations of particular molecules and align their polarities accordingly. For example, a model for planar polarity coordination in *Drosophila* proposes that the level of Frizzled protein activity in neighbouring cells is compared so that the polarity of each cell becomes oriented towards the neighbour with the lowest Frizzled activity (Lawrence et al., 2007; Simon, 2004). Similarly, it has been proposed that plant cells orient their polarity according to the concentration of auxin in neighbours (Jönsson et al., 2006; Smith et al., 2006). Another type of model proposes that polarities are established through differential molecular interactions at cell interfaces, which may be modulated by graded signals. For example, it has been proposed that planar polarity in *Drosophila* depends on establishing different molecular complexes on either side of cell-cell interfaces, with a bias provided by signals that vary across and/or between cells

(Amonlirdviman et al., 2005; Burak and Shraiman, 2009; Le Garrec et al., 2006). Models of plant tissue cell polarity propose that polarity depends on measuring molecular fluxes across cell-cell interfaces, concentration gradients across extracellular spaces, or gradients in stresses across cells (Bayer et al., 2009; Heisler et al., 2010; Mitchison, 1980; Rolland-Lagan and Prusinkiewicz, 2005; Sachs, 1981; Wabnik et al., 2010).

Here, a framework is proposed that is based on cells having the ability to polarise in the absence of asymmetric cues or polarisable neighbours. We call this process intracellular partitioning. Tissue cell polarity may emerge by coordination of polarities established by intracellular partitioning, through coupling between neighbouring cells (cell-cell coupling) and operation of tissue polarity organisers. To illustrate how the intracellular partitioning-based framework may generate tissue cell polarity patterns, I present a series of simple models and explore their consequences through computer simulations, which are run until a stable state is reached (details of how computer simulations are implemented and the range of parameters explored can be found in the models description section). For simplicity, the analysis of tissue cell polarity is restricted to 1D cell files or 2D cell sheets.

Key features of the framework presented here are: (1) It is applicable to both plant and animal tissue cell polarity. Previous models of tissue cell polarity have considered plant and animal systems separately. I show how both systems may be viewed as involving cell-cell coupling which may be direct (animals) or indirect (plants). (2) It leads to a new model for polarity coordination in plants. In contrast to previously proposed plant models, the model proposed here does not invoke measurement of fluxes, comparison of concentrations between cells, response to physical stresses or measurement of gradients across the thickness of cell walls. (3) It allows different cell polarity systems to be placed in an evolutionary context.

2.2 Results

2.2.1 Intracellular partitioning

To illustrate how intracellular partitioning may operate, consider a simple system with two types of molecular component, A and B, the active forms of which will eventually define opposite ends of the cell. In reality, each component may comprise multiple molecular entities but for the sake of simplicity each component is treated as a single entity. The components can be in two states: an inactive cytosolic form, A or B, or an active membrane-bound form, A* or B* (Fig. 2.2 A, B). The inactive forms diffuse more rapidly than the active membrane-bound forms. The active forms are autocatalytic (i.e. A* promotes the activation of A to generate more A*), and cross-inhibitory (i.e. A* promotes deactivation of B* and *vice versa*). I refer to A, A*, B and B* as polarity components.

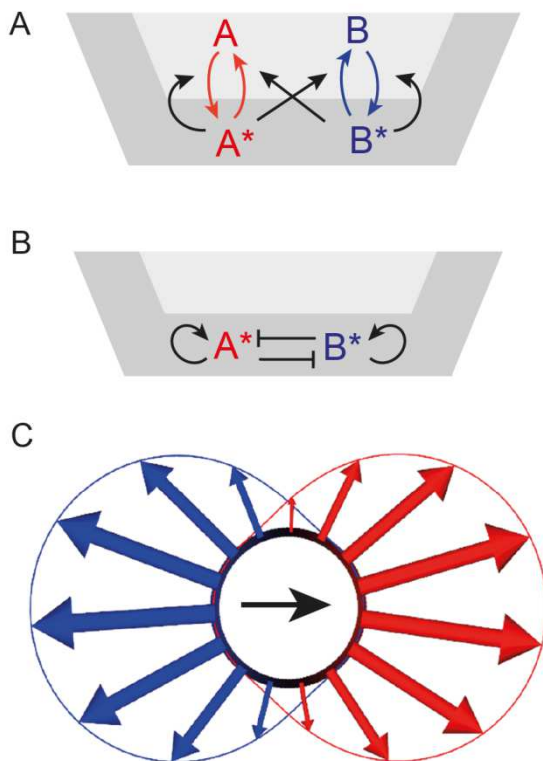


Fig. 2.2 System for intracellular partitioning. (A) Interactions between rapidly diffusing, cytosolic (A, B), and slowly diffusing, membrane-bound (A*, B*), forms of polarity components (dark grey compartment represents the membrane). Each polarity component can inter-convert between the inactive form in the cytoplasm and the active membrane-bound form. The active membrane-bound forms of the polarity components (A*, B*) promote membrane-binding and activation of their own component and promote the unbinding and inactivation of the opposite polarity component. (B) Short-hand notation for the interactions between polarity components, in which an arrow denotes auto-activation, while a line terminated by a small line segment denotes inhibition by the opposite polarity component. (C) Intracellular partitioning resulting from a simulation of the above interactions. The cell outline is indicated with a black circle. The concentration of A* in the cell membrane is indicated by the

distance from the cell outline to the red line (large red arrows indicate a high concentration of A^*), while the concentration of B^* is indicated by the distance to the blue line (large blue arrows indicate a high concentration of B^*). Cell polarity in this figure and in all subsequent figures is indicated by the black arrow in the cell which points from high B^* to high A^* . See model descriptions section for simulation details and parameter values.

Starting from a uniform concentration of polarity components in a cell and small random fluctuations (noise) in the concentration of A^* and B^* in the membrane, such a system may lead to a polarised distribution, with a high concentration of A^* at one end and B^* at the other end of the cell (Fig. 2.2 C; polarity is shown as pointing from the B^* to A^* cell ends in this figure and in all subsequent figures). This system is similar to other reaction-diffusion systems that generate polarity within individual cells (Meinhardt, 2007). With an initially uniform distribution of A^* and B^* across a tissue, and noise within cells (Fig. 2.3 A), intracellular partitioning leads to polarities that are oriented randomly from one cell to the next (Fig. 2.3 B, C). Non-polarised cells arise if intracellular partitioning components are absent or fail to interact effectively.

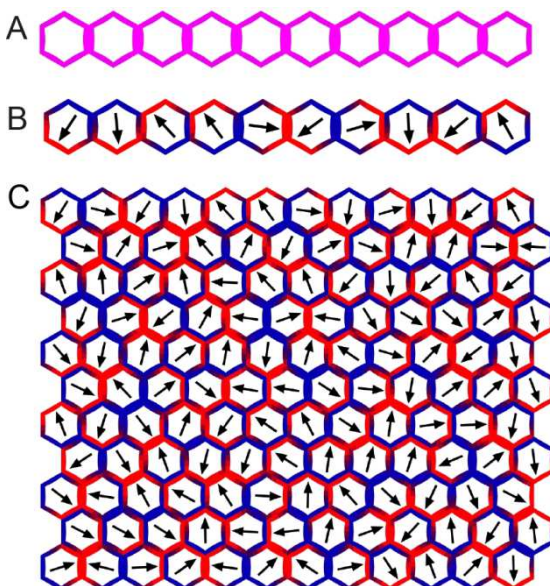


Fig. 2.3 **Polarity pattern generated through intracellular partitioning.**

(A) A single file of cells in the initial state with A^* and B^* having a uniform distribution. **(B)** A single file of cells in the final computed state, with polarities resulting from the intracellular partitioning mechanism with no interaction between cells. **(C)** The result of intracellular partitioning with no interactions between cells for a 2D array of cells.

2.2.2 Cell-cell coupling

Intracellular partitioning may be built upon to generate a more coordinated polarity pattern by incorporating interactions at interfaces of neighbouring cells. This process of cell-cell coupling may lead to local alignment of polarities. Cell-cell coupling may involve direct molecular contacts between juxtaposed cells or indirect interactions mediated by diffusible molecules.

2.2.2.1 Direct Cell-Cell Coupling

Assume that A^* in a given cell can physically interact with B^* in the juxtaposed membrane of its neighbour, forming an intercellular A^*-B^* bridging complex. The intracellular partitioning mechanism described above may be modified such that autoactivation and/or cross-inhibition are influenced by the A^*-B^* complex. For example, suppose the A^*-B^* complex inhibits A^* on the B^* side of the complex (Fig. 2.4 A). Computer simulations of this system show that an initially uniform (but noisy) distribution of A^* and B^* in a single file of cells (Fig. 2.4 C) can eventually give rise to regions of aligned polarity (Fig. 2.4 D).

The role of the A^*-B^* complex may be extended such that all of the auto-activation and cross-inhibition interactions are dependent on it (Fig. 2.4 B). In this case, uncomplexed A^* and B^* have no role other than allowing formation of A^*-B^* complexes, while the rapidly diffusible A and B forms still play a role in intracellular partitioning. This system also gives rise to regions of locally aligned polarity (Fig. 2.4 E). With this model, an isolated cell (i.e. a cell with no neighbours) no longer becomes polarised because it is unable to form A^*-B^* complexes. Nevertheless, an individual cell within a group of cells that are incapable of polarising can become polarised through its own intracellular partitioning system. This may be illustrated by removing the ability of cells to polarise by setting the diffusion rates of A and B to be equal to the diffusion rates of A^* and B^* (Fig. 2.4 F). If fast diffusion of A and B is then restored to a single cell which is flanked by

neighbours with equal diffusion rates of all polarity components, the single cell is able to polarise (Fig. 2.4 G). I use this model (illustrated in Fig. 2.4 B) for all further simulations involving direct cell-cell coupling.

A further step towards dependency on neighbours is illustrated by a model for tissue polarity proposed for *Drosophila* in which a diffusible component (C^*) creates an effective repulsion between the two orientations of the membrane-spanning complexes (A^*-B^* and B^*-A^*) (Burak and Shraiman, 2009). In this model, the B^* end of the complex promotes production of C^* within the same cell, which then inhibits the complexes in which A^* is located within that cell. Considering a cell in isolation, this would lead to all complexes being oriented with B^* pointing into that cell, because inward pointing B^* can inhibit inward A^* but not vice versa. In the presence of neighbouring cells, inhibition becomes mutual because inward A^* can now inhibit inward B^* by influencing production of C^* in the neighbouring cell (via the B^* end of the complex which points into the neighbour). Consequently, in such a model, polarisation of a cell depends on its neighbours also having an intact polarisation system. All above models can give rise to direct cell-cell coupling but can be distinguished experimentally by defining the cellular contexts under which individual cells can become polarised.

When applied to a 2D array of cells, direct cell-cell coupling models lead to locally coordinated groups of cells, or swirled patterns of orientations (e.g. Fig. 2.4 H and (Burak and Shraiman, 2009). In these cases coordination is both longitudinal and lateral.

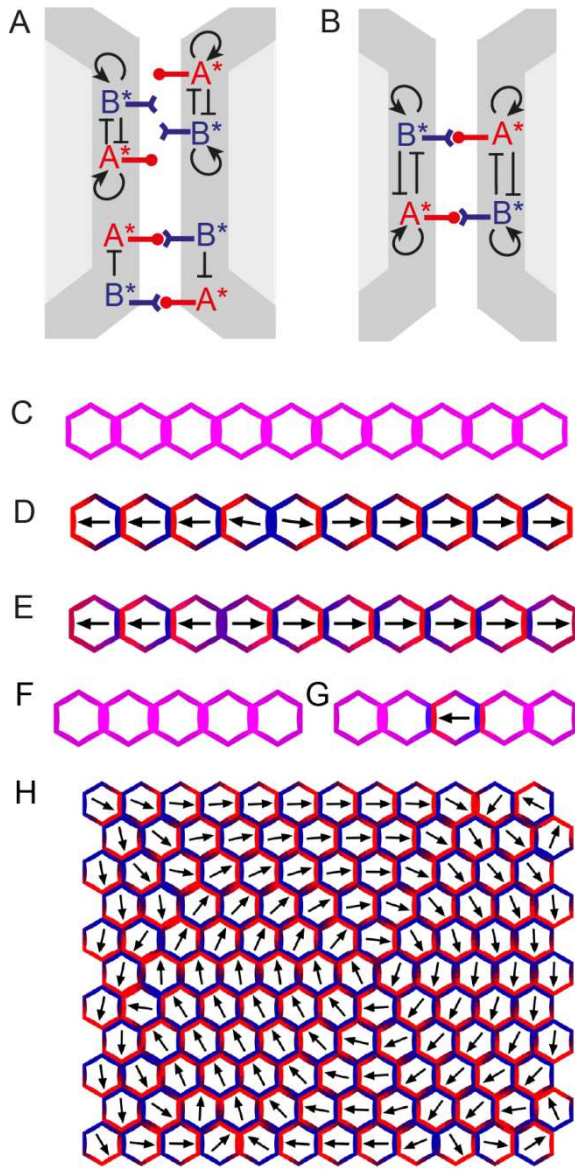


Fig. 2.4 Direct cell-cell coupling.

(A) A model for the direct cell-cell coupling system. A^* and B^* in the membrane of each cell (dark grey compartment) form an intercellular A^* - B^* bridging complex. In the membrane at the B^* side of the complex, A^* - B^* inhibits A^* . Interactions between uncomplexed A^* and B^* components lead to intracellular partitioning. **(B)** Model in which all of the auto-activation and cross-inhibition interactions are dependent on formation of the A^* - B^* bridging complex. **(C)** Initial state of direct cell-cell coupling system for a single file of cells. **(D)** Result of direct cell-cell coupling using the interactions described in A) for a single file of cells. Note that two groups with coordinated polarity have formed. **(E)** Result of direct cell-cell coupling using the interactions described in B) for a single file of cells. **(F)** Cells do not become polarised when the A and B components have the same diffusion constants as A^* and B^* . **(G)** Restoration of the higher diffusion rate for A and B to the central cell leads to it becoming polarised, even though its neighbours retain the lower diffusion rate for A and B . **(H)** Direct cell-cell coupling in a 2D array of cells. Polarities show swirled organisation with local stretches of coordination.

2.2.2.2 Indirect Cell-Cell Coupling

In plants, the presence of the cell wall presents a major barrier to direct interactions between proteins in the plasma-membranes of adjacent cells. (There are channels through plant cell walls, called plasmodesmata, but it is currently unclear whether they play a role in control of tissue cell polarity.) Therefore, I present a way that cell-cell coupling could occur indirectly through use of the small diffusible molecule, auxin. Consider again the direct cell-cell coupling model in which

the only role of the A^* - B^* membrane spanning complex is inhibition of A^* at the B^* end of the complex (Fig. 2.4 A). With this system, A^* in one cell effectively inhibits formation of A^* in the juxtaposed membrane of its neighbour. Fig. 2.5 A shows a parsimonious way of achieving an equivalent process in a system where direct cell-cell contacts cannot be made. In this case, A^* in one cell promotes export of auxin, which can diffuse through the extracellular space. This extracellular auxin triggers a membrane receptor that then locally inhibits A^* in the membrane (i.e. auxin favours B^* over A^*). This system could allow A^* in the cell exporting auxin to inhibit A^* in its neighbour. However, an apparent problem is that extracellular auxin also causes inhibition of A^* in the exporting cell. This is because auxin affects both cells equally (dotted arrows Fig. 2.5 A). Thus, intuitively it seems that such a system may not generate cell-cell coupling.

However, computer simulations show that this indirect system can generate longitudinal coordination of cell polarities in a single file of cells, despite extracellular auxin acting equally on both membranes at each cell-cell interface (Fig. 2.5 B). In these simulations it is assumed that both intracellular and extracellular auxin diffuse rapidly compared to A^* and B^* , and that auxin is produced and degraded at uniform rates in all cells. It is also assumed that auxin can move across the cell membrane independently of polarity components, with a higher permeability for cell entry than exit. A cell that has been polarised through intracellular partitioning thus exports auxin at the A^* -rich end, while importing auxin passively at other locations, giving a flow of auxin along its polarity. Because auxin flows in the same direction as the cell polarity, it tends to accumulate within cells at the end of the cell file to which the polarity points (right end in Fig. 2.5 B). Thus cells end up pointing towards a region with high intracellular auxin concentration.

Local coordination of polarities arises providing that elevated levels of extracellular auxin favour the presence of B^* over A^* in the membrane. This can either be achieved through extracellular auxin promoting the unbinding of A^* from the membrane, or through extracellular auxin

promoting the binding of both A^* and B^* to the membrane, with a higher rate of promotion of B^* compared with A^* . In the simulations presented in the rest of this chapter, I use the simpler assumption that extracellular auxin promotes the unbinding of A^* . However, very similar results are obtained for all simulations presented here if extracellular auxin promotes the binding of both components, with a preference for B^* over A^* .

In this system, cell polarities are generated through the intracellular partitioning system: if A^* and B^* do not autoactivate and cross-inhibit then cells have no polarity (Fig. 2.5 D). Indirect coupling then coordinates polarities between neighbours. To understand how polarity coordination arises, consider a scenario in which all cells have polarity aligned except for one cell (labelled R in Fig. 2.5 C), which has opposite polarity compared to the others. In this situation, extracellular space at the A^* end of the R cell (left end) has high concentrations of extracellular auxin, because it is flanked on both sides by A^* -rich membranes (and A^* promotes export of auxin). These high levels of extracellular auxin diminish A^* at this end of the R cell (as auxin inhibits A^*) as well as along the adjacent membrane of its left neighbour. The other end of the R cell (right end) has low levels of extracellular auxin because auxin is transported away from the extracellular space on both sides. Low levels of auxin favour A^* , both along the right membrane of cell R, as well as along the adjacent membrane of its right neighbour. While cell R is in an unfavourable situation along both membranes, its flanking neighbours are only so along one of their membranes. Taken together, these processes would therefore be expected to reverse the polarity of the R cell alone, and thus align it with the other cells of the file.

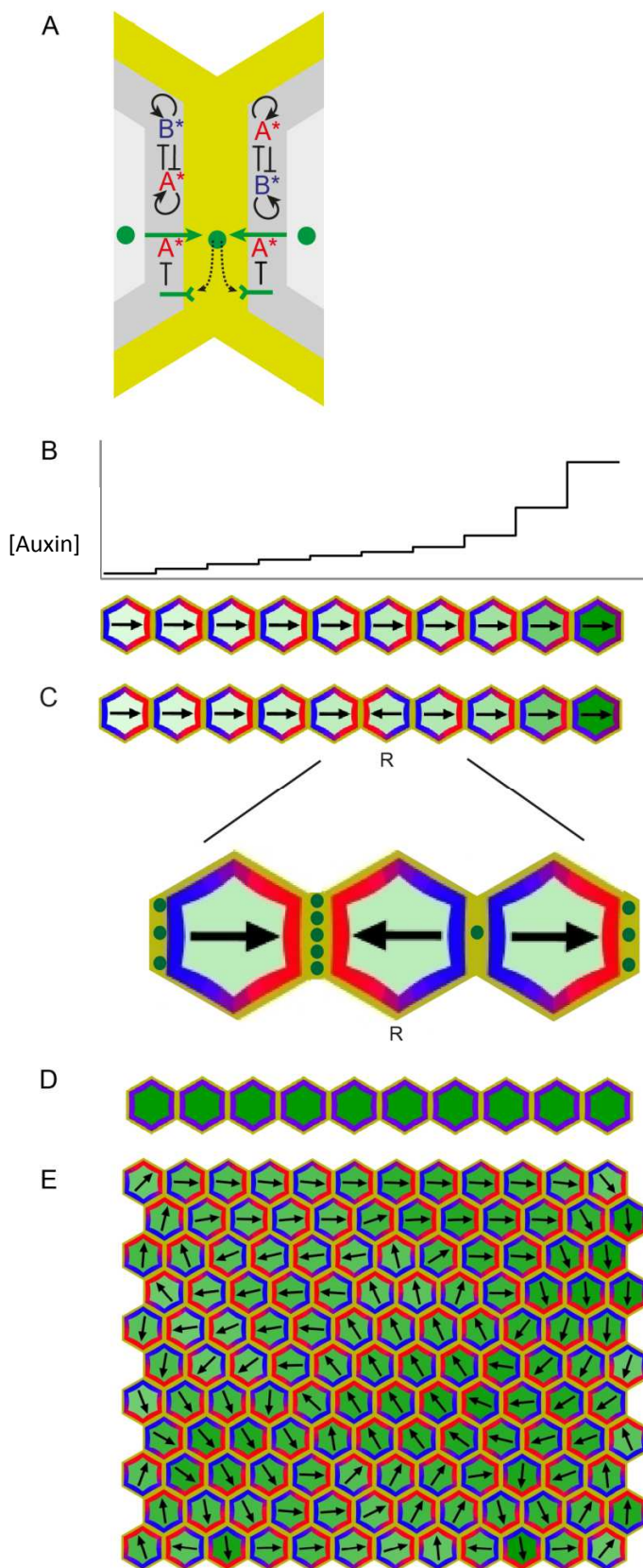


Fig. 2.5 Indirect cell-cell coupling.

(A) Interactions at a cell-cell interface for an indirect cell-cell coupling mechanism in which A^* in the membrane (dark grey compartment) promotes export (green arrow) of auxin, (green dots) that can diffuse through the cell wall (yellow compartment), and trigger a receptor (green Y-shape) that then inhibits A^* . The distributions of A^* and B^* become polarised through intracellular partitioning. **(B)** Indirect cell-cell coupling for a single file of cells. The graph (top) shows the total intracellular concentration of auxin in each cell in the file. The concentration of intracellular auxin in each cell is also indicated by the intensity of green in the file of cells (bottom). For cell walls at the outer boundary of the tissue, there is no exchange of auxin with the surrounding medium. **(C)** The cell labelled R has an opposite polarity with respect to the rest of the cells in the file. In the left wall of cell R, high levels of auxin (green dots) accumulate and inhibit A^* in the adjacent membranes. In the right wall of cell R, low levels of auxin favour A^* . The net result of these interactions is that the polarity of the R cell reverses and thus aligns with the rest of the file. **(D)** If polarity components do not cross-activate and mutually inhibit there is no intracellular partitioning and polarity is lost with an indirect cell-cell coupling system. **(E)** Result of indirect cell-cell coupling for a 2D array of cells. Polarities show swirled organisation with local stretches of coordination.

An attractive feature of indirect cell-cell coupling is that it does not require reading of gradients in auxin across the thickness of the extracellular space or gradients of auxin in the cytoplasm along the length of the cell. Indeed, in this implementation of indirect cell-cell coupling it is assumed that the level of auxin is uniform both within the cytoplasm of a cell and across the thickness of the extracellular space, although the system also works if gradients of auxin are allowed to form within cells.

When the indirect cell-cell coupling model is applied to a 2D array of cells, it leads to locally coordinated groups of cells, or swirled patterns of orientations, which are both laterally and longitudinally coordinated (Fig. 2.5 E). Thus, the outcomes of indirect and direct cell-coupling are comparable (compare Fig. 2.4 H and Fig. 2.5 E).

These models reveal how cell-cell coupling in both plant and animal systems can be viewed as different elaborations of a common underlying intracellular partitioning system. By contrast, it is unclear how previous models, which do not incorporate intracellular partitioning (e.g. (Burak and Shraiman, 2009)) , could be extended to both systems.

2.2.3 Organising polarity across a tissue

In many cases, cell polarity is coordinated across a large domain of tissue, such as a wing or leaf. Moreover, this polarity is related to the overall morphology of the structure, such as its proximodistal axis. Such organisation suggests that there are reference regions in the tissue which actively influence polarity and from where polarity information propagates. I refer to these reference regions as *tissue polarity organisers* (Green et al; 2010). The term organiser has been used in several developmental contexts (e.g. (Sabatini et al., 1999; Spemann and Mangold, 1924)),

but here I use it specifically in relation to the coordination of tissue cell polarity. Because cell polarity can be influenced to point away from or towards organisers, it is convenient to refer to two types of tissue cell polarity organiser, plus (+) or minus (-) respectively, according to their resultant effect on polarity. Although regions of organiser activity are often expected to be associated with sites of polarity divergence (+) or convergence (-), such polarity patterns are not sufficient to infer the local presence of an organiser because they may also arise through polarity propagation from organisers located elsewhere. There are various mechanisms by which tissue cell polarity organisers may influence cell polarity over an extended domain. These mechanisms need not be mutually exclusive. I first show how organisers may function through direct modulations of polarity components, then tissue gradients, and finally through modulation of auxin levels for systems with indirect cell-cell coupling.

2.2.3.1 Direct Modulation of Polarity Components

Cell-cell coupling together with intracellular partitioning generates swirls of polarity in a 2D array of cells (Fig. 2.4 H and Fig. 2.5 E). To produce polarity that is coordinated with respect to the tissue, polarity components of this system can be modulated at tissue boundaries. With direct cell-cell coupling, for example, expression of only A and A* in a column of cells at the left boundary of the tissue and only B and B* in a column at the right boundary, results in a pattern in which polarity points from left to right across the tissue (Fig. 2.6 A). The presence of only A* in leftmost cells causes B* to be elevated in the juxtaposed membrane of their right neighbours, through cell-cell coupling, giving the neighbours a rightwardly oriented polarity (cell polarity points from the B*-rich to the A*-rich end). The same effect then propagates through cell-cell coupling to the cells further along to the right. Similar considerations apply to the right boundary expressing only B*. Using direct modulation of polarity components as organisers of tissue polarity can only coordinate polarity over tissues with a limited size: for tissues with a larger

distance between the left and right boundaries, or with an increased level of noise in the initial conditions of the simulation, coordination breaks down and local swirled patterns of polarity arise (not shown) (Burak and Shraiman, 2009).

As with other models, the effect of introducing mutant patches into this model may be simulated, as these predict patterns that can be evaluated experimentally through creation of clones (Lawrence et al., 2007). When mutant patches are introduced, polarity reversals are generated in the surrounding tissue. For example, a mutant patch that lacks A^* (and thus only expresses B^*) exhibits polarity reversal towards the right end of the patch (Fig. 2.6 B). The patch is effectively acting as a $(-)$ organiser. The outer cell border within the mutant patch exhibits inwardly-oriented polarities with respect to B^* concentrations (polarity points away from the B^* -rich end). This is because the A^* in the wild-type neighbours draws B^* in mutant border cells towards them through cell-cell coupling. The resulting inwardly oriented polarity of mutant cells is restricted to cells on the border of the patch, as cells further in do not have neighbours with A^* .

For indirect cell-cell coupling, polarity coordination may arise in a similar manner (Fig. 2.6 C). In this case coordination arises because cells at the left boundary, which express only A^* , export auxin at all locations around their membranes (A^* promotes auxin export) while cells at the right boundary only import auxin (because they lack A^*). This creates a high level of extracellular auxin at the left boundary of the tissue and a low level at the right boundary. This situation favours A^* at the right end of the cells near the boundaries (extracellular auxin inhibits A^*), biasing the orientation of polarity to point rightwards. The level of intracellular auxin becomes high in the $(-)$ organiser at the right boundary, because cells continually pump auxin towards it.

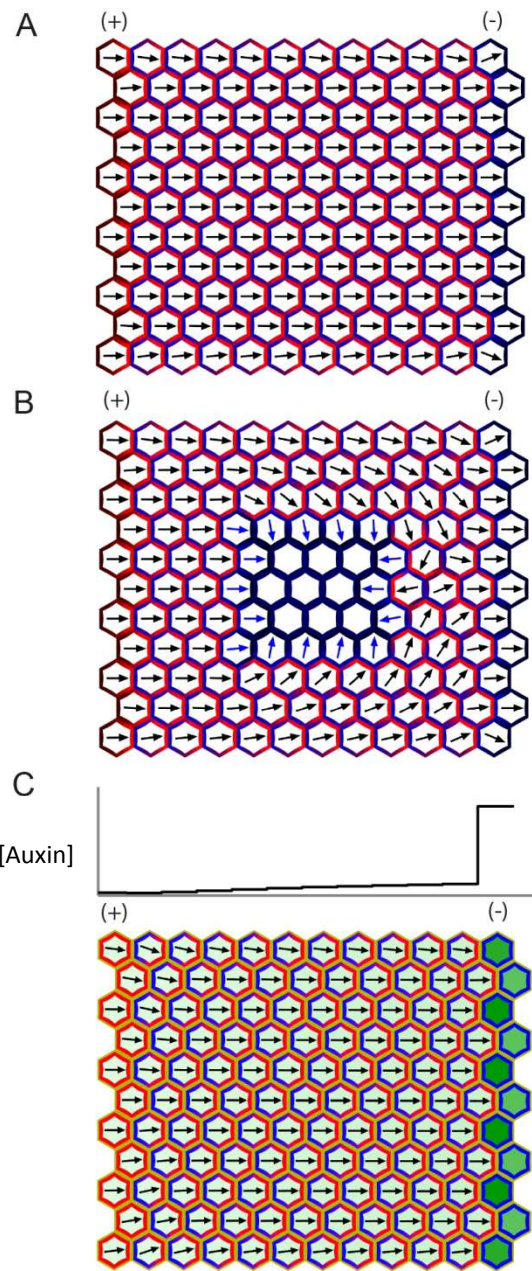


Fig. 2.6 Organisation of polarity through direct modulation of polarity components.

(A) A file of cells at the left expressing only A and A* (+) and a file at the right expressing only B and B* (-), along with direct cell-cell coupling, leads to an organised left-right polarity pattern across the tissue. Polarity in cells expressing only B is shown with respect to B* distribution (arrows point towards regions with the lowest B* concentration). **(B)** A mutant patch of cells lacking A and A* causes polarity reversal of wild-type tissue surrounding the right end of the patch (direct cell-cell coupling). **(C)** As for (A) but with indirect cell-cell coupling. Graph (top) shows the concentration of intracellular auxin per cell for a single row of cells in the grid. The concentration of intracellular auxin is also indicated by the intensity of green within each cell in the grid (bottom).

2.2.3.2 Tissue Gradients

A further way of coordinating tissue cell polarity is through concentration gradients. Suppose there is a concentration gradient along a single file of cells for a signalling molecule S (Fig. 2.7 A).

In principle, the distribution of S carries two types of information. One is the gradient along the length of each cell, as each cell has a higher concentration of extracellular S at its left compared to its right end (Fig. 2.7 B). This is referred to as a cellular gradient. The other type of information is the gradient between cells: the average concentration of S surrounding a cell is higher than that for its right neighbour and lower than that for its left neighbour (Fig. 2.7 C). This is referred to as an intercellular gradient. I next show how the cellular and intercellular aspects of the S gradient

may lead to coordinated polarity for 2D cell arrays.

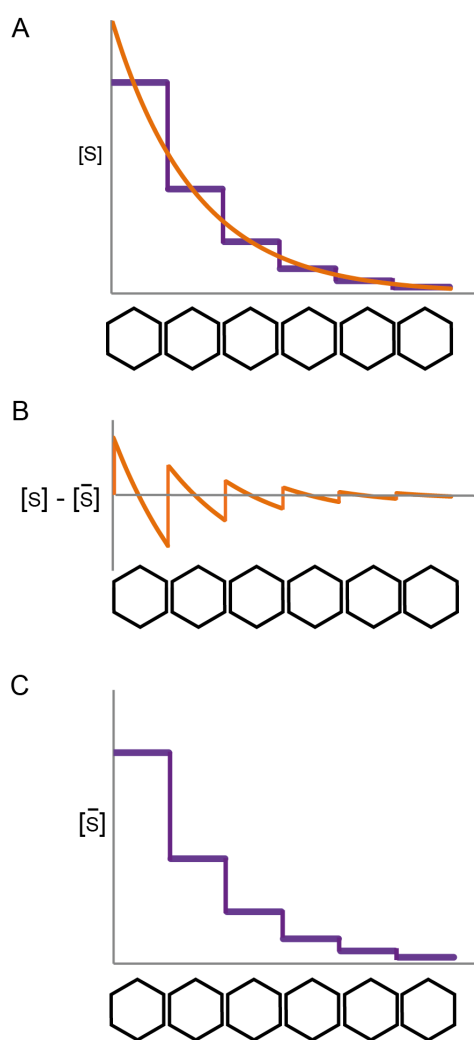


Fig. 2.7 Two aspects of a concentration gradient.

(A) The information in a gradient in $[S]$ across a tissue (orange) can be broken down into two separate types (B and C). **(B)** The cellular gradient (orange line) is displayed by plotting the difference between the concentration of S ($[S]$) at a given point along a cell and the mean concentration of S surrounding that cell ($\bar{[S]}$) i.e. $([S] - \bar{[S]})$. **(C)** The intercellular gradient (purple line) is displayed by plotting the mean concentration of S surrounding a cell ($\bar{[S]}$).

2.2.3.2.1 *Cellular Gradients*

I begin with an array of cells with an intracellular partitioning system but no cell-cell coupling. S is produced at a high rate by the leftmost cells, degraded at a high rate by the rightmost cells, and diffuses in the extracellular space producing a left-to-right graded decline in S concentration. It is assumed that the concentration of S at each location in the extracellular space can be sensed through a membrane-bound receptor for which S is a ligand, and that triggering of the receptor promotes local conversion of A to A*. According to this system, each cell within the array will tend to have more A* in the membrane at its left end, relative to its right end, because of the gradient in S across the cell. This will bias the intracellular partitioning process such that the A*-rich end will form at the left of all cells. Because the gradient in S across the cell has the same orientation for all cells, cell polarities are oriented leftward throughout the tissue, pointing up the S gradient (Fig. 2.8 A). In this case the left boundary cells producing S at a high rate serve as the -organiser, while the right boundary where S is degraded at a high rate acts as a +organiser. If, alternatively, S promoted the conversion of B to B*, cell polarities would be oriented rightward throughout the tissue (down the S gradient), the left boundary would serve as a +organiser and the right boundary would act as a - organiser.

With this system, coordination of polarity depends on the extent to which concentration gradients of S are aligned between cells. Polarity components are not directly involved in tissue coordination and thus act cell autonomously. A patch that lacks A*, for example, does not influence the polarity of the surrounding wild-type cells and the cells within the patch have no polarity (Fig. 2.8 B). By contrast, a mutant patch with a high degradation rate of S will influence the polarity of the tissue surrounding it by influencing neighbouring cellular concentration

gradients (Fig. 2.8 C). The gradient across cells near the right end of the patch will be reversed because they are adjacent to a region with low S concentration. As this mechanism depends on cellular gradients in S, it may become less effective for larger tissues as the gradient becomes shallow.

The above analysis assumes that cellular gradients in S act on a system with intracellular partitioning but no cell-cell coupling. If the system incorporates cell-cell coupling, similar results are obtained, except that a mutant patch lacking A* shows polarity reversal (at its left end, Fig. 2.8 D). In addition, incorporation of cell-cell coupling allows coordinated polarity to extend further into the regions where the gradient in S is shallow (not shown).

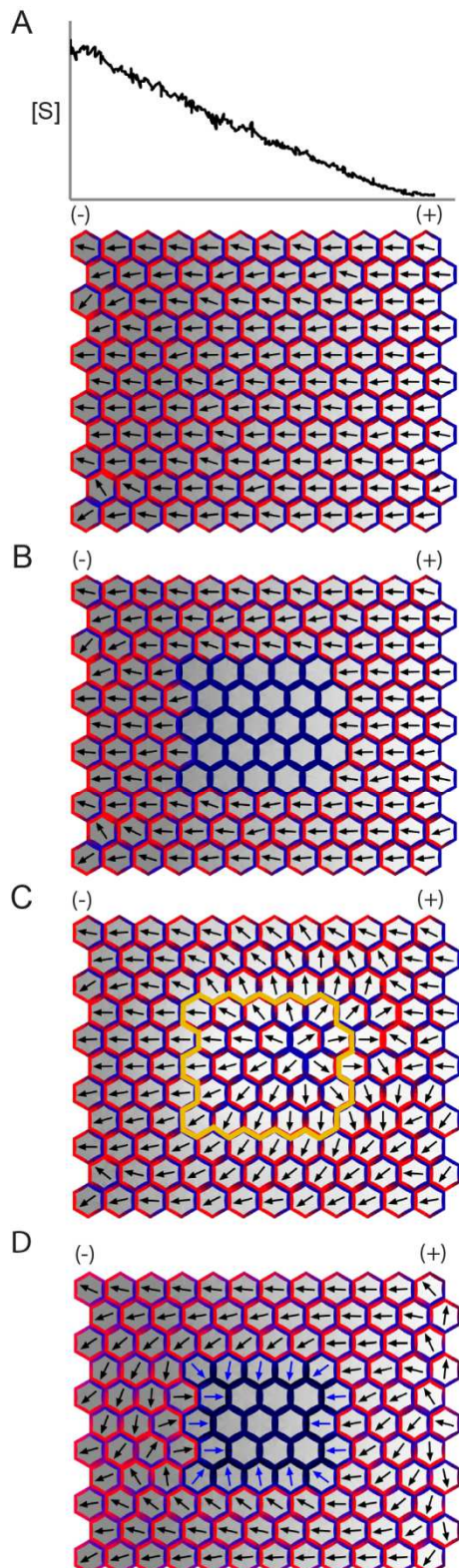


Fig. 2.8 Organisation of polarity through cellular gradients.

(A) With a system of intracellular partitioning without cell-cell coupling, signalling factor S is produced at a high rate in the column of cells at the left boundary (- organiser) and degraded in the column at the right boundary (+ organiser) and diffuses in the extracellular space. Small fluctuations in the concentration of S are also incorporated, yielding a noisy gradient. Extracellular S is detected in the membrane and promotes conversion of A to A*, leading to an organised right-left polarity pattern across the tissue. The graph displays extracellular S concentration, plotted against the position along the x-axis, for a single row of cells in the grid. Intensity of grey within each cell indicates the extracellular [S]. **(B)** A mutant patch lacking A and A* does not interfere with the polarity of the surrounding wild-type tissue because of the absence of cell-cell coupling. Cells within the mutant patch are not polarised. **(C)** A mutant patch with a high degradation rate of S (patch outlined in yellow) causes polarity reversal in cells surrounding the right of the patch. **(D)** In a system where cellular gradients are combined with direct cell-cell coupling, a mutant patch lacking A* shows polarity reversal at its left end.

2.2.3.2.2 Intercellular Gradients

Consider a case in which extracellular S is graded across the tissue and that it promotes production of a factor, F, within each cell, in proportion to the total level of S in the cell surroundings. In this case, the gradient in extracellular S leads to a stepped response, corresponding to the level of F in each cell. F is uniform

within each cell but is graded across the tissue so that each cell has a higher level of F than its right neighbour, forming an inter-cellular gradient (Fig. 2.9 A). Suppose that F within a cell

increases production of the A polarity component above a basal rate of F-independent production. For example, F might be a transcription factor involved in generating A. Such a situation is captured in the model by simply assuming that a higher level of F in the cell leads to raised levels of both A and A* (the concentration of A* is dependent on A). Thus, each cell has a neighbour to its left with a slightly higher overall concentration of both A and A* (except for cells at the left boundary which have no left neighbours). If it is assumed that this promotion of A levels operates in a system with direct cell-cell coupling, the slight excess of A* in the left neighbour will tend to bias B* towards the left of the cell. Polarity will therefore be coordinated to point left to right (from B*-rich to A*-rich ends) across the tissue (lateral and longitudinal coordination). Thus, even in the absence of intracellular gradients in F, an organised pattern of tissue cell polarity emerges (Fig. 2.9 A). In contrast to the cellular gradient mechanism, in this case a high level of S (and thus F) corresponds to a + organiser while a low level corresponds to a - organiser, even though in both cases S is enhancing A* (compare polarity orientations in Figs 8A and 9A). A mutant patch that lacks A* causes polarity reversal at its right end (Fig. 2.9 B). The outer cell border within the mutant patch exhibits inwardly-oriented polarities with respect to B* concentrations, as described earlier (Fig. 2.6 B and Fig. 2.8 D). Similar results have been obtained with other direct cell-cell coupling models (Burak and Shraiman, 2009; Le Garrec et al., 2006).

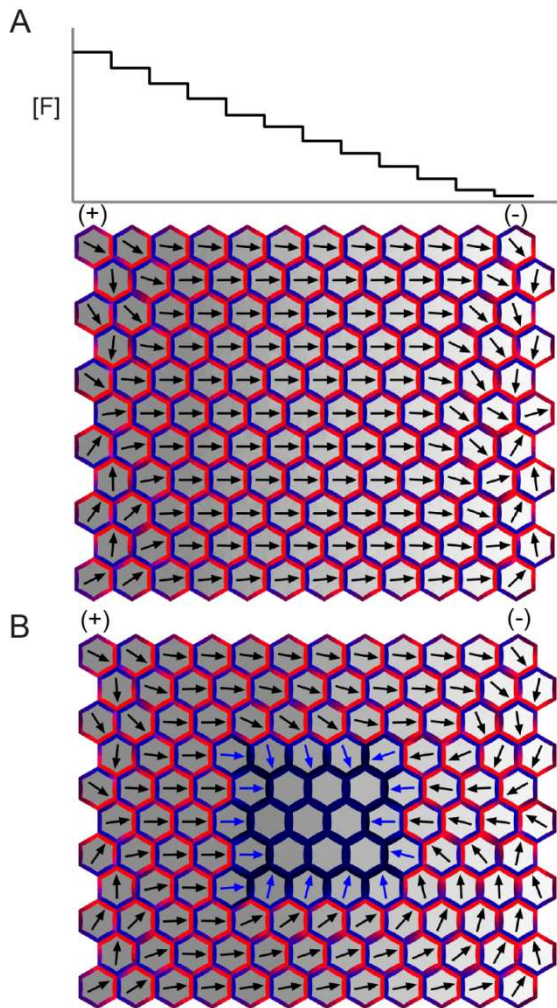


Fig. 2.9 Organisation of polarity through intercellular gradients.

(A) A signalling factor S is produced at a high rate in cells at the left boundary (+ organiser) and degraded at the right boundary (-organiser). S promotes production of a factor, F, within each cell, in proportion to the total level of S in the cell surroundings, creating an intercellular gradient of F across the tissue. The graph displays the concentration of F per cell for a single row of cells in the grid. The intensity of grey within each cell indicates the concentration of F. F promotes the total levels of A (A plus A^*), and the intercellular gradient in A^* leads to an organised left-right polarity pattern across the tissue. The cells near the left and right boundaries of the tissue deviate and do not have a clear left-right polarity orientation because these cells have no neighbours to one side. **(B)** A mutant patch unable to make A^* causes polarity reversal in wild-type tissue surrounding the right border of the patch.

2.2.3.3 Modulating Auxin Levels

For systems based on indirect cell-cell coupling, tissue cell polarity organisers may also act by influencing auxin production or degradation. If auxin is produced at a higher rate in the column of cells at the left boundary and degraded at a higher rate in the column at the right, then polarity can become organised across the tissue, pointing from left to right (lateral and longitudinal coordination, Fig. 2.10 A). This coordination partly arises because the gradient in extracellular auxin across the cells, generated by non-directed transport, inhibits A^* at the left end of each cell, biasing polarity. However, in the absence of indirect cell-cell coupling this would only coordinate polarity of cells near the boundaries, as shown in simulations in which A^* does not affect export of auxin (Fig. 2.10 B). Incorporation of indirect cell-cell coupling then allows this coordination to

propagate through the tissue (Fig. 2.10 A). In this situation the leftmost column of cells is acting as a + organiser while the rightmost column acts as a – organiser.

According to this model, the +organiser corresponds to a region that produces auxin at a high rate while the –organiser corresponds to a region that degrades auxin. The steady state intracellular level of auxin is high in +organiser regions and low in –organiser regions. If the degradation rate of auxin in the right file is not sufficiently high, then auxin can accumulate in the rightmost column of cells through transport. This accumulation in turn leads to high levels of extracellular auxin at the right boundary which may lead to polarity disruption as the cells at the right boundary switch from being sinks to sources of auxin (Fig. 2.10 C). This effect may be counteracted if cells in the rightmost column are unable to export auxin (e.g. lack A*, Fig. 2.10 D). In this situation, the cells on the right can accumulate intracellular auxin through transport towards them, while their extracellular auxin is kept low because of the higher permeability of cells for auxin entry than exit. Thus, the +organiser at the left boundary now has low levels of intracellular auxin as it exports auxin at a high rate, whereas the –organiser at the right boundary has high levels of intracellular auxin as it imports auxin at a high rate. A similar result is obtained if cells at the right boundary import auxin at a higher than basal rate, instead of exporting auxin at a reduced rate.

In all cases auxin flows along the direction of polarity, but it can appear to flow either to a region with high intracellular auxin concentration (Fig. 2.5 B and Fig. 2.10 D) or low intracellular auxin concentration (Fig. 2.10 A), depending on whether organisers influence production and degradation of auxin, and/or export and import of auxin.

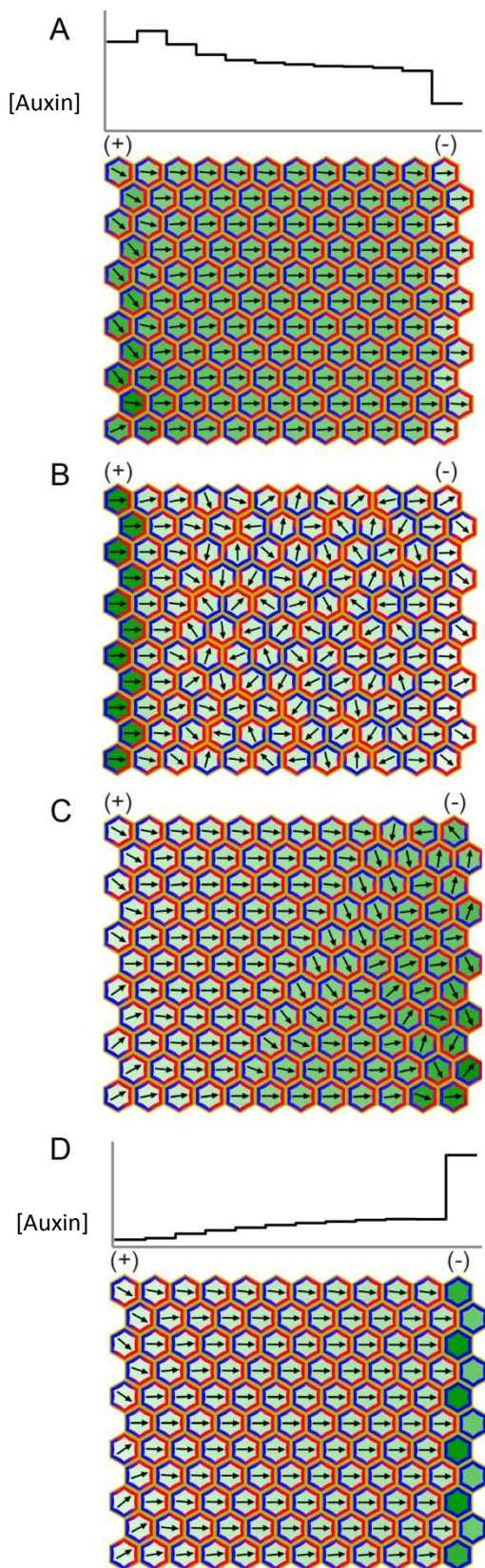


Fig. 2.10 Organisation of polarity by modulation of auxin levels.

(A) With an indirect cell-cell coupling system, a high production rate of auxin in the leftmost column of cells, combined with a high degradation rate in the rightmost column, biases the orientation of polarity across the tissue. The graph shows the concentration of intracellular auxin per cell for the top row of cells of the array. The intensity of green within cells indicates the concentration of intracellular auxin. **(B)** Same as (A) but A^* does not promote export of auxin. **(C)** If the degradation rate of auxin at the rightmost column is not sufficiently high relative to the production rate in the leftmost column, then auxin can accumulate at the right boundary of the tissue, causing disruption and instability of polarity coordination. **(D)** Combining the production and degradation rates used in (C) with removal of A^* in the rightmost column of cells restores coordinated polarity. In this case, intracellular auxin concentration is highest in the rightmost column of cells (-organiser).

2.2.4 Effects of Cell Geometry

The simulations for single cell files show that cell-cell coupling provides an effective mechanism for longitudinal coordination of polarity (Figs. 2.4 D, 2.4 E, 2.5 B). However, analysis of 2D arrays shows that cell-cell coupling also generates a degree of lateral coordination, illustrated by swirled patterns of polarity (Figs. 2.4 H, 2.5 E). Lateral coordination may arise because cells are not organised in distinct files in the 2D arrays but are interlaced. To test this idea, I applied cell-cell coupling to a 2D array comprising a grid of square cells. With this cellular configuration, broad swirls of polarity are no longer observed (Fig. 2.11 A, B). Instead, polarity can be coordinated longitudinally along single cell files, with lateral neighbours often showing opposite polarities as this pattern maximises contact between A^* and B^* in neighbours. However, in contrast to coordination systems based on cell-cell coupling, those involving intracellular partitioning combined with cellular gradients (Fig. 2.8 A-C) are relatively insensitive to cell geometry (Fig. 2.11 C). This is because cell polarity orientation is determined by cell autonomous reading of the gradient in S and is thus independent of cell neighbours. For a system with cell-cell coupling and cellular gradients, the degree of lateral coordination obtained on a grid of square cell depends on the steepness of the gradient in S and the relative strengths of cell-cell coupling and the influence of the gradient (not shown).

These simulations illustrate the effect of cell shape and configurations on cell-cell coupling mechanisms in regular arrays. However, in many biological situations, cells do not have completely regular geometries and sizes. Irregularities are inevitable during periods of cell proliferation if cells divide asynchronously and do not rearrange rapidly. If cell-cell coupling systems are applied to a grid of cells with irregular shapes, both lateral and longitudinal coordination still occur, as evidenced by swirled patterns, but are less effective than with hexagonal cells using the same parameters (Fig. 2.11 D, E, compare with Figs. 2.4H, 2.5E). Similar

effects of lattice disorder on polarity coordination have been described for other models that invoke cell interface interactions (Ma et al., 2008). With irregular cell geometries, organisers of tissue polarity lead to polarity coordination, although this is less effective than for hexagonal cells (Fig. 2.11 F, G, H, I, compare with Figs. 2.6 A, 2.6 C, 2.9 A and 2.10 A).

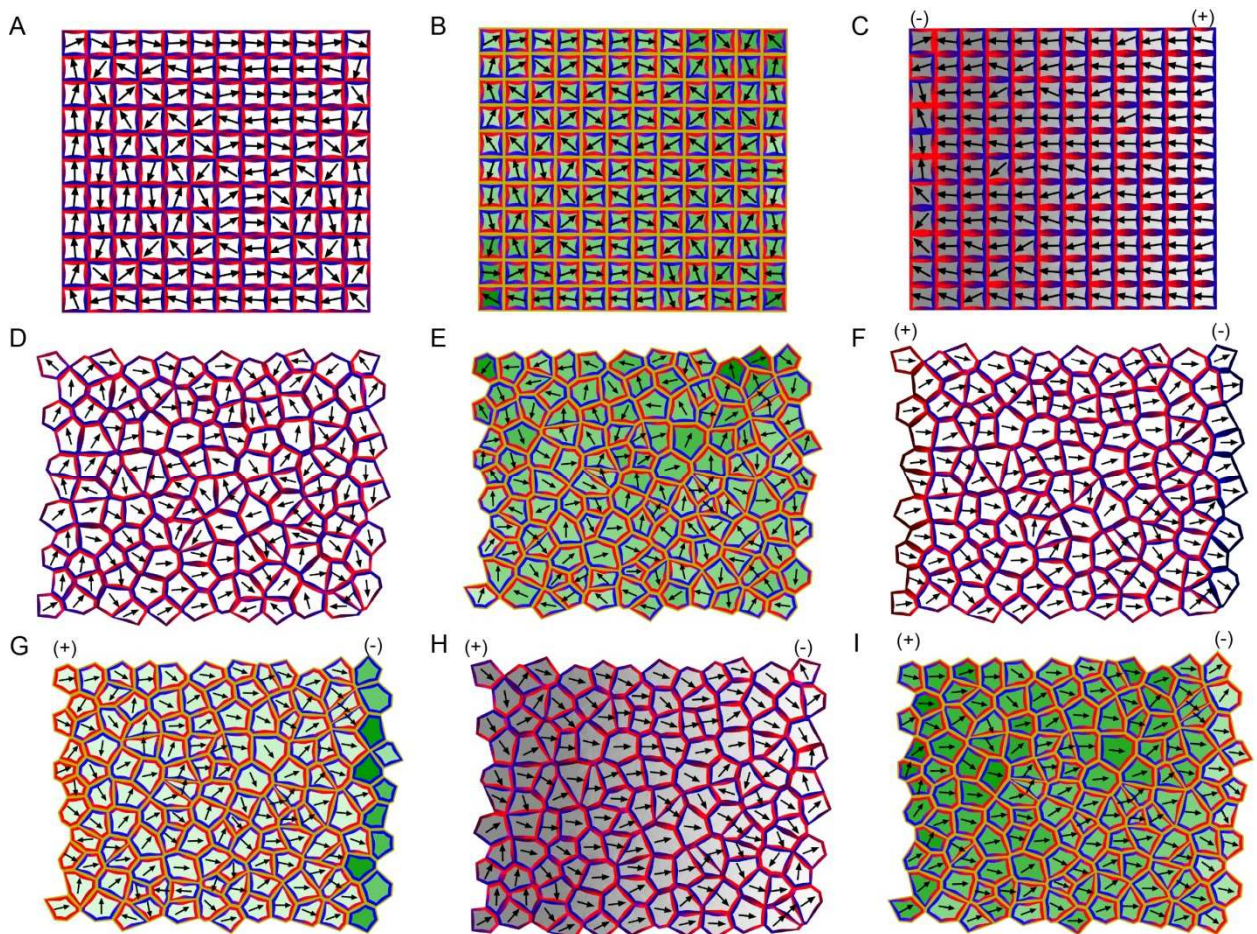


Fig. 2.11 Cell-cell coupling on grids of square or irregular cells.

(A, B) Cell-cell coupling produces longitudinal coordination on a grid of square cells but lateral neighbours often have oppositely oriented polarities. This is the case with direct cell-cell coupling (A) and indirect cell-cell coupling via auxin (B). For (B) the intensity of green shows the concentration of intracellular auxin per cell. **(C)** Cellular gradients combined with intracellular partitioning without cell-cell coupling produces both lateral and longitudinal coordination for a grid of square cells. The file of cells on the left (-) organiser has disorganised polarity because the gradient in S across these cells is shallow. **(D)** and **(E)** Cell-cell coupling is less effective at establishing lateral and longitudinal coordination in a grid of irregular cells. This is the case with direct cell-cell coupling (D) and indirect cell-cell coupling (E). **(F)** and **(G)** Organisers based on modulation of polarity components combined with direct cell-cell coupling (F) or indirect cell-cell

coupling (G) lead to coordination of polarity for an irregular grid, although it is less consistent than for hexagonal cells (compare with Figs.2.6 A and 2.6 C respectively). **(H)** Polarity coordination resulting from inter-cellular gradients combined with direct cell-cell coupling (compare with Fig. 2.9 A). **(I)** In the case of indirect coupling, production of auxin in the leftmost cell column (+ organiser), and its degradation in the rightmost cell column (-organiser) leads to good polarity coordination, although again not quite as consistent as for hexagonal cells (compare with Fig. 2.10 A).

2.2.5 Summary of theoretical analysis

The examples described above show how the intracellular partitioning-based framework provides a hypothesis for the generation of tissue cell polarity in plants and animals. Intracellular partitioning alone provides a mechanism for generating individual cell polarity in the absence of asymmetric cues. This establishes a ground state of randomly oriented polarities. This process may be modified by incorporating cell-cell coupling, which leads to local alignment of polarities. It is shown that cell-cell coupling can operate both directly, through membrane-spanning complexes, or indirectly, through auxin. Incorporation of cell-cell coupling can lead to coordination of polarity across a tissue by selective expression of polarity components in boundary domains. Tissue coordination may be further enhanced through tissue gradients, which may operate at the cellular and/or intercellular level. Several of these mechanisms may act synergistically to establish and maintain polarity over extended domains. These systems can coordinate polarity for tissues with irregular cell geometries such as those generated by cell division and growth, although coordination is less consistent than for regular hexagonal arrays.

It should be noted that, although noise is sometimes added to the polarity simulations presented here, this does not constitute a rigorous assessment of whether the models are robust to noise. In most of the simulations, we only add noise in the initial distributions of the A* and B* polarity components, as this is required for symmetry breakage to occur. To thoroughly determine the effects of noise on the models, stochastic simulations are required in which noise is present in all

the reactions between polarity components. This is beyond the scope of this thesis, but could be addressed in future work.

2.3 Canonical examples from plants and animals

To illustrate how the framework outlined above can be used in different contexts, I discuss its application to some well-studied examples in animals and plants.

2.3.1 PCP in *Drosophila*

The polarised orientation of hairs or bristles in *D.melanogaster* provides one of the best studied tissue cell polarity systems in animals (Goodrich and Strutt, 2011). Several mutants, such as *frizzled* (*fz*) and *Van Gogh* (*Vang*, also known as *strabismus*) have been identified that disrupt the proximo-distal polarity field exhibited by trichomes in the *D.melanogaster* wing. Evidence that these genes play a role in polarity coordination comes from analysis of clonal patches of mutant tissue. Such patches exhibit reversal of polarity for a few rows of wild-type cells at one end of the clone. In some cases, such as *fz*⁻ clones, polarity is reversed at the distal end of the clone, while in other cases, such as *Vang*⁻ clones, polarity is reversed at the proximal end of the clone. *Fz* is a seven-pass membrane protein and is localised to the distal end of developing wing cells, while *Vang* is a four-pass transmembrane protein and is localised at the proximal end. These proteins interact with cytosolic proteins that also show polarised distributions: *Dishevelled* (*Dsh*) and *Diego* (*Dgo*) are localised at the distal end and *Prickle* (*Pk*) at the proximal end (Fig. 2.12). In addition to these components, a seven-pass transmembrane cadherin protein *Flamingo* (*Fmi*, also known as *Starry Night* (*Stan*)) is present at both proximal and distal ends. *Fmi* most likely acts as a bridge between complexes on membranes of neighbouring cells (Lawrence et al., 2004; Strutt and Strutt, 2007; Usui et al., 1999). These six proteins (*Fz*, *Vang*, *Dsh*, *Dgo*, *Pk* and *Fmi*) have been placed in the core PCP pathway (Strutt and Strutt, 2009).

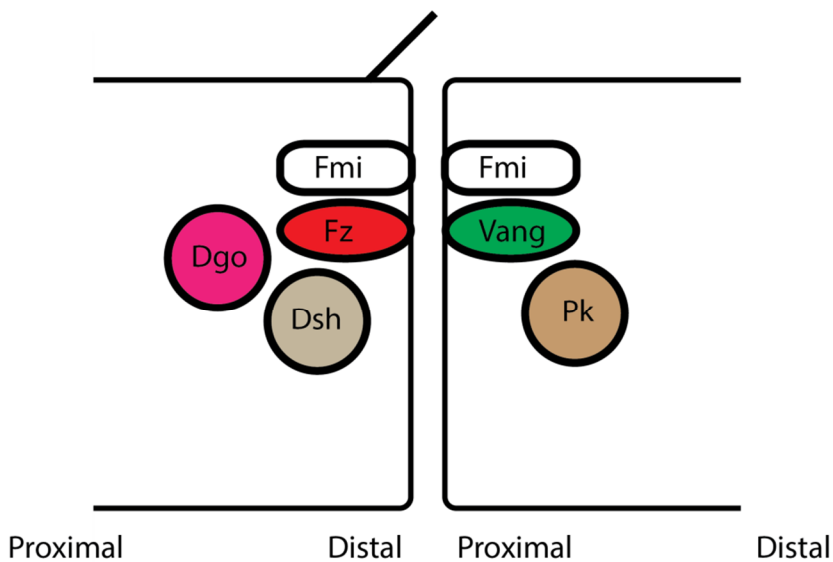


Fig. 2.12 Localisation of core planar cell polarity components at cell-cell interfaces in the *D. melanogaster* wing.

Fz, Dsh and Dgo are localised to distal cell ends, while Vang and Pk are localised at proximal cell ends. Fmi is present at both proximal and distal cell ends. A trichome emerges from the distal end of each cell and points distally (black line).

The observation of polarity reversals in the tissue surrounding mutant patches suggests that the core PCP genes are involved in one or more aspects of polarity coordination. In principle, they could encode components of a cell-cell coupling system (Fig. 2.9 B), or be involved in enhancing degradation or production of a signalling molecule S (Fig. 2.8 C). Two findings support their participation in cell-cell coupling. First, pathway components localise to opposite cell ends. Such a localisation is expected if they are polarity components but not if they are involved in production or degradation of S. Second, reorientation of polarity occurs within *fz*⁻ mutant tissue in a single cell layer that abuts Fz-expressing tissue (Lawrence et al., 2004), as expected for cell-cell coupling models, in which mutant regions contain a single layer of polarised cells (Fig. 2.6B, 2.8D, 2.9B). By contrast, there is no expectation that polarity would extend for only a single cell if Fz influenced the level of S, as a change in the gradient of S could, in principle, extend over several cells.

Several models based on direct cell-cell coupling have been proposed for how the core PCP pathway operates. These models have been designed to account for the observed polarity patterns in mutants, clonal patches, protein localisation and protein interactions. However, the formal relationships between the models have been unclear because each model has been presented as an individual solution. I next describe how these models may be viewed through the framework described here so as to highlight their essential features (i.e. whether they involve intracellular partitioning, cell-cell coupling, cellular or intercellular gradients) and discuss experiments that might distinguish between them.

One model invokes interface interactions combined with an intracellular bias (Amonlirdviman et al., 2005). Complexes are formed at each end of the cell, corresponding to the A* and B* components in the framework presented here. The A* complex involves Fz and Dsh, while the B* complex involves Vang and Pk. There is a bias in each cell such that higher levels of the A* complex are promoted at the distal end. Formation of the A* complex in one membrane promotes formation of the B* complex in the juxtaposed membrane of the neighbouring cell via interactions between Fz and Vang. Antagonism between A* and B* is mediated by B components, Pk and Vang, which inhibit the formation of A* (Dsh binding to Fz). This system is equivalent to having direct cell-cell coupling combined with cellular gradients (Fig. 2.13).

A second model involves cell interface interactions combined with a ligand that is high at the proximal end of the wing and declines distally (Le Garrec et al., 2006). The ligand is graded both along the length of each cell and between cells, and is needed to activate Fz, which then interacts with other components (Dsh, Dgo and Fmi) to generate A*. A* in the membrane of one cell can form a complex with B* (Vang, Pk, Fmi) in the juxtaposed membrane of the neighbouring cell via Fmi bridges. All polarity components can diffuse except for the bridged A*-B* complex. Inhibition between A* and B* is mediated by A components (Dsh and Fz) inhibiting formation of

fully active B* (Vang, Pk, Fmi). With the parameters used in the model, the intercellular gradient in the ligand leads to Fz-containing complex being localised distally within each cell. This system is equivalent to direct cell-cell coupling combined with intercellular gradients (Fig. 2.13).

A third model for PCP in *Drosophila* involves membrane-spanning complexes, with one orientation of the complex across the membrane (A*-B*) inhibiting formation of complexes with the opposite orientation (B*-A*) (Burak and Shraiman, 2009). There is an inhibitory messenger molecule (C*) that diffuses within each cell, creating an effective repulsion between the two possible orientations of the complex when cells have neighbours, thus ensuring that they become localised to the opposite ends of a cell. Tissue coordination is generated most effectively by an intercellular gradient. This model is also equivalent to direct cell-cell coupling combined with intercellular gradients (Fig. 2.13).

Model	ICP	Cell-cell coupling	Cellular gradients	Intercellular gradients
Amonlirdviman et al., 2005	✗	✓	✓	✗
Le Garrec et al., 2006 Burak and Shraiman, 2009	✗	✓	✗	✓

Fig. 2.13. Mechanisms contributing to tissue cell polarity in models of *Drosophila* planar cell polarity.

The first two models assume that polarity is generated in the context of gradients across or between cells (Amonlirdviman et al., 2005; Le Garrec et al., 2006). Cells would therefore be expected to be unpolarised with respect to the PCP proteins in the absence of asymmetric cues, such as ligand or expression gradients. Thus, individual cell polarity is fully dependent on global gradients across the tissue. This dependency does not apply in the case of the third model, because this mechanism generates swirls of polarity in the absence of a global orienting signal (Burak and Shraiman, 2009). However, with this model there is still a strong dependency on neighbours, as a cell cannot become polarised unless its neighbours are polarisable. Thus it should not be possible, experimentally, to produce a single polarised cell (Fig. 2.4F, G). A further step towards independence from neighbours is given by the models described here (Fig. 2.4A, B). These systems have the potential to produce single polarised cells through intracellular partitioning, even when neighbours lack the ability to polarise (Fig. 2.4G). Each of these models could operate for *Drosophila* PCP, but they can be distinguished experimentally by testing the extent to which polarisation of individual cells depends on neighbours and global gradients. Motile breast cancer cells were recently found to have asymmetric distributions of the core PCP proteins when grown as isolated cells in culture (Luga et al., 2012), suggesting that the PCP system may have intracellular partitioning behaviour.

All of the above models involve direct cell-cell coupling, but a seemingly different type of model has been proposed based on cell-cell comparisons (Adler et al., 1997; Lawrence et al., 2004). According to this model, cells compare levels of Fz activity with their neighbours, via Fmi bridges, and orient polarity so as to point to the neighbour with lowest Fz activity. However, this model does not provide an explicit mechanism for how cells are able to compare Fz concentrations with their neighbours, or how individual cell polarity is established and becomes aligned with the Fz activity gradient. As shown here and by others (Burak and Shraiman, 2009; Le Garrec et al., 2006), the combination of direct cell-cell coupling and intercellular tissue gradients can lead to cells

orienting polarities according to differences in the level of polarity components (i.e. the level of A*, Fig. 2.9). The system behaves *as if* cells are comparing levels with neighbours and orienting their polarity accordingly. However, this behaviour is not an explicit input to the model but an outcome of molecular interactions. Thus cell-cell comparison models can be seen as a different level of description rather than contradictory to direct cell-cell coupling models.

A further complication with evaluating models is that the core PCP genes do not provide the only polarity components. If they did, then mutants in these genes would be expected to give cells lacking polarity. This result is observed with respect to the position in the cell where the hair initiates: complete loss of core PCP proteins leads to hairs initiating in the cell centre instead of distally (Wong and Adler, 1993). However, with regard to hair orientation, individual cell polarity is still evident in the mutants as each cell hair does not point vertically out of the tissue plane but in a direction along the plane. Moreover, this individual cell polarity is still coordinated to some extent between neighbours, giving swirls or broad domains of alignment (Wong and Adler, 1993). These observations suggest that the polarity system has redundancy and does not only depend on the core PCP pathway. In tissues such as the abdomen, some of this redundancy reflects the operation of a second pathway, involving the Fat (Ft) and Dachsous (Ds) cadherin proteins (Lawrence et al., 2007). However, even double mutants which lack activity in both the core PCP and Ft/Ds pathways have hairs pointing along the plane of the tissue, and even show swirled organisation in some areas (Casal et al., 2006), indicating that further levels of redundancy are involved. In support of this conclusion, a *frizzled*-independent system based on septate junction proteins Gliotactin (Gli) and Coracle (Cora) has been described, which is also involved in alignment of hair polarity (Venema et al., 2004).

A further question is how organisers act to coordinate polarity over the tissue. For example, hairs point distally with respect to the *D.melanogaster* wing. This suggests that organisers are most

likely located at the hinge region at the proximal edge of the wing and/or at the distal tip of the wing which is defined by the intersection of the anteroposterior and dorsoventral compartment boundaries (Goodrich and Strutt, 2011). Tissue boundaries are thus expected to be locations where polarity components are modulated, and/or sources or sinks of underlying tissue gradients. Wing cells exhibit irregular shapes at early stages (Classen et al., 2005). At these stages, PCP proteins such as Vang, already show preferential orientations towards the wing margin and cells are still dividing (Aigouy et al., 2010). Thus, coordinated polarity of core PCP proteins occurs in the context of irregular cell geometries. Such coordination may arise through organisers based on modulation of polarity components and/or tissue gradients (Fig.2.11 F, 2.11H).

Evidence for tissue gradients playing a role comes from analysis of planar polarity in the *D.melanogaster* eye. Cells in the eye become polarised through preferential distribution of the cadherin Ds (A*) to one cell end and its binding partner the cadherin Ft (B*) to the opposite cell end (Ambegaonkar et al., 2012; Brittle et al., 2012). Planar polarity patterns are specified by opposite gradients in expression of Ds, and the Golgi-associated protein Four-jointed (Fj) (Simon, 2004). Fj expression is highest at the equator while Ds expression is highest at the pole. As these transcriptional gradients operate through the nucleus they act at the intercellular level. As shown in Fig. 2.9, an intercellular gradient in A* levels is expected to orient polarity such that the B*-rich end of the cell is oriented towards regions with higher A* expression. This is consistent with the observation that Ft-rich (B*-rich) ends are oriented towards regions with higher Ds (A*) expression at the pole. Fj has been proposed to modify Ft or Ds so that the ability of Ft (B*) to form intercellular bridges is enhanced relative to Ds (A*) (Brittle et al., 2010; Simon et al., 2010). Thus the expression gradient in Fj is equivalent to an intercellular gradient in B*levels, and should orient the A*-rich end of the cell towards regions with higher B* (Fj) expression. Consistent with this expectation, Ds-rich ends are oriented towards regions with high Fj expression at the equator. The tissue gradients in Ds and Fj expression depend on graded distributions of

morphogens such as Wingless that emanate from tissue and compartment boundaries. Thus, in terms of our framework, graded Wingless takes the place of S, regulating the expression of Ds and of Fj.

2.3.2 PIN localisation in plants

The intracellular partitioning-based framework presented here represents a new type of model for tissue cell polarity of PIN proteins. Unlike previous models, which assume that a cell does not become polarised in the absence of auxin gradients or flux across it, we propose that cells can become polarised even in the absence of asymmetries in auxin, through intracellular partitioning. Auxin then acts as a mediator which coordinates polarities through indirect cell-cell coupling. As shown in the theoretical examples, if the A* component leads to enhanced PIN activity (auxin export) and extracellular auxin inhibits A*, polarities become coaligned with directions of auxin flow, similar to the outcome of with-the-flux models. According to the intracellular partitioning-based model, polarity points away from regions with high extracellular auxin (+organisers) and towards regions with low extracellular auxin (-organisers). However, the level of intracellular auxin need not correlate with these extracellular levels. Intracellular auxin can be high at a +organiser because of high auxin production rates (Fig. 2.10A), or it may be high at a -organiser because auxin may accumulate there through transport (provided that extracellular auxin is kept low, Figs. 2.6C, 2.10D). The latter outcome is consistent with polarities pointing towards regions with high expression of auxin-inducible gene markers, such as DR5 (Heisler et al., 2005). Thus the intracellular partitioning-based model is equally compatible with observed PIN polarity patterns associated with up-the-gradient or with-the-flux models. However, unlike previous models, the intracellular partitioning-based model does not invoke cell-cell comparisons, measurements of flux, detection of stresses, or detection of gradients across cell walls. Instead, alignments arise through the interplay between intracellular partitioning and auxin transport processes.

A distinctive feature of the model proposed here is that there is a separable mechanism for intracellular partitioning. Candidate components for intracellular partitioning are the Rho-GTPases, a family of small G-proteins that may be either membrane bound or cytosolic (Yang, 2008). The inactive form is released from the membrane and becomes cytosolic through interaction with guanine nucleotide dissociation inhibitor proteins (GDIs). In animals, polarity of migrating cells is associated with segregation of different members of the Rho-GTPase family, typically with high levels of active Rac and Cdc42 (equivalent to A*) at the front region of the cells and high levels of active Rho (equivalent to B*) at the back region. Computational modelling has shown that this asymmetry can be accounted for through mutual inhibition of the A* and B* forms together with faster diffusion of the cytosolic GDI-linked A and B forms (Jilkine et al., 2007; Maree et al., 2006). A similar model has been proposed to underlie polarity of pavement cells in plants, although in this case multiple polarities are present in a single cell (Grieneisen et al 2012 submitted). Here, different members of Rho-like GTPases from plants, called ROPs, are thought to antagonise each other such that ROP2 (equivalent to A*) becomes localised to regions that form protrusions (lobes) while ROP6 (equivalent to B*) becomes localised to indentations (Fu et al., 2005; Xu et al., 2010). As with the model for animal cells, the inactive cytosolic forms, associated with GDIs, play a key role in allowing the pattern to form.

If intracellular partitioning through ROPs is linked to tissue polarity with auxin acting as a mediator of cell-cell coupling, ROPs would be expected to influence auxin transport, while auxin levels should influence ROPs. Localisation of PIN1 is highly correlated with that of ROP2 and its effectors in pavement cell lobes, consistent with ROP2 enhancing local PIN1 levels and thus auxin export (Xu et al., 2010). Auxin has also been shown to activate ROPs within minutes through a local membrane-bound auxin receptor (ABP1), consistent with auxin feeding back to influence intracellular partitioning (Xu et al., 2010). Based on these findings, an indirect cell-cell coupling model has been proposed for coordinating polarity between neighbouring pavement cells, where

active ROP2 (A*) increases auxin efflux, through promoting functional PIN1 localisation (Grieneisen et al., 2013). Although the pavement cell model is designed to account for coordinated interdigitation between adjacent cells, the principles are very similar to those described here for indirect cell-cell coupling of tissue cell polarity.

Many aspects of the intracellular partitioning-based framework for plant tissue cell polarity remain to be explored and tested further. For example, it is unclear whether this framework could be used to account for observed spacing of leaf primordia at a plant apex, or vascular patterns such as those seen in leaves. Several distinctive predictions of the framework also remain to be tested experimentally. For example, the framework predicts that cells should be able to polarise in the absence of asymmetric cues. It has been shown that separation of plant cells by cell wall digestion and protoplast formation leads to a loss of asymmetric PIN1 localisation (Boutte et al., 2006), which could be taken as evidence against intracellular partitioning. However, it is unclear whether such treatments affect activity of polarity components and also whether polarity has indeed been fully lost, as PIN1 is not a determinant of intracellular partitioning but only a target that enables cell-cell coupling. Thus, further polarity markers and ways of generating cells in uniform environments are needed.

Another prediction is that polarity should point away from regions with high extracellular auxin. At first sight, this prediction seems inconsistent with experiments in which microdroplets containing auxin are applied to apical meristems (Bayer et al., 2009). PIN polarity is seen to converge towards the site of auxin application, suggesting that polarity is being oriented up the extracellular auxin gradient. However, these experiments do not lead to generation of polarity convergence points in new locations, but at positions at which primordia are about to emerge (known as I2 positions). It is therefore possible that auxin application is simply accelerating

formation of a pattern that is nascent in the meristem, rather than specifying a new convergence point.

A further prediction concerns the effect of cell ablation. PIN polarity has been shown to be oriented away from sites of ablation in nearby cells (Heisler et al., 2010). The local effect of ablation is not disrupted by the auxin transport inhibitor NPA, nor by uniform application of external auxin; observations which have been taken to suggest that mechanical signals rather than auxin transport are responsible for coordinating PIN polarity (Heisler et al., 2010). An alternative explanation is that cell ablation causes an increase in extracellular auxin, which orients polarity according to the model described here. I show that even in the absence of active efflux (i.e. when A^* does not promote auxin export), coordination of polarity can extend over a few cells because of the gradient in extracellular auxin across the cells, generated by non-directed transport (left cells of Fig. 2.10B). Uniform application of external auxin need not disrupt polarity coordination as local gradients may still arise and be propagated through indirect cell-cell coupling.

A further test would be to determine whether polarity organisers act in the manner predicted. According to the intracellular partitioning-based framework, organisers correspond to regions where intracellular partitioning components or auxin levels are modulated. This modulation could involve ROP/GDI activity, auxin biosynthesis (Zhao, 2010), auxin export (Krecek et al., 2009), auxin conjugation (Ludwig-Muller, 2011) or auxin import (Yang et al., 2006). These processes would therefore be targets of genes expressed in candidate regions of organiser activity, such as the root tip, base and tip of organ primordia, or base and tip of leaf serrations. Genes expressed in such boundary domains have been described and include *LATERAL SUPPRESSOR*, members of the NAC and LBD families, and *PLETHORA* (Aida et al., 2004; Aida and Tasaka, 2006; Greb et al., 2003; Majer and Hochholdinger, 2011). In later chapters I test whether some of these genes

influence polarity components and auxin distributions in a manner predicted by the intracellular partitioning-based framework.

2.3.3 Concluding remarks

The intracellular partitioning-based framework presented here provides a hypothesis for how tissue cell polarity may be established in plants and animals. Intracellular partitioning components can be modulated by incorporating interface interactions to produce cell-cell coupling which generates local alignment. Alignment across a tissue is established through tissue polarity organisers located at boundary regions. These organisers can act by modulating polarity components directly and/or through tissue gradients. In animal cells, molecules may bridge from one cell to another, allowing direct cell-cell coupling. Plant cells, however, are separated by cell walls, and polarities may be coupled more indirectly through transport of small mediator molecules such as auxin.

The intracellular partitioning-based framework allows different cell polarity systems to be placed in an evolutionary context. Cell polarity can be exhibited by individual cells in the absence of external molecular asymmetries (Wedlich-Soldner and Li, 2003). This is evident both for unicellular organisms such as yeast (Johnson et al., 2011; Mogilner et al., 2012) and individual cells from multicellular organisms, such as fish epidermal keratocytes (Maree et al., 2012; Verkhovsky et al., 1999). Thus, systems for generating intracellular partitioning are widespread and evolutionarily ancient, suggesting that they may provide a basic building block for establishing tissue polarity (Meinhardt, 2007). The tissue polarity mechanisms observed in plants and animals would then reflect the distinct constraints of each system during the evolution of multicellularity from unicellular ancestors, which already possessed intracellular partitioning systems.

2.4 Model descriptions

Models were created using the VVe modelling environment, an extension of the VV system (Smith et al., 2003), which in turn is an extension of L-systems. During the implementation of all models, tissue is represented by a graph consisting of multiple vertices and edges (connections) between neighbouring vertices. Each cell is represented by multiple vertices, representing the cytoplasm and membrane. Details of tissue representations and the equations governing model behaviour are given below for each model.

2.4.1 Intracellular partitioning

The intracellular partitioning system is used as a building block for all models in this chapter. It involves interactions between rapidly diffusing inactive polarity components in the cytoplasm (A and B) and slowly diffusing, active polarity components in the membrane (A^* and B^*). I only consider the inter-conversion between A and A^* (and B and B^*), and thus assume a fixed total amount for each polarity component within a cell. This captures the fact that molecular switches typically interconvert on a much faster time scale than their regulated production or breakdown (Jilkine et al., 2007; Maree et al., 2006).

During the implementation of intracellular partitioning, tissue is represented by a graph containing two types of vertex: central vertices, which are positioned in the centre of each cell, and peripheral vertices positioned around the perimeter of each cell (Fig. 2.14). All peripheral vertices of a cell are arranged to form a one dimensional closed region. Each peripheral vertex from the same closed region is connected to the central vertex of the same cell and to its immediately neighbouring peripheral vertices of the same cell. Each peripheral vertex of a cell is also connected to the juxtaposed peripheral vertex of the neighbouring cell, unless the vertex is on the border of the tissue.

In all models, the membrane of each cell is represented by peripheral vertices and the region of membrane represented by a peripheral vertex is referred to as a membrane compartment. I assume the membrane is one dimensional (I consider it to have zero thickness) and consider the concentration of polarity components in the membrane (of dimension quantity of substance per unit length) to have arbitrary units per micron ($A_u/\mu\text{m}$). In most models, the single central vertex of each cell is used to represent the cytoplasm of that cell and the cytoplasm is not further discretised. This is because diffusion of the inactive polarity components (A and B) in the cytoplasm is assumed to be relatively fast. Therefore, for simplicity, the concentrations of A and B are assumed to always be evenly distributed throughout the cytoplasm, removing the need for further discretisation of the cytoplasm and simulation of diffusion. In the simulation used to generate Figs. 2.4F and 2.4G, where effective diffusion rates in the cytoplasm are set to be the same as those in the membrane, diffusion in the cytoplasm is simulated. In these simulations diffusion in the cytoplasm is treated in the same way as diffusion in the membrane, to ensure comparability. This is done by using each peripheral vertex to represent a region of the cytoplasm underlying the membrane. In the following descriptions, the region of cytoplasm represented by a central or a peripheral vertex is referred to as a cytoplasmic compartment. In all simulations except those used to generate Figs. 2.4F and 2.4G, the concentration of polarity components in the cytoplasm is considered to have arbitrary units (A_u) per unit area ($A_u/\mu\text{m}^2$). In the simulations used to generate Figs. 2.4F and 2.4G, the cytoplasmic polarity components have units of $A_u/\mu\text{m}$.

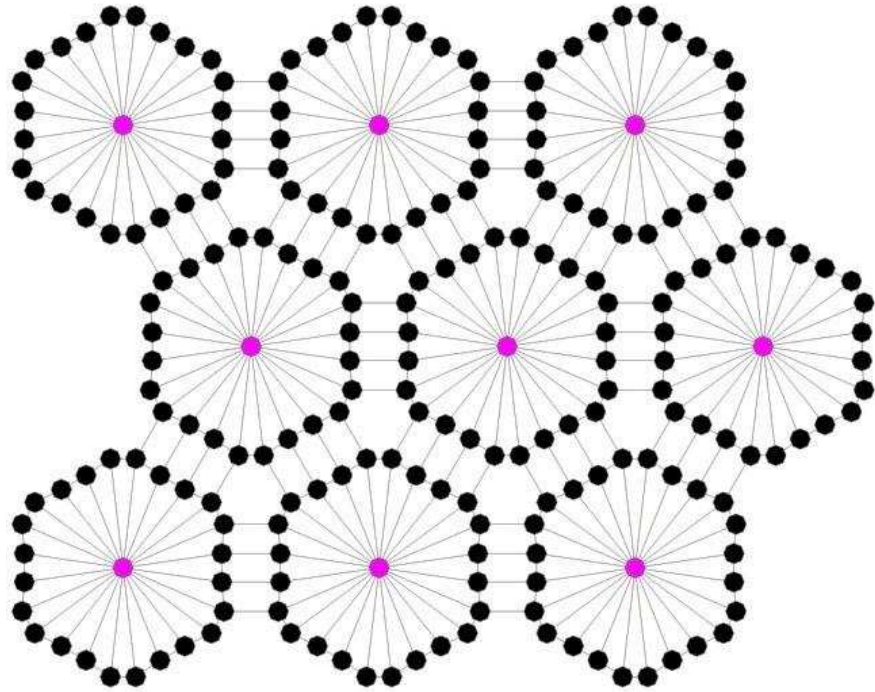


Fig. 2.14 The intracellular partitioning graph.

Cells are represented by a single central vertex (magenta dots) surrounded by multiple peripheral vertices (black dots). The grey lines indicate the connections between vertices. Each central vertex is connected to all its surrounding peripheral vertices. Each peripheral vertex is connected to the central vertex of the same cell, its neighbouring peripheral vertices in the same cell and the juxtaposed peripheral vertex of the adjacent cell.

In the case where cells have regular hexagonal geometries, each of the six edges of the hexagon is considered to have a length of $10 \mu\text{m}$. Each of the six edges is represented by four peripheral vertices (black dots in Fig. 2.14), therefore each cell contains 24 peripheral vertices. Each peripheral vertex has a length associated with it of $2.5 \mu\text{m}$. The area of each cell is $260 \mu\text{m}^2$ and the minimal diameter of the cell is $17.3 \mu\text{m}$. In simulations with square cells, each of the four edges of the cell has a length of $13 \mu\text{m}$ and is represented by five peripheral vertices, each with a length of $2.6 \mu\text{m}$. The area of the cell is $169 \mu\text{m}^2$. In simulations with irregular cell geometries, the average dimensions are approximately the same as for regular cells, but the exact dimensions

may vary between cells and the lengths associated with peripheral vertices may vary slightly within an individual cell. The dimensions of all cells remain the same throughout all simulations.

In the case where the cytoplasm is represented by the single central vertex of each cell, the area of the cytoplasm is considered to be equal to the geometrical area of the whole cell. In all simulations, the length of each membrane compartment is the length associated with the peripheral vertex it is represented by. In the simulations used to generate Figs. 2.4F and 2.4G, the length associated with each compartment of cytoplasm is the same as the length of the peripheral vertex used to represent it.

At the beginning of all simulations, the intracellular partitioning system is initialised with a default concentration of polarity components in each cytoplasmic compartment,

$$A(t = 0) = c_A \quad (2.1a)$$

$$B(t = 0) = c_B \quad (2.1b),$$

where $A(t=0)$ and $B(t=0)$ are the initial concentrations of A and B polarity components in cytoplasmic compartments and c_A and c_B are the default initial concentrations of A and B polarity components respectively.

In all simulations except those used to generate Figs. 2.4F, 2.4G, 2.6, 2.10D, 2.11F and 2.11G, $c_A = c_B = 0.02 \text{ A}_u/\mu\text{m}^2$ in all cells. In the simulations used to generate Figs. 2.6, 2.11F and 2.11G, in the column of cells on the left of the tissue (which has only A and A*) $c_B = 0 \text{ A}_u/\mu\text{m}^2$ and in the column of cells on the right of the tissue (which has only B and B*) $c_A = 0 \text{ A}_u/\mu\text{m}^2$. In Fig. 2.10D, $c_A = 0 \text{ A}_u/\mu\text{m}^2$ in the column of cells on the right of the tissue. In Fig. 2.4F and 2.4G, $c_A = c_B = 0.2 \text{ A}_u/\mu\text{m}$. All parameter values are provided in Table 2.1.

Noise is added to the system during the initialisation of the concentrations of A^* and B^* . In each of the membrane compartments, the concentration of A^* and B^* is set to a default concentration plus or minus a randomly-generated value:

$$A^*(t = 0) = d_A(1 + \theta_A) \quad (2.2a),$$

$$B^*(t = 0) = d_B(1 + \theta_B) \quad (2.2b),$$

$$\theta_{A,B} \in [-\varepsilon, \varepsilon] \quad (2.2c).$$

Here $A^*(t=0)$ and $B^*(t=0)$ are the initial concentrations of polarity components in a given membrane compartment and d_A and d_B are the default initial concentrations of A^* and B^* membrane bound polarity components respectively. θ_A and θ_B are independently-generated random numbers uniformly distributed between an upper and lower limit, ε . This method used to initialise the system introduces small differences between the total amounts of the A polarity component ($A^* + A$) and the total amounts of the B polarity component ($B^* + B$) in each cell. It also introduces variation between cells in the total amounts of polarity components per cell. In all simulations except those used to generate Figs. 2.6, 2.10D, 2.11F and 2.11G, $d_A = d_B = 0.3 \text{ A}_u/\mu\text{m}$ and $\varepsilon = 0.0417$ for all cells. In Figs. 2.6, 2.11F and 2.11G, in the column of cells on the left of the tissue $d_B = 0 \text{ A}_u/\mu\text{m}$ and in the column of cells on the right of the tissue $d_A = 0 \text{ A}_u/\mu\text{m}$. In Fig. 2.10D, $d_A = 0 \text{ A}_u/\mu\text{m}$ in the column of cells on the right of the tissue.

Following initialisation of the system, reactions between the polarity components are simulated. All changes in concentration are solved numerically using an explicit Euler integration method. Reactions are first described for the case where the cytoplasm is represented by the single central vertex of each cell (all simulations except those used for Figs. 2.4F and 2.4G). With intracellular

partitioning, the concentrations of A^* and B^* in a given membrane compartment depend on five processes. (1) A and B bind to the membrane; (2) A^* and B^* unbind from the membrane; (3) membrane-bound polarity components promote the membrane-binding of their own polarity component through auto-activation (i.e. A^* in a membrane compartment promotes the binding of A to that membrane compartment); (4) membrane bound polarity components promote the unbinding of the opposite polarity component through mutual inhibition (i.e. A^* in a membrane compartment promotes the unbinding of B^* from that membrane compartment and vice-versa); (5) membrane-bound polarity components diffuse between the membrane compartments of the same cell. The equation describing the rate of change of A^* concentration for a given membrane compartment is

$$\frac{\partial A^*}{\partial t} = (\rho + \eta A^*)A - (\mu + \alpha B^*)A^* + D_{A^*} \nabla^2 A^* \quad (2.3a),$$

where A^* and B^* are the concentrations of the polarity components in the membrane compartment with units of $A_u/\mu\text{m}$ and A is the concentration of the A polarity component in the cytoplasmic compartment of the same cell with units of $A_u/\mu\text{m}^2$. ρ is the membrane-binding rate of polarity components with units of $\mu\text{m}/\text{s}$, η describes the extent to which membrane-bound polarity components promote the binding of their own polarity component (auto-activation) and has units of $\mu\text{m}^2/\text{A}_u\cdot\text{s}$, μ is the unbinding rate with units of $/s$, and α is the rate of cross-inhibition between membrane-bound polarity components with units of $\mu\text{m}/\text{A}_u\cdot\text{s}$. D_{A^*} is the diffusion constant of A^* in the membrane with units of $\mu\text{m}^2/\text{s}$.

The corresponding equation describing the rate of change of B^* concentration for a given membrane compartment is:

$$\frac{\partial B^*}{\partial t} = (\rho + \eta B^*)B - (\mu + \alpha A^*)B^* + D_{B^*} \nabla^2 B^* \quad (2.3b),$$

where B^* and A^* are the concentrations of the polarity components in the membrane compartment and B is the concentration of the B polarity component in the cytoplasmic compartment of the same cell. ρ , η , μ and α are as described for equation 2.3a (for simplicity it is assumed that both polarity components behave with the same dynamics). D_{B^*} is the diffusion constant of B^* in the membrane with units of $\mu\text{m}^2/\text{s}$ (I assume $D_{A^*} = D_{B^*}$). Since there is only one cytoplasmic compartment per cell, the concentrations of A and B available to each membrane compartment of a cell are the same. This captures the relatively high diffusion rates that are assumed for the inactive polarity components.

In simulations where the basic intracellular partitioning mechanism is modified by introduction of cell-cell coupling or interactions with tissue gradients, equations 2.3a and 2.3b are modified. In order to describe these modifications to intracellular partitioning, it is useful to describe intracellular partitioning in terms of more general equations. Equations 2.3a and 2.3b can be described in terms of a general binding function, a general unbinding function and a diffusion term. In the case of intracellular partitioning, the binding and unbinding functions each have a single argument, and therefore the general functions are described as having a single argument below. However, in different model variants, the binding and unbinding functions can have A^* or B^* or both as arguments. The equations for intracellular partitioning in membrane compartments (equations 2.3a and 2.3b) in general terms are

$$\frac{\partial A^*}{\partial t} = f_A(A^*)A - g_A(B^*)A^* + D_{A^*} \nabla^2 A^* \quad (2.4a),$$

where

$$f_A(A^*) = \rho + \eta A^* \quad (2.4b),$$

$$g_A(B^*) = \mu + \alpha B^* \quad (2.4c),$$

and

$$\frac{\partial B^*}{\partial t} = f_B(B^*)B - g_B(A^*)B^* + D_{B^*} \nabla^2 B^* \quad (2.4d),$$

where

$$f_B(B^*) = \rho + \eta B^* \quad (2.4e),$$

$$g_B(A^*) = \mu + \alpha A^* \quad (2.4f).$$

Here, $f_A(A^*)$ and $f_B(B^*)$ are the general functions determining membrane-binding of A and B respectively and $g_A(B^*)$ and $g_B(A^*)$ are the general functions determining unbinding of A^* and B^* respectively.

For simplicity, the polarity components are assumed to undergo conversion between cytoplasmic and membrane-bound forms without any change in the total amounts of $A + A^*$ or $B + B^*$ (there is no production or degradation of polarity components). Over a given time interval, the changes in the total amounts of A and B in a cytoplasmic compartment are the opposite of the sum of the changes in the total amounts of A^* and B^* in all the membrane compartments of a cell. The rate of change in the concentration of the A polarity component in the cytoplasmic compartment (c) of a cell is

$$\frac{\partial A}{\partial t} = \frac{-1}{R_c} \sum_{n \in N(c)} l_n (f_A(A_n^*) A - g_A(B_n^*) A_n^*) \quad (2.5)$$

where A is the concentration of the A polarity component in the cytoplasmic compartment, c , and A_n^* is the concentration of the A^* polarity component in the membrane compartment n , in the neighbourhood of c ($N(c)$). R_c is the area of the cytoplasmic compartment and l_n is the length of the n th membrane compartment. $f_A(A_n^*)$ is the general function determining binding of A and $g_A(B_n^*)$ is the general function determining unbinding of A_n^* , for the membrane compartment n in the same cell as the cytoplasmic compartment. In the case of intracellular partitioning alone, $f_A(A_n^*)$ is the same as described by equation 2.4b and $g_A(B_n^*)$ is the same as described by equation 2.4c. The equation for the B polarity component is equivalent to that shown above for A .

In all simulations, the parameters values used for intracellular partitioning are: $\rho = 0.02 \mu\text{m} / \text{s}$, $\eta = 0.2 \mu\text{m}^2 / \text{A.u.s}$, $\mu = 0.002 / \text{s}$, $\alpha = 0.04 \mu\text{m} / \text{A.u.s}$. $D_A = D_B = 0.1 \mu\text{m}^2 / \text{s}$. This value for the diffusion constant is the same as previously estimated for membrane bound G-proteins (Postma et al., 2004; Postma and Van Haastert, 2001). In simulations with regular hexagons, $R_c = 260 \mu\text{m}^2$ and $l_n = 2.5 \mu\text{m}$. In simulations with irregular hexagonal geometries, the average values are $R_c = 260 \mu\text{m}^2$ and $l_n = 2.5 \mu\text{m}$ but the exact values can vary between cells and between membrane compartments of the same cell. In simulations with square cells, $R_c = 169 \mu\text{m}^2$ and $l_n = 2.6 \mu\text{m}$.

2.4.2 Direct cell-cell coupling

In simulations involving direct cell-cell coupling (Fig. 2.4E, 2.4F, 2.4G, 2.4H, Fig. 2.6A, B, Fig. 2.8D, Fig. 2.9, Fig. 2.11A, 2.11D, 2.11F, 2.11H), A^* in a membrane compartment of a given cell (cell 1) is assumed to interact with B^* in the juxtaposed membrane compartment of an adjacent cell (cell 2) to form an intercellular A^* - B^* bridging complex. The intracellular partitioning mechanism described above is modified such that auto-activation and cross-inhibition depend on formation of this complex. The A^* - B^* bridging complex enhances A^* and inhibits B^* in the membrane compartment of cell 1 (which is at the A^* side of the complex), while enhancing B^* and inhibiting

A^* in the juxtaposed membrane compartment of cell 2 (which is at the B^* side of the complex).

Thus, in the case of direct cell-cell coupling, the binding and unbinding functions of the general equations (2.4a and 2.4d) have complex-dependent auto-activation and cross-inhibition terms. In the case of direct cell-cell coupling, the binding and unbinding functions take two arguments. For example, in addition to A^* , the binding function for A^* (f_A) takes B^* in the juxtaposed membrane compartment of the neighbouring cell (which I refer to as $B^{*''}$) as an argument. The binding and unbinding functions for direct cell-cell coupling, which can be inserted into the general equations 2.4a and 2.4d are

$$f_A(A^*, B^{*''}) = \rho + \omega A^* B^{*''} \quad (2.6a),$$

$$g_A(B^*, A^{*''}) = \mu + \nu B^* A^{*''} \quad (2.6b),$$

$$f_B(B^*, A^{*''}) = \rho + \omega B^* A^{*''} \quad (2.6c),$$

$$g_B(A^*, B^{*''}) = \mu + \nu A^* B^{*''} \quad (2.6d).$$

where A^* and B^* are the concentrations of polarity components in a given membrane compartment and $B^{*''}$ and $A^{*''}$ are the concentrations of polarity components in the juxtaposed membrane compartment of the neighbouring cell. Thus, I assume that the concentrations of A^* - B^* and $B^{*''}$ - A^* complexes are proportional to $A^*B^{*''}$ and $B^{*''}A^*$ respectively. Such a mass-action term is a reasonable approximation if the concentration of complexed polarity components is small relative to the uncomplexed components. ω is the rate at which a polarity component complex promotes the membrane binding of the inwardly-pointing polarity component type in the same membrane compartment (auto-activation) with units of $\mu\text{m}^3/\text{A}_u^2\text{s}$. ν is the rate at which a polarity component complex promotes unbinding from the membrane of the polarity

component type opposite to that which is inwardly pointing in the complex (cross-inhibition) with units of $\mu\text{m}^2/\text{A}_u^2\cdot\text{s}$.

In all simulations involving direct cell-cell coupling, except the simulations used to generate Fig. 2.4F and Fig. 2.4G, the parameter values used are $\omega = 0.54 \mu\text{m}^3/\text{A}_u^2\cdot\text{s}$ and $v = 0.023 \mu\text{m}^2/\text{A}_u^2\cdot\text{s}$. The values of ρ and μ are the same as for intracellular partitioning alone ($\rho = 0.02 \mu\text{m}/\text{s}$, $\mu = 0.002/\text{s}$).

In the simulations used to generate Figs. 2.4F and 2.4G, in order to simulate diffusion in the cytoplasm, it is represented by peripheral vertices. The rates of change of active, membrane bound polarity components in a given membrane compartment depend on the concentrations of inactive polarity components in the associated cytoplasmic compartment which is represented by the same peripheral vertex as the given membrane compartment. The simulation of direct cell-cell coupling for membrane bound polarity components is as described above (equations 2.6a-2.6d along with equations 2.4a and 2.4d). However, the general equation describing the rate of change of concentration of the inactive polarity component, A , in a given cytoplasmic compartment (equation 2.5) is changed to include a diffusion term:

$$\frac{\partial A}{\partial t} = -(f_A(A^*, B^{*'})A - g_A(B^*, A^{*'})A^*) + D_A \nabla^2 A$$

(2.7a),

where A is the concentration of the inactive polarity component A in a given cytoplasmic compartment, A^* and B^* are the concentrations of active polarity components in the membrane compartment represented by the same peripheral vertex and $A^{*'}$ and $B^{*'}$ are the concentrations in the juxtaposed membrane compartment. D_A is the diffusion constant for A in the cytoplasm, with units of $\mu\text{m}^2/\text{s}$. Unlike equation 2.5, these equations do not involve multiplication by the

length of the membrane compartment and division by the area of the cytoplasmic compartment because in this case the cytoplasmic compartment has the same dimensions as the membrane compartment with which polarity components are being exchanged. The equation for B is equivalent to that shown for A.

The specific binding and unbinding functions, and the parameter values used, are as described above for direct cell-cell coupling (equations 2.6a, b, c, d) except that here, ρ has units of /s with a value of 0.002 and ω has units of $\mu\text{m}^2/\text{A}_u^2\cdot\text{s}$ with a value of 0.054. In all cells in Fig.2.4F, and in all cells except the central cell in Fig.2.4G, $D_{A^*} = D_{B^*} = D_A = D_B = 0.1 \mu\text{m}^2/\text{s}$. In the central cell in Fig.2.4G, $D_{A^*} = D_{B^*} = 0.1 \mu\text{m}^2/\text{s}$ and $D_A = D_B = 2.5 \mu\text{m}^2/\text{s}$.

A model for direct cell-cell coupling is presented in which the $A^* - B^*$ membrane spanning complex inhibits A^* at the B^* end of the complex while uncomplexed A^* and B^* undergo autoactivation and cross-inhibition (Fig.2.4A, 2.4D). In this model, the binding and unbinding and functions are

$$f_A(A^*) = \rho + \eta A^* \quad (2.8a),$$

$$g_A(B^*, A^{*'}) = \mu + \alpha B^* + \nu B^* A^{*'} \quad (2.8b),$$

$$f_B(B^*) = \rho + \eta B^* \quad (2.8c),$$

$$g_B(A^*) = \mu + \alpha A^* \quad (2.8d),$$

where A^* and B^* are the concentrations of polarity components in a given membrane compartment and $A^{*''}$ is the concentration of A^* in the juxtaposed membrane compartment of the neighbouring cell. v is the complex-dependent cross-inhibition rate with units of $\mu\text{m}^2/\text{A}_u^2\cdot\text{s}$ (as for equations 2.6b and 2.6d, the same parameter value was used), ρ , μ , η and α and the values used for these parameters are as described for intracellular partitioning (as for equation 2.3a).

2.4.3 Tissue gradients

Simulations involving gradients of a signal, S , (Figs. 2.8, 2.9, 2.11C, 2.11H) are performed in two phases. In the first phase, a gradient in S is established in an extracellular space without simulation of intracellular partitioning or direct cell-cell coupling. In the second phase, the distribution of S is assumed to remain constant and intracellular partitioning or direct cell-cell coupling under the influence of S (or factor F , produced in response to S) is simulated.

The intracellular partitioning graph (Fig. 2.14) does not include a representation of the extracellular space. Therefore, the production, degradation and diffusion of S is simulated on a different graph which represents only the extracellular space (Fig. 2.15). This extracellular space graph contains multiple vertices and connections between them. Each vertex of the extracellular space graph is positioned at a vertex of the cell and each edge of the extracellular space graph corresponds to a cell edge. I refer to each vertex of the extracellular space graph as an extracellular space compartment. In simulations where both the extracellular space graph and the intracellular partitioning graph are used, the peripheral vertices of the intracellular partitioning graph are positioned so that they map on to the extracellular space graph (four peripheral vertices of the intracellular partitioning graph are positioned along each edge of the extracellular space graph). In simulations using cells with regular hexagonal geometries, the distance between neighbouring vertices in the extracellular space graph is $10\ \mu\text{m}$, which is equivalent to the length

of hexagon edges in the intracellular partitioning graph. In simulations using cells with square geometries, the distance between vertices is $13 \mu\text{m}$. In simulations with irregular cell geometries, the dimensions of the extracellular space graph may vary but on average are approximately the same as in simulations with regular cell geometries. The concentration of S is per unit length of the extracellular space compartment and has units of $\text{A}_u/\mu\text{m}$.

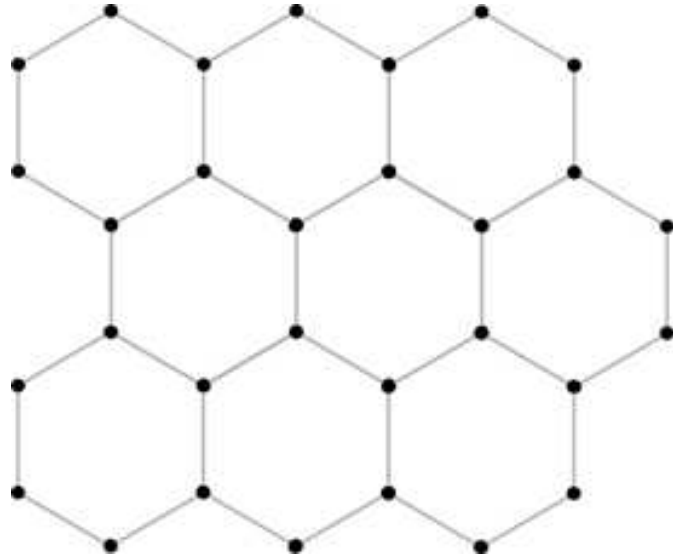


Fig. 2.15. The extracellular space graph.

The extracellular space graph contains multiple vertices (black dots), each representing a compartment of extracellular space. Each vertex is connected to immediately neighbouring vertices (grey lines).

The equation governing the rates of change of S concentration in extracellular space compartments is

$$\frac{\partial S}{\partial t} = \rho_s - \mu_s S + D_s \nabla^2 S \quad (2.9),$$

where ρ_s is the production rate of S (which is high in the file of cells acting as a source of S) with units of $\text{A}_u/\mu\text{m.s}$. μ_s is the degradation rate of S (which is high in the file of cells acting as a sink for

S) with units of $/s$ and D_s is the diffusion rate of S within the extracellular space with units of $\mu\text{m}^2/\text{s}$.

In all simulations involving cellular gradients, $\rho_s = 10^{-5} \text{ A}_u/\mu\text{m.s}$ and $\mu_s = 10^{-4}/\text{s}$ everywhere except in the column of cells at the left tissue boundary which acts as a source of S , where $\rho_s = 5 \times 10^{-4} \text{ A}_u/\mu\text{m.s}$ and in the column of cells at the right tissue boundary which acts as a sink of S , where $\mu_s = 7.5 \times 10^{-3}/\text{s}$. $D_s = 5 \mu\text{m}^2/\text{s}$. In the simulation used to generate Fig. 2.8 C where a mutant patch is introduced which degrades S at a higher rate than the background degradation rate in surrounding cells, in all cells except those in the left/rightmost columns of cells which act as a source/sink for S , $\rho_s = 10^{-4} \text{ A}_u/\mu\text{m.s}$, and $\mu_s = 10^{-4}/\text{s}$. In the leftmost column of cells which acts as a source of S , $\rho_s = 5 \times 10^{-4} \text{ A}_u/\mu\text{m.s}$ and in the rightmost column of cells which acts as a sink of S , $\mu_s = 4 \times 10^{-3}/\text{s}$. In the mutant patch, $\mu_s = 0.014/\text{s}$.

After the distribution of S becomes stable, the concentrations of S in the extracellular space graph are used to influence components in the intracellular partitioning graph. It is assumed that extracellular S triggers receptors in cell membranes, and that the activity of these receptors influences the intracellular partitioning system. The extracellular space graph is more coarsely discretised than the intracellular partitioning graph (there are fewer vertices surrounding a cell in the extracellular space graph (Fig. 2.15) than peripheral vertices surrounding a cell in the intracellular partitioning graph (Fig. 2.14)). Therefore, before using concentrations of S from the extracellular space graph to influence components in the intracellular partitioning graph, the concentrations of S are linearly interpolated between vertices in the extracellular space graph. These interpolated concentrations, S_i , are then used to set S_p (the perceived concentration of extracellular S) in membrane compartments represented by peripheral vertices in the intracellular partitioning graph. At the boundary between two adjacent cells, the membrane compartments of both cells are given the same concentration of S_i (i.e. there are no gradients in S or S_i across the

thickness of the intercellular space). After transferring the concentrations of S to the intracellular partitioning graph, noise is added to the concentration of S in the membrane compartments to simulate stochasticity involved in the establishment and perception of the S gradient:

$$S_p = S_i \pm (\theta_s * \sqrt{S_i}) \quad (2.10a),$$

$$\theta_s \in [-\varepsilon_s, \varepsilon_s] \quad (2.10b),$$

where S_p is the concentration of S perceived in a given membrane compartment with units of $\text{A}_u/\mu\text{m}$, S_i is the interpolated concentration of S and θ_s is a random number uniformly distributed between an upper and lower limit, ε_s . In all simulations, $\varepsilon_s = 0.125$. Noise is added to the concentration of S_i in proportion to $\sqrt{S_i}$.

In the second phase of simulations involving cellular gradients in S_p influencing the intracellular partitioning system (Figs. 2.8, 2.11C), the concentrations of S_p in membrane compartments are assumed to remain constant and S_p is used to promote the membrane binding of the A^* polarity component. In the case where S_p promotes the activation of A, the binding and unbinding functions of the basic intracellular partitioning system (equations 2.4b, 2.4c) are modified so that the functions for A^* in a given membrane compartment are

$$f_A(A^*, S_p) = \rho + \gamma_s S_p + \eta A^* \quad (2.11a),$$

$$g_A(B^*) = \mu + \alpha B^* \quad (2.11b),$$

Where γ_s is a constant describing the strength of promotion of A binding by S_p with units of $\mu\text{m}^2/\text{A}_u\text{s}$. The functions for B^* are the same as for intracellular partitioning alone (equations 2.4e, 2.4f).

In all simulations where cellular gradients influence intracellular partitioning except that used for Fig. 2.8D (Figs. 2.8A, B, C, 2.11C), $\gamma_s = 0.25 \mu\text{m}^2/\text{A}_u\text{s}$.

In the simulation used to generate Fig. 8D, cellular gradients operate in combination with the direct cell-cell coupling system and the direct cell-cell coupling equations (2.6a and 2.6b) are modified as follows:

$$f_A(A^*, B^{*'}, S_p) = \rho + \gamma_s S_p + \omega A^* B^{*'} \quad (2.12a),$$

$$g_A(B^*, A^{*'}) = \mu + \nu B^* A^{*'} \quad (2.12b),$$

In this simulation, $\gamma_s = 0.5 \mu\text{m}^2/\text{A}_u\text{s}$

In simulations where the intercellular gradient in S is used to influence polarity coordination (Figs. 2.9A, 2.9B, 2.11H), S_p promotes production of a factor, F, within each cell. In these simulations, after the calculation of concentrations of S_p in the membrane compartments of the intracellular partitioning graph, including the addition of noise, the concentration of F in cytoplasmic compartments is calculated. The concentration of F in cytoplasmic compartments is assumed to be proportional to the total concentration of S perceived by membrane compartments and is calculated as

$$F = \lambda \frac{1}{R_c} \sum_{n \in N(c)} l_n S_n \quad (2.13),$$

where F is the concentration of F in a given cytoplasmic compartment with units of $A_u/\mu\text{m}^2$, λ is a dimensionless constant describing the relationship between the concentration of S_p in membrane compartments and the concentration of F in the cell and R_c is the area of the cytoplasmic compartment. S_n is the concentration of S (S_p) in the membrane compartment n in the neighbourhood of the cytoplasmic compartment c ($N(c)$), with units of $A_u/\mu\text{m}$, l_n is the length of the membrane compartment n , with units of μm . In all simulations, $\lambda = 0.1$.

Once the concentration of F in cytoplasmic compartments has been calculated, F is used to influence the levels of A in cytoplasmic compartments (and therefore the total level of $A + A^*$ in a cell) during the initialisation of the intracellular partitioning system:

$$A(t = 0) = c_A(1 + \Omega F) \quad (2.14a),$$

$$B(t = 0) = c_B \quad (2.14b),$$

where $A(t=0)$ and $B(t=0)$ are the initial concentrations of polarity components in a given cytoplasmic compartment, F is the concentration of F in the cytoplasmic compartment, c_A and c_B are the default concentrations of A and B respectively in the cytoplasm, and Ω is a constant with units of $\mu\text{m}^2/A_u$, describing the strength of promotion of the levels of A by F . The initialisation of A^* and B^* concentrations in membrane compartments occurs as described for intracellular partitioning in the previous section and is not influenced by F . In all simulations, $\Omega = 70 \mu\text{m}^2/A_u$.

Following the F -influenced initialisation of the system, the interactions between the polarity components are simulated in the same way as for direct cell-cell coupling.

2.4.4 Indirect cell-cell coupling

For the implementation of indirect cell-cell coupling, the intracellular partitioning graph is modified to include another set of vertices in addition to central and peripheral vertices. I refer to this modified graph as the cell wall graph (Fig. 2.16). The additional set of vertices is arranged to form a one dimensional network surrounding the cells. Each of these vertices represents a region of the cell wall (extracellular space) and the region of cell wall represented by one vertex is referred to as a cell wall compartment. Each cell wall compartment is connected to its immediately neighbouring cell wall compartments and to the neighbouring membrane compartments which belong to the two cells separated by the wall. Therefore, in indirect cell-cell coupling models, membrane compartments of adjacent cells are always separated by a single cell wall compartment. This means concentration gradients cannot occur across the thickness of the cell wall.

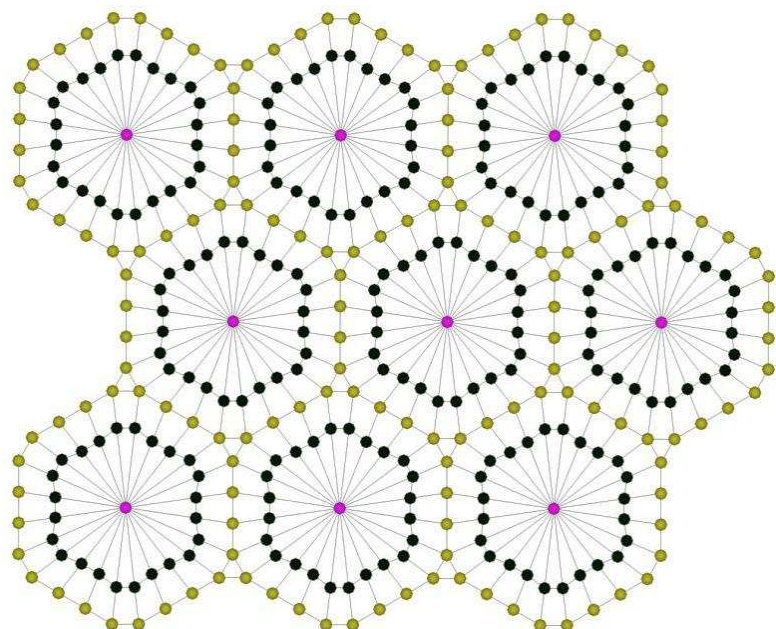


Fig. 2.16. The cell wall graph.

As for the intracellular partitioning graph, cells are represented by a single central vertex (magenta) surrounded by multiple peripheral vertices (dark grey) which represent membrane compartments. In the cell wall graph, additional vertices surround cells and represent cell wall compartments (yellow). Using this representation, cell wall compartments separate the membrane compartments of adjacent cells. Cell wall compartments are connected to adjacent cell wall compartments and to the membrane compartments of adjacent cells which are separated by the cell wall. The grey lines indicate the connections between vertices.

In simulations involving indirect cell-cell coupling in Chapter 2 (Figs. 2.5, 2.6C, 2.10, 2.11B, E, G, I), auxin coordinates polarities by interacting with the intracellular partitioning system. In all simulations of indirect cell-cell coupling, the cytoplasm is represented by the single central vertex of each cell. Auxin is present in the cytoplasm (intracellular auxin) and in wall compartments (extracellular auxin) but is not present in membrane compartments. Auxin can diffuse between neighbouring cell wall compartments in the extracellular space. The diffusion of auxin within the cytoplasm is assumed to be relatively fast and therefore, for simplicity, auxin is assumed to always be evenly distributed in the cytoplasm. Simulations using the alternative assumption that auxin is not uniformly distributed throughout the cytoplasm were performed and gave similar results to those presented. The diffusion of auxin in the extracellular space is assumed to be 100-fold faster than diffusion of polarity components in the membrane. This assumption of a two order of magnitude difference is based on experimental estimates of the diffusion constant of auxin in the plant cell wall being between 2.5 and 32 $\mu\text{m}^2/\text{s}$ (Kramer et al., 2007), compared with 0.1 $\mu\text{m}^2/\text{s}$ for membrane bound proteins (Postma and Van Haastert, 2001). The units of auxin concentration in the cytoplasm and in the wall are $\text{A}_u/\mu\text{m}^2$. During initialisation of the simulation, auxin concentrations in cell wall compartments are set to zero and auxin concentrations in the cytoplasm are set to $0.8 \text{ A}_u/\mu\text{m}^2$. The wall is assumed to have uniform thickness (1 μm).

Auxin is produced and degraded in the cytoplasm. In simulations with irregular cell geometries, production of auxin occurs in proportion to the area of the cytoplasm. Using an alternative assumption, that each cell has the same total production of auxin, rather than producing auxin in proportion to the area of the cytoplasm, gives qualitatively similar results. In addition to diffusing through the extracellular space, auxin undergoes permeation between the cell wall and the cytoplasm. The permeability rate of auxin into the cell (into the cytoplasmic compartment from a wall compartment) is assumed to be 15-fold higher than the permeability rate of auxin out of the cell (into a wall compartment from a cytoplasmic compartment). Auxin is transported out of cytoplasmic compartments in an A^* -dependent manner (A^* in each membrane compartment promotes export of auxin from the cytoplasm to the adjacent wall compartment). The rate of change in auxin concentration in a given cytoplasmic compartment for cells with regular geometries is calculated as

$$\frac{\partial Aux}{\partial t} = \rho_{Aux} - \mu_{Aux} Aux + \frac{1}{R_c} l_w \sum_{n \in N(c)} (v_{in} Aux_w - v_{out} Aux - \psi A_n^* Aux) \quad (2.15),$$

where Aux is the concentration of auxin in the cytoplasmic compartment, Aux_w is the concentration of auxin in the wall compartment neighbouring the membrane compartment n in the neighbourhood of the cell c ($N(c)$), ρ_{Aux} is the production rate of auxin with units of $A_u/\mu\text{m}^2\cdot\text{s}$, R_c is the area of the cytoplasmic compartment, and μ_{Aux} is the degradation rate of auxin with units of $/s$. A_n^* is the concentration of A^* in the n th membrane compartment of the cell. v_{in} is the background permeation rate of auxin into the cytoplasm from the wall with units of $\mu\text{m}/\text{s}$ and v_{out} is the background permeation rate of auxin into the wall from the cytoplasm with units of $\mu\text{m}/\text{s}$. ψ is the rate of A^* -dependent active efflux of auxin from the cytoplasm into the wall with units of $\mu\text{m}^2/A_u\cdot\text{s}$. The permeation and active efflux terms ($v_{in} Aux_w - v_{out} Aux - \psi A_n^* Aux$) describe the flux

of mediator between the cytoplasm and the wall compartment adjacent to the n th membrane compartment and have units of number of molecules per unit time per unit length of contact between the cell wall compartment and the cell ($A_u/\mu\text{m} \cdot \text{s}$). In order to convert the flux terms into a concentration of auxin in the cytoplasm, flux terms are multiplied by the length of the cell wall compartment into/out of which flux is occurring (l_w) (this gives the total number of molecules per unit time), and divided by the area of the cytoplasm (R_c) (this converts the total number of molecules to a concentration for the cytoplasmic compartment).

The corresponding equation for cell wall compartments is

$$\frac{\partial Aux_w}{\partial t} = -\frac{1}{R_w} l_w \sum_{n \in N(w)} (v_{in} Aux_w - v_{out} Aux_c - \psi A_n^* Aux_c) + D_{Aux} \nabla^2 Aux_w \quad (2.16),$$

where R_w is the area of the wall compartment, l_w is the length of the wall compartment, Aux_w is the concentration of auxin in the wall compartment, A_n^* is the concentration of A^* in the membrane compartment n in the neighbourhood of the given wall compartment w ($N(w)$) and Aux_c is the concentration of auxin in the cytoplasm of the same cell as the membrane compartment n . D_{Aux} is the diffusion constant for auxin within the cell wall with units of $\mu\text{m}^2/\text{s}$ (this constant relates to lateral diffusion between wall compartments as it is assumed that the concentration of auxin is uniform across the thickness of the wall).

In all simulations, $D_{Aux}=10 \mu\text{m}^2/\text{s}$, $v_{in}=0.75 \mu\text{m}/\text{s}$, $v_{out}=0.05 \mu\text{m}/\text{s}$, $\psi=7.5 \mu\text{m}^2/A_u \cdot \text{s}$. In all cells and in all simulations, except in the left and rightmost files of cells in the simulations used to generate Figs. 2.10A, 2.10B, 2.10C, 2.10D and 2.11I, $\rho_{Aux}=1.3 \times 10^{-4} A_u/\mu\text{m}^2 \cdot \text{s}$ and $\mu_{Aux}=0.02 \text{ /s}$. In the simulation used to generate Figs. 2.10A, 2.10B, and 2.11I, in the leftmost column of cells which

acts as a source of auxin, $\rho_{Aux} = 10^{-3} A_u / \mu\text{m}^2 \cdot \text{s}$ and in the right-most column of cells which acts as a sink of auxin, $\mu_{Aux} = 0.3 / \text{s}$. In the simulations used to generate Figs. 2.10C and 2.10D, in the left-most column of cells which acts as a source of auxin, $\rho_{Aux} = 3 \times 10^{-4} A_u / \mu\text{m}^2 \cdot \text{s}$ and in the right-most column of cells which acts as a sink auxin, $\mu_{Aux} = 0.05 / \text{s}$.

In the simulations used to generate the figures presented here, extracellular auxin within each cell wall compartment interacts with the intracellular partitioning system by promoting the unbinding of A^* in the adjacent membrane compartments. The influence of extracellular auxin on A^* is described by the following modification to the general unbinding function for A^* in a given membrane compartment:

$$g_A(B^*, Aux_w) = \mu + \alpha B^* + \gamma_{Aux} Aux_w \quad (2.17),$$

where B^* is the concentration of the B^* polarity component in the given membrane compartment, Aux_w is the concentration of auxin in the adjacent wall compartment and γ_{Aux} is the strength of auxin-promoted conversion from A^* to A with units of $\mu\text{m}^2 / A_u \cdot \text{s}$. The binding function for A^* , as well as the binding and unbinding functions for B^* , remain the same as for the basic intracellular partitioning mechanism (equations 2.4b, 2.4e, 2.4f respectively). In all simulations involving indirect cell-cell coupling $\gamma_{Aux} = 0.3 \mu\text{m}^2 / A_u \cdot \text{s}$.

Very similar results to those presented here are generated if extracellular auxin promotes the binding of both A^* and B^* to the membrane, with a higher rate of promotion of B^* binding compared with A^* . In this scenario, the influence of extracellular auxin on A^* and B^* is described by the following modification to the general binding functions for A^* and B^* in a given membrane compartment:

$$f_A(A^*, Aux_w) = \rho + \eta A^* + \alpha_{Aux} Aux_w \quad (2.18a),$$

$$f_B(B^*, Aux_w) = \rho + \eta B^* + \beta_{Aux} Aux_w \quad (2.18b).$$

Where Aux_w is the concentration of extracellular auxin in the juxtaposed cell wall compartment, α_{Aux} is the strength of auxin-promoted conversion from A to A^* with units of $\mu\text{m}^3/\text{A}_u\cdot\text{s}$ and β_{Aux} is the strength of auxin-promoted conversion from B to B^* with units of $\mu\text{m}^3/\text{A}_u\cdot\text{s}$. All other symbols are as described previously for equations 2.4b and 2.4e. Polarities become coupled between neighbouring cells if $\alpha_{Aux} = 1 \mu\text{m}^3/\text{A}_u\cdot\text{s}$ and if $\beta_{Aux} = 4 \mu\text{m}^3/\text{A}_u\cdot\text{s}$.

Symbol	description	unit	value	range tested and found functional
Δt	numerical time step	s (seconds)	0.01	
R_c	area of cytoplasmic compartment	μm^2	260* / 169**	
R_w	area of cell wall compartment	μm^2	2.5* / 2.6**	
l_e	length of extracellular space compartment	μm	15* / 26**	
l_n	length of membrane compartments	μm	2.5* / 2.6**	
l_w	length of wall compartments	μm	2.5* / 2.6**	

c_A, c_B	default initial concentrations of A and B polarity components respectively	A_u (arbitrary units)/ μm^2	0.02 ^{‡, #}	
d_A, d_B	default initial concentrations of A^* and B^* polarity components respectively	$A_u/\mu\text{m}$	0.3 [‡]	
ε	limit for noise addition during initialisation of A^* and B^* concentrations	dimensionless	0.0417	
D_{A^*}, D_{B^*}	diffusion coefficients of membrane-bound polarity components	$\mu\text{m}^2/\text{s}$	0.1	0.05 - 1.25
ρ	membrane-bound polarity component default binding rate	$\mu\text{m}/\text{s}$	0.02 [#]	0.004 – 0.1
μ	membrane-bound polarity component default unbinding rate	/s	0.002	0.0004 - 0.008
η	membrane-bound polarity component auto-activation rate	$\mu\text{m}^2/A_u.\text{s}$	0.2	0.1 – 1.0
α	membrane-bound polarity component cross-inhibition rate	$\mu\text{m}/A_u.\text{s}$	0.04	0.02 – 0.2
ω	complex-dependent auto-activation rate	$\mu\text{m}^3/A_u^2.\text{s}$	0.54 [#]	0.27 – 2.7
ν	complex-dependent cross-inhibition rate	$\mu\text{m}^2/A_u^2.\text{s}$	0.023	0.0046-1.15

ρ_s	production rate of S	$A_u/\mu m.s$	$10^{-5\ddagger}$	
μ_s	degradation rate of S	/s	$10^{-4\ddagger}$	
D_s	extracellular S diffusion constant	$\mu m^2/s$	5	
γ_s	S-dependent promotion of A to A* conversion	$\mu m^2/A_u.s$	0.25 [#]	
ε_s	limit for noise addition to get $[S_p]$	dimensionless	0.25	
λ	promotion of F by S_p	dimensionless	0.1	
Ω	promotion of [A] by F during initialisation	$\mu m^2/A_u$	70	
ρ_{Aux}	production rate of Auxin	$A_u/\mu m^2.s$	$1.3 \times 10^{-4\ddagger}$	$0.26 \times 10^{-4} - 6.5 \times 10^{-4}$
μ_{Aux}	degradation rate of Auxin	/s	0.02 [‡]	0.004-0.1
v_{in}	influx auxin permeability	$\mu m/s$	0.75	0.15 - 3.75
v_{out}	background auxin efflux permeability	$\mu m/s$	0.05	0.01 – 0.25
ψ	A^* -dependent auxin permeability	$\mu m^2/A_u.s$	7.5	1.5 - 37.5
γ_{Aux}	Auxin-dependent promotion of A^*	$\mu m^2/A_u.s$	0.3	0.06 - 1.5

	to A conversion			
D_{Aux}	Auxin diffusion constant in the cell wall	$\mu\text{m}^2/\text{s}$	10	2-50

Table 2.1. Parameter values used for simulations

* In simulations with regular hexagonal cell geometries. In simulations with irregular hexagonal cell geometries, the exact value may vary from this average value.

** In simulations with square cell geometries.

[†]See text for details of cases where this may differ in organiser regions at tissue boundaries.

[#]See text for details of simulations where this value may differ from the default value given.

To test the functional ranges of parameter values, the values of parameters involved in intracellular partitioning and cell-cell coupling were individually increased or decreased by a factor of 5 and the effects on the generation of cell polarities and on the coordination of polarities in a 1D file of cells were assessed. For most parameters tested (ε , D_{Aux} , v_{in} , v_{out} , γ_m , ψ , ρ_{Aux} , μ_{Aux} , v) a five-fold increase or decrease in the value used does not disrupt polarity generation or coordination and the values of all parameters tested can be at least halved or doubled while preserving the general model behaviours.

3 Comparison of models of auxin-regulated polarity

3.1 Introduction

In the previous chapter, I show that intracellular partitioning, which generates cell polarities without the need for pre-established asymmetries or polarisable neighbours, can provide a basis for the generation of tissue cell polarity. In this model, polarities are established by an auxin-independent intracellular partitioning system and become coordinated between neighbours by an auxin-mediated cell-cell coupling system. This intracellular partitioning-based model with indirect cell-cell coupling model provides a new hypothesis for how auxin may regulate tissue cell polarity. The model can capture behaviours of the flux-based and up-the-gradient models of auxin-regulated polarity. Like the flux-based model, polarities tend to orient away from auxin sources towards auxin sinks, and like the up-the-gradient model, polarities may orient towards cells with high intracellular auxin (Fig. 2.10). However, the extent to which these three models of auxin-regulated polarity behave similarly in a range of scenarios has not been thoroughly investigated.

Analyses of the up-the-gradient and flux-based models suggest that these models behave differently to the indirect cell-cell coupling mechanism. In the former two models, polarity is generated through a feedback between asymmetries in auxin distribution and PIN localisation. Therefore, unlike the indirect cell-cell coupling model, they lack a mechanism to establish polarity independently from auxin. Published simulations of the flux-based model show polarity generation in the presence of pre-established auxin gradients or auxin sources and /or sinks, suggesting that external asymmetries in auxin concentration are required for cells to polarise (Stoma et al., 2008; Bayer et al., 2009; Mitchison, 1980; Rolland-Lagan and Prusinkiewicz, 2005). The up-the-gradient model has been shown to generate polarised fields of cells given an initially noisy distribution of auxin concentrations (Smith et al., 2006; Jönsson et al., 2006). Although noise in auxin concentrations does not provide a persistent external bias, it provides an initial external

asymmetry to cells, which may be required for polarisation. Due to the apparent dependence of these models on asymmetries in auxin concentration, I and others previously proposed that the flux-based and up-the-gradient models lack an intracellular-partitioning system (Abley et al., 2013). However, whether these models are able to establish cell polarity in the absence of pre-established asymmetries or polarisable neighbours has not been formally tested.

In this chapter, I perform simulations to compare intracellular partitioning and cell-cell coupling behaviours in different models. I explore the behaviours of models in the absence of pre-established asymmetries, for single cells without polarisable neighbours, and for 2D arrays of cells. I also compare the assumptions required for different models to generate centres of polarity convergence and coordinated polarity across an array of cells. The results reveal previously unidentified similarities and differences between models and suggest a classification system for models of polarity.

3.2 Assumptions of the flux and up-the-gradient models

3.2.1 Flux-based model

The basic assumption of flux-based models is that PIN is allocated to each cell edge in proportion to the rate of auxin efflux across that edge. Published models make the simplifying assumption that auxin moves directly from a given cell into its neighbouring cells and do not include an explicit representation of the cell wall (Feugier et al., 2005; Rolland-Lagan and Prusinkiewicz, 2005; Stoma et al., 2008; van Berkel et al., 2013). It is assumed that if the auxin efflux rate is below 0 (if there is a net auxin *influx*), there is no flux-dependent allocation of PIN. Models also assume that PIN unbinds from each cell edge at a background rate, therefore in the absence of flux-dependent PIN allocation to a cell edge, PIN will be removed from that edge (Rolland-Lagan and Prusinkiewicz, 2005; Stoma et al., 2008).

Flux between two neighbouring cells, A and B, occurs due to both passive permeation and PIN-mediated transport. The flux due to passive permeation depends on the difference in auxin concentration between the two cells, and on the auxin permeation rate. If cell A has a higher concentration of auxin than cell B, passive flux will occur from A to B, encouraging PIN allocation to the edge of cell A. The flux due to PIN-mediated transport depends on the concentrations of auxin and PIN in the given cell and in the neighbour. If cell A has a higher concentration of PIN at the cell edge between A and B, and a higher concentration of auxin, then PIN mediated efflux will occur from cell A, into cell B. This will encourage further allocation of PIN to the edge of cell A, and prevent accumulation of PIN at the edge of cell B (because this edge has a net influx).

Some models assume that the allocation of PIN to a cell edge is linearly proportional the rate of auxin efflux, and some assume that PIN allocation is proportional to the efflux squared (Feugier et al., 2005; Stoma et al., 2008). Also, some models assume that each cell may allocate unlimited amounts of PIN proteins to the membrane (Rolland-Lagan and Prusinkiewicz, 2005; Stoma et al., 2008) while others assume that each cell has a fixed pool of PIN proteins, from which PIN must be recruited to the membrane (Feugier et al., 2005). Here, I explore the behaviours of different implementations of the flux-based model, with and without limited pools of PIN, and with linear and quadratic relationships between flux and PIN allocation.

3.2.2 Up-the-gradient model

The basic assumption of the up-the-gradient model is that cells allocate PIN preferentially to the edge which is closest to the neighbour with the highest auxin concentration (van Berkel et al., 2013). All implementations of the model assume that each cell has a limited pool of PIN. PIN is allocated to each cell edge according to how much of the total auxin in all the neighbours of the cell is present in the neighbour juxtaposed with that edge. Some models assume that PIN

allocation to the cell edge increases linearly with increasing auxin concentration in the neighbouring cell, and some assume that PIN allocation occurs according to an exponential function of auxin concentration in the neighbour (van Berk et al., 2013). Both assumptions are sufficient to account for the formation of spaced centres of PIN polarity convergence with high auxin such as those involved in phyllotactic patterning (Jönsson et al., 2006).

Similar to flux-based models, all implementations of the up-the-gradient model assume that auxin moves directly between cells and do not include an explicit representation of the cell wall (Bilsborough et al., 2011; Jönsson et al., 2006; Smith and Bayer, 2009; Smith et al., 2006). As in the flux based model, auxin is assumed to move between cells through PIN-mediated transport and passive permeation.

To account for phyllotactic patterns with up-the-gradient models, extra assumptions are made about the effects of auxin concentration on PIN expression levels and polarisation (Jönsson et al., 2006; Smith et al., 2006). Here, I use a simple implementation of the up-the-gradient model described by Bilsborough et al., 2011, which allows an investigation of the behaviours of the basic up-the-gradient mechanism. This implementation assumes that all cells have a background rate of auxin production, and respond in the same way to auxin. It also assumes an exponential relationship between auxin concentration in neighbouring cells and PIN allocation to cell edges (Bilsborough et al., 2011).

3.3 Results

3.3.1 Testing intracellular partitioning behaviour

To determine which models exhibit intracellular partitioning behaviour, I test whether the indirect cell-cell coupling, flux-based, and up-the-gradient models enable single cells to polarise in the

absence of pre-established asymmetries or polarisable neighbours. To do this, I ran simulations in which a single central cell is surrounded by non-polarisable neighbours. I assume that all cells have equal concentrations of auxin at the start of the simulations and that auxin can move passively between all cells. In the initial state of the simulation, noise is added to the concentrations of membrane bound proteins (PIN or A* and B*) in the central cell. If a model can generate cell polarity under these conditions, I conclude that it exhibits intracellular partitioning behaviour.

In the indirect cell-cell coupling model, I do not explicitly model PIN. However, PIN is represented in the model by assuming that the A* polarity component promotes auxin export (which represents recruitment of PIN to the A* end of the cell). The A* distribution in each cell is therefore equivalent to the predicted distribution of PIN in each cell.

3.3.1.1 Intracellular partitioning in the indirect cell-cell coupling model

In the previous chapter, I show that intracellular partitioning alone, or combined with a direct cell-cell coupling system, can generate random polarity orientations in single cells in the absence of polarisable neighbours or pre-established asymmetries (Fig. 2.2C, Fig. 2.3B, C, Fig. 2.4G). However the behaviour of the indirect cell-cell coupling model in this scenario was not tested.

In the indirect cell-cell coupling model, where extracellular auxin promotes the unbinding of A*, if the A* and B* polarity components are present in a single central cell, but absent from its neighbours (Fig. 3.1 A), and noise is added to the initial levels of polarity components in the membrane, the cell becomes polarised (Fig. 3.1 B). This polarisation occurs due to the auto-activating and mutually inhibitory interactions between the A* and B* polarity components. Since only the central cell has A*, which promotes auxin export, the auxin concentration of the central cell is lower than that of all the surrounding cells (indicated by yellow colour in Fig. 3.1 B). As a

consequence of elevated auxin export rates from the A^* -rich end of the central cell, auxin concentrations are elevated in the neighbour closest to the A^* -end (Fig. 3.1 B). Thus, in this simulation, the indirect cell-cell coupling model generates polarity independently of pre-established asymmetries or polarisable neighbours. The establishment of polarity in the central cell causes generation of an auxin gradient in the surrounding tissue.

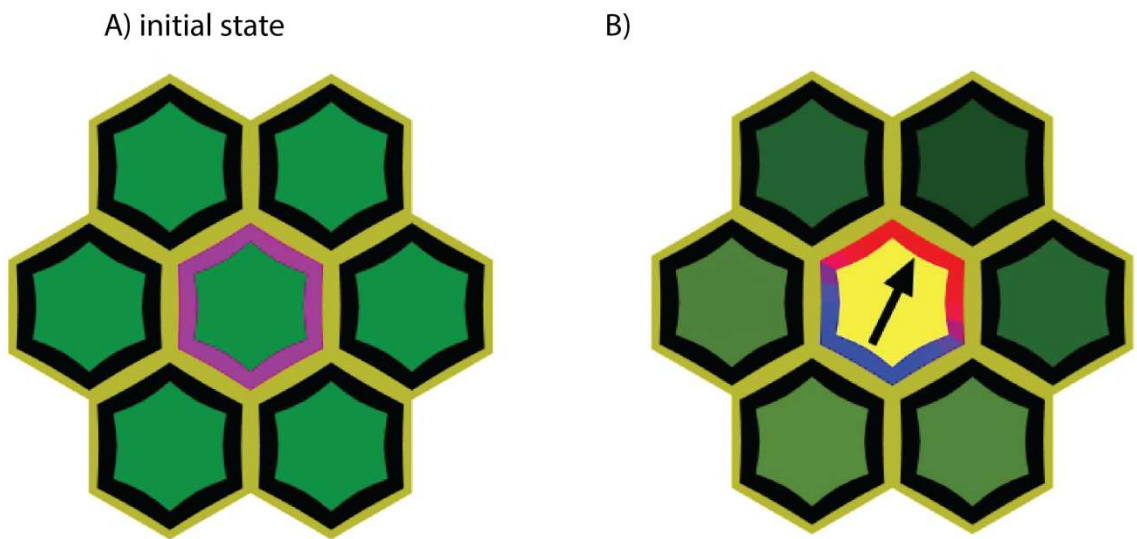


Fig. 3.1 Intracellular partitioning in the indirect cell-cell coupling model.

A) Initial state of the simulation. All cells have the same concentration of auxin (darkness of green indicates auxin concentration). The central cell has uniform but noisy concentrations of A^* and B^* polarity components in the membrane (indicated by magenta outline), other cells lack polarity components (black outlines). **B)** Final state of the simulation. The central cell has polarised A^* and B^* distributions (indicated by arrow and by A^* (red) and B^* (blue) distributions in the cell outline) and low auxin (yellow indicates low auxin concentration). The auxin concentration is highest (darkest green) in the outside cell close to the A^* rich end of the central cell.

3.3.1.2 *The up-the-gradient model also exhibits intracellular partitioning behaviour.*

I found that the up-the-gradient model is also able to generate cell polarity in the absence of pre-established asymmetries in auxin concentration or polarisable neighbours. A single central cell

with noise in the levels of PIN at each cell edge, surrounded by neighbours which do not have PIN (Fig. 3.2 A), becomes polarised so that almost all of its PIN is located at one cell edge (Fig. 3.2 B). The polarity of the central cell points towards a neighbour with elevated auxin concentration (Fig. 3.2 B).

Polarity arises in this model because, if the initial state of the model has a slightly elevated level of PIN at a given cell edge (due to noise), this causes a slight elevation of the auxin concentration in the neighbouring cell (due to higher PIN-mediated auxin export towards this cell). Elevation of the auxin concentration in the neighbouring cell then feeds back to recruit more PIN to the given cell edge. This provides a positive feedback loop which localises PIN preferentially towards a cell edge which initially had slightly elevated PIN due to noise in initial concentrations.

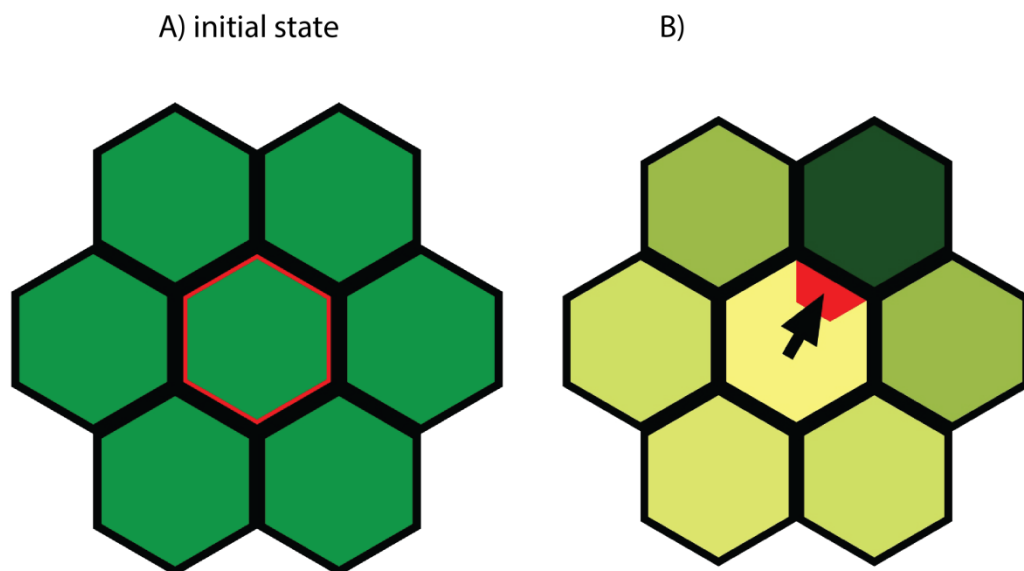


Fig. 3.2 Intracellular partitioning in the up-the-gradient model.

A) Initial state of the model. All cells have the same concentration of auxin (indicated by intensity of green). Only the central cell has PIN (indicated by red line, thickness of line indicates amount of PIN in the membrane) and can recruit PIN to the membrane. There is a small amount of noise in the initial concentration of PIN in the membrane (the differences in PIN concentration are too small to be visible). **B)** Final state of the up-the-gradient model. The central cell becomes highly polarised and has lower auxin (yellow) than surrounding cells. The neighbour closest to the PIN-rich end of the central cell has the highest auxin concentration (dark green cell). Arrow points to the region with the highest PIN concentration.

3.3.1.3 The flux-based model exhibits intracellular partitioning behaviour

The flux-based model also allows the establishment of polarity in a single cell surrounded by non-polarisable neighbours (Fig. 3.3 A, B). In the initial state of the simulation, the central cell has noise in the levels of PIN at each cell edge. Only the central cell can allocate PIN to the membrane throughout the simulation. Polarisation of the central cell occurs with all implementations of the flux-based model: with linear or quadratic relationships between flux and PIN allocation and with limited or non-limited pools of PIN.

Polarisation occurs because, if a given cell edge has a slightly elevated level of PIN due to noise, then PIN-mediated auxin efflux over that edge will increase. Through positive feedback between flux and PIN recruitment, this causes a further recruitment of PIN to the given cell edge. In the implementation where there is a limited pool of recruitable PIN, all the edges of a cell directly compete with each other for PIN, so elevated levels of PIN at a given cell edge cause a reduction in PIN recruitment to other edges, promoting the establishment of polarity.

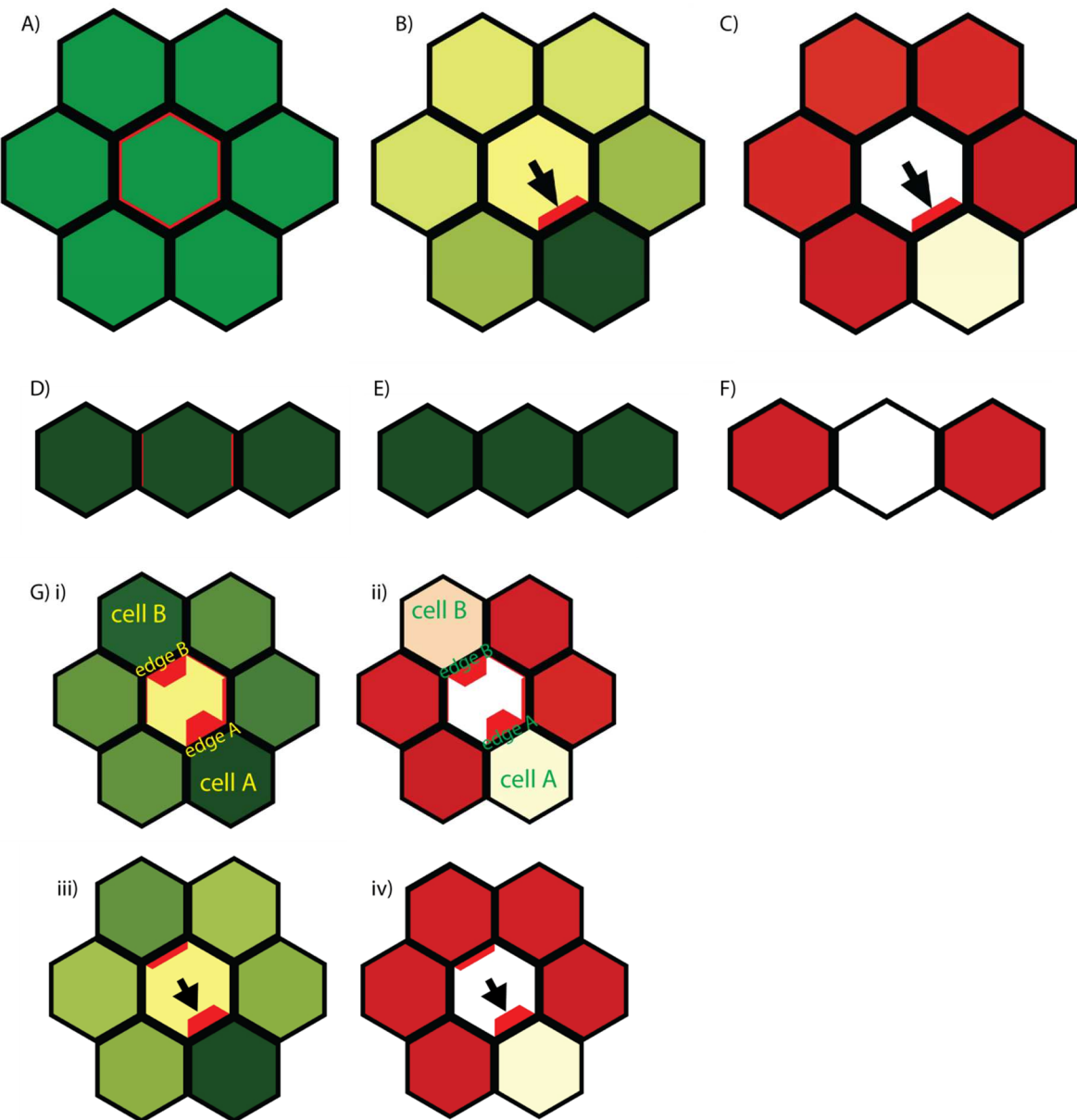


Fig. 3.3 Intracellular partitioning in the flux-based model.

A) Initial state of the model. All cells have the same concentration of auxin (indicated by intensity of green). Only the central cell has PIN (indicated by red line, thickness of line indicates amount of PIN at an edge) and can recruit PIN to its edges. Noise is present in the initial concentrations of PIN at each cell edge. **B)** Final state of the flux-based model. The central cell becomes polarised and has a lower auxin concentration (yellow colour) than surrounding cells. The neighbour closest to the PIN-rich end of the central cell has the highest auxin concentration (darkest green cell). Arrow points to the region with the highest PIN concentration. To generate the simulation result shown, the model was implemented with a non-limited pool of PIN and assuming that the rate of PIN allocation to cell edges is linearly proportional to flux. Other implementations give the same result. **C)** Ratio of current auxin concentration in a peripheral neighbour to the concentration at which PIN allocation to the adjacent edge of the central will no longer occur (R), for the model shown in B. Red colour indicates $R > 1$ (ie. the auxin concentration in the peripheral neighbour is equal to or above that at which PIN allocation to the adjacent edge of the central cell stops). Cream or pale pink indicates $R < 1$, the darker the pink the closer the ratio is to 1. **D)** Initial state of a 1D simulation with a central polarisable cell which has non-polarisable left and right neighbours. Noise is present in the initial concentrations of PIN at the left and right-most edges of the central

cell. **E**) End state of the simulation, the central cell does not polarise. **F**) The lack of polarity in the central cell occurs because the left and right neighbours acquire auxin concentrations above those at which PIN allocation to the membrane stops ($R > 1$, dark red cells). **G**) Unstable intermediate states prior to the generation of the result shown in B, where edge A and B of the central cell both have elevated PIN concentrations. i) and ii) show a state towards the beginning of a simulation, with auxin concentrations shown in i) and R values shown in ii). Initially edge A has a slightly higher PIN concentration than edge B, and therefore cell A has a slightly higher auxin concentration than cell B. Since the auxin gradient between cell A and its neighbours is steeper than the gradient between cell B and its neighbours, cell A loses more auxin due to passive permeation. This allows the auxin concentration in cell A to remain further from the concentration at which PIN allocation to edge A will stop (R remains below 1 for cell A, cell A has a lighter colour than cell B in ii). iii) and iv) A later stage of the simulation. The auxin concentration in cell B has reached that at which PIN allocation to edge B can no-longer occur ($R > 1$), so the amount of PIN at edge B decreases due to default unbinding of PIN.

In the implementation where the pool of PIN is unlimited in each cell, PIN can be recruited to each membrane independently, so an increase in the level of PIN at one cell edge doesn't directly compete with an increase at another cell edge. However, one edge of the central cell can indirectly prevent the accumulation of PIN at the opposite end of the cell through competition between edges to export auxin into their neighbours.

In the implementation with a non-limited pool of PIN, accumulation of auxin in peripheral neighbours of the central cell counteracts the allocation of PIN to its edges. If a peripheral neighbour adjacent to a given edge of the central cell accumulates enough auxin, the auxin influx into the central cell across the edge (due to passive permeation from the neighbour) may balance the rate of auxin efflux across the edge (due to PIN mediated transport and passive permeation). When there is no net flux across the membrane, PIN allocation to the membrane will fall to zero, and PIN will be removed from the membrane due to a background rate of unbinding. The allocation of PIN to an edge of the central cell therefore depends on the extent to which the auxin concentration in the peripheral neighbour is lower than the auxin concentration at which efflux across the cell edge will be balanced by influx from the neighbour. The ratio (R) of the auxin

concentration in the peripheral neighbour to the steady-state auxin concentration (at and above which PIN will not be allocated to an edge of the central cell) may be calculated (as described in the model descriptions section of this chapter) and used to understand why polarisation occurs. If the value of R for a peripheral neighbour is less than 1, PIN can still be allocated to the adjacent edge of the central cell, but if $R \geq 1$, PIN can no-longer be allocated to the adjacent edge.

If the simulation is run for a 1D file of cells, with a single polarisable central cell with non-polarisable cells to the left and right of it, the central cell does not polarise (Fig. 3.3 D, E). Because the peripheral neighbours cannot lose auxin through passive permeation into other peripheral neighbours, their auxin concentrations reach the steady-state concentration at which PIN can no longer be allocated to the membrane of the central cell ($R > 1$) (Fig. 3.3 F).

However, in the 2D scenario, there is the possibility for auxin to leave a peripheral cell by passive permeation into neighbouring cells, which may prevent the loss of polarity seen in the 1D case (Fig. 3.3 C). In the scenario shown in Fig. 3.3 B, although there is high auxin in the peripheral neighbour of the edge with elevated PIN, this peripheral neighbour has an auxin concentration below the steady-state concentration at which PIN allocation to the membrane will stop (Fig. 3.3 C). This is due to loss of auxin, by passive permeation, into neighbouring peripheral cells. As a consequence of loss of auxin from the high auxin cell into other peripheral cells, all the other peripheral cells have an R value of > 1 . This explains why edges of the central cell adjacent to these neighbours lack PIN.

With this system, if two edges, A and B, at opposite ends of a central cell initially have elevated levels of PIN, the edges will indirectly compete to establish high levels of PIN through auxin export into peripheral neighbours (Fig. 3.3 G). If edge A has slightly higher PIN, there will be higher auxin in the adjacent peripheral neighbour (cell A), and a steeper auxin gradient between neighbour A

and its neighbours (Fig. 3.3 Gi). Neighbour A will therefore lose auxin at a higher rate to neighbouring cells than peripheral neighbour B will. This will allow the auxin concentration in cell A to remain further from the concentration at which PIN allocation to edge A will stop (R remains below 1 for cell A, cell A has a lighter colour than cell B in Fig. 3.3 G ii). As a consequence of passive permeation of auxin from neighbour A to its peripheral neighbours, the auxin gradient between B and its neighbours will become shallower (Fig. 3.3 G iii), reducing the ability of cell B to maintain an R value of less than 1 (Fig. 3.3 G iv). Consequently, PIN will no longer be allocated to edge B, and only edge A will maintain elevated levels of PIN.

3.3.2 Behaviours of groups of cells in the absence of tissue-wide biases

For a 2D array of cells with no pre-established asymmetries, but with noise in the initial conditions, the indirect cell-cell coupling model generates swirled patterns of polarity (Fig. 2.5 E). Cell polarities are locally coordinated longitudinally and laterally, but not coordinated across the tissue. In the previous chapter, I propose that these swirled patterns are a feature of a system with intracellular partitioning combined with cell-cell coupling (Abley et al., 2013).

In the indirect cell-cell coupling model, the A* polarity component promotes auxin export and extracellular auxin inhibits the presence of the A* polarity component in adjacent membrane regions. As a consequence, convergent polarities, where two juxtaposed membranes of neighbouring cells have high levels of A*, are unstable (Fig. 2.5 C). In this model, the mechanism of auxin signalling between cells also promotes the emergence of tandemly coordinated polarity orientations. Consider a file of cells in which only one cell (cell P) is polarised, and all other cells have not yet become polarised (this scenario may arise if noise is only added to A* and B* concentrations in one cell) (Fig. 3.4 i). In this scenario, the polarity orientation of the P cell will bias the polarity orientations that are established in its neighbours. If the P cell has a rightward

polarity, then extracellular auxin will accumulate at its right end (Fig. 3.4 ii). This elevated extracellular auxin will favour the presence of B^* over A^* in the juxtaposed membrane of the right neighbour. The right neighbour's polarity will therefore orient rightwards and align in tandem with the polarity of the polarised cell (Fig. 3.4 iii).

The polarised cell may also influence the polarity of its left neighbour. As a consequence of the P cell establishing elevated levels of A^* -mediated auxin export at its right end, its intracellular auxin concentration will be low compared with other cells in the file (Fig. 3.4 ii). Assuming some passive outward permeation of auxin, the reduction in intracellular auxin in the P cell will tend to reduce its passive auxin efflux. Also, if it is assumed that there is a limited amount of A^* in each cell, then recruitment of A^* to the right end of the P cell will reduce the level of A^* at its left end. Both of these effects will tend to lower the extracellular auxin level at the left end of the P cell (Fig. 3.4 ii). In turn, this promotes A^* in the adjacent membrane region of the left neighbour (because extracellular auxin inhibits A^*). The left neighbour will therefore orient its polarity rightwards, aligning with the P cell (Fig. 3.4 iii). Once the neighbours of the P cell become polarised, they may propagate their polarity orientation in the same way.

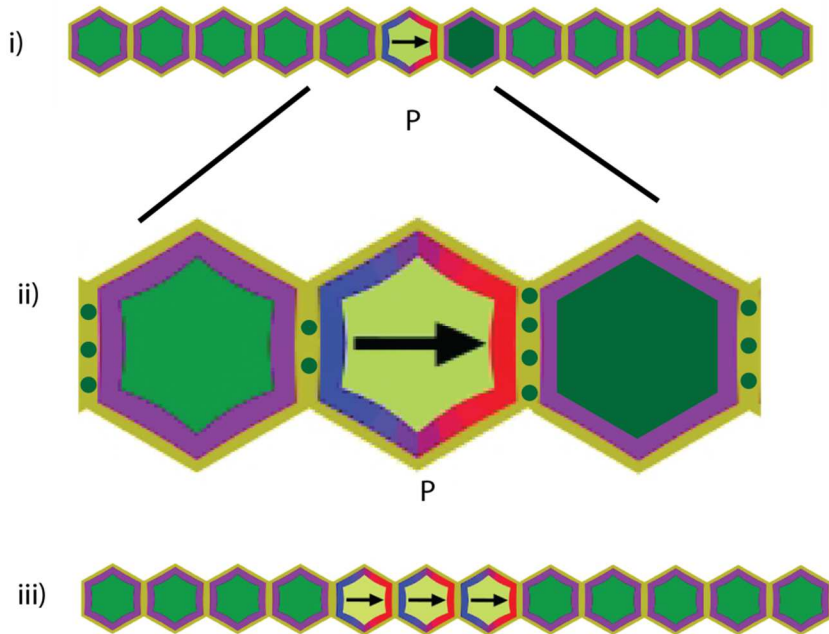


Fig. 3.4 Generation of locally coordinated polarities in an indirect cell-cell coupling model.

i) In an indirect cell-cell coupling model, if one cell (marked P) becomes polarised before the other cells in the file, it will influence the levels of extracellular auxin at its left and right. ii) At the left end of the P cell, the extracellular auxin levels are lower than background levels, due to reduced levels of A^* in the left membrane of the P cell and due to reduced passive permeation from that cell (because of its lower auxin concentration). At the right end of the P cell, extracellular auxin levels are elevated because of A^* -dependent auxin export from the P cell. (iii) These changes in extracellular auxin levels will favour the presence of B^* in the adjacent membrane of the right neighbour and A^* in the adjacent membrane of the left neighbour, promoting establishment of coordinated polarity orientations in the neighbouring cells.

3.3.2.1 *The up-the-gradient model generates centres of polarity convergence in the absence of pre-established asymmetries.*

Like the indirect cell-cell coupling model, the up-the-gradient model exhibits intracellular partitioning and has auxin-mediated signalling between cells. This raises the question of whether

this model can also generate swirled (locally coordinated) patterns of polarity in the absence of pre-established asymmetries.

For a 2D array of cells, with noise in the concentrations of auxin in each cell added at each step of the simulation, the up-the-gradient model generates regions of PIN polarity convergence with high auxin at their centre (Fig. 3.5 A) (Jönsson et al., 2006; Smith et al., 2006). For the 2D array used here, cells at the edge of the array lack outer neighbours, so polarities of cells at the boundary are biased to point inwards (because PIN cannot be localised to the outside cell edge). This boundary effect provides some bias, but this is minimised at the centre of a large array (Fig. 3.5 A).

To overcome the boundary effect bias, simulations may be run where cells at opposite edges of the tissue are connected (periodic boundary conditions). For a 1D file of cells with periodic boundary conditions, centres of polarity convergence with high auxin still form (Fig. 3.5 B). Centres of polarity convergence also form for 2D arrays with periodic boundary conditions (Jönsson et al., 2006; Smith et al., 2006).

Adding noise in the levels of PIN at each cell edge at the beginning of the simulation is sufficient for centres of PIN convergence to form even if the concentrations of auxin are initially equal in all cells (Fig. 3.5 C). This reveals that small asymmetries in auxin concentration (due to noise in initial auxin concentrations) are not required for the emergence of centres of polarity convergence in the up-the-gradient model.

Centres of convergence that arise in this model are spaced from each other, with a minimum distance between neighbouring centres. At either side of a polarity convergence, short stretches of cells have longitudinally and, in 2D, laterally, coordinated polarities. However, polarities always

converge towards a cell-cell interface where two juxtaposed membranes both have high levels of PIN (Fig. 3.5). This is in contrast to swirled patterns of polarity generated by the indirect cell-cell coupling model, in which polarities of neighbouring cells do not converge, but tend to align in tandem (Fig. 2.5 E).

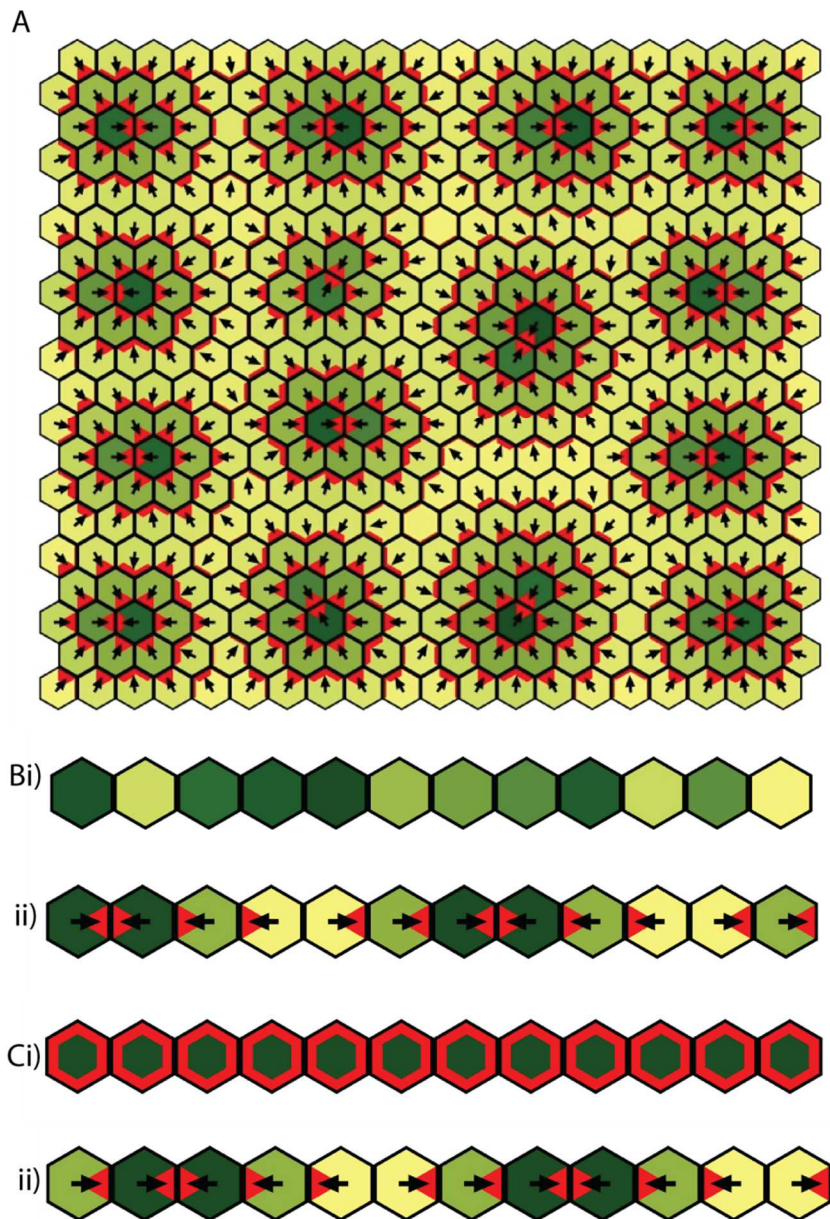


Fig. 3.5 Up-the-gradient model for tissues with no pre-established asymmetries in auxin concentration.

A) Up-the-gradient model for a 2D tissue with noise in auxin concentrations added at each step of the simulation. The tissue has open boundaries, which provides a bias for boundary cells to have

inwardly oriented polarities, therefore a large array of cells is shown, in which boundary effects are minimised far from boundaries. Intensity of green indicates the concentration of auxin (dark green indicates high auxin, yellow indicates low auxin concentration). Arrows point to the region of the cell with the highest level of PIN. Red lines indicate the localisation of PIN, with thicker lines indicating a higher concentration of PIN at the cell edge. **B**) Up-the-gradient model for a 1D file of cells with noise in initial auxin concentrations (i), with periodic boundary conditions (the left neighbour is linked to the right neighbour), showing that in the absence of boundary effects, the model generates centres of PIN convergence (ii). As in A), noise was added to auxin concentrations at each time step of the simulation. **C**) As for B, but for noise in the initial concentrations of PIN in the membrane, with equal concentrations of auxin in all cells at the start of the simulation. i) shows the initial state, ii) shows the final state of the simulation.

To illustrate how centres of PIN convergence arise in this model, consider a 1D file of cells with periodic boundary conditions (and therefore no boundary effects). If a central cell has a slightly elevated auxin concentration at the start of the simulation (Fig 3.6 i), with small amounts of noise added to the concentrations of auxin in each cell throughout the simulation, a stable polarity convergence forms centred on the initial high auxin cell (Fig 3.6 v). This happens because, as a consequence of higher auxin in the central cell, neighbouring cells orient their PIN proteins preferentially towards it (Fig 3.6 ii). The auxin concentrations of the neighbours of the central cell then become elevated, due to diffusion of auxin from the central cell (Fig 3.6 ii). This causes their more peripheral neighbours begin to orient PINs towards them, so that two cells on each side of the central cell have their polarity oriented towards it (Fig 3.6 ii and iii). The central cell initially allocates PIN proteins equally to both of its neighbours, since both have similar auxin concentrations (Fig 3.6 ii). At this stage, there are therefore two cell-cell interfaces with convergent polarity, one on either side of the central cell. As the simulation progresses, auxin levels increase in the neighbours of the central cell, as a result of transport in this direction, and diffusion from the central cell (Fig 3.6 iii). Due to noise in the simulation, the left neighbour of the central cell happens to acquire slightly more auxin than the right neighbour, causing the central cell to begin to orient its PIN preferentially towards its left neighbour (Fig 3.6 iv). Once the polarity of the central cell is oriented towards its left neighbour, the system is stable. Due to diffusion of

auxin away from the centre of convergence, an auxin gradient is created which spans over 3 cells on either side of the convergence (Fig 3.6 v). Thus, the polarities of cells around the convergence will remain oriented “up-the-gradient” to its centre. Since auxin levels are locally highest in the central cell and the left neighbour, neither of these cells will reorient their polarity.

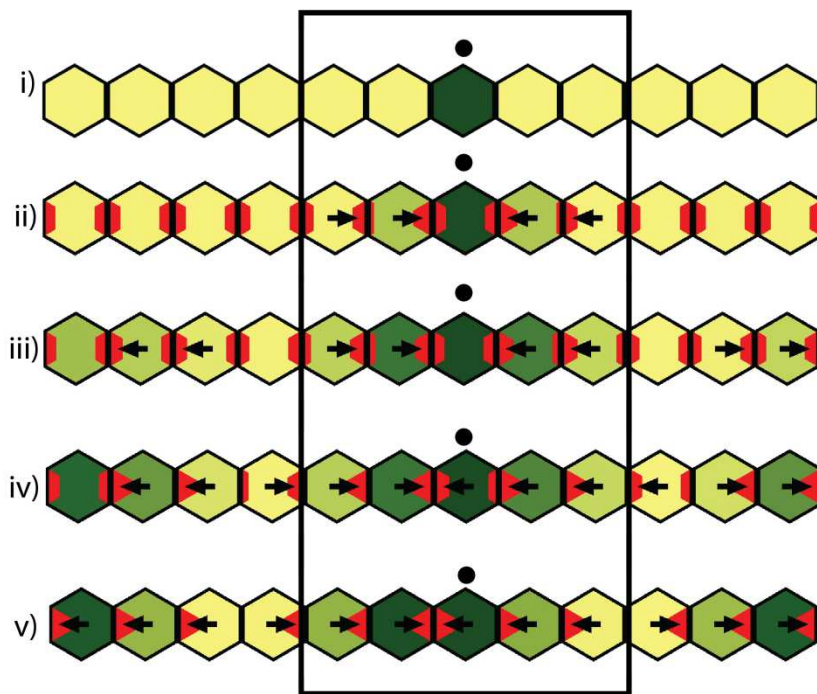


Fig. 3.6 Formation of a polarity convergence in an up-the-gradient model.

i) Initial state of the simulation, a cell, indicated by the black dot (referred to as the central cell) is given a slightly elevated auxin concentration compared with other cells in the file. In all images auxin concentration is indicated by the intensity of green. Dark green indicates the highest auxin concentration, yellow indicates the lowest auxin concentration. PIN localisation is shown in red (thickness of red line is proportional to the PIN levels in the membrane), and indicated by the arrows. ii)-vi) Trajectory of the system. Noise is added to the auxin concentrations in each cell at each time step of the simulation ii) As a consequence of elevated auxin in the central cell, its neighbouring cells orient their PIN proteins preferentially towards it. The auxin concentration of the neighbours is elevated due to diffusion of auxin from the central cell, causing their peripheral neighbours begin to orient PINs towards them. The central cell allocates PIN proteins equally to both of its neighbours, since both have similar auxin concentrations. iii) Auxin levels increase in cells closest to the central cell, as a result of transport in this direction, and diffusion from the central cell. iv) Due to noise in the simulation, the left neighbour of the central cell acquires more auxin than the right neighbour, causing the central cell to begin to orient its PIN preferentially

towards the left neighbour. v) Once the polarity of the central cell is oriented towards its left neighbour, and a single site of polarity convergence is generated, the system is stable.

3.3.2.2 The flux-based model generates swirled patterns of polarity in the absence of pre-established asymmetries.

In contrast to the up-the-gradient model, and similar to the indirect cell-cell coupling model, the flux-based model generates swirled patterns of polarity for a 2D array with noise either in auxin or PIN distributions. For an implementation of the flux based model where PIN allocation increases linearly with increased flux across a cell edge, and where there is no limit on the total amount of PIN in a cell, most cells in the tissue acquire polarised PIN, and polarities show local lateral and longitudinal coordination (Fig. 3.7 A, B). With this implementation of the model, some cells have two or three peaks of PIN, at separate cell edges, and are therefore unpolarised.

For the flux based model with a limited pool of PIN and with PIN allocation increasing quadratically with increased auxin efflux, all cells become polarised, and polarities tend to become coordinated between neighbouring cells (Fig. 3.7 C). In this version of the model, PIN becomes restricted to a single edge of each cell. This reduces the extent to which neighbouring cells align their polarity compared with when a non-limiting pool of PIN and a linear relationship between flux and PIN recruitment are assumed.

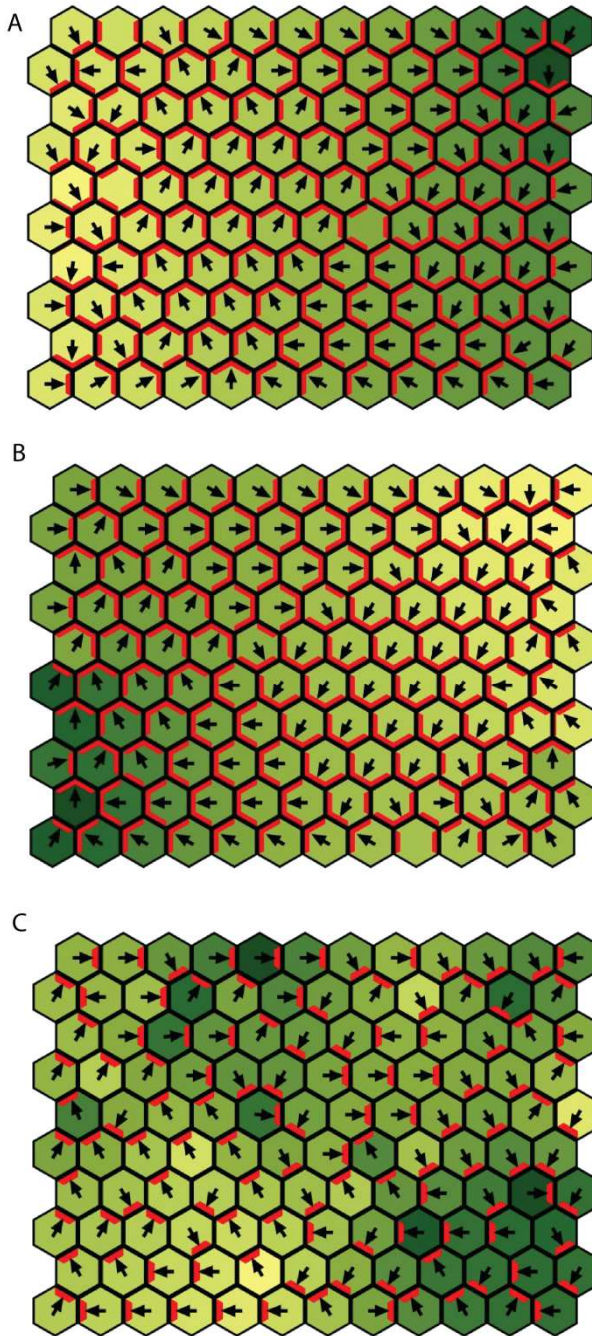


Fig. 3.7 Flux based model for tissues with no pre-established asymmetries in auxin concentration.

A) Flux based model with PIN allocation to an edge increasing linearly with flux, and with an unlimited pool of PIN. Noise was added to auxin concentrations in the initial state of the simulation, and at every subsequent step. Intensity of green indicates the concentration of auxin (dark green indicates high auxin, yellow indicates low auxin concentration). Arrows point to the region of the cell with highest level of PIN. Red lines indicate the localisation of PIN, with thicker lines indicating a higher concentration of PIN at the cell edge. **B)** Same as A, but with noise in the levels of PIN in each membrane compartment added in the initial state of the simulation and at each subsequent time step. At the start of the simulation, the auxin concentration was equal in every cell. **C)** As for A (noise added to auxin concentrations in each cell in the initial state and at each time step), but with an implementation of the model with a limited pool of PIN in each cell, and with a quadratic relationship between auxin efflux and PIN allocation to cell edges.

In these flux-based models, swirled patterns of polarity arise because, as for the indirect cell-cell coupling model, convergent polarity orientations are unstable. To illustrate this, consider a group of cells with polarities aligned to point rightwards in a 1D file, where one cell of the file (cell R) is given a reversed polarity with respect to the other cells (Fig. 3.8 Ai). At the interface between the R cell and its left neighbour, PIN is localised to both juxtaposed cell edges. If both the R cell and its left neighbour have approximately the same concentration of auxin, then the net flux across the

interface between them will be close to zero (because flux due to passive permeation will be close to zero, and flux due to PIN-mediated transport will be balanced in both directions). The rate of PIN allocation (which depends on flux) to this cell-cell interface will therefore be low in both the R cell and in the left neighbour. Also, as a consequence of this convergent PIN polarity between the R cell and its left neighbour, the auxin concentration of these cells will tend to increase as auxin cannot be transported away from this region. Therefore, there will be a net flux, due to passive permeation, from the R cell into its right neighbour, which has a lower auxin concentration (dotted white arrow in Fig. 3.8 Ai). This will encourage the binding of PIN to the right cell edge of the R cell, and its removal from the left cell edge. The R cell will therefore tend to reverse its polarity and align in tandem with other cells in the file (Fig. 3.8 Aii).

As for the indirect cell-cell coupling model, in the flux-based model, a single polarised cell will tend to promote neighbouring cells to adopt the same polarity orientation. For a 1D file of cells, consider a cell, P, which is polarised to point right-wards, with non-polarised neighbours on both sides (Fig. 3.8 Bi). As a consequence of PIN-mediated auxin transport, from the P cell, to its right neighbour, the right neighbour of the P cell will acquire an elevated auxin concentration. Due to this elevated auxin concentration, there will be a net efflux from the right neighbour, towards its right neighbour (due to passive permeation of auxin) (white arrow, Fig. 3.8Bi). This will cause the right neighbour of the P cell to acquire a rightward polarity, which is aligned with the polarity of the P cell (Fig. 3.8 Bii). Also, as a consequence of rightwards auxin transport from the P cell, its auxin concentration will drop. There will therefore be a net auxin efflux (due to passive permeation) from the left neighbour of the P cell into the P cell. The left neighbour will therefore allocate PIN rightwards, towards the P cell, so that their polarities are aligned (Fig. 3.8 Bii). These effects may propagate a coordinated polarity orientation through a tissue away from a polarised cell (Fig. 3.8 B ii).

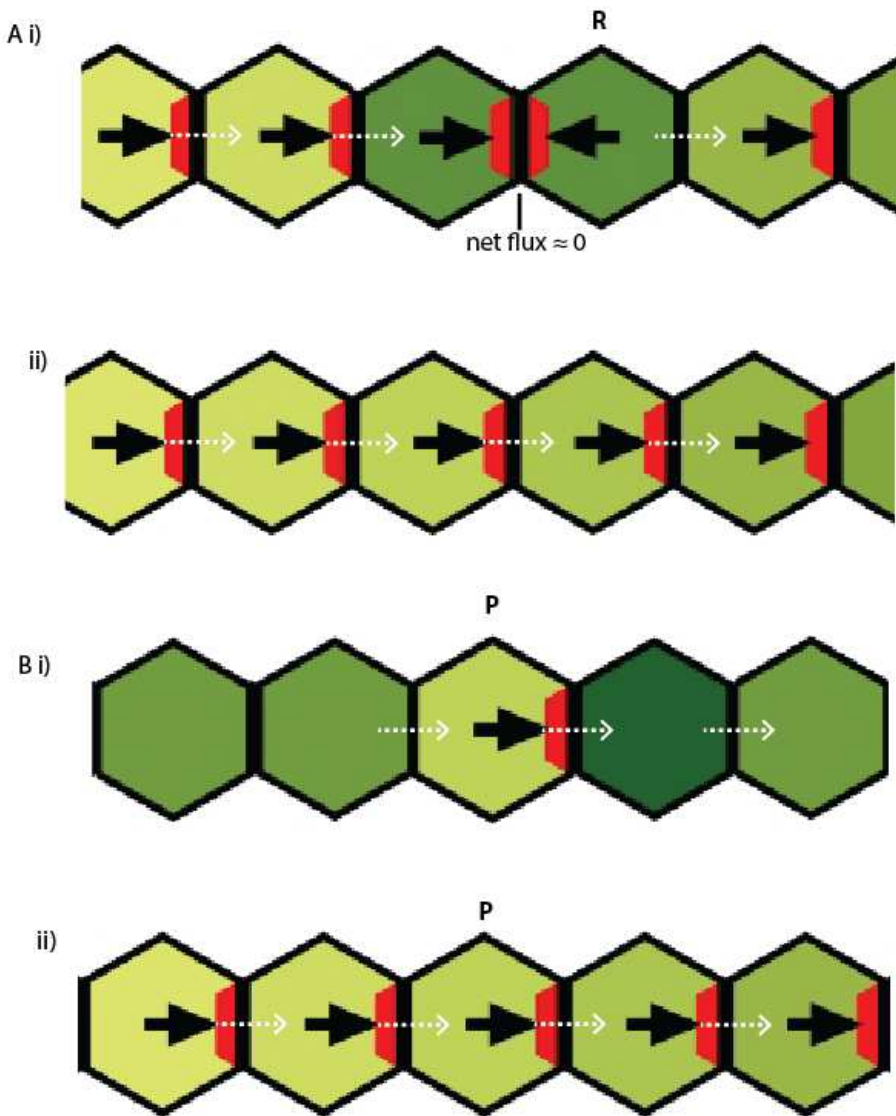


Fig. 3.8 Emergence of coordinated polarity orientations in the flux-based model.

A) Scenario where the polarity of one cell, cell R, is forced to reverse, creating a convergence of polarity between cell R and its left neighbour. White arrows show the direction of net auxin flux at cell-cell interfaces. Darkness of green indicates auxin concentration, with dark green indicating a high concentration and yellow indicating a low concentration. At the interface between the R cell and its left neighbour, the net flux is close to zero because both cells have similar auxin concentrations (so the flux due to passive permeation is low) and both cells have equal levels of PIN at both sides of the cell-cell interface. PIN allocation to this interface will therefore tend to be low. As a consequence of the forced polarity convergence, the R cell has high intracellular auxin, as auxin cannot be transported away from it along the file of cells. There will therefore be a net efflux of auxin over the right cell edge of the R cell, due to passive permeation of auxin between the R cell and its right neighbour. This will encourage PIN localisation to the right cell of the R cell.

ii) As a consequence, the polarity of the R cell will converge and align with the other cells in the file. **B)** Scenario where one cell (marked P) becomes polarised and is surrounded by unpolarised neighbours. As a consequence of PIN-mediated auxin transport, from the P cell, to its right neighbour, the right neighbour of the P cell will acquire an elevated auxin concentration. Due to

this elevated auxin concentration, there will be a net auxin efflux from the right neighbour, towards its right neighbour (due to passive permeation). The right neighbour will therefore allocate PIN to its right cell edge, but not to its left cell edge which has a net influx due to PIN-mediated transport from the P cell. The right neighbour will therefore align its polarity with the P cell (ii). Also, as a consequence of rightwards auxin transport from the P cell, its auxin concentration will drop. There will therefore be a net efflux, due to passive permeation, from the left neighbour of the P cell into the P cell. The left neighbour will therefore allocate PIN towards the P cell, aligning its polarity with that established in the P cell.

3.3.3 Generation of centres of polarity convergence in indirect cell-cell coupling and flux-based models

Although the indirect cell-cell coupling and flux based models generate swirled patterns of polarity for 2D tissues in the absence of pre-established asymmetries, these models may generate centres of polarity convergence in the presence of regions that remove auxin. For the flux based model, centres of convergence may form around a cell with elevated levels of auxin degradation (Fig. 3.9 A). Auxin degradation in the cell lowers its intracellular auxin concentration, causing a net auxin influx into it due to passive permeation. In neighbouring cells, this promotes the allocation of PIN to edges closest to the cell with elevated degradation. This depletes the level of auxin in the immediate neighbours of the cell with elevated degradation, causing more peripheral neighbours to orient their PIN towards the auxin degrading cell. The auxin-degrading cell therefore acts as a minus organiser of polarity. In the indirect cell-cell coupling model, a centre of convergence may also form in the presence of a cell with elevated auxin degradation, although the centres of convergence tend to be unstable (not shown). In contrast to the up-the-gradient model, these centres of convergence tend to have low intracellular auxin concentrations (Fig. 3.9 A, compare with Fig. 3.5 A).

A centre of polarity convergence with elevated intracellular auxin (similar to those generated in the up-the-gradient model) can be established by introduction of a cell with elevated rates of both auxin degradation and auxin import (Fig. 3.9 B, C). In the flux based model, elevated import

in a minus organiser cell with elevated auxin degradation rates increases auxin flux from surrounding cells towards it. This encourages PIN polarities to orient towards the minus organiser cell and allows accumulation of elevated intracellular auxin within it (providing auxin degradation rates in the minus organiser are not too high) (Fig. 3.9 B). In the indirect cell-cell coupling model, elevated auxin import in a cell which also has elevated auxin degradation rates reduces extracellular auxin concentrations around the cell, and encourages neighbouring cells to orient their A* end towards it (Fig. 3.9 C). As in the flux based model, elevated auxin import also

promotes accumulation of intracellular auxin in the minus organiser cell.

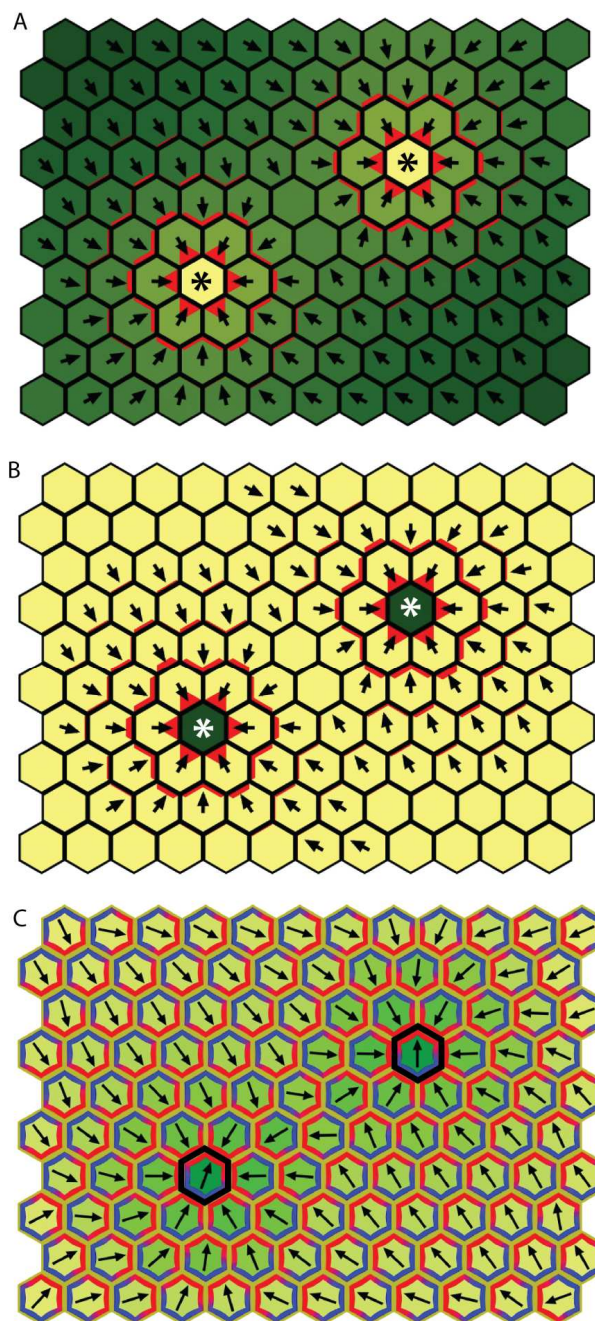


Fig. 3.9 Generation of centres of polarity convergence in flux-based and indirect cell-cell coupling models.

A) Generation of centres of convergence in the flux-based model with a non-limited pool of PIN and a linear relationship between flux and PIN allocation, in the presence of cells (marked by asterisks) that have an elevated rate of auxin degradation and therefore act as minus organisers of polarity. Note low intracellular auxin concentrations (yellow) in the minus organiser cells. **B)** Same as A, but with elevated rates of both auxin degradation and import in the minus organiser cells. Note high intracellular auxin concentrations (dark green) in the minus organiser cells. **C)** Formation of polarity convergences in the indirect cell-cell coupling model with elevated rates of auxin degradation and import in minus organiser cells (marked with back outlines).

One difference between the indirect cell-cell coupling and flux-based models is that the indirect cell-cell coupling model generates a polarity convergence centred on a cell-cell interface (similar to the up-the-gradient model), whereas the flux based model generates a polarity convergence with a non- polarised cell (the minus organiser) at the centre. This is because, in the flux based model, the minus organiser cell has a net auxin influx across all its cell edges, therefore cannot allocate PIN to the membrane.

This may reflect the way that the two models were implemented, rather than representing a fundamental difference between model behaviours. Unlike the indirect cell-cell coupling model, the flux based model does not have a representation of the cell wall and auxin flux occurs directly from one cell to another. If a representation of the cell wall was added to the model, it might be possible for centres of polarity convergence to form centred on a cell-cell interface. In the presence of a cell wall compartment, if a cell with elevated auxin import was added to the model, the cell wall surrounding it would have a low concentration of extracellular auxin. Both the cell with elevated auxin import, and the neighbouring cells, might therefore have a net auxin efflux into the cell wall with low extracellular auxin, allowing all cells to allocate PIN to the membrane.

3.3.4 Generation of coordinated polarity across tissues

In the previous chapter, I show that the indirect cell-cell coupling model can generate coordinated polarity across a tissue if the levels of extracellular auxin are modulated at tissue boundaries. In this model, polarities point away from regions with elevated levels of extracellular auxin and towards regions with relatively low levels of extracellular auxin (Fig. 2.6 C, Fig. 2.10). Plus organisers (regions that cause polarity to orient away from them) may have elevated auxin production rates (Fig. 2.10 A), or elevated levels of A* in the membrane (and thus elevated rates of auxin export) (Fig. 2.6 C). Minus organisers (regions that cause polarity to orient towards them)

may have elevated rates of auxin degradation (Fig. 2.10 A), or elevated rates of auxin import (Fig. 2.6 C). If the minus organiser has an elevated rate of auxin degradation, it will tend to have a relatively low intracellular auxin concentration (Fig. 2.10 A). Polarities will therefore appear to point down the concentration gradient of auxin. However, if the minus organiser has an elevated rate of auxin import, it may have a relatively high intracellular auxin concentration, and thus polarity points towards an intracellular auxin maximum (Fig. 2.6 C, Fig. 2.10 D).

3.3.4.1 Coordinated polarity across a tissue for an up-the-gradient model

The up-the-gradient model may also generate coordinated polarity across a tissue in the presence of organiser regions at tissue boundaries (Fig. 3.10). In this model, a minus organiser region must have elevated concentrations of intracellular auxin so that neighbouring cells orient their PIN proteins towards it. This can be achieved by having elevated auxin production rates in minus organiser regions. Cells at the minus organiser form small regions of polarity convergence with immediately neighbouring cells. A plus organiser must have low levels of intracellular auxin so that neighbouring cells orient their polarities away from it, towards a neighbour with higher auxin. This can be achieved by having an elevated rate of auxin removal in plus organiser regions. Thus, the behaviours of plus and minus organisers must be different to those in the indirect cell-cell coupling model. The differences in behaviour of organiser regions may not be reflected in their intracellular auxin concentrations. A minus organiser may have high intracellular auxin in all three models, but for different reasons: in the flux or indirect coupling model this is because of high auxin import in minus organiser regions, but in the up-the-gradient model this is because of high auxin biosynthesis.

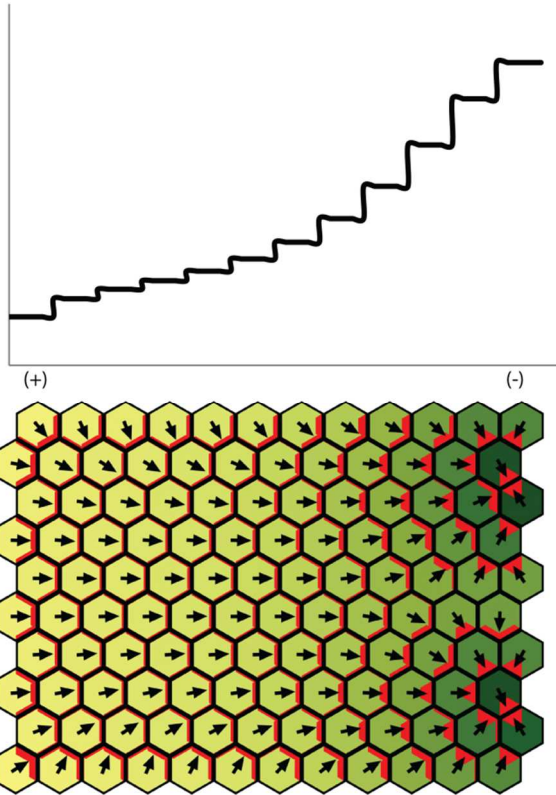


Fig. 3.10 Coordination of polarity across a 2D array of cells for the up-the-gradient model.
 Polarity points away from a file of cells on the left of the tissue with elevated auxin degradation rates (+ organiser), and towards a file of cells on the right of the tissue with elevated auxin production (- organiser). Graph shows the concentrations of intracellular auxin for a single row of cells.

3.3.4.2 Coordinated polarity across a tissue for a flux-based model

Similar to the indirect cell-cell coupling model, the flux-based model may generate a left-right coordinated polarity field in the presence of a file of cells with elevated auxin production (which acts as a plus organiser) at the left of the tissue, and a file of cells with elevated auxin degradation rates (which acts as a minus organiser) at the right of the tissue (Fig. 3.11 A). Elevated auxin production in plus organiser cells at the left of the tissue raises their intracellular auxin concentration, promoting passive auxin efflux, and therefore PIN localisation, towards neighbouring cells on the right. This raises the auxin concentration of the right neighbours, and allows the polarisation to propagate rightwards. As in the indirect cell-cell coupling model, in this

model, auxin may either be low or elevated in minus organiser cells. If the rate of auxin degradation in the minus organiser is relatively high, its intracellular auxin concentration will be low compared with other regions of the array (Fig. 3.11 A). However, if the rate of auxin degradation in the minus organiser cell is relatively low (but above background levels) and the minus organiser has an elevated rate of auxin import, auxin may accumulate in the minus organiser cell as a consequence of transport towards it and elevated import rates (Fig. 3.11 B). With certain parameter combinations, the flux based model may generate polarities oriented towards cells with slightly elevated auxin degradation rates even in the absence of auxin import in these cells. Auxin may also accumulate in minus organiser cells in this scenario (Stoma et al., 2008).

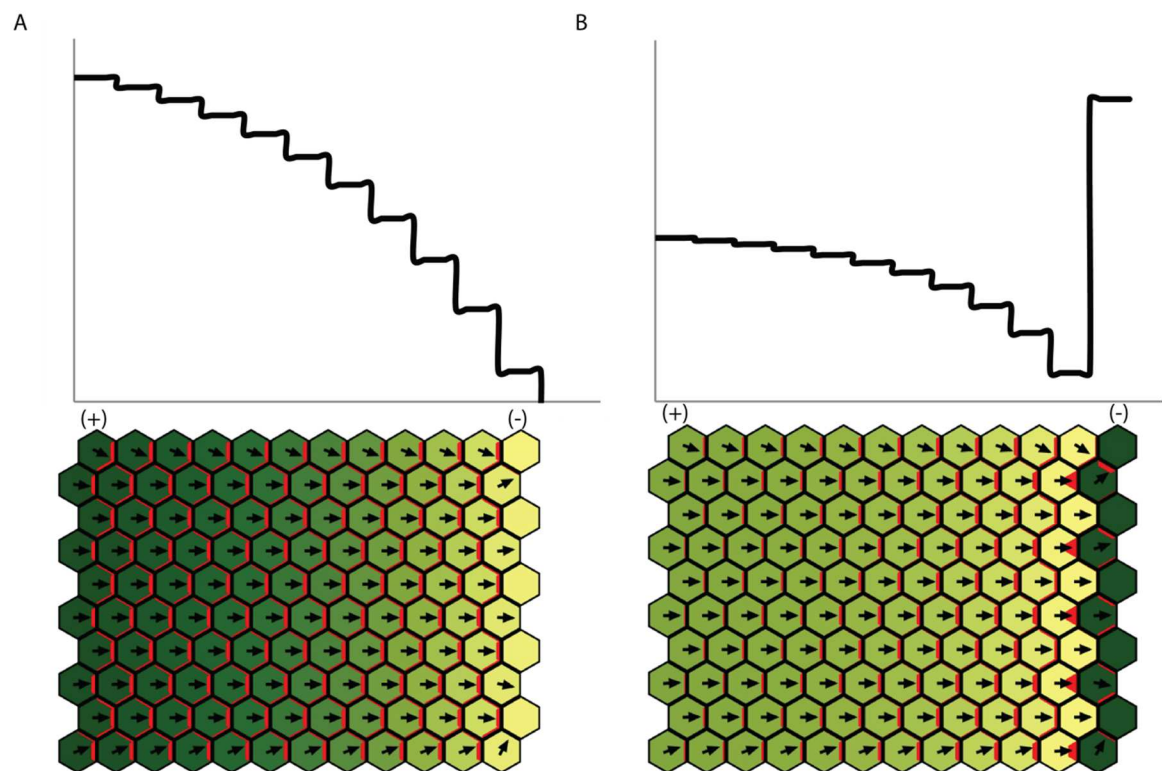


Fig. 3.11 Coordination of polarity across a 2D array of cells for the flux-based model.

A) Polarity coordination for a flux based model with a non-limited pool of PIN and a linear relationship between flux and PIN allocation in the presence of a file of cells at the left border of the tissue with elevated rates of auxin production (+ organiser), and file of cells with elevated auxin degradation rates (- organiser) at the right border of the tissue. Graph shows intracellular

auxin concentration for a single row of cells running from left to right across the tissue. **B)** As for A, except the right file of cells has an elevated rate of auxin degradation (which is lower than the degradation rate in the right file of cells in A) and an elevated rate of auxin import. Graph is as for A.

3.4 Discussion

3.4.1 Classification of models

Here, I show that, given the definition of intracellular partitioning used in chapter 2 (that cells can polarise in the absence of pre-established asymmetries or polarisable neighbours), the up-the-gradient and flux-based models of plant polarity exhibit intracellular partitioning behaviour. In contrast, apart from the direct cell-cell coupling model, no other models of animal polarity have intracellular partitioning behaviour (Fig. 3.12). Two models of animal polarity fields, proposed by Le Garrec et al., 2006 and Amonlirdviman et al., 2005, involve a global bias which influences the orientation of polarity by modulating the activity or levels of a polarity component which participates in formation of A*-B* complexes across cell-cell interfaces. An analysis of these models by Fischer et al., 2013 reveals that they require at least a transient pre-established asymmetry to generate polarity, and to robustly generate cell polarity fields, the global bias must persist throughout the establishment of polarity. Another model of animal polarity establishes polarity independently of pre-established asymmetries, but requires polarisable neighbours for polarity to be established (discussed in chapter 2) (Burak and Shraiman, 2009). Therefore, models may be broadly classified into those which exhibit intracellular partitioning, which includes all plant models analysed here and the direct cell-cell coupling model of animal polarity, and those which don't, which includes several models of animal polarity.

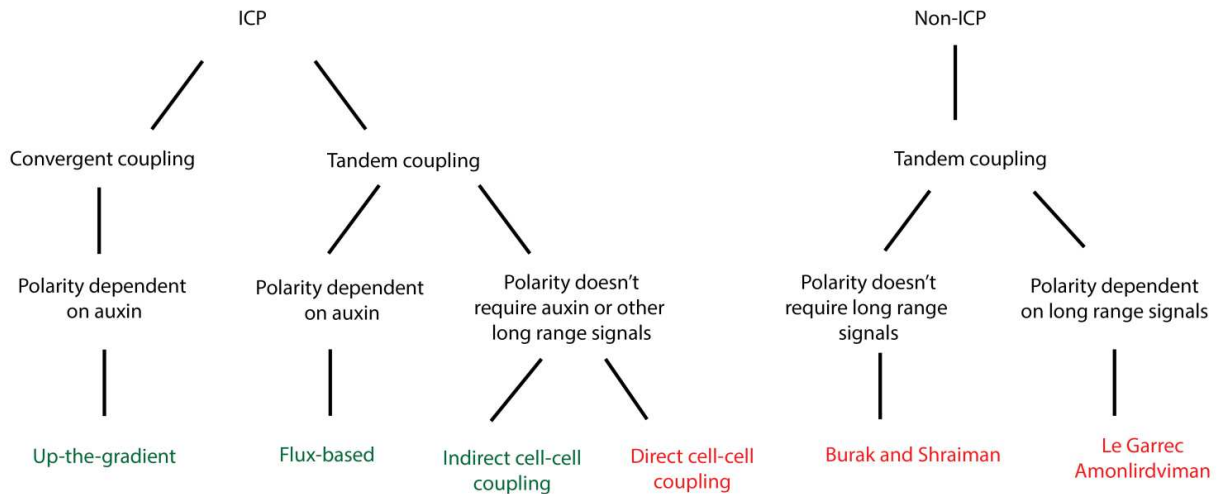


Fig. 3.12 Classification of polarity models.

Models may be broadly classified into those which exhibit intracellular partitioning (ICP) behaviour and those which do not. Models of animal polarity are shown in red, models of plant polarity are shown in green. All models which do not exhibit intracellular partitioning are models of animal polarity. Of these models, two types require both polarisable neighbours and pre-established asymmetries for cells to become polarised (Le Garrec et al., 2006 and Amonlirdviman et al., 2005), and one type requires polarisable neighbours but not pre-established asymmetries (Burak and Shraiman, 2009). Models can be further classified according to how local interactions between neighbouring cells tend to align polarities. One sub-class of intracellular partitioning models causes convergent coupling of neighbouring cells' polarities. This class includes the up-the-gradient model of plant polarity (Jönsson et al., 2006; Smith et al., 2006). Another sub-class of intracellular partitioning models, which includes flux-based, indirect cell-cell coupling and direct cell-cell coupling models generates tandem coupling of neighbouring cells' polarities (Abley et al., 2013; Rolland-Lagan and Prusinkiewicz, 2005; Stoma et al., 2008). The non-ICP models of animal polarity also tend to coordinate polarities of neighbouring cells in tandem, and thus are all tandem coupling models. Models may also be grouped according to the requirement of long-range diffusible signals, such as auxin, for the establishment of polarity. The convergent coupling (up-the-gradient) model, and the flux-based tandem coupling model require auxin for the establishment of polarity. However, other tandem coupling models, including the indirect cell-cell coupling model and the direct cell-cell coupling model (chapter 2, and (Abley et al., 2013)) do not require any inter-cellular diffusion of signalling molecules for the establishment of polarity, instead such signals only play a role in orienting polarity. Of the non-ICP models, the models of Le Garrec et al., 2006 and Amonlirdviman et al., 2005 require long range signals to generate polarity, whilst the model of Burak and Shraiman et al., 2009 only requires long range signals to orient cell polarities.

Although all three models of plant polarity tested can establish polarity in a single cell surrounded by non-polarisable neighbours, the models may behave differently for isolated single cells without

neighbours. The indirect cell-cell coupling model will generate polarity for an isolated cell, provided that the auxin concentration of the surrounding medium is permissive for the intracellular-partitioning system to operate. The version of the flux based model with a limited pool of PIN may also generate polarity for an isolated cell, provided that an auxin flux can be maintained across the cell (which depends on the auxin synthesis rate of the cell and the auxin concentration in the surrounding medium). In contrast, the up-the-gradient model may not be able to generate polarity for an isolated cell. If it is assumed that auxin must be present within neighbouring cells (ie that auxin acts intracellularly within neighbouring cells) to influence the allocation of PIN to the edge of a given cell, then a cell with no neighbours will not be able to polarise. Alternatively, if it is assumed that extracellular auxin can influence PIN allocation to cell edges, an isolated cell would be able to polarise if it could maintain a sufficiently strong gradient in extracellular auxin across it. Given the high diffusion rate of extracellular auxin, whether this is would be possible is unclear. These different requirements for isolated cells to polarise could be used to distinguish between models experimentally using cell culture systems.

Models that exhibit intracellular partitioning have different behaviours for groups of cells in the absence of pre-established asymmetries. Under these conditions, with noise in auxin levels or PIN concentrations in the membrane, the up-the-gradient model generates centres of polarity convergence with high auxin at their centre (Fig. 3.5) (Jönsson et al., 2006; Smith and Bayer, 2009; Smith et al., 2006). In contrast, the flux-based model and indirect and direct cell-cell coupling models generate swirled patterns of polarity, where polarities of neighbouring cells tend to align in tandem (Fig. 2.5 E and Fig. 3.7). This is because the indirect cell-cell coupling and flux-based mechanisms both destabilise the formation of polarity convergences and promote the tandem alignment of neighbouring cells (Fig. 3.4 and Fig. 3.8). The intracellular partitioning-based models may therefore be classified into convergent coupling (up-the-gradient) and tandem coupling (flux based, direct and indirect cell-cell coupling) models (Fig. 3.12).

In support of this classification, the two tandem coupling models investigated both behave similarly to each other, and differently to the convergent coupling model, in multiple scenarios. In order to generate centres of polarity convergence with high auxin, the up-the-gradient model only requires noise in auxin or PIN concentrations (Fig. 3.5), whereas the cell-cell coupling and flux-based models require the presence of minus organisers, with elevated auxin degradation and import (Fig. 3.9). Also, the two tandem coupling models polarise away from auxin sources and towards auxin sinks, whereas the opposite is true of the convergent coupling model (Fig. 2.10, Fig. 3.11 B, compare with Fig. 3.10). These similarities between the tandem coupling models exist despite polarity establishment being dependent on auxin in the flux-based model, but independent of any diffusible intercellular signalling molecules in the indirect cell-cell coupling model (Fig. 3.12).

Other models, which were not analysed here, can be related to the convergent and tandem coupling classes. One model proposed to account for phyllotaxis offers a more explicit mechanism by which the up-the-gradient model could work (Heisler et al., 2010). This model assumes that differences in auxin concentrations between the neighbours of a cell generate differential physical stresses from one end of the cell to the other (because the expansion of cells is proportional to their auxin concentration). PINs are assumed to be preferentially allocated to membranes next to walls under the highest stress, leading to PIN polarity pointing towards neighbouring cells with the highest auxin (Heisler et al., 2010). This model therefore behaves like the up-the-gradient model and fits into the convergent coupling class.

Another model, first proposed by Wabnik et al., 2010, exhibits behaviours of both tandem and convergent coupling models (Wabnik et al., 2013). This model assumes that two adjacent membranes at a cell-cell interface effectively compete for extracellular auxin which promotes the presence of elevated levels of PIN in the membrane. Unlike the indirect cell-cell coupling model,

differences in extracellular auxin concentrations are assumed to occur across the thickness of the cell wall. At a cell-cell interface, whichever membrane already has a higher concentration of PIN will tend to have a higher concentration of extracellular auxin at its side of the cell wall. PIN localisation is therefore favoured in the membrane which initially had higher PIN. Similar to tandem coupling models, polarities tend to align away from auxin sources, towards auxin sinks (Wabnik et al., 2010, 2013). However, for files of cells with equal rates of auxin production in a cells and noise in auxin concentrations, the model generates centres of convergence (Wabnik et al., 2013). Why the model has these two different behaviours is not intuitive and should be more extensively explored in the future.

The finding that convergent and tandem coupling models behave differently in several scenarios may make it possible to distinguish between these classes experimentally. For example, this could be done by assessing the behaviour of cultured plant tissues in the absence of pre-established asymmetries. If PIN proteins form convergent polarities in groups of cells, this would support the convergent coupling class of models and the Wabnik et al., 2010 model, whereas if swirled patterns were formed, this would support the tandem coupling class. Also, since the two classes of models make different predictions about the nature of plus and minus organisers, they could be distinguished by looking at the patterns of auxin synthesis relative to PIN polarity fields. The convergent coupling models predict that auxin synthesis should be elevated in minus organiser regions, whereas the tandem coupling and Wabnik et al., 2010 models predict that auxin synthesis is elevated in plus organiser regions. I go on to test these predictions in the following chapter.

3.4.2 Tandem coupling models make different predictions about the precise mechanism of polarisation

The similarities of the indirect cell-cell coupling and flux-based models make it difficult to distinguish between them experimentally by patterns of PIN expression, auxin accumulation, and organiser distributions. However, the models make different predictions about the molecular mechanisms involved in cell polarisation, which could be used to distinguish them.

For example, the indirect cell-cell coupling model predicts that cells lacking expression of functional PIN proteins could still have polarised distributions of the intracellular partitioning components, and perhaps of other proteins which might respond to the intracellular partitioning system. To test this prediction, it would be necessary to identify the components of the hypothesised auxin-independent intracellular partitioning system. As mentioned in chapter 2, ROP (Rho-GTPases of Plants) proteins are candidate intracellular partitioning components (Yang, 2008) . Consistent with the model, polarised ROP2 recruits PIN in pavement cells (Xu et al., 2010). However, whether ROP proteins can establish cell polarities in the absence of PIN-mediated auxin signalling is unknown.

The flux-based model predicts a molecular mechanism for sensing flux between one cell and another and allocating PIN accordingly. One way that flux of auxin could be sensed is through a tally molecule, which is made or released as auxin leaves a cell, and removed or sequestered as auxin enters a cell (Coen et al., 2004; Mitchison, 1980). The tally molecule would then accumulate at membranes that had a net efflux of auxin, and be depleted at membranes with a net auxin influx. If PIN allocation to a membrane occurred in proportion to the concentration of the tally molecule, this would provide an explicit mechanism by which PIN could be allocated to membranes with elevated efflux. However, flux-based models involve allocation of PIN to the

membrane in proportion to two types of flux: passive permeation and active PIN-mediated transport from one cell to another. There would therefore need to be two tally systems, one for each type of flux, and PIN would have to be allocated to the membrane in proportion to their sum.

3.4.3 Feedback between orienting signals and polarity

The comparisons between models presented in this chapter highlight behaviours of the up-the-gradient and flux-based models which have been overlooked up until now. Previously, it was thought that pre-established asymmetries in auxin concentration, or polarisable neighbours, were required for cells to become polarised according to these mechanisms (Abley et al., 2013). One reason that this misconception arose is because, in the flux and up-the-gradient models, auxin gradients are both a cause, and a consequence, of cell polarity (Fig. 3.13). In the presence of pre-established auxin gradients, cell polarities will align either up or down the gradient for the two models. However, I show here that a pre-established gradient and polarisable neighbours are not required for polarity to emerge. This is because noise in the levels of PIN in the membrane of a single polarisable cell is sufficient to create a small gradient in auxin in the cell's neighbours, and a gradient in auxin efflux rates across the cell. The up-the-gradient model results in positive feedback between shallow inter-cellular auxin gradients and PIN allocation to the membrane, and the flux based model results in positive feedback between auxin efflux and PIN allocation. Because in both models the polarity of the cell influences the auxin gradient (and the auxin flux), which in turn influence the polarity, an initial noise in PIN concentrations is sufficient to polarise the cell. In the indirect cell-cell coupling model, polarities can be established independently from auxin and PIN, and auxin acts to orient polarities. However, the feedback between cell polarity and auxin gradients still exists.

This is in contrast to animal models of polarity, where there is no feedback between the planar cell polarity components (which become polarised in each cell) and the gradients which act to influence the generation or orientation of the polarity (Amonlirdviman, 2005; Burak and Shraiman, 2009; Le Garrec et al., 2006) (Fig. 3.13). Partly as a consequence of this lack of feedback between polarity and external gradients, most of these models do not exhibit intracellular partitioning. The models of Amonlirdviman, 2005 and Le Garrec et al., 2006, which require global biasing cues for polarity establishment, would be less dependent on persistent global biases if they involved a feedback between cell polarities and the gradients which help to create them. However, the planar cell polarity system is not known to influence the transport of any hypothesised biasing cues (Strutt and Strutt, 2009). If animals do exhibit intracellular partitioning behaviour, it is therefore likely to occur independently of feedback between planar cell polarity components and biasing cues. The direct cell-cell coupling model presented in chapter 2 provides a mechanism by which this could occur.



Fig. 3.13 Differences between animal and plant models for the generation of cell polarity fields.

In animal models, graded signals influence the generation (Amonlirdviman, 2005; Le Garrec et al., 2006) and orientation (Abley et al., 2013; Burak and Shraiman, 2009) of cell polarities, but the polarity does not feed-back to influence the signal gradient. In plants, graded signals may also influence the generation (Jönsson et al., 2006; Rolland-Lagan and Prusinkiewicz, 2005; Smith and Bayer, 2009; Smith et al., 2006; Stoma et al., 2008) and orientation (Abley et al., 2013) of polarity. In all plant models, there is a feedback between the polarity and the graded signal which influences the polarity. In some cases, this feedback can constitute an intracellular partitioning system.

3.4.4 Conclusions

Here I have shown that intracellular partitioning behaviour is not restricted to the direct and indirect cell-cell coupling models of tissue cell polarity presented in chapter 2, as flux-based and up-the-gradient models of plant polarity also have intracellular partitioning behaviour. Models of plant polarity differ in their behaviour for groups of cells in the absence of pre-established asymmetries as both flux and indirect cell-cell coupling models cause tandem coupling of neighbouring cells' polarities whilst the up-the-gradient model causes convergent coupling. All models may generate centres of convergence and coordinated polarities across an array of cells, but have different requirements for local modulation of auxin biosynthesis, degradation and import. The two tandem coupling models require local auxin sinks to generate centres of polarity convergence, whereas these centres arise spontaneously in the up-the-gradient model. Also, the tandem coupling models cause polarities orient away from auxin sources, towards auxin sinks, whilst the opposite is true of the up-the-gradient model. These differences in the behaviours of models give rise to testable predictions. In the following chapter I use some of these predictions to distinguish between up-the-gradient and tandem coupling models in the context of polarity patterns found in leaves.

3.5 Model descriptions

All models are implemented using VVe. The indirect cell-cell coupling model is implemented as described in chapter 2.4.4 (unless otherwise detailed below) and details of the implementations of flux-based and up-the-gradient models are given below.

3.5.1 Indirect cell-cell coupling simulation details.

For the simulation used to illustrate intracellular partitioning with the indirect cell-cell coupling model (Fig.3.1), parameter values are as described previously in Table 2.1. In the simulation used to illustrate the formation of centres of convergence in the indirect cell-cell coupling model (Fig 3.9 C), cells with elevated rates of auxin import and degradation are added to the array. In this simulation, all parameter values are as described in Table 2.1, except, ρ_{Aux} , the production rate of auxin, is $2 \times 10^{-5} \text{ A}_u/\mu\text{m}^2.\text{s}$ in all cells. Also, in cells with elevated rates of auxin degradation and import, the degradation rate of auxin, $\mu_{Aux} = 1 / \text{s}$, and the inwards permeation rate of auxin, $v_{in} = 15 \mu\text{m} / \text{s}$.

3.5.2 Tissue representation for up-the-gradient and flux-based models

For the up-the-gradient and flux-based models presented in this chapter, the graph used to represent the tissue is simpler than that used for the indirect cell-cell coupling model (compare Fig. 3.14 with Fig. 2.16). This is because I implemented both models as described in previous publications (Bilsborough et al., 2011; Stoma et al., 2008), in which there is no representation of the cell wall, and each cell has a single concentration of PIN per edge, allowing each cell edge to be represented by a single compartment. This contrasts with the indirect cell-cell coupling model where the cell wall is represented explicitly with cell wall compartments and each edge of the cell is discretised into several membrane and wall compartments. Also, in published implementations

of flux and up-the-gradient models, there is no diffusion along the length of each cell edge, removing the need for connections between vertices representing edge compartments.

Therefore, for simulations of flux-based and up-the-gradient models, each cell is represented by seven vertices: a single central vertex represents the cytoplasm (magenta circles in Fig. 3.14), and six peripheral vertices represent the six cell edges (black circles in Fig. 3.14). Each central vertex will be referred to as a cytoplasmic compartment, and each peripheral vertex will be referred to as an edge compartment. Each peripheral vertex of a cell is connected to the central vertex of the same cell (grey lines in Fig. 3.14) and to the juxtaposed peripheral vertex of the neighbouring cell (black lines in Fig. 3.14), unless the vertex is on the border of the tissue. Each central vertex and the cytoplasmic compartment it represents has an area associated with it of $65 \mu\text{m}^2$ and each peripheral vertex and the edge compartment it represents has a length associated with it of $5 \mu\text{m}$.

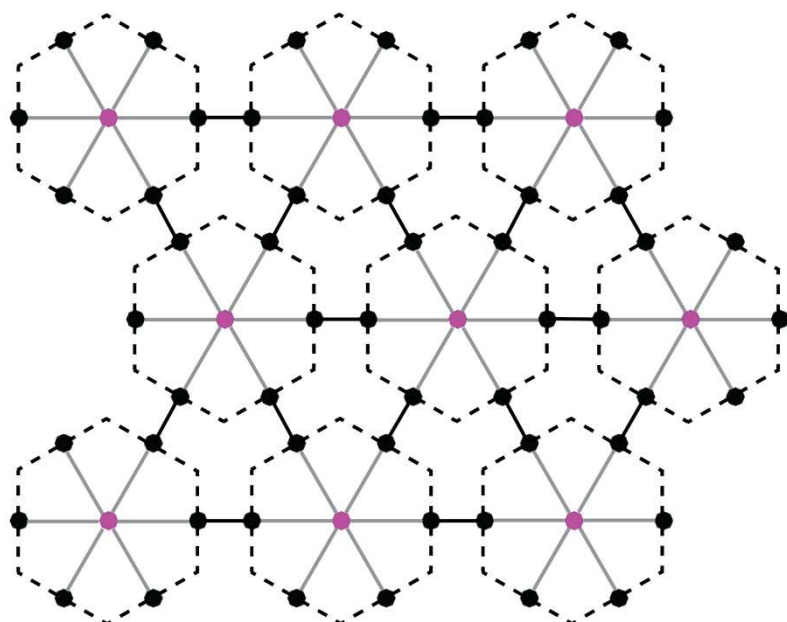


Fig. 3.14 Graph used to represent the tissue for up-the-gradient and flux-based models. Magenta circles indicate positions of central vertices (which represent cytoplasmic compartments) and black circles indicate positions of peripheral vertices (which represent cell edge compartments). Solid black lines show connections between the peripheral vertices of

neighbouring cells and grey lines show the connections between each central vertex and the surrounding peripheral vertices in the same cell. Dashed lines indicate cell outlines.

3.5.3 Up-the-gradient model

I implement the up-the-gradient model as described by Bilsborough et al., 2011. In contrast to in Bilsborough et al., 2011, for consistency with the description of indirect cell-cell coupling, here I add units to the parameters when describing the up-the-gradient model.

At the beginning of all up-the-gradient simulations, the system is initialised with auxin in each cytoplasmic compartment. In simulations where noise is added to auxin levels, the auxin concentration in each cytoplasmic compartment is set to a default concentration plus or minus a randomly-generated value:

$$A(t = 0) = c_A(1 + \theta_A) \quad (3.1a),$$

$$\theta_A \in [-\varepsilon, \varepsilon] \quad (3.1b).$$

where $A(t=0)$ is the initial concentration of auxin in cytoplasmic compartments and c_A is the default initial concentration of auxin, with units of $A_u/ \mu\text{m}^2$. θ_A is a random number uniformly distributed between an upper and lower limit, ε .

In all simulations $c_A = 0.01 A_u/ \mu\text{m}^2$ in all cells. In the simulations used to generate Figs. 3.2, 3.5 C and 3.10, $\varepsilon = 0.0$. In the simulation used to generate Fig. 3.5 A and B, $\varepsilon = 0.1$.

In some simulations, the system is initialised without PIN at cell edges (those used to generate Figs. 3.5A and B, and Fig. 3.10). However, in other simulations, the system is initialised with noisy PIN concentrations at each cell edge:

$$PIN_{edge}(t = 0) = c_{PIN_{edge}}(1 + \theta_{PIN}) \quad (3.2a),$$

$$\theta_{PIN} \in [-\varepsilon_{PIN}, \varepsilon_{PIN}] \quad (3.2b).$$

where $PIN_{edge}(t=0)$ is the initial concentration of PIN at a given edge compartment, with units of $A_u/\mu\text{m}$ and $c_{PIN_{edge}}$ is the default initial concentration of PIN at an edge compartment. θ_{PIN} is a random number uniformly distributed between an upper and lower limit, ε_{PIN} . In the simulations used to generate Fig 3.2 and 3.5 C, $c_{PIN_{edge}} = 0.1 A_u/\mu\text{m}$ and $\varepsilon_{PIN} = 0.005$.

Following initialisation of the system, the up-the-gradient model is simulated. In this model, PIN only exists in cell edge compartments. At each time step of the simulation, the concentration of PIN at each cell edge compartment is calculated according to the distribution of auxin concentrations in the neighbours of the cell. Each cell has a total concentration of PIN available to cell edges. This total concentration of PIN is distributed between cell edges according to an exponential function of the auxin concentrations in neighbouring cells. The equation describing the concentration of PIN in a given edge compartment in cell i , at the interface between cell i and j , at a given time step is:

$$PIN_{ij} = PIN_i \frac{b^A_j}{\sum_k b^A_k} \quad (3.3)$$

Where PIN_{ij} is the concentration of PIN at the cell edge between cells i and j , in cell i . PIN_i is the total PIN concentration available to be divided between all the edges of cell i (with units of $A_u/\mu\text{m}$).

μm), A_j is the concentration of auxin in the neighbour j and A_k is the auxin concentration in the neighbour k of cell i . The exponentiation base, b , controls the extent to which the auxin distribution in neighbouring cells influences PIN protein distribution at cell edges.

In all simulations except that used to generate Fig. 3.2, $\text{PIN}_i = 0.2 A_u / \mu\text{m}$. In the simulation used to generate Fig. 3.2, $\text{PIN}_i = 0.57 A_u / \mu\text{m}$. In all simulations, $b = 6$.

The rate of change of auxin concentration for a given cytoplasmic compartment depends on the rates of auxin production and degradation, and the rates of auxin flux between the given cell and its neighbours. The rate of auxin production is assumed to decrease and then fall to zero as the concentration of auxin in the cell approaches and reaches a target auxin concentration. This is described by the following equation:

$$\frac{\partial A_i}{\partial t} = \sigma(H - A_i) - \mu A_i - \frac{1}{R_i} \sum_{j \in N(i)} (\Phi_{i \rightarrow j}) l_{ij} \quad (3.4)$$

Where A_i is the auxin concentration of cell i , σ is the auxin production rate, with units of $/s$, H is the target auxin concentration, with units of $A_u / \mu\text{m}^2$, μ is the auxin degradation rate, with units of $/s$ and R_i is the area of the cell i , with units of μm^2 . $\Phi_{i \rightarrow j}$ is the auxin flux (with units of $A_u / \mu\text{m.s}$) out of cell i , across the interface between cells i and j , in the neighbourhood of cell i ($(N(i))$). l_{ij} is the length of the cell edge at the interface between cells i and j , with units of μm .

In all simulations except that used to generate Fig. 3.10, $\sigma = 0.4 /s$, $H = 0.1 A_u / \mu\text{m}^2$ and $\mu = 0.005 /s$. In the simulation used to generate coordinated polarity across an array of cells (Fig. 3.10), $\sigma = 0 /s$ and $\mu = 0 /s$ in all cells apart from in the file of cells at the left of the tissue, where $\sigma = 0.5 /s$, and in the file of cells at the right of the tissue where $\mu = 0.05 /s$. In all simulations, $R_i = 65 \mu\text{m}^2$ and $l_{ij} = 5 \mu\text{m}$.

All changes in auxin concentration are solved numerically using an explicit Euler integration method. The time step for all simulations was 0.01s (simulations run with a smaller time step did not produce different results). All simulations were run until a stable state was reached.

In this chapter, and in Bilsborough et al., 2011, the flux of auxin between a cell, i , and a neighbouring cell, j , depends on passive permeation of auxin between cell i and cell j and PIN mediated transport between the cells. In simulations presented in later chapters (4 and 5) I assume that the flux of auxin may also be influenced by auxin import into cells (I describe this additional assumption now to simplify descriptions of later models). I assume that the rate of auxin import into a cell depends on the auxin import rate of the given cell and the concentration of auxin in the juxtaposed neighbour. The equation governing the flux of auxin from cell i , to cell j , at a given time step of the simulation assuming total flux is influenced by passive permeation, PIN mediated transport, and import is:

$$\Phi_{i \rightarrow j} = D (A_i - A_j) + T(PIN_i A_i - PIN_j A_j) + I_j A_i - I_i A_j \quad (3.5)$$

where $\Phi_{i \rightarrow j}$ is the flux across a given cell-cell interface, from cell i to cell j , with units of $A_u / \mu\text{m . s}$, D is a constant describing the passive permeability of auxin, with units of $\mu\text{m/ s}$, A_i is the concentration of auxin in cell i , A_j is the concentration of auxin in cell j , PIN_i is the concentration of PIN at the given cell edge in cell i , and PIN_j is the concentration of PIN in the juxtaposed cell edge in cell j . T is a constant describing the rate of PIN-mediated auxin transport, with units of $\mu\text{m}^2/ A_u \cdot \text{s}$. I_j and I_i are parameters describing the auxin import rates of cells j and i respectively, with units of $\mu\text{m/ s}$. In the simulations used in this chapter, $I = 0 \mu\text{m/ s}$ in all cells in all simulations (because I do not simulate auxin import until later chapters).

In all simulations $D = 32.4 \mu\text{m}/\text{s}$. In all simulations except that used to generate Fig. 3.2, $T = 51.9 \mu\text{m}^2/\text{A}_u\text{s}$. In the simulation used to generate Fig. 3.2, $T = 103.9 \mu\text{m}^2/\text{A}_u\text{s}$.

In the simulations used to generate Fig 3.5A and Fig.3.5B, every 0.01 seconds, noise is added to the auxin concentrations in each cytoplasmic compartment, according to the following equation:

$$A_n = A + (\theta_A * \sqrt{A}) \quad (3.6),$$

where A_n is the concentration of auxin in a given cytoplasmic compartment after the addition of noise with units of $\text{A}_u/\mu\text{m}^2$, A is the concentration of auxin in that compartment before the addition of noise (with the same units), θ_A is a random number drawn from a normal distribution, with mean 0, and standard deviation 2×10^{-5} . Noise is added to the concentration of auxin in proportion to the square root of the auxin concentration.

Symbol and units	\mathbf{c}_A $\text{A}_u/\mu\text{m}^2$	$\mathbf{\epsilon}$	$\mathbf{c}_{\text{PINedge}}$ $\text{A}_u/\mu\text{m}$	$\mathbf{\epsilon}_{\text{PIN}}$	\mathbf{p}_{PIN} $\text{A}_u/\mu\text{m}$	\mathbf{b}	σ $/\text{s}$	\mathbf{H} $\text{A}_u/\mu\text{m}^2$	\mathbf{R} μm^2	\mathbf{I} μm	$\mathbf{\mu}$ $/\text{s}$	\mathbf{D} $\mu\text{m}/\text{s}$	\mathbf{T} $\mu\text{m}^2/\text{A}_u\text{s}$
Fig: 3.2	0.01	0	0.1	0.005	0.57	6	0.4	0.1	65	5	0.005	32.4	103.9
3.5 A, B	0.01	0.1	0	0	0.2	6	0.4	0.1	65	5	0.005	32.4	51.9
3.5 C	0.01	0	0.1	0.005	0.2	6	0.4	0.1	65	5	0.005	32.4	51.9
3.10	0.01	0	0	0	0.2	6	0	0	65	5	0	32.4	51.9

Table 3.1. Parameter values used in up-the-gradient simulations.

C_A is the default initial concentration of auxin in cytoplasmic compartments, ε is the limit for noise addition to C_A , $C_{PINedge}$ is the default initial concentration of PIN at each cell edge, ε_{PIN} is the limit for noise addition to $C_{PINedge}$, PIN_i is the total amount of PIN available for binding to the membrane in cell i , b is the exponentiation base for PIN allocation to the membrane, σ is the auxin production rate, H is the target auxin concentration, R is the area of cytoplasmic compartments, l is the length of cell edge compartments, μ is the auxin degradation rate, D is the passive permeability of auxin and T is the rate of PIN-mediated auxin transport. Figure numbers for simulations in which specific parameter sets were used are given in bold on the left.

3.5.4 Flux-based model

To implement the flux-based model, I represent the tissue as described above, with the same areas associated with each cytoplasmic compartment, and lengths associated with each edge compartment, as described for the up-the-gradient model.

To simulate the flux-based model, I use an implementation which is based on that described by (Stoma et al., 2008). However, in Stoma et al., 2008, cells are represented by 3D volumes with 2D membranes. Here, for consistency with the indirect cell-cell coupling and up-the-gradient models, I use 2D cells and 1D cell edges to represent cell membranes. Therefore, the units of parameters that I use differ from those described in Stoma et al., 2008. I also add the assumptions that there is a maximum density of PIN proteins that can exist at a cell edge ((Rolland-Lagan and Prusinkiewicz, 2005) and that auxin can be actively imported into cells by auxin import carriers. Also, for some simulations, I modify the published equations of Stoma et al., 2008 to include a limited pool of PIN from which PIN must be recruited to the membrane.

At the beginning of all simulations, the system is initialised with auxin in cytoplasmic compartments and PIN at edge compartments, as described above for the up-the-gradient model (equations 3.1 and 3.2, parameter values for the flux-based model are given in Table 3.2). In the version of the flux-based model with a limited pool of PIN in each cell (used to test intracellular partitioning behaviour, and to generate Fig.3.7 C), the system is initialised with PIN in cytoplasmic compartments:

$$PIN_{cyto}(t = 0) = c_{PIN_{cyto}} \quad (3.7),$$

Where $PIN_{cyto}(t=0)$ is the initial concentration of PIN in a cytoplasmic compartment, and $c_{PIN_{cyto}}$ is the default initial concentration of PIN in cytoplasmic compartments.

In all simulations, c_A , the initial concentration of auxin = $0.01 \text{ A}_u/\mu\text{m}^2$ in all cells. In all simulations except those used to generate Fig. 3.7A and Fig. 3.7C, noise is not added to auxin concentrations (ε , the limit for noise addition to the auxin concentration = 0.0). In the simulation used to generate Fig. 3.7A, $\varepsilon = 0.0025$ and in the simulation used to generate Fig. 3.7 C, $\varepsilon = 0.5$. To simulate intracellular partitioning in the scenario shown in Fig. 3.3 A and B, using a limited pool of PIN and PIN allocation increasing linearly with auxin flux, $c_{PIN_{cyto}} = 0.01 \text{ A}_u/\mu\text{m}$. For simulation of intracellular partitioning using a limited pool of PIN and PIN allocation increasing quadratic with flux, $c_{PIN_{cyto}} = 0.2 \text{ A}_u/\mu\text{m}$. For the simulation used to generate Fig. 3.7 C, $c_{PIN_{cyto}} = 0.01 \text{ A}_u/\mu\text{m}$.

In the simulations used to demonstrate intracellular partitioning (Fig. 3.3 A, B), for all versions of the model used, $c_{PIN_{edge}} = 0.001 \text{ A}_u/\mu\text{m}$ and $\varepsilon_{PIN} = 0.5$. In the simulations used to generate Fig. 3.7A, Fig. 3.7C, Fig. 3.9A and Fig. 3.11 A and B, $c_{PIN_{edge}} = 0 \text{ A}_u/\mu\text{m}$ and $\varepsilon_{PIN} = 0$. In the simulation used to generate Fig. 3.7B, $c_{PIN_{edge}} = 0.1 \text{ A}_u/\mu\text{m}$ and $\varepsilon_{PIN} = 0.0025$.

Following initialisation of the system, the flux based model is simulated and all changes in concentration are solved numerically using an explicit Euler integration method, with a time step of 0.05 seconds. For the model with a non-limiting pool of PIN in each cell, PIN is recruited to a cell edge depending on the rate of auxin flux across that edge, and PIN is removed from the edge at a background rate. The equation describing the rate of change of PIN concentration for a given cell edge, between cells i and j, is:

$$\frac{\partial PIN_{ij}}{\partial t} = f(\phi_{i \rightarrow j}) - \gamma PIN_{ij} \quad (3.8)$$

Where PIN_{ij} is the concentration of PIN in cell i, at the cell edge between cells i and j, f is a function describing flux-dependent PIN allocation to the edge and $\phi_{i \rightarrow j}$ is the auxin flux across the interface between cells i and j, with units of $A_u / \mu\text{m.s}$. Outgoing fluxes, from cell i, to cell j are considered to be positive, and incoming fluxes are considered to be negative. γ is the unbinding rate of PIN from the cell edge, with units of $/s$. In all simulations, $\gamma = 0.1 /s$.

In the case of a linear increase in PIN allocation with increasing flux,

$$f(\phi_{i \rightarrow j}) = \alpha(\phi_{i \rightarrow j}/\phi_{ref}) \quad (3.9a)$$

and, in the case of a quadratic increase in PIN allocation with increasing flux,

$$f(\phi_{i \rightarrow j}) = \alpha(\phi_{i \rightarrow j}/\phi_{ref})^2 \quad (3.9b)$$

Where α is a constant parameter determining the extent to which flux promotes PIN allocation to the membrane, with units of $A_u / \mu\text{m.s}$ and ϕ_{ref} is an arbitrary reference flux used to keep constant units in the equations. For negative fluxes (entering the cell i, across the cell edge between cell i and cell j), the value of $f(\phi_{i \rightarrow j})$ is truncated to zero. In these simulations, as described in (Rolland-Lagan and Prusinkiewicz, 2005), I assume that once the concentration of PIN at the cell edge reaches a threshold value, P_{max} , PIN can no-longer be allocated to the edge. This is equivalent to assuming that there is a maximum density of PIN proteins which may be present in the plasma membrane. In all simulations, $P_{max} = 0.01 A_u / \mu\text{m}$.

In all simulations, $\phi_{ref} = 1$. In the simulation of intracellular partitioning using a linear increase in PIN allocation with increasing flux (Fig. 3.3), $\alpha = 5 \times 10^{-4} \text{ A}_u / \mu\text{m.s}$, and in the simulation of intracellular partitioning using a quadratic increase in PIN allocation with increasing flux, to the membrane, $\alpha = 0.8 \text{ A}_u / \mu\text{m.s}$. In the simulation used to generate Fig. 3.7 A and B, $\alpha = 3 \times 10^{-4} \text{ A}_u / \mu\text{m.s}$. In the simulations used to generate Figs. 3.9A and B, $\alpha = 4 \times 10^{-4} \text{ A}_u / \mu\text{m.s}$, and in the simulations used to generate Figs. 3.11A and B, $\alpha = 5 \times 10^{-5} \text{ A}_u / \mu\text{m.s}$.

To simulate the presence of a limiting pool of PIN in the cell, I assume that each cell has a fixed total amount of PIN, which can interconvert between a cytoplasmic form and a membrane bound form at the cell edge. In this version of the flux-based model, allocation of PIN to a given cell edge depends on the concentration of PIN in the cytoplasm of the same cell. The equation describing the rate of change of PIN allocation to the edge in cell i, between cells i and j, then becomes:

$$\frac{\partial PIN_{ij}}{\partial t} = (f(\phi_{i \rightarrow j}))PIN_{cyto} - \gamma PIN_{ij} \quad (3.10)$$

where (PIN_{cyto}) is the concentration of PIN in the cytoplasm of cell i and f , $\phi_{i \rightarrow j}$ and γ are as described above for equation 3.8.

In this version of the model, in the case of a linear increase in PIN allocation with increasing flux,

$$f(\phi_{i \rightarrow j}) = k(\phi_{i \rightarrow j}/\phi_{ref}) \quad (3.11a)$$

and, in the case of a quadratic increase in PIN allocation with increasing flux,

$$f(\phi_{i \rightarrow j}) = k(\phi_{i \rightarrow j}/\phi_{ref})^2 \quad (3.11b)$$

where k is a constant controlling the rate of flux-dependent allocation of PIN to the given cell edge, and has units of $\mu\text{m/s}$.

In the simulations of intracellular partitioning using a limited pool of PIN (and a linear or quadratic increase in PIN allocation with increasing flux) $k = 200 \mu\text{m/s}$. In the simulation used to generate Fig. 3.7C, $k = 3 \mu\text{m/s}$.

In the presence of a limited pool of PIN in the cell, the rate of change of PIN concentration in the cytoplasm of a given cell, i , depends on the rate of PIN recruitment to, and unbinding from, all the edges of the cell, and is given by:

$$\frac{\partial \text{PIN}_i}{\partial t} = -\frac{1}{R_i} \sum_{j \in N(i)} (f(\phi_{i \rightarrow j}) \text{PIN}_i - \gamma \text{PIN}_{ij}) l_{ij} \quad (3.12a)$$

Where PIN_i is the concentration of PIN in the cytoplasmic compartment of cell i , R_i is the area of the cytoplasmic compartment of cell i , PIN_{ij} is the concentration of PIN at the edge between cell i and cell j , in the neighbourhood of cell i ($N(i)$). $f(\phi_{i \rightarrow j})$ and γ are as described above for equation 3.8 and l_{ij} is the length of the cell edge between cell i and cell j .

In all versions of the model, the flux across a given cell edge, from cell i to cell j , at a given time point depends on passive permeability of auxin between cells and PIN-mediated auxin export. In the simulations used to generate Fig. 3.9 B and 3.11 B, I also assume that auxin may be actively imported into cells, and that the rate of import depends on the auxin import rate of a given cell, and the auxin concentration in its neighbours. As for the up-the-gradient model, the flux across a given cell edge, from cell i to cell j , at a given time point is therefore given by

$$\phi_{i \rightarrow j} = D(A_i - A_j) + T(\text{PIN}_i A_i - \text{PIN}_j A_j) + I_j A_i - I_i A_j \quad (3.13)$$

Where $\phi_{i \rightarrow j}$ is the flux across a given cell-cell interface, from cell i to cell j , D is a constant describing the passive permeability of auxin, with units of $\mu\text{m} / \text{s}$, A_i is the concentration of auxin in cell i , A_j is the concentration of auxin in cell j , PIN_i is the concentration of PIN at the cell edge in cell i , and PIN_j is the concentration of PIN in the juxtaposed cell edge in cell j . T is a constant describing the rate of PIN-mediated auxin transport, with units of $\mu\text{m}^2 / \text{A}_u \cdot \text{s}$. I_j and I_i are parameters describing the auxin import rates of cells j and i respectively, with units of $\mu\text{m} / \text{s}$.

In all simulations, $D = 6.5 \mu\text{m} / \text{s}$ and $T = 1.30 \mu\text{m}^2 / \text{A}_u \cdot \text{s}$. In all simulations except those used to generate Fig. 3.9 B and 3.11 B, $I = 0 \mu\text{m} / \text{s}$ for all cells. In the simulation used to generate Fig. 3.9 B, in cells marked with asterisks (minus organisers), $I = 5 \mu\text{m} / \text{s}$, and in the simulation used to generate Fig. 3.11 B, in the file of cells on the right of the tissue, $I = 40 \mu\text{m} / \text{s}$.

The rate of change of auxin concentration in the cytoplasm of a given cell, i , depends on the production and degradation rates of auxin, and its flux into adjacent cells and is given by:

$$\frac{\partial A_i}{\partial t} = \rho - \mu A_i - \frac{1}{R_i} \sum_{j \in N(i)} (\phi_{i \rightarrow j}) l_{ij} \quad (3.14)$$

Where ρ is the production rate of auxin, with units of $\text{A}_u / \mu\text{m}^2 \cdot \text{s}$, μ is the degradation rate of auxin, with units of $/ \text{s}$, A_i is the concentration of auxin in the cytoplasm of cell i and R_i is the area of the cell i . ϕ_{ij} is the flux of auxin across the interface between cells i and j , in the neighbourhood of the cell i ($N(i)$) and l_{ij} is the length of the cell edge at the interface between cells i and j .

In all cells in all simulations except those used to generate Fig. 3.11 and Fig. 3.9 A and B, $\rho = 0.002 \text{A}_u / \mu\text{m}^2 \cdot \text{s}$ and $\mu = 0.005 / \text{s}$. In Fig. 3.9 A, in cells marked by an asterisk (minus organiser cells), $\mu = 1 / \text{s}$, and in Fig 3.9 B, in cells marked by an asterisk, $\mu = 0.1 / \text{s}$. In all other cells, $\mu = 0.005 / \text{s}$. In the simulations used to generate Fig. 3.11 A and B, in all cells except plus and minus organiser cells,

$\rho = 0.008 \text{ A}_u / \mu\text{m}^2 \cdot \text{s}$ and $\mu = 0 / \text{s}$. In both simulations, plus organiser cells have a production rate of $\rho = 0.08 \text{ A}_u / \mu\text{m}^2 \cdot \text{s}$. In the simulation used to generate Fig. 3.11A, in minus organiser cells, $\mu = 0.2 / \text{s}$ and in the simulation used to generate Fig. 3.11B, $\mu = 0.1 / \text{s}$ in minus organiser cells.

In the simulations used to generate Figs. 3.7 A and C, noise is added to the concentration of auxin at every 0.05 seconds, as described by equation 3.6. In the case of Fig. 3.7A, the noise parameter, θ_A , is a random number drawn from a normal distribution, with mean 0, and standard deviation 5×10^{-7} . In the case of Fig 3.7 C, θ_A is a random number drawn from a normal distribution, with mean 0, and standard deviation 1×10^{-5} .

In the simulation used to generate Fig 3.7B, noise is added to the concentration of PIN at each cell edge every 0.05 seconds of the simulation:

$$PIN_n = PIN + (\theta_{PIN} * \sqrt{PIN}) \quad (3.15),$$

where PIN_n is the concentration of PIN at a given cytoplasmic compartment after the addition of noise with units of $\text{A}_u/\mu\text{m}$, PIN is the concentration of PIN in that compartment before the addition of noise (with the same units), θ_A is a random number drawn from a normal distribution, with mean 0, and standard deviation 2.5×10^{-5} . Noise is added to the concentration of PIN in proportion to the square root of the PIN concentration.

In the simulation of intracellular partitioning presented in Fig. 3.3, I calculate the ratio of auxin concentration in the peripheral neighbour of a central polarisable cell : concentration in the peripheral neighbour at which PIN allocation to the adjacent edge of the central cell will stop. To calculate the auxin concentration in the peripheral neighbour at which PIN allocation to the adjacent edge of the peripheral cell will stop, I ignore passive permeation between the peripheral

neighbour and other peripheral neighbours. I then calculate the auxin concentration in the peripheral neighbour at which passive permeation from the peripheral neighbour into the central cell balances permeation and PIN-mediated transport out of the central cell. I assume that when this auxin concentration is reached in the peripheral neighbour, the rate of change of its auxin concentration is equal to zero, and is given by :

$$\frac{\partial A_x}{\partial t} = (T PIN_c + D)A_c l_{cx} \frac{1}{R_x} - DA_x l_{cx} \frac{1}{R_x} + \rho - \mu A_x = 0 \quad (3.16),$$

where A_x is the auxin concentration in the peripheral neighbour, x , A_c is the concentration of auxin in the central polarisable cell c , l_{cx} is the length of the cell edge between the central cell c and the peripheral cell x and R_x is the area of the peripheral neighbour. PIN_c is the concentration of PIN in the edge of central cell, c , adjacent to cell x . All other symbols are as described above (T is a constant describing the rate of PIN mediated auxin export, D is the passive permeation rate of auxin, ρ is the auxin production rate and μ is the auxin degradation rate. The first term of the equation describes the rate of PIN-mediated and passive auxin export into the peripheral cell from the central cell. The second term describes the rate of auxin efflux due to passive permeation into the central cell, and the last two terms describe auxin production and decay. If A_x is equal to the steady-state auxin concentration \bar{A}_x , at which the rate of change of auxin concentration in the peripheral neighbour is zero, then equation 3.16 can be rearranged to give:

$$\bar{A}_x \left(D l_{cx} \frac{1}{R_x} + \mu \right) = (T PIN_c + D)A_c l_{cx} \frac{1}{R_x} + \rho \quad (3.16)$$

and therefore

$$\bar{A}_x = \frac{(T PIN_c + D)A_c l_{cx} + \rho R}{D l_{cx} + \mu R} \quad (3.17)$$

The ratio between the current auxin concentration in the peripheral neighbour x and the steady-state auxin concentration is therefore:

$$\frac{A_x}{A_x} = \frac{A_x(Dl_{cx} + \mu R)}{(T \text{PIN}_c + D)A_c l_{cx} + \rho R} \quad (3.18)$$

Symbol and units:	c_A $A_u / \mu\text{m}^2$	ϵ	$c_{PINedge}$ $A_u / \mu\text{m}$	ϵ_{PIN}	PIN_{cyto} $A_u / \mu\text{m}^2$	μ /s	D $\mu\text{m}/\text{s}$	T $\mu\text{m}^2 / A_u \cdot \text{s}$	γ /s	α $A_u / \mu\text{m} \cdot \text{s}$	κ $\mu\text{m}/\text{s}$	ρ $A_u / \mu\text{m}^2 \cdot \text{s}$
Fig: 3.3 B i)	0.01	0	0.001	0.5	N/A	0.005	6.5	1.30	0.1	5×10^{-4}	N/A	0.002
3.3 B ii)	0.01	0	0.001	0.5	N/A	0.005	6.5	1.30	0.1	0.8	N/A	0.002
3.3 B iii)	0.01	0	0.001	0.5	0.001	0.005	6.5	1.30	0.1	N/A	200	0.002
3.3 B iv)	0.01	0	0.001	0.5	0.02	0.005	6.5	1.30	0.1	N/A	200	0.002
3.7A	0.01	0.0025	0	0	N/A	0.005	6.5	1.30	0.1	3×10^{-4}	N/A	0.002
3.7B	0.01	0	0.01	0.0025	N/A	0.005	6.5	1.30	0.1	3×10^{-4}	N/A	0.002
3.7C	0.001	0.5	0	0	0.001	0.005	6.5	1.30	0.1	N/A	3	0.002
3.9 A, B	1	0	0	0	N/A	0.005	6.5	1.30	0.1	4×10^{-4}	N/A	0.002
3.11 A, B	1	0	0	0	N/A	0	6.5	1.30	0.1	5×10^{-5}	N/A	0.008

Table 3.2 Parameter values used in simulations of the flux-based model.

Fig. 3.3 B i) refers to the simulation of intracellular partitioning using a non-limited pool of PIN, with a linear increase in PIN allocation with increasing flux (this simulation was used to generate Fig 3.3B). Fig. 3.3 B ii) refers to the simulation of intracellular partitioning using a non-limited pool of PIN, with a quadratic increase in PIN allocation with increasing flux, Fig. 3.3 B iii) refers to the simulation of intracellular partitioning using a limited pool of PIN, with a linear increase in PIN allocation with increasing flux. Fig. 3.3 B iv) refers to the simulation of intracellular partitioning using a limited pool of PIN, with a quadratic increase in PIN allocation with increasing flux. Fig. 3.3 B ii – iv) are not shown in figures). C_A is the default initial concentration of auxin in cytoplasmic compartments, ε is the limit for noise addition to C_A , $C_{PINedge}$ is the default initial concentration of PIN at each cell edge, ε_{PIN} is the limit for noise addition to $C_{PINedge}$, PIN_{cyto} is the initial concentration of PIN in cytoplasmic compartments for versions of the model with a non-limiting pool of PIN, μ is the auxin degradation rate, D is the passive permeability of auxin and T is the rate of PIN-mediated auxin transport. γ is the rate of PIN unbinding from the membrane, α and k are constant parameters determining the extent to which flux promotes PIN allocation to the membrane for versions of the model with non-limiting and limiting pools of PIN respectively. ρ is the auxin production rate. R and I (the areas of cytoplasmic compartments and the lengths of cell edge compartments) are as described in Table 3.1 and I , the auxin import rate, is described in the text. In the simulations used to generate Figs. 3.9 and 3.11, some cells have different parameter values than the rest of cells in the array, these cases are described in the text above.

4 Mechanisms underlying the generation of centres of polarity convergence

4.1 Introduction

Models of plant tissue cell polarity can be classified into two groups (tandem and convergent coupling models) according to how they behave for groups of cells in the absence of pre-established asymmetries. Simulations presented in chapters 2 and 3 revealed that both types of model can generate coordinated polarity fields in 2D arrays of cells. However, the extent to which the different models can capture *in planta* polarity patterns and auxin distributions during the establishment of new polarity fields has not been investigated. The simulations already presented indicate that the two classes of models make different predictions about how polarity fields are related to organiser regions with elevated auxin production, degradation or import rates. Therefore, one way to distinguish between models is to investigate patterns of expression of candidate organiser genes involved in influencing auxin distributions during the establishment of new polarity fields.

The emergence of new polarity fields can be studied in the context of the shoot apical meristem where the polarity patterns of leaf and flower primordia are established as these primordia initiate at the meristem flanks. The position of each new primordium is specified by a centre of PIN1 polarity convergence with elevated activity of the auxin responsive promoter, *DR5* (Heisler et al., 2005; Reinhardt et al., 2003). As organs develop, the PIN1 polarities of all cells are oriented distally, towards the organ tip (Heisler et al., 2005; Scarpella et al., 2006). One way to address how polarity fields associated with new outgrowths are established is to test different models in the context of the shoot apical meristem. However, the polarity pattern of the shoot apical

meristem is complex and dynamic (Heisler et al., 2005), and live imaging of this tissue is challenging.

Another possibility is to test models in the context of leaf development, after the emergence of leaves from the meristem. An advantage of the leaf is that its epidermal proximo-distal polarity pattern is simpler than the polarity pattern of the meristem, and expression patterns of a number of genes related to auxin distributions have been characterised in this context. For example, an auxin biosynthesis enzyme, *YUC1*, is expressed at the leaf base (Wang et al., 2011) and auxin importers are expressed at the tip (Bainbridge et al., 2008). However, a problem with testing models in the context of leaf development is that the epidermal polarity field of the wild-type leaf does not change, except during serration development at the leaf margin (Scarpella et al., 2006), which is not readily accessible for time-lapse imaging. Wild-type leaves can therefore be used to investigate the maintenance of existing polarity fields but can't readily be used to investigate the emergence of new ones.

Here, I explore *kanadi1 kanadi2* (*kan1kan2*) double mutants as an alternative system to investigate the generation of new polarity fields in the context of the leaf. *kan1kan2* mutants lack functional copies of two transcription factors that specify abaxial leaf identity and develop ectopic 3D outgrowths from their abaxial leaf surface (Eshed et al., 2004) (Fig. 4.1). The development of these ectopic outgrowths has been proposed to be due to juxtaposition of adaxial and abaxial tissue identities and to be similar to the development of new leaves and leaf serrations (Eshed et al., 2004; Nakata et al., 2012; Wang et al., 2011). Similar to the whole leaf and to serrations, outgrowths are associated with specific patterns of *YUC*-driven auxin biosynthesis, and the tips of outgrowths have elevated expression of the auxin-responsive promoter, DR5 (Wang et al., 2011). However, the patterns of PIN1 polarity, and dynamics of auxin accumulation and gene expression have not been investigated during outgrowth development.

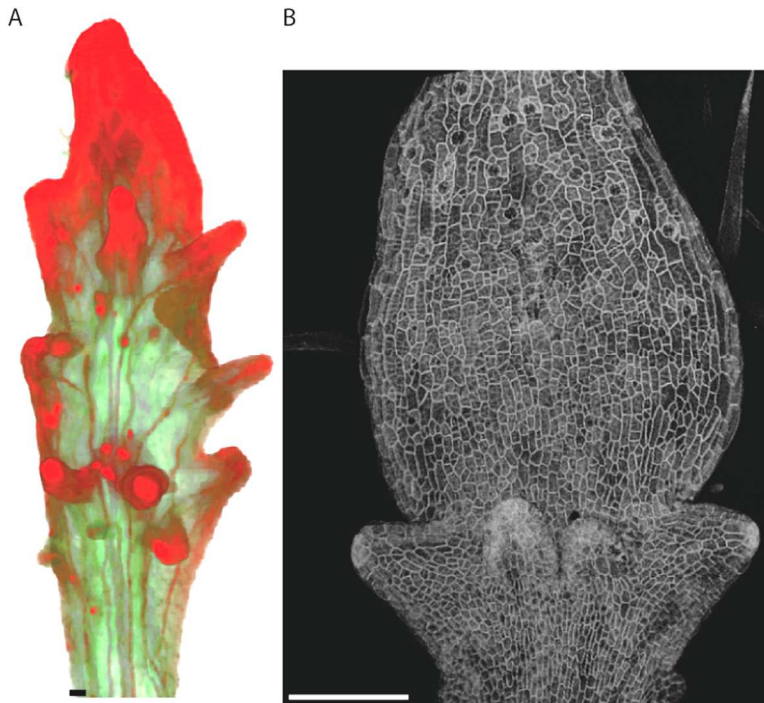


Fig. 4.1. Ectopic outgrowths in *kan1kan2* mutant leaves.

A) Optical projection tomography (OPT) image of a mature *kan1kan2* leaf (the image is artificially coloured to emphasise the 3D shape). B) Confocal image of a *kan1kan2* leaf primordium, expressing a plasma-membrane targeted RFP marker.

Although the relevance of ectopic *kan1kan2* outgrowths for understanding the generation of wild-type organs is unknown, they offer a convenient experimental system due to the accessibility of leaves for imaging. Ectopic *kan1kan2* outgrowths begin to emerge from the proximal third of the lamina (Eshed et al., 2004) (Fig. 4.1 B), and their development can readily be tracked over time using live imaging. This allows patterns of gene expression during outgrowth development to be investigated, and allows easy characterisation of mutant phenotypes.

In this chapter, I characterise the dynamics of PIN1 polarity patterns and auxin distributions during the development of WT and *kan1kan2* leaves, and compare the ability of tandem and

convergent cell-cell coupling models to account for the experimental observations. I then generate new predictions about patterns of auxin biosynthesis and import in WT and *kan1kan2* leaves, which I use to distinguish between the models experimentally.

4.2 Results

4.2.1 PIN1 polarity patterns in WT and *kan1kan2* leaves

To investigate whether changes in epidermal tissue cell polarity are associated with *kan1kan2* outgrowths, I characterised PIN1 polarity patterns in *kan1kan2* and WT leaves. I imaged a *PIN1::PIN1:GFP* reporter in the abaxial side of the first leaf of *kan1kan2* or WT seedlings. Leaves were tracked over four to five days to allow the PIN1 polarities and fates of cells to be monitored. The experiment was started when leaves were approximately 50 μm in width (with about 50 to 70 cells in the abaxial epidermis). For *kan1kan2* leaves, this was approximately two days before outgrowths were observed to form.

4.2.1.1 Centres of PIN1 polarity convergence predict the positions of *kan1kan2* outgrowths

To determine the PIN1 polarity pattern of a leaf from a confocal image of PIN1:GFP signal, it is necessary to know which cell each region of GFP signal originated from. However, in the confocal images generated (an example is shown in Fig. 4.2 A), it is difficult to assign each region of PIN1:GFP signal to a specific cell. This is because it is not possible to resolve fluorescent signals arising from two juxtaposed plasma-membranes of neighbouring cells. The fluorescent signal detected around each cell could therefore have been generated from PIN1:GFP in the membrane of that cell, and /or in the juxtaposed membranes of neighbouring cells.

However, depending on the pattern of PIN1:GFP signal surrounding a cell, it may be possible to infer a polarity or axiality of the PIN1 distribution. If an equal intensity of PIN1:GFP signal is detected at all edges of a cell (Fig. 4.2 Bi), it is possible that the real distribution of PIN1 was unpolarised (Fig. 4.2 B ii) or polarised (Fig. 4.2 B iii), so a polarity cannot be inferred. If a cell has PIN1:GFP signal at two opposite ends (Fig. 4.2 Ci), it is possible that the cell had a bipolar distribution of PIN1 (Fig. 4.2 C ii), or that it was polarised (Fig. 4.2 C iii and iv), thus, axiality can be inferred but not polarity. In such cases, I use a line to indicate the axis of the PIN1 distribution (Fig. 4.2 Ci). If an arc of PIN1 signal is observed at one end of a cell (Fig. 4.2 D i and E i), I assume that the signal belongs to the cell in which the arc fits. If the opposite end of the same cell has a lower level of GFP signal (Fig. 4.2 D), or an arc belonging to the neighbouring cell (Fig. 4.2 E), I assume that the PIN1 distribution was polarised and draw an arrow to represent the polarity (Fig. 4.2 D i and E i). I used these criteria to infer PIN1 polarity distributions in confocal images.

kan1kan2 leaves displayed centres of PIN1 polarity convergence at the tips of emerging ectopic outgrowths (Fig. 4.2 A, F). Cells at the centres of convergence had highly polarised PIN1, oriented towards the interface between three or four neighbouring cells.

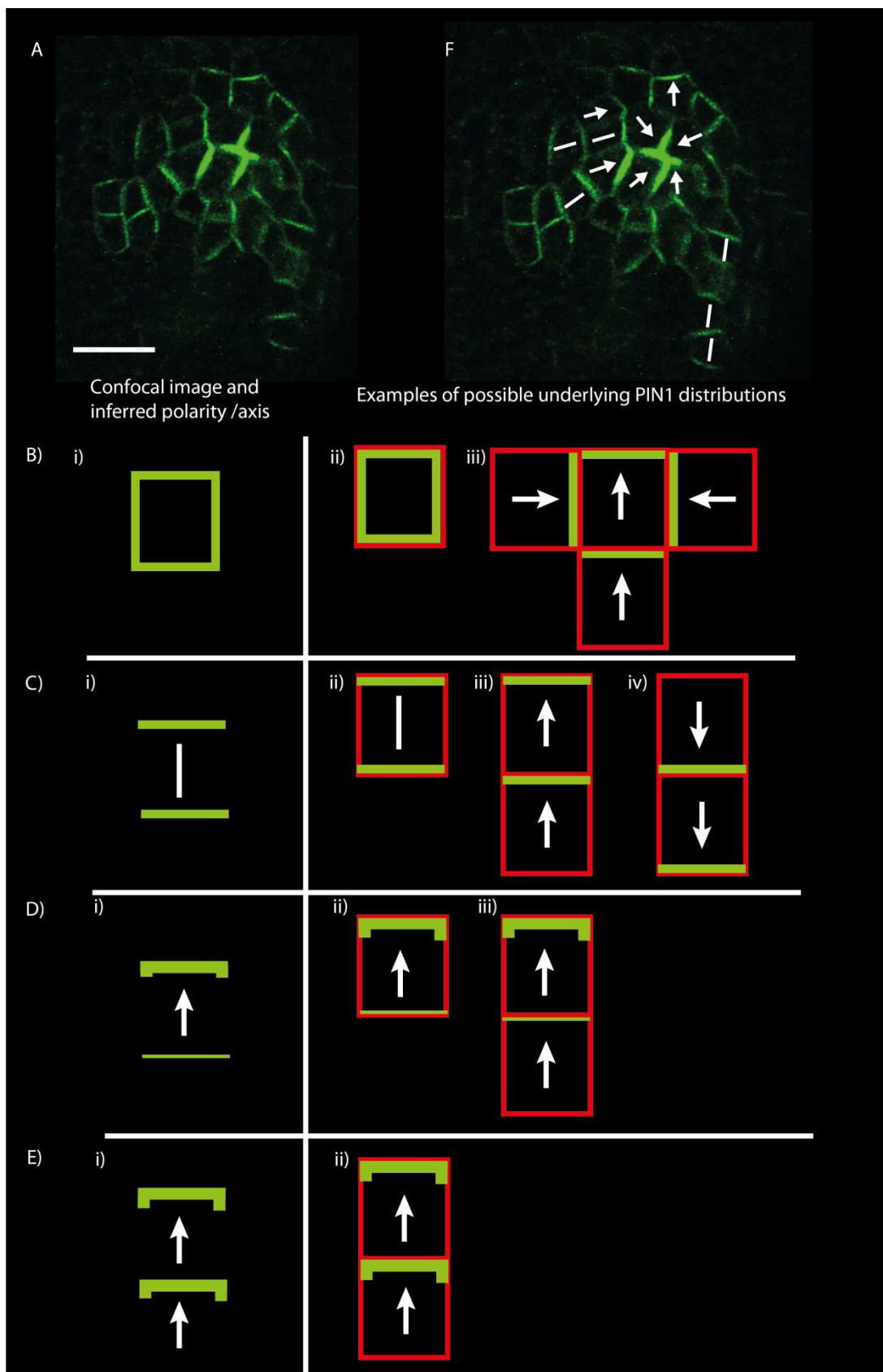


Fig. 4.2 Inferring cellular PIN1 distributions from confocal images of leaves expressing *PIN1::PIN1:GFP*.

A) Example of a confocal image of PIN1:GFP signal at the tip of an emerging *kan1kan2* outgrowth. **B)-E)** Schematic examples of signal from a confocal image of PIN1:GFP and inferred axialities or polarities. **B)** Example where it is not possible to infer the cellular distributions of PIN1. i) If PIN1:GFP signal is detected at all edges of a cell, the cell may either be unpolarised (ii) or polarised (iii). **C)** Example where the axis, but not the polarity, of cellular PIN1 distributions can be inferred. If PIN1:GFP signal is detected as lines at proximal and distal ends of a cell (i), it is possible that the cell has PIN1 at both its proximal and distal ends (ii), or that two neighbouring cells have PIN1 at their distal (iii), or proximal (iv) cell ends. Therefore only the axis of the PIN1 distribution can be inferred. **D)** and **E)** Examples where the polarity of the PIN1 distribution can be inferred. If PIN1:GFP is present as an arc which follows the contours of a cell, I assume that the signal originated from the cell in which the arc fits. (D) (i) If a cell has an arc of PIN1 polarity at one end, and a lower level of PIN1 signal at the other, I assume the cell's polarity points towards the PIN1 arc and that the PIN1 is distributed as shown in (ii) or (iii). E) (i) If a cell has an arc of PIN1 polarity at one end, and an arc in the neighbouring cell at the opposite cell end, I assume the cell's polarity points towards its own arc of PIN1:GFP signal and that the PIN1 is distributed as shown in (ii). **F)** Confocal image of PIN1:GFP at the tip of an emerging *kan1kan2* outgrowth, with polarities and axes inferred according to the criteria described above. This image is representative of the *PIN1::PIN1:GFP* signal observed in 8 out of 8 *kan1kan2PIN1::PIN1:GFP* leaves that had similar sized outgrowths. Scale bars in A and F =20 μ m.

To determine whether these centres of convergence formed before or after outgrowth emergence, cell lineages that gave rise to them were tracked back through the time-course of the live imaging experiment (Fig.4.3 A, C, yellow dots, arrows and lines indicate which cells gave rise to the centres of convergence). To correlate the patterns of PIN1 polarity seen in the epidermis with the time relative to outgrowth emergence, I used Volviewer software to generate a 3D rendering of the confocal z-stacks (Fig.4.3 B, D). The side views of these 3D renderings show the contours of the abaxial epidermis and allow the time points at which outgrowths emerged to be identified (Fig.4.3 B, D). This revealed that cells closest to the centre of convergence at the outgrowth tip descended from one or two cells, which were already at the centre of a polarity convergence at early stages of leaf development, prior to an obvious outgrowth emergence (Fig.4.3 Ai and Ci and ii). Notice PIN1 polarity orientations around cells that gave rise to the centre of convergence, some of which already converge towards a central region or are oriented along the medio-lateral leaf axis at the earliest stages imaged. These early centres were observed

approximately one to two days before an outgrowth could be identified in the 3D rendering (Fig.4.3 Ai, Bi and Ci, ii, Di,ii). In total, six centres of convergence, from five different leaves were tracked back in time and in all cases this revealed polarity reorientations prior to outgrowth emergence. Thus, centres of PIN1 polarity convergence mark the sites of future outgrowth development.

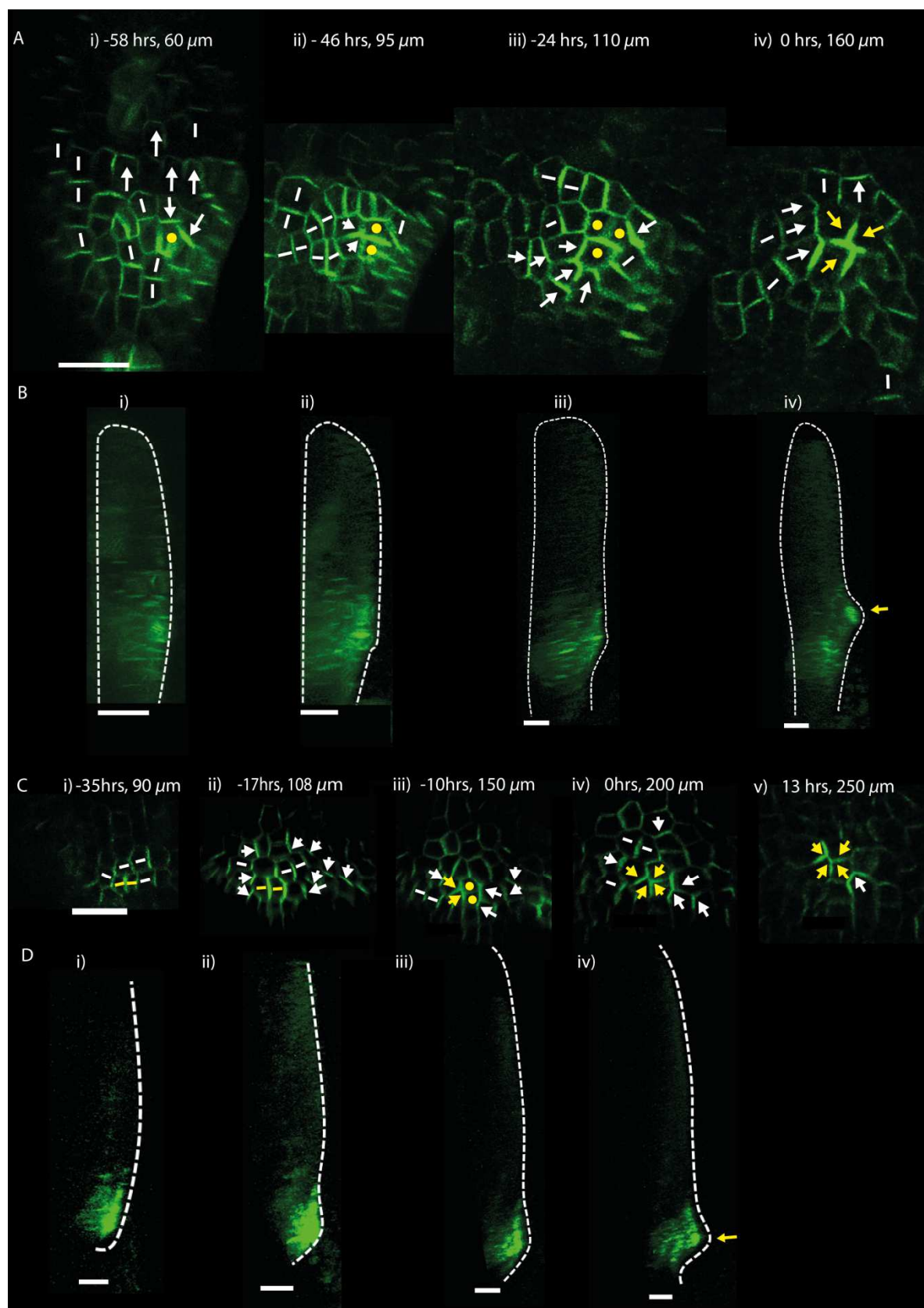


Fig.4.3. Two examples of the *PIN1:GFP* polarity pattern preceding *kan1kan2* outgrowth development.

A) Confocal images of the *PIN1::PIN1:GFP* marker prior to the development of a centre of convergence at an outgrowth tip. The time relative to outgrowth emergence and the leaf width are given above each image. iv) Shows a centre of convergence at the tip of an emerging outgrowth. i) to iii) show the same region of the leaf shown in iv), at earlier stages of development. Yellow dots, arrows and lines indicate the cells which form the centre of convergence in iv). Arrows indicate PIN1 polarities and lines indicate axes of PIN1 distributions (inferred as described in Fig. 4.2) **B)** Side views of 3D renderings of the leaf in A showing the emergence of the ectopic outgrowth. Times relative to outgrowth emergence are the same as shown in A. Dashed white lines show leaf contours (these lines were drawn by increasing the brightness and contrast of the image to reveal the contour even in regions where the signal is weak). Yellow arrow points to the tip of the outgrowth, where the centre of convergence shown in A) is located. **C)** and **D)**. Same as A) and B), but for another leaf, imaged at smaller time intervals. Scale bars = 20 μ m.

Prior to the formation of centres of PIN1 polarity convergence, at even earlier stages of *kan1kan2* leaf development, the cell polarities marked by PIN1 appeared to be oriented towards the leaf tip. *PIN1::PIN1:GFP* signal was detected on proximal and distal cell-cell interfaces, and where cell geometries made it possible to detect the direction of polarity, PIN1 appeared to be localised on distal cell edges (Fig. 4.4). This suggests that centres of convergence arise within a distally

oriented polarity field in *kan1kan2*

leaves.

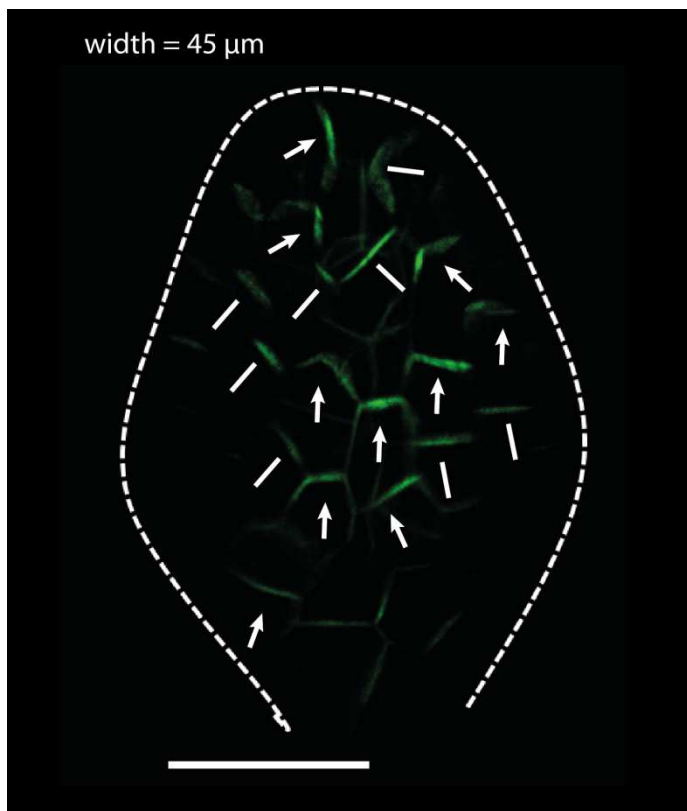


Fig. 4.4 *PIN1:GFP* polarity pattern in an early *kan1kan2* leaf primordium.

A young *kan1kan2* leaf expressing the *PIN1::PIN1:GFP* marker. Dashed line indicates an approximation of the leaf outline (revealed by increasing the brightness and contrast of the image). Arrows show inferred PIN1 polarity orientations, lines show inferred axes of polarity. Scale bar = 20 μ m. This image is representative of 8 out of 8 images obtained of young *kan1kan2* primordia.

4.2.1.2 WT leaves have a globally coordinated, distally-oriented PIN1 polarity field

To test whether the centres of convergence are an ectopic feature of *kan1kan2* leaves, I performed live imaging of the *PIN1::PIN1:GFP* reporter in a WT background. Consistent with previous reports (Scarpella et al., 2006; Wenzel et al., 2007), centres of PIN1 polarity convergence were not observed in the main lamina of WT leaves. In young WT leaf primordia (less than 100 μm in width), *PIN1::PIN1:GFP* signal appeared to be localised to distal-most cell ends, with polarities converging at the leaf tip (white arrows in Fig. 4.5 i and ii). In some cases, it was not possible to infer PIN1 polarity, but the GFP signal was strongest on the proximal and distal ends of cells compared with lateral cell sides, consistent with the presence of a globally coordinated, distally-oriented polarity field (white lines in Fig. 4.5 i) and ii)). The expression of *PIN1::PIN1:GFP* was weak and often undetectable in the lamina of WT leaf primordia greater than 100 μm in width (Fig. 4.5 iii and iv). The formation of centres of PIN1 polarity convergence in the abaxial lamina therefore appears to be specific to *kan1kan2* mutants.

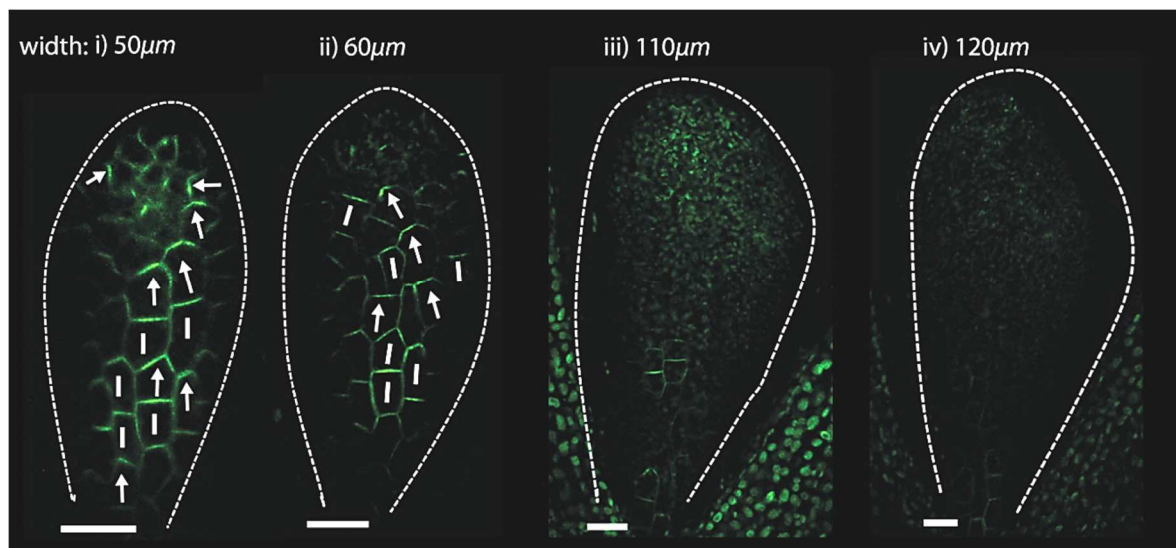


Fig. 4.5. *PIN1::PIN1:GFP* expression in a WT leaf primordium.

i) to iv) show confocal images of *PIN1::PIN1:GFP* in the same WT leaf imaged over a period of 2 days (times from the beginning of the experiment are i) 0 hrs, ii) 14 hrs, iii) 37.5 hrs, iv) 47.5 hrs. White arrows indicate the inferred direction of PIN1 polarity and white lines indicate axes of PIN1 localisation. Scale bars = 50 μ m. Dashed white lines indicate an approximation of the leaf outline. The leaf margins (which were previously reported to express *PIN1::PIN1:GFP* in leaf primordia below and greater than 100 μ m in width (Wenzel et al., 2007)) are not in focus in these images. The data set shown is representative of that obtained from time-lapse imaging of two other WT leaves and is also consistent with snapshot images taken at different time points.

4.2.1.3 Ectopic centres of polarity convergence were not observed in *kan1kan2* leaves that did not generate outgrowths

In live imaging experiments, some *kan1kan2* leaves did not generate ectopic centres of PIN1 polarity convergence and this was correlated with a failure to generate outgrowths. The failure to form outgrowths was most likely due to effects of the growth chamber used for live imaging as *kan1kan2* seedlings not grown in the chamber consistently generated outgrowths in all leaves (15 out of 16 *kan1kan2* seedlings grown on plates and imaged developed outgrowths from their first two leaves). Approximately two-thirds of *kan1kan2* seedlings grown in the chamber did not generate centres of convergence or outgrowths from their first leaf, but went on to develop ectopic outgrowths from subsequent leaves which developed outside of the chamber. All *kan1kan2PIN1::PIN1:GFP* leaves that did not develop outgrowths also did not show *PIN1::PIN1:GFP* centres of convergence during the imaging period (13 leaves, from 13 seedlings, were imaged in total). In these leaves, *PIN1::PIN1:GFP* signal was sometimes seen on all cell edges (circles in Fig. 4.6), on proximal and distal edges, or on lateral edges (lines, Fig. 4.6) and there was no clear pattern of tissue cell polarity. These findings show that the formation of centres of PIN1 polarity convergence is associated specifically with the development of *kan1kan2* outgrowths.

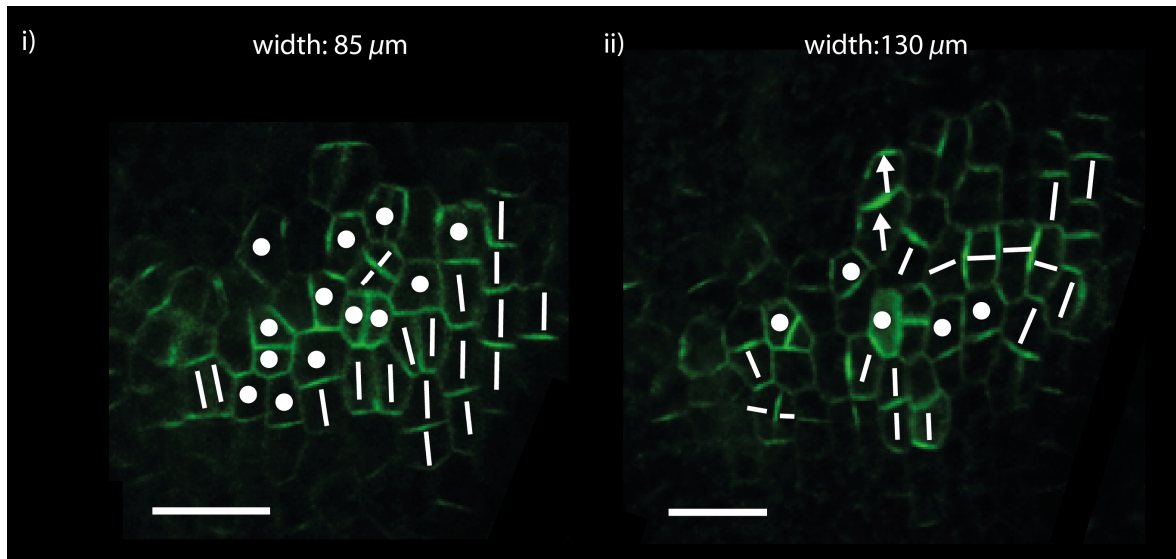


Fig. 4.6 PIN1:GFP signal in a *kan1kan2* leaf that did not generate an ectopic outgrowth.

Confocal images of the *PIN1::PIN1:GFP* pattern in a *kan1kan2* that did not generate an ectopic outgrowth, imaged at two successive time points, 24 hours apart. The leaf is a similar width to that shown in Fig.4.3 A ii and iii, where a PIN1 polarity convergence can be seen. Lines show inferred axes of PIN1 localisation, arrows show inferred polarities and circles indicate cells that have approximately equal PIN1:GFP signal on all regions of the membrane. Scale bars =20 μ m.

4.2.2 Ectopic auxin-activity maxima precede outgrowths

Given that outgrowths are associated with centres of PIN1 polarity convergence, I investigated how this pattern of auxin transporters is related to the dynamics of intracellular auxin accumulation. In the shoot apical meristem of *A.thaliana*, centres of PIN1 polarity convergence are associated with elevated levels of intracellular auxin, assayed by the activity of the auxin responsive promoter, *DR5* (Heisler et al., 2005). Sites of elevated intracellular auxin have been proposed to be both a consequence and a cause of the PIN1 polarity pattern (Heisler et al., 2005; Jönsson et al., 2006; Smith et al., 2006), and to be important for the growth of new organs (Reinhardt et al., 2000; Reinhardt et al., 2003). To investigate whether *PIN1::PIN1:GFP* centres of convergence at the tips of *kan1kan2* outgrowths are associated with elevated intracellular auxin levels, I imaged a *DR5::GFP* reporter in the abaxial side of the first leaf of *kan1kan2* seedlings over a period of 3 days. At early stages, *DR5::GFP* signal was detected at the leaf tip (Fig 4.7 i), similar to the pattern described for the WT leaf (Mattsson et al., 2003; Scarpella et al., 2006).

Approximately one day prior to outgrowth development, locally elevated points of *DR5::GFP* signal were detected in groups of epidermal cells in the proximal lamina, where outgrowths typically form (Fig 4.7 ii, white arrow). At later stages, these regions of *DR5::GFP* expression persisted, and could be found throughout emerging outgrowths (Fig 4.7 iii-iv). These auxin maxima appear to be a feature of outgrowth formation since foci of elevated *DR5::GFP* activity were not detected in the abaxial lamina of a *kan1kan2* leaf that did not develop ectopic outgrowths (Fig. 4.8). This is similar to what is observed in WT leaves, where *DR5::GFP* expression is detected at the leaf tip, and at the tips of serrations, but is absent from the main lamina (Mattsson et al., 2003; Scarpella et al., 2006).

Overall, these findings reveal that both auxin activity maxima and centres of PIN1 polarity convergence are specifically associated with the tips of developing *kan1kan2* outgrowths, and that both are present in regions of the abaxial lamina prior to outgrowth emergence.

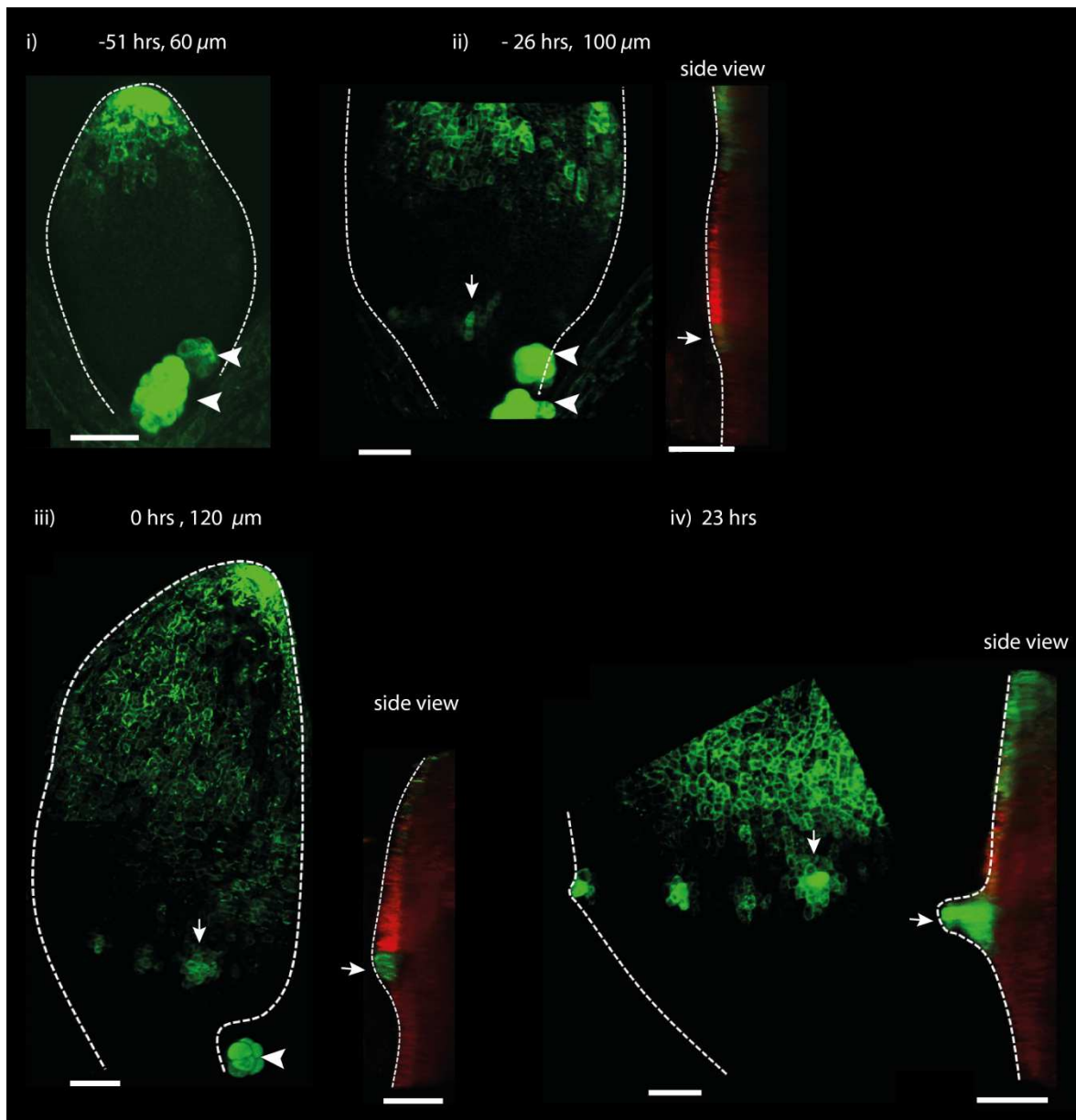


Fig 4.7 *DR5::GFP* expression in a *kan1kan2* leaf during outgrowth development.

Confocal images of *DR5::GFP* in the same *kan1kan2* leaf imaged over a period of 3 days. Times relative to outgrowth emergence, and leaf widths are given above images. Side views show optical sections through 3D confocal images including *DR5::GFP* (green) and auto-fluorescence plus *CUC2::RFP* (red) channels (here *CUC2::RFP* is only used to help show the leaf outline, its expression pattern will be described in the following chapter). White arrows in iv) indicate the region of *DR5::GFP* activity at the tip of an outgrowth. In images shown in i) to iii), the white arrows indicate the same *DR5::GFP* expressing cells as those in iv), tracked back in time. Arrow heads indicate high *DR5::GFP* signal in stipules. Scale bars =20 μ m. This data set is representative of that obtained from tracking two other *kan1kan2DR5::GFP* leaves which gave rise to outgrowths, and with snapshot images of *kan1kan2 DR5::GFP* leaves.

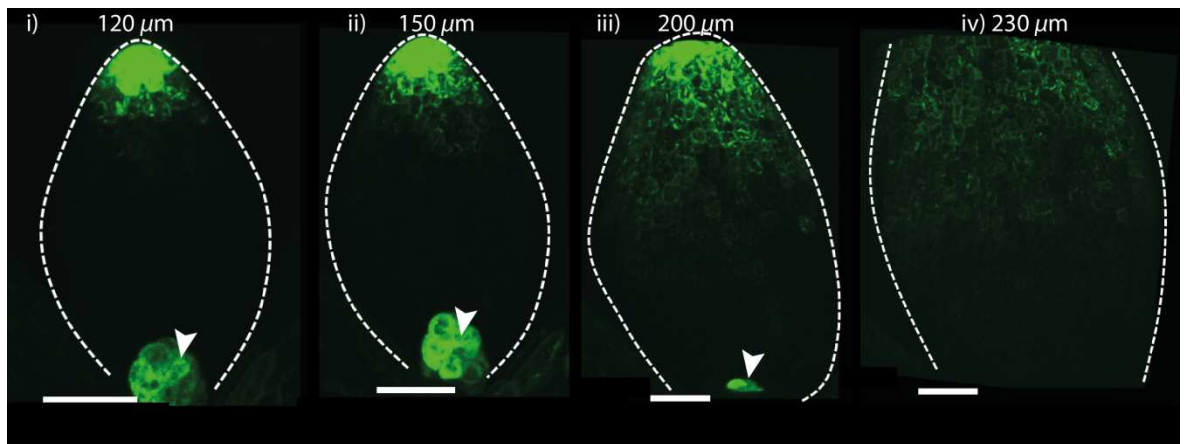


Fig. 4.8 *DR5::GFP* expression pattern in a *kan1kan2* leaf that did not generate an ectopic outgrowth.

Confocal images of *DR5::GFP* in the same *kan1kan2* leaf, which did not generate an ectopic outgrowth, over a period of approximately 3 days (times from the beginning of the experiment are : i) 0 hrs, ii) 14 hrs, iii) 40 hrs, iv) 64 hrs). White arrow heads indicate a stipule. Scale bars =50 μ m. This is the only *kan1kan2DR5::GFP* leaf that did not generate an outgrowth that I tracked, therefore the experiment should be repeated.

4.2.3 Models for the generation of centres of PIN1 polarity convergence.

The findings presented above suggest that PIN1 polarity reorientations and auxin activity maxima may play a role in the development of ectopic *kan1kan2* outgrowths. However, the mechanism underlying the formation of centres of PIN1 polarity convergence and the relationship between the PIN1 polarity field and auxin accumulation is unclear. I therefore compare the ability of tandem and convergent coupling models of auxin-regulated PIN1 polarisation to account for the main features of the *kan1kan2* polarity pattern. I use the indirect cell-cell coupling model as representative of the class of tandem cell-cell coupling models, and the up-the-gradient (convergent coupling) model. I try to capture two aspects of the data described above

- 1) The formation of a stable ectopic centre of polarity convergence, arising within the context of a distally oriented polarity field. This polarity convergence should be centred

on an interface between cells, and those cells closest to the centre of convergence should have highly polarised PIN1.

- 2) Intracellular auxin should be elevated at the ectopic centre of polarity convergence.

Below, all figures of model outputs show a snapshot taken at the end of the simulation, when the system has reached stability. Here I use grids of square or rectangular cells, rather than hexagons (which were used in previous chapters).

4.2.3.1 Up the gradient model

4.2.3.1.1 Generation of a proximo-distal polarity field with the up-the-gradient model.

In the up-the-gradient model, an auxin gradient across the tissue is required for the establishment of a globally coordinated polarity field equivalent to the proximo-distal polarity field observed in WT and *kan1kan2* leaves. As shown in the previous chapter, if a row of cells at the distal (top) end of an array of cells produces auxin at an elevated rate, whilst the proximal-most (bottom) row of cells has an elevated rate of auxin degradation, a distally oriented polarity field is generated (Fig 4.9 A i-ii). The concentration of auxin at the distal end of the array is further enhanced through transport towards this region (Fig 4.9 A iii). In this model, cells with an elevated rate of auxin production act as minus organisers of polarity (they cause polarity to orient towards them), and cells with an elevated rate of auxin removal act as plus organisers (they cause polarity to orient away from them). If the plus organiser is removed and all cells degrade auxin at an equal rate, cells in the proximal regions of the array are unable to polarise because the intercellular auxin gradient in this region is too shallow (Fig 4.9 B i-iii). Therefore, to match the observed proximo-distal polarity field in WT and young *kan1kan2* leaves, this model predicts that the base of the leaves acts as an auxin sink.

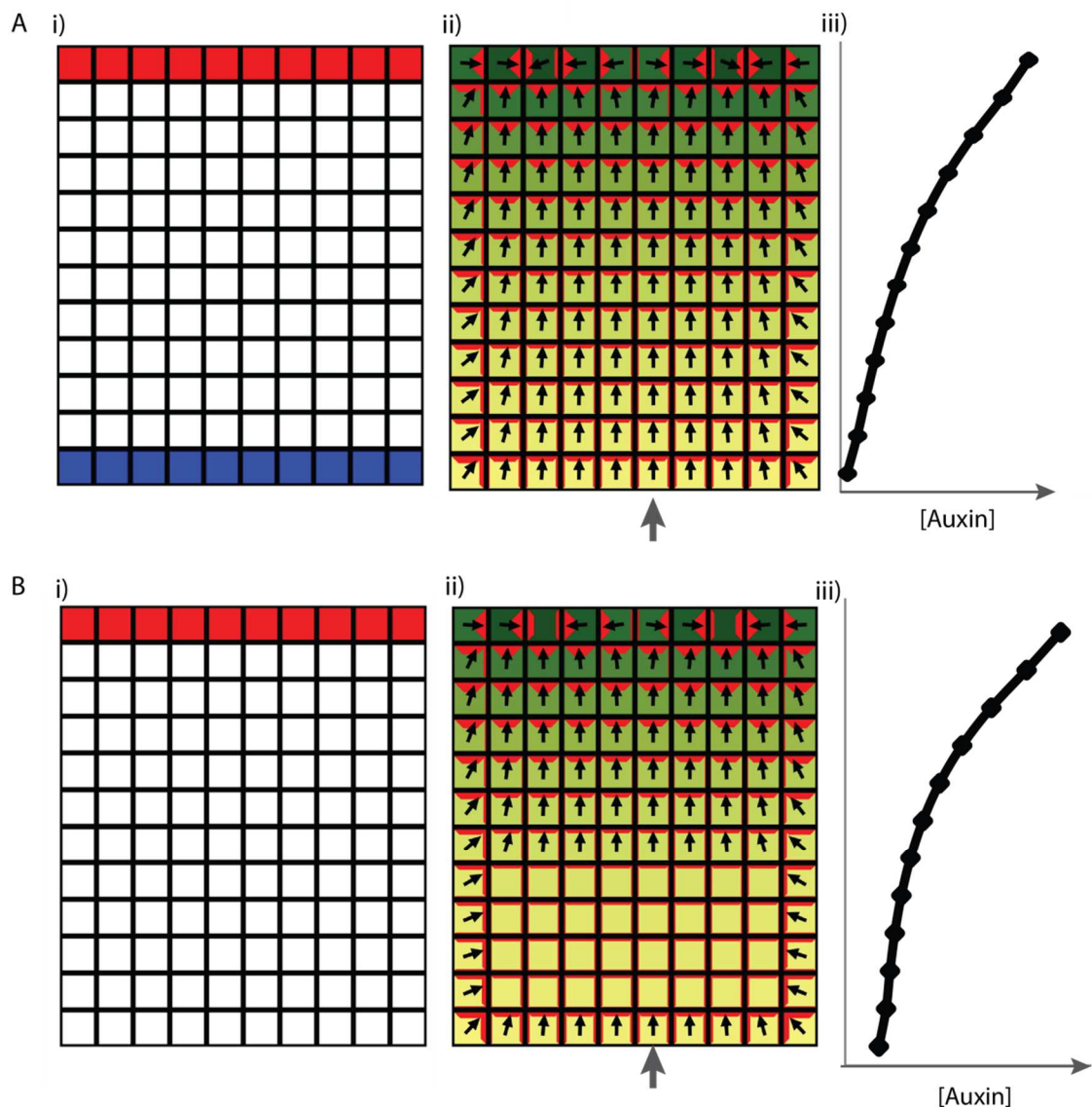


Fig 4.9 Generation of a proximo-distal polarity field in an up-the-gradient model.

A) Generation of distally oriented polarities throughout the array due to the presence of a row of cells with an elevated auxin production rate at the distal end, and a row of cells with elevated auxin degradation at the proximal end. i) Location of cells with elevated auxin production rate (shown in red) and elevated auxin removal rate (shown in blue). All other cells do not produce auxin. ii) PIN and auxin distributions in the final state of the model, with specified conditions shown in i). Red lines show PIN distributions, with thicker lines indicating a higher concentration of PIN at a cell edge. Intensity of green indicates intracellular auxin concentration, with darker green indicating a higher concentration and yellow indicating a lower concentration. Arrows show direction of PIN polarity. Note that all cells have polarised PIN, because, in the presence of an auxin sink at the proximal end of the tissue, the intercellular auxin gradient is relatively steep. iii) Graph of intracellular auxin concentration for the column of cells marked with the grey arrow in ii). **B)** As for A, but in the absence of elevated auxin degradation in the most proximal row of cells (all cells degrade auxin at a background rate). i) Location of cells with elevated auxin production rate (shown in red). All other cells do not produce auxin. ii) PIN and auxin distributions in the final

state of the model, with specified conditions shown in i). Cells towards the proximal region of the array have very weak or no polarity, due to a shallow intercellular auxin gradient. iii) Graph of intracellular auxin concentration for the column of cells marked with the grey arrow in ii).

4.2.3.1.2 *Generation of centres of polarity convergence in up-the-gradient model*

At early stages of *kan1kan2* leaf development, initial polarity reorientations had a single cell at their centre (Fig.4.3 Ai, cell with yellow dot). These single cells then gave rise to approximately three cells at tip of an outgrowth that had convergent PIN1 polarities (Fig.4.3 A iv, yellow arrows). Below, I simulate these polarity reorientations without simulating growth and cell division. I do this by running two simulations for each model. In one simulation, I add minus organiser identity to a single cell, to model an initial polarity reorientation with a single cell at its centre. In a second simulation, I add minus organiser identity to four cells, to model later stages of the convergence point, when I assume the initial minus organiser has divided, and its daughters have retained minus organiser identity.

In the context of the proximo-distal polarity field generated above by the up-the-gradient model, an ectopic centre of PIN polarity convergence may be generated by elevating the auxin concentration of a cell within the array. For example, this may be done by elevating the auxin production rate from zero in a cell (red cell in Fig 4.10 A i). The cell with an elevated auxin production rate acts as a minus organiser of polarity, and causes neighbouring cells to establish PIN polarities that are oriented towards it (Fig 4.10 A ii). As observed in the *kan1kan2* leaf, the centre of PIN convergence generated is centred on a cell-cell interface and cells closest to its centre have highly polarised PIN distributions (Fig 4.10 A ii). Plotting the concentrations of auxin for a column of cells, which includes the minus organiser cell at the centre of the convergence, shows that, consistent with DR5::GFP activity in *kan1kan2* leaves, the centre of convergence and the distal end of the array have elevated intracellular auxin (Fig 4.10 A iii). If elevated auxin

production is added to four cells in the array, a centre of convergence forms, centred on the interface between the four cells (Fig 4.10 Bi). This PIN polarity pattern at the centre of convergence is similar to that observed experimentally (Fig.4.3 A iv).

The centres of polarity convergence generated in the up-the-gradient model are stable and self-reinforcing. This can be illustrated by adding a transient increase in auxin concentration to a cell in an array with auxin production at the distal end but no auxin removal at the proximal end (Fig 4.10 C i). This alone is sufficient to cause the formation of a stable centre of polarity convergence with high auxin (Fig 4.10 C ii and iii). This is because, when a cell's auxin concentration becomes locally elevated, neighbouring cells localise PIN1 preferentially towards this high auxin cell. Through positive feedback, this raises the auxin concentration of that cell, further reinforcing localisation of PIN from neighbouring cells towards it. Therefore, in this model, the elevated intracellular auxin concentration at the centre of convergence is both an initial cause, and a consequence, of the convergent PIN polarity pattern.

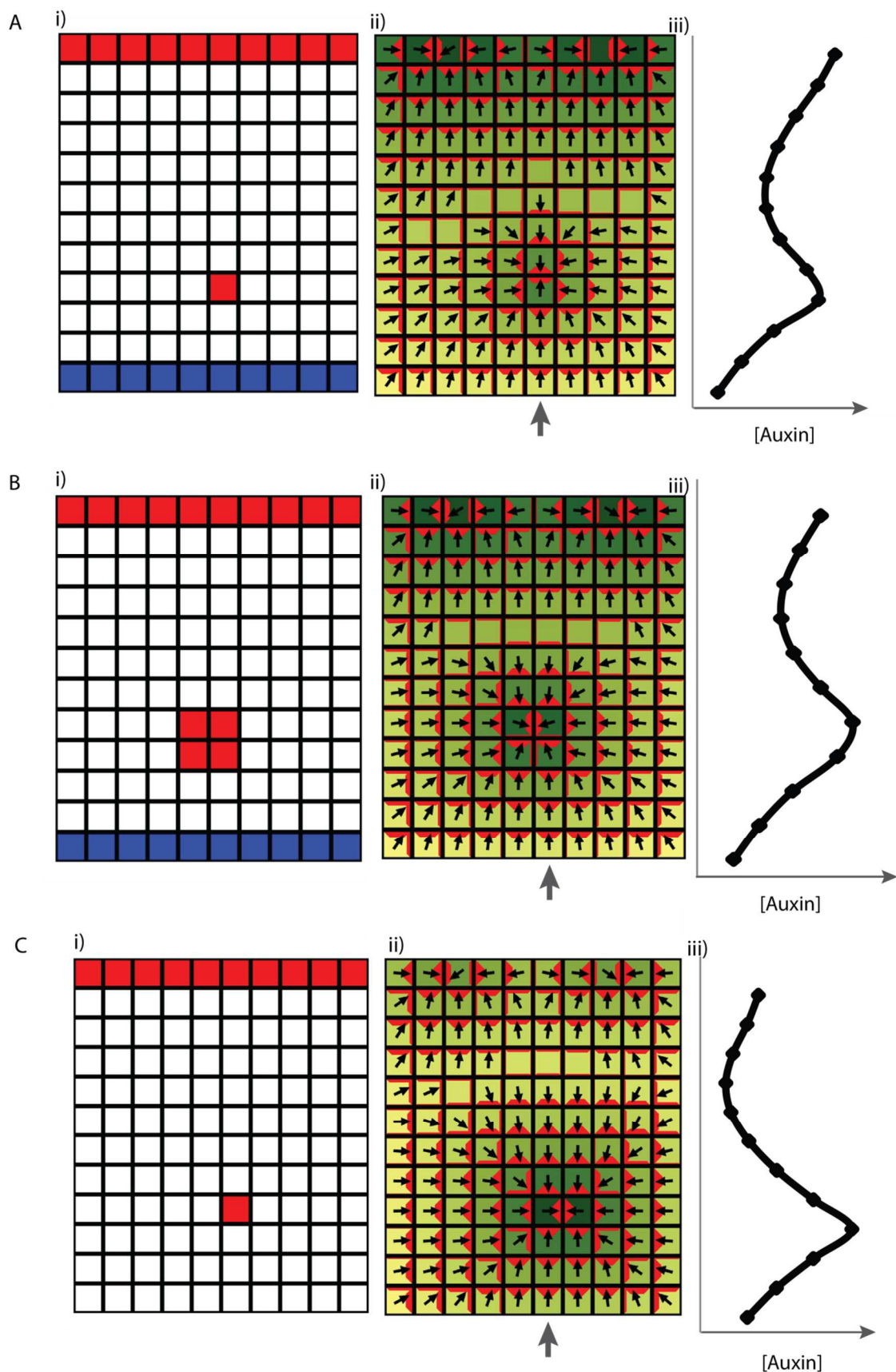


Fig 4.10 Formation of centres of polarity convergence in an up-the-gradient model.

A) Generation of a centre of convergence due to the presence of a cell with an elevated auxin production rate. i) Positions of organiser regions. The distal row of cells (red) has an elevated auxin production rate, and the proximal row of cells has an elevated auxin removal rate (blue). An isolated cell with an elevated auxin production rate (shown in red), is added to the simulation once a distally oriented polarity field is established. ii) PIN polarity pattern and auxin distribution in the final state of the model. Red lines show PIN distributions, with thicker red lines indicating a higher concentration of PIN at a cell edge. Intensity of green indicates intracellular auxin concentration, with darker green indicating a higher concentration, and yellow indicating a lower concentration. Arrows show direction of PIN1 polarity. Note that the region of convergence is centred on a cell-cell interface, and all cells near the centre of the convergence have highly polarised PIN. iii) Graph of intracellular auxin concentration for the column of cells marked with the grey arrow in ii). **B)** As for A, but with elevated auxin production added to four cells (group of four red cells in (i)). **C)** Generation of a stable centre of convergence due to a transient elevation of auxin concentration in the isolated red cell shown in i). ii) and iii) are as described for A.

4.2.3.2 Indirect cell-cell coupling model

4.2.3.2.1 Generation of a proximo-distal polarity field with the indirect cell-cell coupling model.

I next address whether the indirect cell-cell coupling model can account for the *kan1kan2* PIN1 polarity pattern. In the version of this model explored in chapters 2 and 3, it was assumed that the membrane-bound A* polarity component promotes the export of auxin. In this implementation of the model, PIN was not represented explicitly. Here, to facilitate comparisons between models, I introduce an explicit representation of PIN into the ICP-based model. I assume that PIN can bind and unbind from the membrane passively, and that it is recruited to the membrane in proportion to the local concentration of A* and causes the export of auxin. Arrows indicating cell polarities point towards membrane regions with the highest PIN concentration.

Consistent with results presented in chapters 2 and 3, in this implementation, a proximo-distal pattern of polarity can be generated by assuming an elevated rate of auxin production at the proximal end of the array (plus organiser) and an elevated rate of auxin degradation at the distal

end of the array (minus organiser) (Fig. 4.11 A). However, this model does not generate elevated intracellular auxin concentrations at the distal end of the tissue because of the high auxin removal rate in this region (Fig. 4.11 A). This is incompatible with data showing elevated activity of the *DR5::GFP* auxin responsive reporter at the leaf tip. This aspect of the data can be captured by adding elevated auxin import, instead of elevated auxin degradation, to distal cells of the model (Fig. 4.11 B). This allows auxin to accumulate in these cells and causes depletion of auxin from the surrounding extracellular space, encouraging polarities to point towards this region and allowing it to act as a minus organiser of polarity (Fig. 4.11 B). In this case, elevated intracellular auxin concentrations at the minus organiser are a consequence, rather than a cause, of the tissue cell polarity pattern.

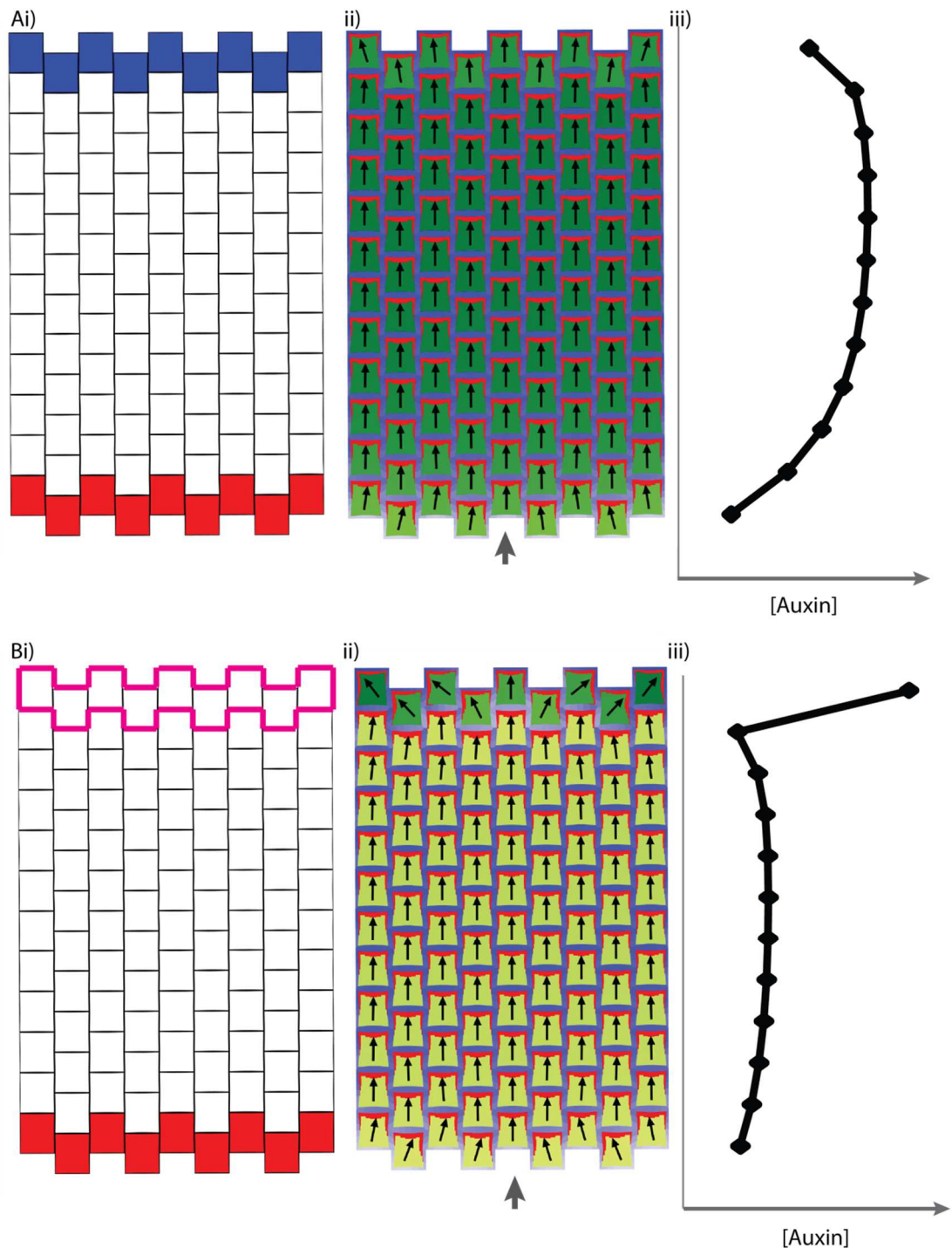


Fig. 4.11 Generation of a proximo-distal polarity field in an indirect cell-cell coupling model with an explicit representation of PIN.

A) Polarity coordination with elevated auxin production at the proximal end of the tissue (plus organiser, red cells in i), and elevated auxin degradation the distal end of the tissue (minus organiser, blue cells in i). ii) PIN1 and auxin distributions at the end of the simulation. Arrows point to regions with maximum levels of PIN. The intensity of green indicates the concentration of intracellular auxin (the darkest green region in a tissue cell indicates the highest intracellular auxin). The intensity of blue in the wall surrounding

cells indicates the concentration of extracellular auxin (darkest blue in an array of cells indicates the highest concentration of extracellular auxin). PIN1 is shown in red, with the thickness of each line representing the concentration of PIN1 in a region of the membrane. iii) Graph showing intracellular auxin concentrations for the column of cells indicated by the grey arrow in ii). **B)** As for A, but with a minus organiser at the distal end of the tissue with an elevated rate of auxin import (pink cell outlines in i). Note that intracellular auxin accumulates at the distal end of the tissue.

4.2.3.2.2 *Generation of centres of polarity convergence in an indirect cell-cell coupling model*

Since the PIN-rich end of each cell is oriented towards regions with low extracellular auxin, a natural way to generate a polarity convergence is to add an elevated rate of auxin import to a cell in the array after the establishment of proximo-distal polarity (Fig. 4.12A). The elevated import depletes auxin from the surrounding cell walls, and therefore favours the presence of A* and PIN in the adjacent membranes of neighbouring cells. Reversal of polarity in the distal neighbour of the high import cell is sensitive to parameter values and only occurs if the background level of extracellular auxin is sufficiently high (which can be achieved through a high background rate of auxin production). This is because, in the presence of high background extracellular auxin concentrations, the maximum levels of A* in the membrane are lower (due to inhibition of A* by extracellular auxin) and so the cell polarity is weaker and easier to reverse (Fig. 4.12A ii).

A less parameter sensitive mechanism for generating polarity reorientations is to introduce elevated rates of auxin import and degradation to a cell (Fig. 4.12 B). The elevated auxin import and degradation act synergistically to lower extracellular auxin concentrations surrounding the cell and generate a centre of polarity convergence centred on it (the cell acts as a minus organiser). Elevated auxin import alone is not effective because it leads to very high levels of intracellular auxin in the minus organiser cell (due to auxin import from the extracellular space, and due to PIN-mediated transport towards the minus organiser). This intracellular auxin is then exported by distally-localised PIN in the minus organiser cell. Therefore, despite the elevated rate

of auxin import, the concentration of extracellular auxin at the PIN-rich end of the minus organiser cell may remain relatively high, preventing the distal-most neighbour from reversing its polarity. However, with elevated auxin removal from the minus organiser cell, its intracellular auxin concentration is reduced and thus, PIN-dependent auxin export is also reduced. As a consequence, extracellular auxin levels at the distal end of the minus organiser cell are lower, allowing the distal most neighbour to reverse its polarity (Fig. 4.12 B ii).

Consistent with experimental observations of auxin activity distributions, a minus organiser cell with elevated auxin import and degradation may have an elevated concentration of intracellular auxin in relation to the surrounding tissue (Fig. 4.12 B ii and iii). When a group of four minus organiser cells have elevated auxin import and removal, all cells at the centre of convergence have polarised distributions of PIN, and the convergence is centred on the cell wall between adjacent cells (Fig. 4.12 C ii).

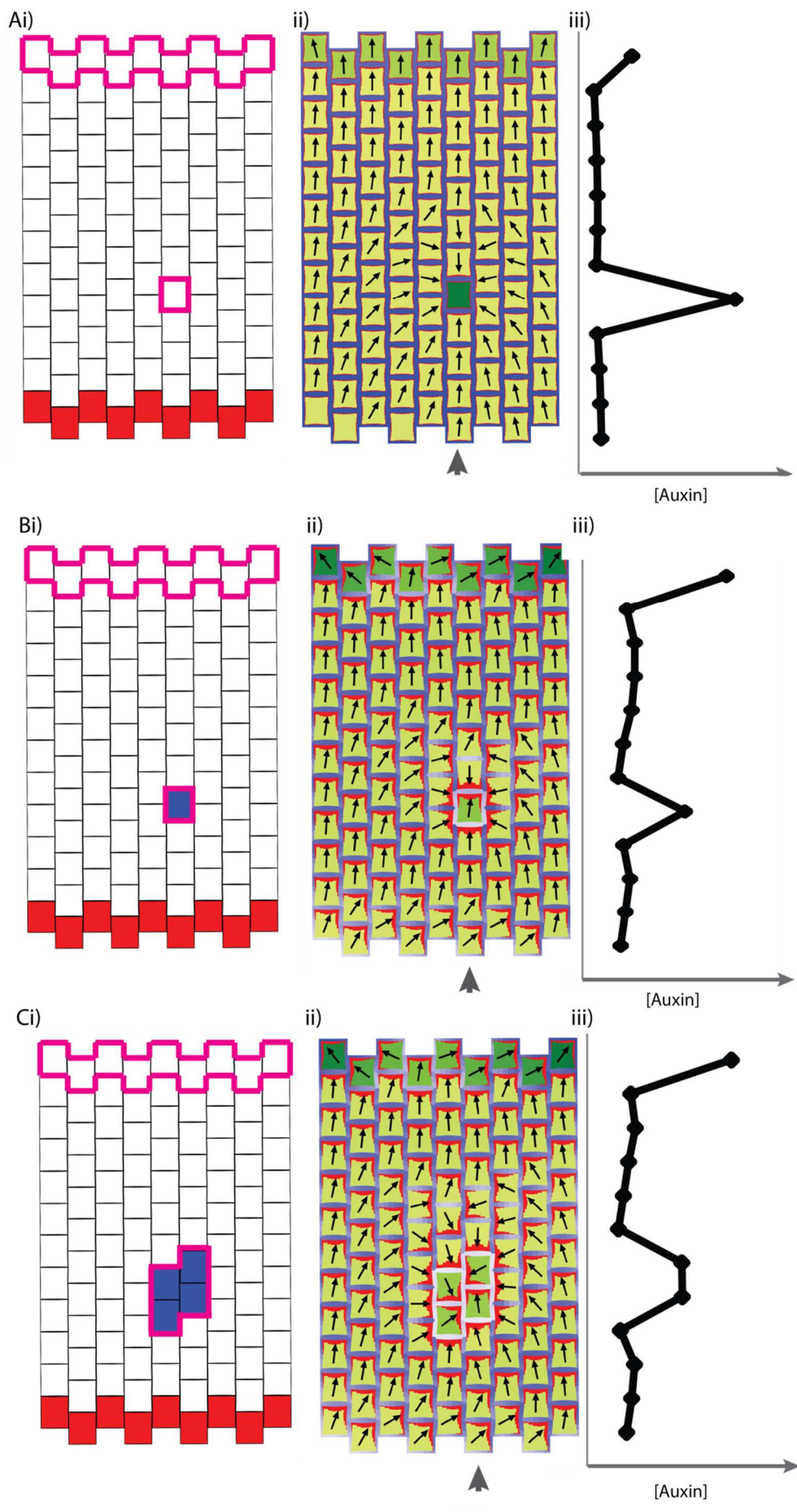


Fig. 4.12 Formation of centres of polarity convergence in an indirect cell-cell coupling model.
A) PIN polarity convergence formation in the presence of a minus organiser cell with an elevated rate of auxin import (cell with pink outline in i). A 10-fold increase in the background rate of auxin import was added to the minus organiser cell. ii) PIN and auxin distributions in the final state of the model. Note the weakly polarised PIN distributions (red lines), which is due to high background levels of extracellular auxin that are needed to generate a centre of convergence through elevated import rates alone. iii) Graph of intracellular auxin concentration for the column of cells marked by the grey arrow in ii). **B)** Same as A, but with the presence of a minus organiser cell with an elevated rate of auxin import (10 fold increase) and an elevated rate of auxin degradation (23 fold increase compared with the background degradation rate) (isolated blue cell with pink outline in i). **C)** Same as B, but with a group of four minus organiser cells with an elevated rate of auxin degradation and import.

This comparison of models shows that both the indirect cell-cell coupling model and the up-the-gradient model can capture the main features of the *kan1kan2* leaf polarity pattern: both can capture the formation of a centre of polarity convergence with high auxin from an initial proximo-distal polarity field. However, the models require different assumptions about the patterns of auxin import, auxin biosynthesis and auxin removal. The indirect cell-cell coupling model predicts that the leaf tip and the tips of outgrowths have elevated rates of auxin import. In contrast, the up-the-gradient model does not require elevated auxin import rates to account for polarity and auxin distribution patterns. Also, the indirect cell-cell coupling model predicts that auxin biosynthesis is elevated at the base of the leaf, and auxin removal rates are elevated at the leaf tip. In contrast, the up-the-gradient model predicts the opposite: that the leaf base acts as an auxin sink and the leaf tip acts as an auxin source. In the following section I test these predictions by determining the expression pattern of, and requirement for, genes involved in auxin import and auxin biosynthesis, during the changes in the polarity pattern of *kan1kan2* leaves.

4.2.4 Patterns of auxin importer expression in WT and *kan1kan2* leaves

To investigate whether auxin import rates are elevated at the tips of *kan1kan2* outgrowths, I looked at the expression of auxin importer genes in WT and *kan1kan2* backgrounds. The *AUX/LAX*

family of auxin importers includes four genes in *A.thaliana* (*AUXIN RESISTANT 1 (AUX1)*, *LIKE AUXIN RESISTANT 1 (LAX1)*, *LIKE AUXIN RESISTANT 2 (LAX2)*, and *LIKE AUXIN RESISTANT 3 (LAX3)*) which encode proteins that actively transport auxin from the extracellular space into the cytoplasm (Parry et al., 2001; Peret et al., 2012; Yang et al., 2006).

Here I focus on reporters of *AUX1* and *LAX1* expression since *LAX2::GUS* and *LAX3::GUS* were not expressed in the leaf epidermis (*LAX2::GUS* was expressed in developing vascular tissue of WT and *kan1kan2* leaves and there was no detectable expression of *LAX3::GUS* in leaves of either background (not shown)). I also perform a genetic analysis of the role of all four *AUX/LAX* genes in the generation of *kan1kan2* outgrowths.

4.2.4.1 *LAX1* is expressed at the leaf tip and ectopically expressed in the lamina prior to outgrowth emergence

Comparisons of *LAX1::GUS* expression between leaves of *kan1kan2* and WT seedlings suggest that *LAX1* is expressed ectopically prior to, and during, outgrowth emergence. In WT, *LAX1::GUS* expression was detected at the tips of young primordia, in vascular tissue, and at the tips of serrations, but its expression was excluded from the rest of the lamina (Fig. 4.13 A). In *kan1kan2* leaves, *LAX1::GUS* was expressed in the same regions as in WT, but was also ectopically expressed in groups of a few cells in proximal regions of the abaxial epidermis (Fig. 4.13 B). These groups of cells were found at the tips of developing outgrowths (Fig. 4.13 B ii and iii). To investigate whether *LAX1::GUS* expression precedes outgrowth emergence, I made transverse sections through *kan1kan2LAX1::GUS* seedlings stained to reveal GUS activity. This revealed that *LAX1::GUS* expression was present prior to outgrowth emergence (Fig. 4.13 C i and ii).

Assuming that regions of *LAX1* expression correlate with regions of elevated auxin import, these findings support the prediction of the indirect cell-cell coupling model that minus organisers of polarity (at the leaf tip, and in regions of the lamina prior to outgrowth formation) have elevated auxin import rates.

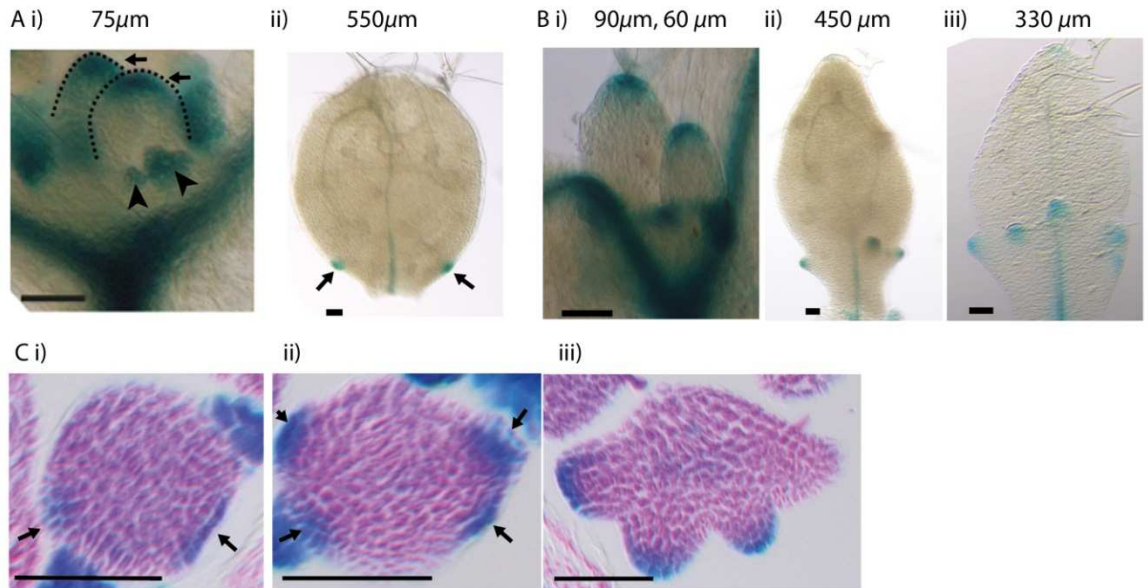


Fig. 4.13 . Expression of *LAX1::GUS* in WT and *kan1kan2* leaves.

A) Expression pattern of *LAX1::GUS* in WT leaves. *LAX1::GUS* was expressed at the tips of developing primordia (arrows in (i), black dashed lines indicate leaf outlines, arrow heads indicate stipules) and at the tips of serrations (ii) (arrows indicate serrations). Leaf widths are given above images. **B)** Expression pattern of *LAX1::GUS* in *kan1kan2* leaves. *LAX1::GUS* is expressed at the tips of primordia (i) and at the tips of outgrowths (ii and iii). ii) shows leaf 1, iii) shows leaf 3, treated with chloral hydrate to clear the tissue. The images of wild-type and *kan1kan2* leaves in A) and B) are representative of at least 6 out of 6 images obtained for different seedlings with leaves at each developmental stage shown. **C)** Transverse sections through GUS stained *kan1kan2 LAX1::GUS* seedlings, showing points of *LAX1::GUS* expression before outgrowths have emerged (black arrows in i) and ii)) and at the tips of developing outgrowths (ii and iii)). The pink colour of the tissue is due to eosin staining of the tissue prior to sectioning. The images in i) and ii) show *LAX1::GUS* expression in 2 out of 2 young leaves that were successfully sectioned and imaged. The image shown in iii) is representative of 3 out of 3 leaves that were sectioned and imaged. Scale bars = 50 μ m.

4.2.4.2 *AUX1* is expressed at the tips of emerging outgrowths

AUX1::AUX1:YFP expression was also locally elevated in developing outgrowths, but not prior to their emergence. Expression of this transgene was detected in distal regions of the abaxial surface of *kan1kan2* leaves. In proximal regions, expression was absent, except in cells of emerging outgrowths (Fig. 4.14 A, arrow). Time-lapse confocal imaging revealed that, in three out of three young *kan1kan2* leaf primordia that were tracked, prior to outgrowth formation, *AUX1::AUX1:YFP* expression was absent from proximal regions (Fig. 4.14 Biii, iv, yellow arrow). As outgrowths began to emerge, the expression of *AUX1::AUX1:YFP* became locally elevated in outgrowth cells (Fig. 4.14 Bv –iv, yellow arrows). Elevated expression of *AUX1::AUX1:YFP* was also detected in developing serrations (Fig. 4.14 Biii-vi, white arrows), but was not present at earlier time points before serrations emerged (Fig. 4.14B i-ii, white arrows). These observations suggest that *AUX1* could play a role in maintaining centres of polarity convergence at the tips of outgrowths (and serrations), but is not involved in their initial development.

In contrast to *kan1kan2* leaves, WT leaves had a more uniform expression pattern of *AUX1::AUX1:YFP* in the abaxial epidermis. In six out of six observed WT leaves between 60 μm and 180 μm in width, the reporter was expressed in all cells of the abaxial epidermis, and signal was particularly strong in the leaf margin, especially at the leaf tip (Fig. 4.14 C i). For leaves of similar sizes, *AUX1::AUX1:YFP* was expressed in proximal regions in WT, but not in *kan1kan2* (compare Fig. 4.14 Ai and Biii with Ci). This suggests that expression of *AUX1* may be repressed in the proximal region of *kan1kan2* leaves. In both *kan1kan2* and WT leaves, expression of *AUX1::AUX1:YFP* was excluded from the adaxial epidermis, except in cells close to the leaf margin (Fig. 4.14 Cii).

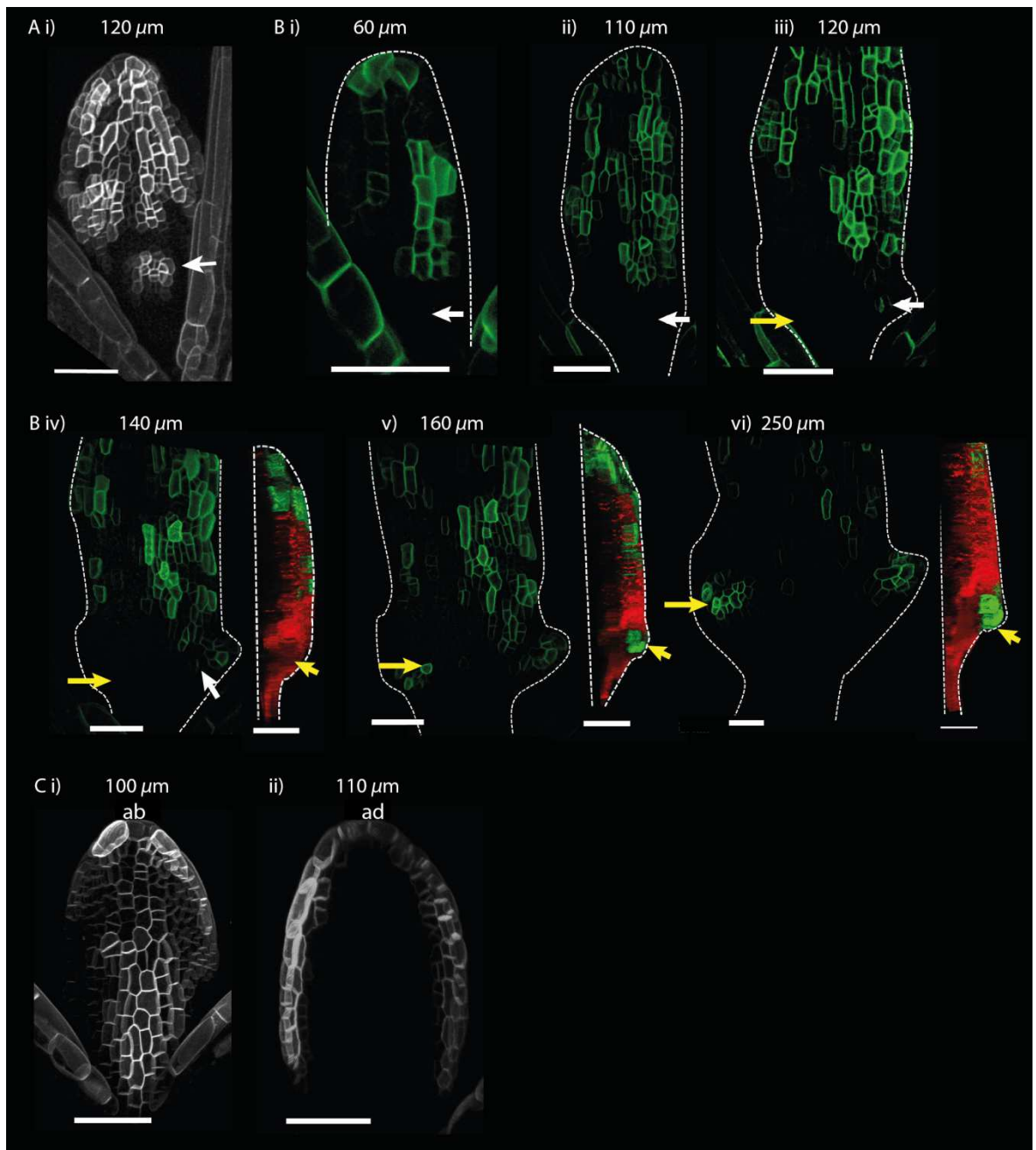


Fig. 4.14 Expression of *AUX1::AUX1:YFP* in WT and *kan1kan2* leaves.

A) *AUX1::AUX1:YFP* expression in leaf 1 of a *kan1kan2* mutant, showing abaxial surface. Arrow points to the tip of an emerging outgrowth with locally elevated *AUX1::AUX1:YFP* signal. **B)** Time-lapse imaging of *AUX1::AUX1:YFP* in the abaxial epidermis of the first leaf of a *kan1kan2* mutant seedling. White arrows mark the positions of cells that eventually gave rise to the *AUX1::AUX1:YFP* expressing cells in the developing serration on the right side of the leaf. Yellow arrows mark the positions of cells which eventually gave rise to the tip of the ectopic outgrowth on the left side of the leaf. Red and green images in iv), v) and vi) show side views, from the left hand side of the leaf (showing that the outgrowth emerged at the time point shown in v). The red colour shows autofluorescence and a *CUC2::RFP* marker (here this marker is just used to show the contour of the leaf, its expression will be described in the following chapter), and the green colour

shows *AUX1::AUX1:YFP* signal. Times from the beginning of the experiment at which images were taken are: i) 0hrs, ii) 22hr 40min, iii) 31hr 10min, iv) 46hr 40min, v) 55hr 40min, vi) 74hr 40min. This data set is representative of 3 out of 3 *kan1kan2 AUX1::AUX1:YFP* tracking experiments. **C)** *AUX1::AUX1:YFP* expression in leaf 1 of WT, showing abaxial surface (i) and adaxial surface (ii) of two different leaves. Each image is representative of those obtained for six WT leaves in total. Scale bars = 50 μ m.

4.2.5 Loss of *AUX/LAX* auxin importers causes a loss of ectopic outgrowths.

To investigate whether *AUX/LAX* auxin importers are needed for the generation of ectopic outgrowths, I crossed *kan1kan2+/-* plants with *aux1lax1lax2lax3* quadruple mutant plants and used PCR-based genotyping to identify *kan1kan2aux1lax1lax2lax3* hextuple mutants in an F3 progeny (see methods for details). Loss of all four *AUX/LAX* genes caused a reduction in the mean number of outgrowths per leaf from 12 (in *kan1kan2* mutants) to 1.5 (in *kan1kan2aux1lax1lax2lax3* mutants) (Fig 4.15 A, example images of *kan1kan2* and *kan1kan2aux1lax1lax2lax3* leaves are shown in Fig 4.15 C). The number of outgrowths per leaf varied through the leaf heteroblastic series in both *kan1kan2* and *kan1kan2aux1lax1lax2lax3* backgrounds, with earlier leaves developing fewer outgrowths than later leaves (not shown). In *kan1kan2* plants, all rosette leaves observed produced at least one outgrowth, and the median number of outgrowths per leaf was 7, with a maximum number of observed outgrowths per leaf of 35 (n= 84 leaves) (Fig 4.15 B). In contrast, in the *kan1kan2aux1lax1lax2lax3* background, most leaves did not produce any outgrowths (the median number of outgrowths was 0), but some higher order leaves produced up to 20 outgrowths (n=200 leaves) (Fig 4.15 B). These findings support a role for *AUX/LAX* auxin importers in the generation of ectopic outgrowths.

LAX2::GUS and *LAX3::GUS* were not found to be expressed in the *kan1kan2* leaf epidermis, therefore it is possible that these genes do not contribute to the development of ectopic outgrowths. To determine whether mutations in *LAX2* and *LAX3* contribute to the loss of

outgrowths in the hextuple mutant, I also selected *kan1kan2aux1lax1* and *kan1kan2aux1lax1lax2* plants from an F3 progeny of the cross between *kan1+/-kan2* and the *aux/lax* quadruple mutant. This revealed that *kan1kan2aux1lax1* plants have a small reduction in the number of outgrowths per leaf compared with *kan1kan2* plants (Fig 4.15 A, n =110 leaves). This reduction is further increased by loss of *LAX2*, since *kan1kan2aux1lax1lax2* mutants have a further loss of outgrowths (Fig 4.15 A, n =148 leaves). Since *LAX2::GUS* expression was only detected in sub-epidermal tissue, this finding supports a role of sub-epidermal auxin importer expression in the generation of outgrowths. *kan1kan2aux1lax1lax2* mutants generated more outgrowths than *kan1kan2aux1lax1lax2lax3* mutants (Fig 4.15 A), suggesting that, despite the absence of *LAX3::GUS* reporter expression in leaves, *LAX3* may function redundantly with other members of the *AUX/LAX* family in the generation of ectopic outgrowths.

The *kan1kan2+/-* line used to generate the hextuple mutants was in a Landsberg erecta (Ler) background, and the *aux/lax* quadruple mutant was in a Columbia (Col-0) background. To check that the loss-of outgrowth phenotype in hextuple mutants was not due to the introduction of an unknown genetic element from the Col-0 background, I determined whether the reduction in the number of outgrowths segregated with mutant alleles of the *AUX/LAX* genes. To do this, I used an F3 family of plants that segregated for mutations in *KAN2* and *LAX1*, but was homozygous for *kan1*, *aux1*, *lax2* and *lax3* mutant alleles. Of 156 *kan1kan2aux1lax2lax3* plants segregating for *lax1*, 120 (77%) developed many outgrowths and 36 (23%) had a reduced number and size of outgrowths. All of the plants with few outgrowths were homozygous for the *lax1* mutation, whilst all siblings with many outgrowths that were genotyped (40 in total) all had a wild-type copy of *LAX1*. Thus, in a *kan1kan2aux1lax1+/-lax2lax3* background, a reduction in the number of outgrowths segregates with *lax1*.

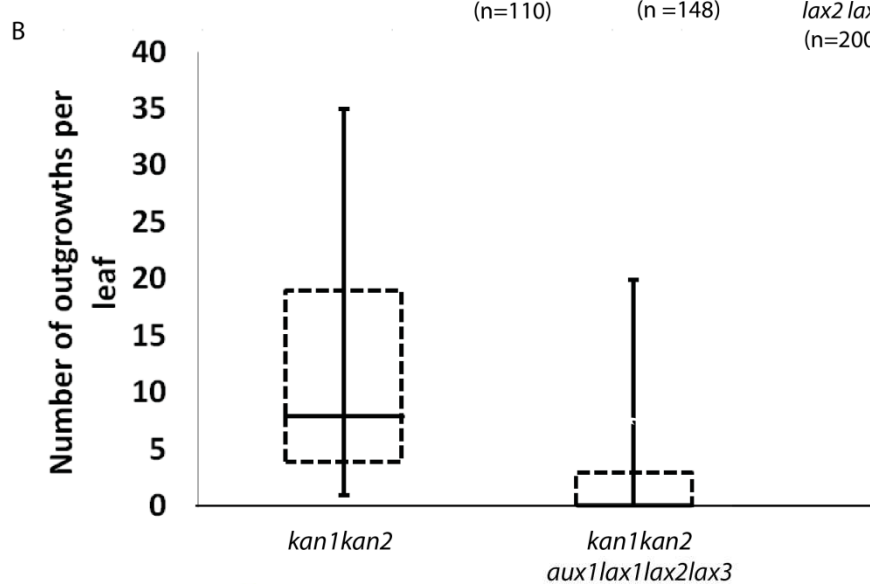
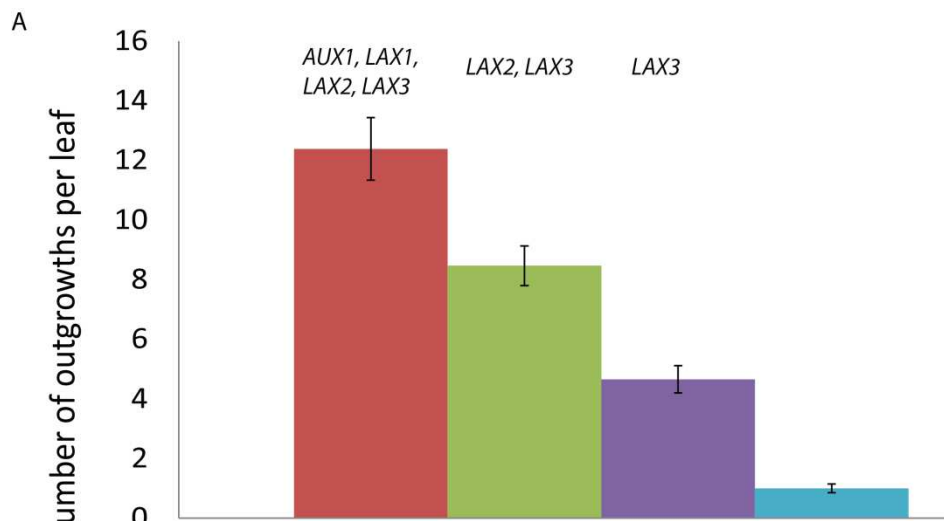


Fig 4.15 Numbers of outgrowths in *kan1kan2 aux/lax* mutants.

A) Mean number of outgrowths (+/- standard error of the mean) in rosette leaves of *kan1kan2* plants carrying mutant alleles of *AUX/LAX* genes. Labels above the bars indicate which *AUX/LAX* family members are functional in the different genetic backgrounds. **B)** Box plot showing numbers of outgrowths in *kan1kan2* and *kan1kan2aux1lax1lax2lax3* mutants. **C)** Images of individual leaves of *kan1kan2* and *kan1kan2aux1lax1lax2lax3* mutants. Scale bars = 5mm.

4.2.6 The pattern of auxin importer expression is compatible with up-the-gradient model

The finding that the expression of auxin importers is elevated at the tips of outgrowths, and plays a role in their formation, supports the predictions of the indirect cell-cell coupling model presented earlier (Fig. 4.12B). However, the behaviour of the up-the-gradient model was not tested in the presence of elevated auxin import as modulation of auxin import was not required to generate centres of polarity convergence with elevated auxin. To test whether the findings related to auxin importers may also be compatible with up-the-gradient model, I introduce sites of elevated auxin import to simulations of PIN polarity patterns.

The proximo-distal leaf polarity pattern arises in the up-the-gradient model if it is assumed that auxin is synthesised only at the distal end of the tissue, and degraded at the base (Fig 4.9 A). If elevated auxin import is added to the distal row of cells with auxin production, cells within the distal half of the array acquire a proximo-distal PIN polarity, but cells in the proximal region of the tissue have weak or no polarity (Fig. 4.16 A). This is because the presence of elevated auxin import in the auxin-producing minus organiser restricts the spread of auxin away from the distal end of the tissue into more proximal regions. Consequently, the distal minus organiser acts as a weak source of auxin, causing a shallow tissue-wide auxin gradient and weak polarisation of PIN (Fig. 4.16A iii, compare with Fig 4.9 A iii).

However, if the distal minus organiser region has elevated auxin import and all cells in the tissue have a background rate of auxin production, all cells may acquire proximo-distally oriented PIN polarity with elevated auxin at the distal end of the tissue (Fig. 4.16 B). This is at least partly because the presence of a background rate of auxin production, combined with auxin degradation in the plus organiser at the base, creates a proximo-distal intercellular auxin gradient, leading to distal-wards polarisation. If the background rate of auxin production is too high, or if the proximal plus organiser with elevated auxin removal rates is absent, cells in the proximal half of the tissue generate centres of polarity convergence (Fig. 4.16 C).

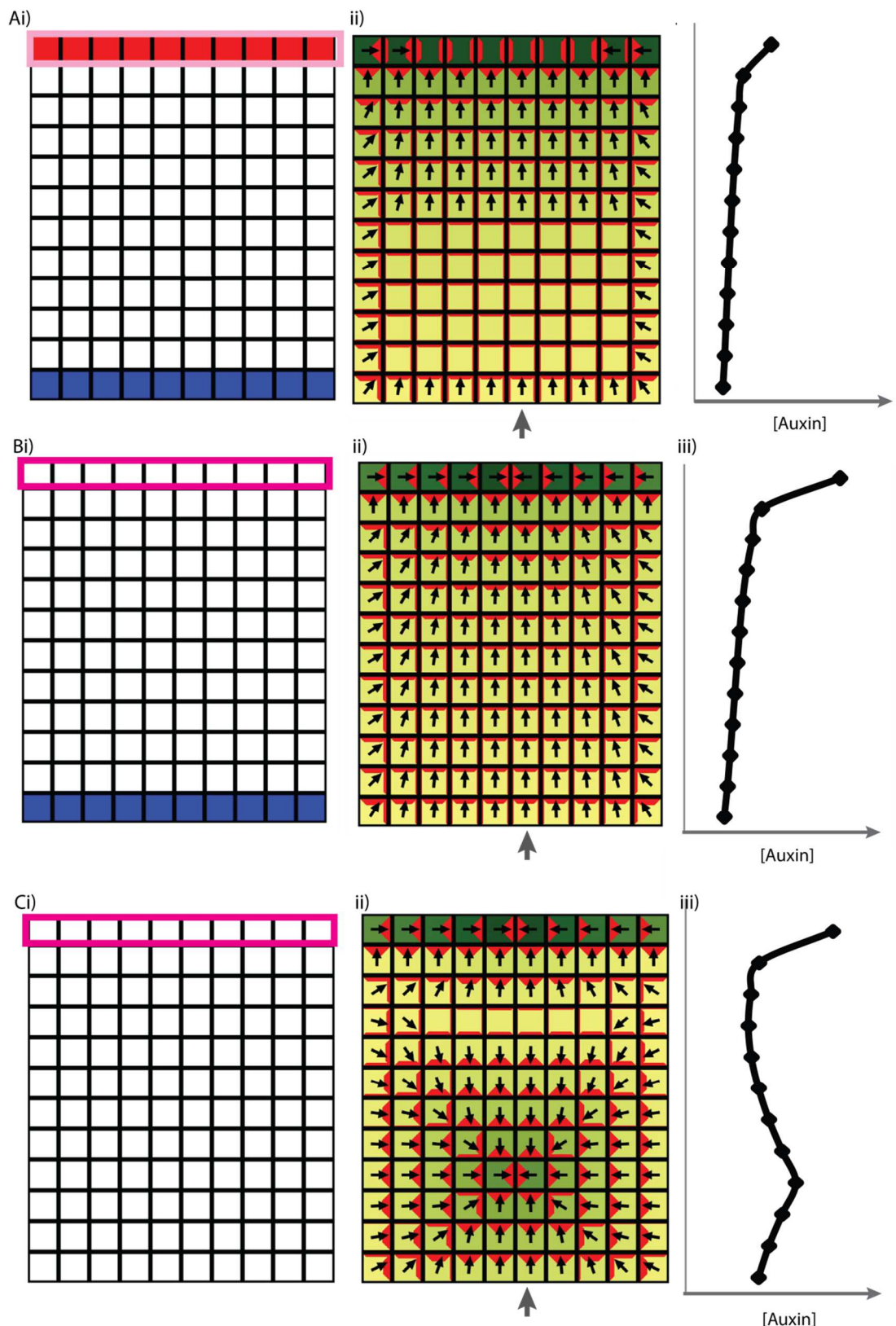


Fig. 4.16. Generation of a proximo-distal polarity field in an up-the-gradient model with elevated auxin import in the distal minus organiser.

A) If the minus organiser at the distal end has both elevated auxin production and import (red cells with pink outline in i), with no background production of auxin, and an auxin sink in the proximal file of cells (blue cells), cells near the distal end of the tissue acquire a proximo-distal PIN1 polarity, but cells in the proximal end remain unpolarised (ii). iii) Shows the concentrations of intracellular auxin for the column of cells marked by the grey arrow in ii). **B)** If the minus organiser at the distal end has elevated import (cells with pink outline in i), and the proximal file of cells has an elevated rate of auxin removal (blue cells), with a background rate of auxin production in all cells, all cells acquire a proximo-distal PIN1 polarity (ii) and auxin is elevated at the distal end of the tissue. **C)** Same as B), but without the elevated rate of auxin removal in the proximal file of cells (auxin is degraded at a background rate in all cells). In the absence of elevated auxin removal in the proximal-most file of cells, a centre of polarity convergence forms towards the proximal end of the tissue.

If a cell with elevated auxin import is added in the context of the proximo-distal polarity field generated by a proximal plus organiser with elevated auxin removal rates and a distal minus organiser with elevated auxin import, a centre of polarity convergence may be generated (Fig. 4.17 A). The minus organiser cell at the centre of convergence does not acquire a polarised PIN1 distribution because all of its neighbours have a similar intracellular auxin concentration (Fig. 4.17 ii). However, if the minus organiser with elevated auxin import is located in two or four cells, rather than in a single cell, cells close to the centre of convergence acquire highly polarised PIN1 distributions similar to what was observed experimentally (Fig. 4.17 B, C). Thus, high levels of auxin import at the tip of the leaf and at centres of PIN1 polarity convergence are not incompatible with the up-the-gradient model.

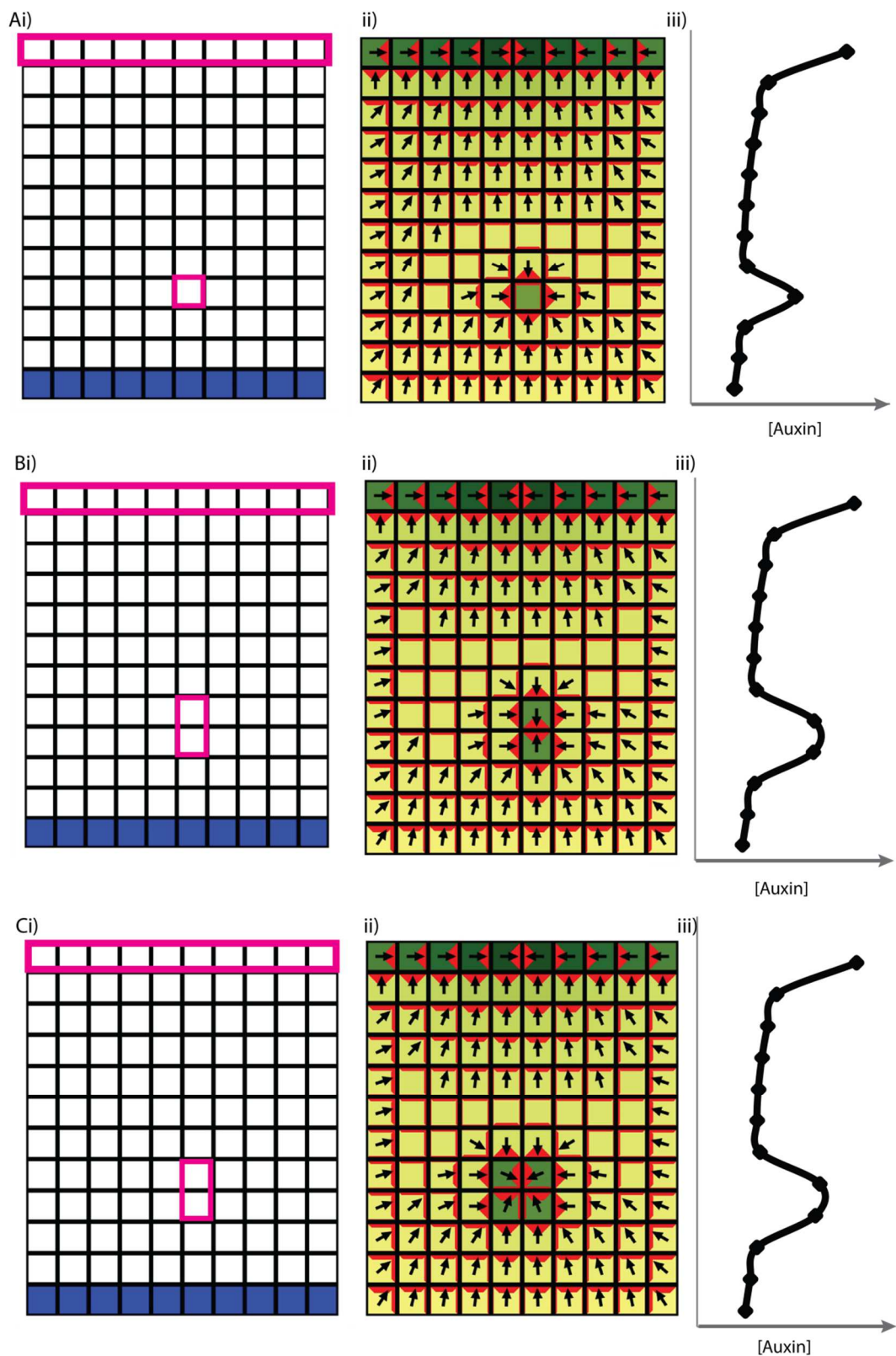


Fig. 4.17 Generation of centres of convergence in an up-the-gradient model with elevated auxin import in minus organisers

A) Generation of a centre of convergence due to addition of a minus organiser cell with elevated auxin import (isolated cell with pink outline) to an array with elevated auxin import in the distal minus organiser region (cells with pink outline) and elevated auxin removal rates in the proximal plus organiser region (blue cells). ii) Shows effect on PIN1 and auxin distribution. Note that the polarity convergence is centred on the minus organiser cell, which does not have a polarised PIN distribution. iii) Graph showing concentration of intracellular auxin for the column of cells marked with the grey arrow in ii). **B)** and **C)** Same as A), but adding the minus organiser with elevated auxin import to two and four cells, respectively, within the array (cells with pink outline in B ii and C ii).

Although both up-the-gradient and indirect cell-cell coupling models are compatible with the patterns of auxin import in WT and *kan1kan2* leaves, as determined by *AUX1* and *LAX1* expression patterns, there is an important difference between the two models: the up-the-gradient model predicts the base of the leaf acts as an auxin sink, whilst the indirect cell-cell coupling model predicts it acts an auxin source. Also, since polarities tend to point away from auxin sources in the indirect cell-cell coupling model, it is expected that if this type of model operates in the *kan1kan2* leaf, auxin production should be absent from ectopic regions of polarity convergence. Therefore, the models may be distinguished by looking at the patterns of auxin biosynthesis in wild-type and *kan1kan2* leaves.

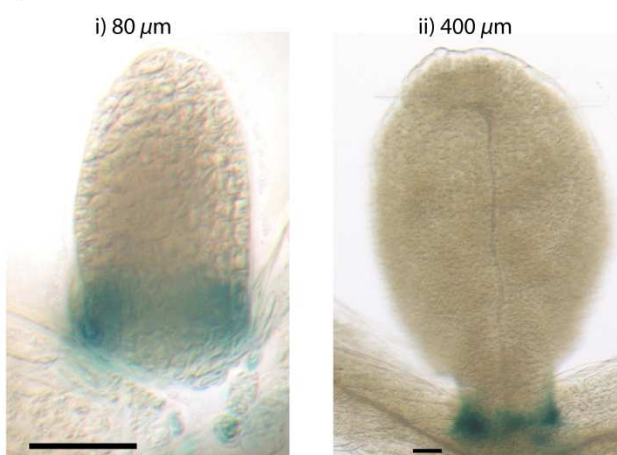
4.2.7 Patterns of auxin biosynthesis enzyme expression in WT and *kan1kan2* leaves

To distinguish between models, I looked at the expression patterns of *YUCCA* auxin-biosynthesis enzymes in WT and *kan1kan2* leaves. *A.thaliana* has six *YUCCA* genes, three of which (*YUCCA1* (*YUC1*), *YUCCA2* (*YUC2*) and *YUCCA4* (*YUC4*)) are reported to be expressed in the leaf (Wang et al., 2011). The expression of *YUC4* and *YUC2* was previously shown to be similar, and mainly restricted to sub-epidermal tissue, in WT and *kan1kan2* leaves (Wang et al., 2011). I therefore focussed on analysing the expression of *YUC1* using a *YUC1::GUS* reporter.

YUC1::GUS is expressed at the base of WT leaves, in all cell layers, including epidermal cells (Wang et al., 2011). In WT leaves of around 80 μm in width, *YUC1::GUS* expression was restricted to the proximal-most 25% of the tissue (Fig. 4.18 Ai). Expression was also detected at the base of *kan1kan2* leaves, but in a slightly larger domain. In mutant leaves of approximately 50 μm in width, GUS staining was detected throughout the proximal-most 40% of the leaf (Fig. 4.18 Bi). In slightly older *kan1kan2* leaves, of around 95 μm in width, expression was detected throughout the proximal-most third of the leaf (Fig. 4.18 Bii). WT and *kan1kan2* leaves maintained expression of *YUC1::GUS* at their base until later stages of their development (expression was still detected at the base of leaves 400-500 μm in width). (Fig. 4.18 A ii, B v).

In *kan1kan2* leaves, the expression pattern of *YUC1::GUS* changed as outgrowths developed. Before the formation of *kan1kan2* outgrowths, *YUC1::GUS* was expressed in a band, a few cells wide, running across the leaf, approximately one-third of the way from the base (Fig. 4.18 B iii, black arrow). As outgrowths emerged, the band of *YUC1::GUS* expression was at their distal base (Fig. 4.18 B iv and v, black arrow) and absent from the outgrowth tips (Fig. 4.18 B iv, black arrow head). This absence of auxin biosynthesis at emerging outgrowth tips is consistent with the indirect cell-cell coupling model which predicts that the epidermis in these regions should act as an auxin sink to allow the formation of stable centres of PIN1 polarity convergence.

A) WT *YUC1::GUS*



B) *kan1kan2 YUC1::GUS*

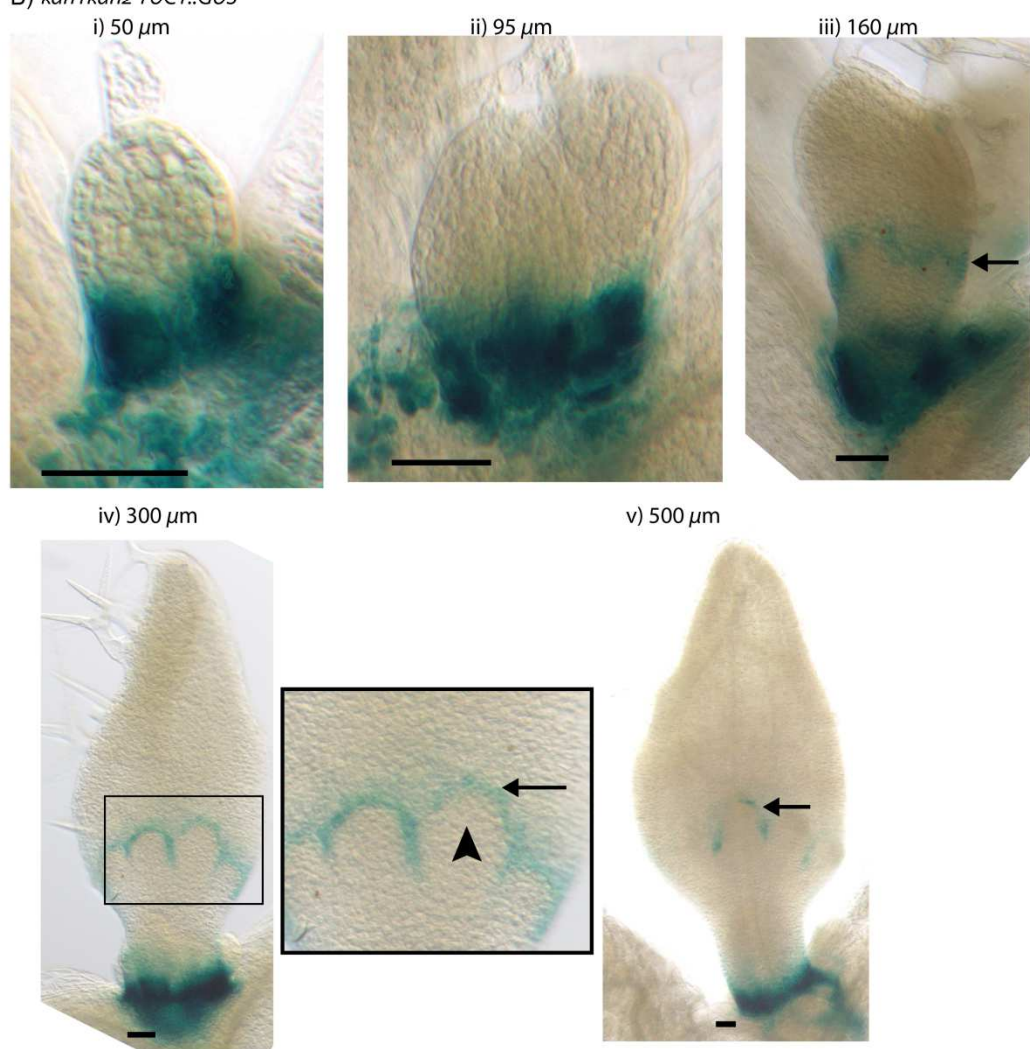


Fig. 4.18 Expression pattern of *YUCCA1::GUS* in WT and *kan1kan2* leaves.

A) Expression of *YUC1::GUS* in WT leaf primordia. **B)** Expression of *YUC1::GUS* in *kan1kan2* mutant primordia at different stages of development. Black arrows indicate the band of *YUC1::GUS* expression, which is at the distal base of outgrowths in iv) and v). Arrow heads indicate an outgrowth tip which does not express *YUC1::GUS*. Scale bars = 50 μ m. Each image is representative of those obtained for at least 6 seedlings with leaves at the developmental stages shown.

4.2.8 The pattern of auxin biosynthesis in WT and *kan1kan2* leaves in inconsistent with the up-the-gradient model

The above experiments reveal that auxin is synthesised in the epidermis at the base of the leaf, which matches a prediction of the indirect cell-cell coupling model (Fig. 4.11, Fig. 4.12). In contrast, the pattern of *YUCCA1*-mediated auxin production is not readily reconciled with the up-the-gradient model, in which the base of the leaf epidermis must act as an auxin sink for a proximo-distal polarity field to be robustly generated (Fig 4.9, Fig. 4.16). In this model, elevated auxin production in the proximal row of cells, combined with elevated auxin import in the distal row, generates a divergent polarity field (Fig. 4.19), with proximally oriented polarities in the proximal half of the tissue, and distally oriented polarities the distal half (Fig. 4.19). Cells towards the centre of the array have weak or no polarity. This polarity pattern is inconsistent with the proximo-distal *PIN1* polarity patterns observed in young WT and *kan1kan2* leaves. Thus, the pattern of *YUC1*-mediated auxin biosynthesis is difficult to reconcile with the generation of a proximo-distal polarity field in the up-the-gradient model.

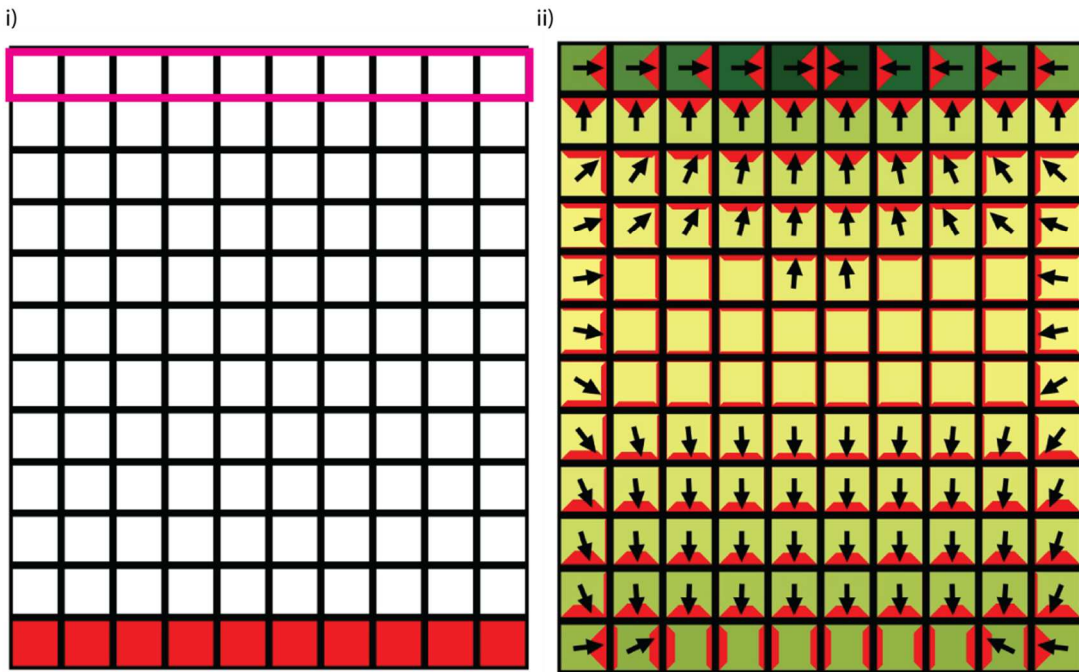


Fig. 4.19 The effect of auxin production in proximal regions of tissue in an up-the-gradient model.

In the presence of elevated auxin production in the proximal row of cells (red in i), and elevated auxin import in the distal row of cells (pink outline in i), the up-the-gradient model generates a divergent polarity field, with proximally oriented polarity in the bottom half of the tissue, and distally oriented polarity in the distal half (ii).

As *kan1kan2* outgrowths emerge, *YUC1::GUS* expression is absent from cells at the outgrowth tip, where the centre of PIN1 convergence forms, but maintained in a band at the distal base of the outgrowth (Fig. 4.18 B iv and v). To test whether this pattern of *YUC1::GUS* expression close to outgrowths is compatible with the indirect cell-cell coupling model, I ran simulations introducing elevated auxin production rates at the distal side of the minus organiser with elevated auxin import and degradation. If elevated auxin synthesis is added to a row of 3 cells on the distal side of the minus organiser, a polarity convergence, centred on the minus organiser, still forms (Fig. 4.20 A i, ii). In this implementation of the model, the band of elevated auxin synthesis acts as a plus organiser, causing polarities of neighbouring cells to point away from it, and therefore

promotes a polarity reversal in cells distal to the minus organiser. Therefore, in the indirect cell-cell coupling model, a band of cells with elevated auxin synthesis on the distal side of the minus organiser functions cooperatively with the minus organiser in the generation of a centre of convergence.

However, if elevated auxin production is added to the equivalent region in the up-the-gradient model, polarities converge towards this region instead of towards a minus organiser with elevated import (Fig. 4.20 B i, ii). This occurs if the rate of auxin production in the band of cells distal to the minus organiser is sufficiently high to outweigh the effect of elevated import in the minus organiser. In the *kan1kan2* leaf, if a PIN1 convergence formed with elevated *YUC1* expression at its centre, *YUC1::GUS* expression would be found at outgrowth tips, rather than at their distal base. Thus, the local pattern of *YUC1::GUS* expression around developing outgrowths does not support the up-the-gradient model.

In summary, the patterns of *YUC1*-mediated auxin biosynthesis, both in WT and in *kan1kan2* mutant leaves, are compatible with the indirect cell-cell coupling model, but incompatible with the up-the-gradient model.

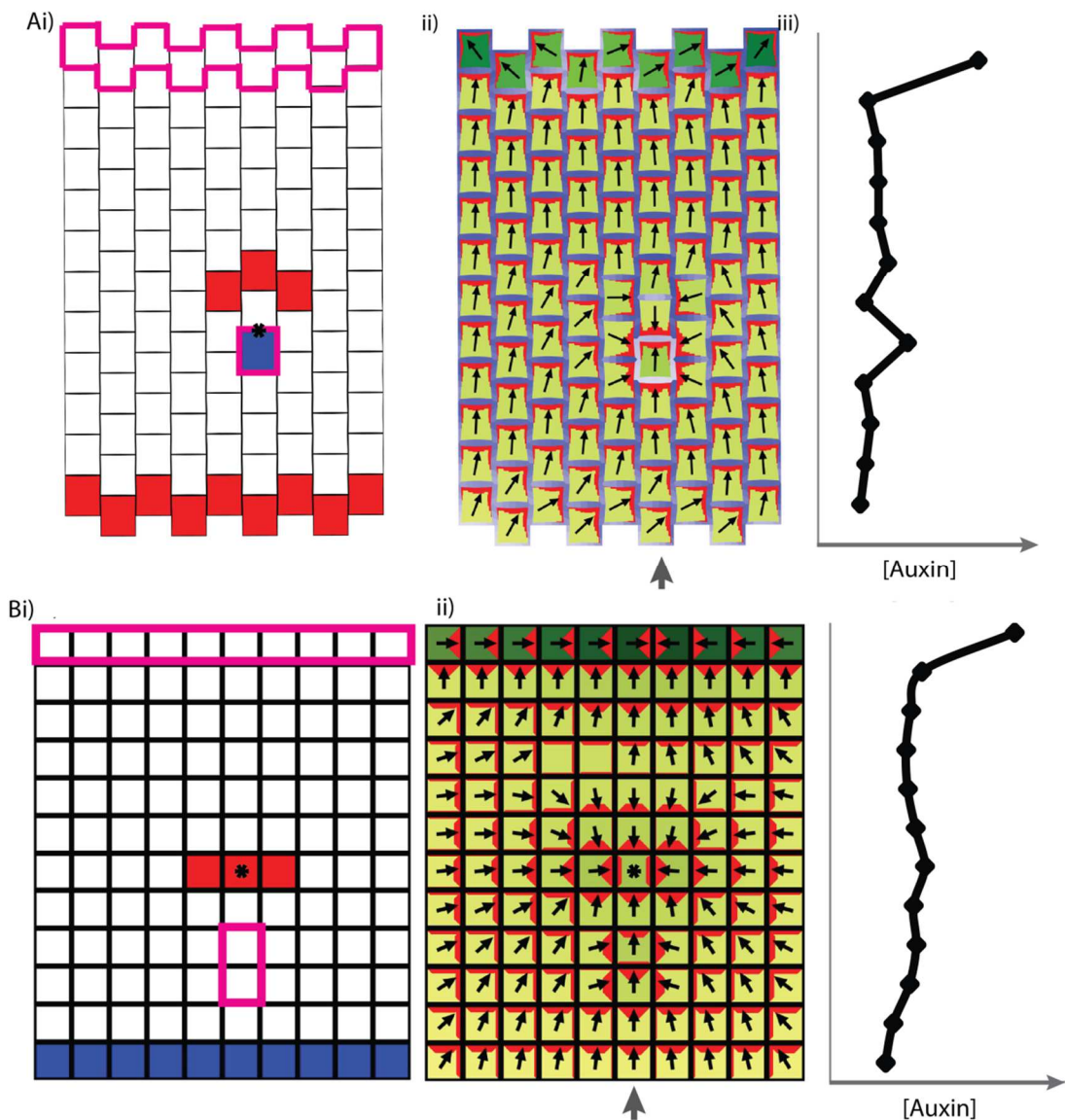


Fig. 4.20 The effect of a band of cells with elevated auxin synthesis distal to a cell with elevated import in indirect cell-cell coupling and up-the-gradient models.

A) Indirect cell-cell coupling model. Effect of adding elevated auxin production to the three isolated red cells in (i), where cells in the proximal row also have elevated auxin production (red cells) and minus organiser cells at the tip of the leaf have elevated rates of auxin import (pink cell outlines). The minus organiser cell within the array has elevated auxin removal rates and elevated auxin import (blue cell with pink outlines in (i)). ii) A centre of polarity convergence forms, centred on the cell-cell interface between the minus organiser cell and its distal neighbour (black asterisk in (i) shows position of centre of convergence relative to organiser locations). iii) Graph of intracellular auxin concentrations for the column of cells marked by the grey arrow in ii). **B)** Same as for A), but for the up-the-gradient model, where distal minus organiser cells have elevated rates of auxin import and the base of the leaf has an elevated rate of auxin degradation. Three cells with elevated auxin production are positioned at the distal side of two cells with elevated

auxin import. Note that the polarity convergence forms centred on an auxin-producing cell, rather than on the cells with high import. Black asterisks in i) and ii) indicate the centre of convergence.

4.3 Discussion

4.3.1 Models make different predictions about patterns of auxin biosynthesis, which can be used to distinguish them experimentally.

I have shown that the up-the-gradient (convergent coupling) and indirect cell-cell coupling (tandem cell-cell coupling) models make different experimentally testable predictions about patterns of auxin biosynthesis in WT and *kan1kan2* leaves. The indirect cell-cell coupling model generates cell polarities oriented away from auxin sources, towards auxin sinks. This model therefore predicts that, to generate a proximo-distal polarity field, like that seen in the epidermis of young WT and *kan1kan2* leaf primordia, auxin is synthesised at an elevated rate at the base of the leaf (Fig. 4.11). In contrast, in the up-the-gradient model, polarities point away from regions with low auxin, towards regions with high auxin. To account for the epidermal PIN1 polarity pattern, the up-the-gradient model therefore predicts that the base of the leaf acts as an auxin sink (Fig 4.9 and Fig. 4.16). This assumption was also included in a previous implementation of the up-the-gradient model to account for PIN1 polarities in the leaf margin, where, at early stages, polarities point distally as seen in the main lamina (Bilsborough et al., 2011).

Experimental observations of *YUC1::GUS* expression suggest that *YUC1*-driven auxin synthesis occurs at an elevated rate in epidermal cells at the leaf base, suggesting this region acts as an auxin source (as predicted by the indirect cell-cell coupling) rather than a sink (as predicted by the up-the-gradient model). Previous work has shown that *YUC1::GUS* is expressed at the base of WT leaves, at the sinus of serrations, and at the base of mature *kan1kan2* outgrowths on their distal side (Cheng et al., 2007; Wang et al., 2011)). However, this is the first time that a detailed

description of *YUC1::GUS* expression has been given for early stages of *kan1kan2* leaf development, showing that initially *YUC1::GUS* is expressed in a broad region at the base of these leaves. The domain of *YUC1::GUS* expression in young *kan1kan2* leaves is similar to the domain from which new outgrowths first emerge, raising the possibility that auxin biosynthesis in this region may be involved in specifying the region from which outgrowths can form. I explore this hypothesis in the next chapter.

Other members of the *YUC* family are expressed mainly in sub-epidermal cells at the leaf tip and at tips of serrations (Wang et al., 2011), suggesting that the base of the leaf is the main site of *YUC*-driven epidermal auxin synthesis. However, I cannot rule out that other auxin biosynthetic enzymes (of which there are several (Mano and Nemoto, 2012)) are expressed at high levels in other regions of the leaf, and that the leaf base is therefore not the main auxin source for the epidermis. Despite this caveat, the current experimental data suggest that an up-the-gradient mechanism does not underlie the generation of a proximo-distal PIN1 polarity field in the leaf epidermis (Table 4.1).

Experimental observation	Up-the-gradient	Indirect cell-cell coupling
Distally oriented, globally coordinated polarity field in WT and <i>kan1kan2</i> leaves with elevated intracellular auxin at leaf tip	✓	✓
Formation of stable convergence points with elevated auxin	✓	✓
Convergence point centred on a cell-cell interface, with highly polarised PIN1 in all cells closest to convergence point	✓	✓
Elevated auxin import at leaf and outgrowth tips	✓	✓
Elevated auxin production at leaf base	✗	✓
Elevated auxin production in cells distal to emerging outgrowths	✗	✓

Table 4.1. Summary of the compatibilities of up-the-gradient and indirect cell-cell coupling models with different aspects of data obtained for WT and *kan1kan2* leaves.

The up-the-gradient model was originally proposed to account for the generation of centres of PIN1 polarity convergence in the meristem, which grow to become new leaf or floral primordia (Jönsson et al., 2006; Smith et al., 2006). The apparent incompatibility of the model with *YUC1*-driven auxin synthesis at the leaf base raises the question of whether *YUC1* is expressed at the leaf-meristem boundary at early stages of leaf initiation in the meristem. If it is, then the up-the-gradient model predicts that polarities would point towards boundary regions. Contrary to this prediction, PIN1 polarities have been observed to diverge from boundary regions in the meristem (Heisler et al., 2005). If *YUC1* is expressed in boundary regions, then the divergent polarity in this region would support the indirect cell-cell coupling or flux-based models. A detailed analysis of

expression patterns of auxin biosynthetic enzymes in the shoot apical meristem should therefore be included in future work to distinguish between models for phyllotaxis.

The *YUC1::GUS* expression pattern in the *kan1kan2* leaf also suggests that the up-the-gradient model may not underlie formation of centres of polarity convergence in this system. *YUC1::GUS* is ectopically expressed in cells at the distal boundary between each outgrowth and the main lamina (Fig. 4.18 and Wang et al., 2011) and, in support of a functional role of *YUC1*, *kan1kan2yuc1yuc2yuc4* mutants do not develop ectopic outgrowths (Wang et al., 2011). Auxin biosynthesis in the region distal to developing outgrowths can be accounted for with the indirect cell-cell coupling model, where it promotes polarity reorientation, but is difficult to reconcile with the up-the-gradient model, where it can disrupt the formation of a polarity convergence centred on a more proximal minus organiser cell (Fig. 4.20).

4.3.2 Predictions of the indirect cell-cell coupling model

A prediction of the indirect cell-cell coupling model is that regions with low extracellular auxin, which may be generated through elevated rates of auxin import, cause the generation of centres of PIN1 polarity convergence. In support of the model, I showed that the genes encoding auxin importers, *AUX1* and *LAX1*, are expressed at the tips of outgrowths, that *LAX1* expression precedes outgrowth development, and that the four *AUX/LAX* genes function redundantly in outgrowth generation. However, it is possible that the expression of *AUX/LAX* genes at the tips of outgrowths promotes their growth independently from generation of centres of PIN1 polarity convergence. For example, expression of *AUX1* and *LAX1* might be induced after the formation of centres of PIN1 convergence and promote local accumulation of auxin, causing local differences in auxin-controlled growth rates. Future experiments should therefore test whether the reduction in the number of outgrowths in *kan1kan2aux1lax1lax2lax3* mutants correlates with a reduction in

the number of centres of PIN1 convergence in this background. Some meristems of *aux1/lax1/lax2/lax3* quadruple mutants were previously shown to have a loss of emerging primordia (Bainbridge et al., 2008). Consistent with a role of *AUX/LAX* genes in the formation of centres of PIN1 convergence, meristems lacking primordia outgrowths also lacked centres of PIN1 convergence (Bainbridge et al., 2008).

The finding that *kan1kan2aux1/lax1/lax2/lax3* mutants still form some outgrowths, albeit much fewer than in WT, suggests that at least some centres of PIN1 convergence are still able to form in this background. This seems to contradict the indirect cell-cell coupling model, which predicts that auxin import plays an important role in the generation of centres of convergence. However, several other processes could function redundantly with *AUX/LAX*-mediated auxin import to generate minus organiser regions with low extracellular auxin. As observed in the shoot apical meristem, centres of PIN1 convergence in the *kan1kan2* leaf epidermis form concurrently with sub-epidermal strands of cells with elevated PIN1 expression ((Bayer et al., 2009) chapter 6). Within these strands, PIN1 is oriented away from the epidermis, towards the centre of the leaf. Consistent with the indirect cell-cell coupling model, these PIN1 strands could allow removal of auxin from the epidermis, causing a local depletion of extracellular auxin and a polarity reorientation. Indeed, in the indirect cell-cell coupling model, a combination of locally elevated auxin removal (which could either be through auxin degradation, or through removal into another tissue layer) functions cooperatively with elevated auxin import to cause centres of PIN1 convergence (Fig. 4.12 B and C). It is possible that in the *kan1kan2aux1/lax1/lax2/lax3* background, some centres of convergence form through the effect of sub-epidermal PIN1 strands without locally elevated auxin import.

Support for redundant functions of auxin import and sub-epidermal PIN1 strands in the formation of epidermal centres of PIN1 convergence comes from a study on the shoot apical meristem of

A.thaliana. It was shown that meristems that express functional PIN1 in the epidermis, but not in the sub-epidermis, have WT patterns of phyllotaxis. However, if AUX/LAX gene function is also lost from this context, then phyllotaxis and organ initiation is disrupted, presumably due to disruption of centres of polarity convergence (Kierzkowski et al., 2013).

In addition to expression of AUX/LAX auxin importers and formation of sub-epidermal PIN1 strands, there are other factors that could contribute to minus organiser function by reducing extracellular auxin levels. For example, locally elevated intracellular auxin concentrations may increase auxin influx rates through effects on cell wall pH (Steinacher et al., 2012). Auxin is a weak acid, and its ability to move passively from the cell wall (apoplast) into cells depends on what fraction of apoplastic auxin exists in an un-dissociated form with neutral charge (Rubery and Sheldrake, 1974). There is evidence that intracellular auxin activates plasma membrane proton pumps, which acidifies the cell wall, and increases the proportion of apoplastic auxin which is un-dissociated and can therefore passively enter cells (Hager, 2003; Rayle and Cleland, 1992; Steinacher et al., 2012). This could contribute to minus organiser function (low extracellular auxin) in regions with high intracellular auxin.

Another possibility is that the expression of auxin efflux carriers other than PIN1 decreases in cells hypothesised to be minus organisers. *PIN3* is expressed in epidermal cells of leaf primordia (Guenot et al., 2012), but its expression pattern in cells at centres of PIN1 convergence formed during *kan1kan2* outgrowth, or leaf serration development, has not been described. Also, the expression of members of the PCP/MDR/ABCB family of auxin transporters could change in cells hypothesised to be minus organisers. Two members of this family (PGP1 and PGP19) promote auxin export and function redundantly with PIN1 in leaf development and organ initiation (Blakeslee et al., 2007; Petrášek and Friml, 2009), while another member (PGP4) promotes auxin import (Terasaka et al., 2005). However, detailed expression patterns of these transporters during

the formation of new outgrowths (in meristems, during serration development or in *kan1kan2* leaves) have not been described. Future tests of the indirect cell-cell coupling model should involve investigation of these possible contributors to minus organiser function. Another possibility would be to carry out a mutant screen in the *kan1kan2aux1lax1lax2lax3* background to identify additional mutations which suppress the formation of ectopic outgrowths.

4.3.3 Relevance of *kan1kan2* outgrowth development for the formation of organs in the shoot apical meristem.

The experimental observations made in the *kan1kan2* mutant system in this study are similar to findings from the shoot apical meristem, suggesting that ectopic outgrowth formation occurs via a similar developmental pathway to organ initiation in WT plants. As seen in the meristem, the development of *kan1kan2* outgrowths is preceded by centres of PIN1 polarity convergence with locally elevated activity of the DR5 auxin responsive promoter (Heisler et al., 2005). Expression of *AUX1* and *LAX1* at the tips of *kan1kan2* outgrowths is also similar to their expression at sites of emerging primordia in the shoot apical meristem (Bainbridge et al., 2008). Finally, the finding that auxin importers contribute the development of ectopic outgrowths is consistent with *aux1lax1lax2lax3* mutants having irregular phyllotactic angles, transient arrest of organ initiation, and formation of fewer centres of PIN1 polarity convergence than in WT (Bainbridge et al., 2008).

However, there are some differences between the two systems. In *kan1kan2* leaves, PIN1 centres of convergence emerge from a simpler PIN1 polarity field compared with that of the shoot apical meristem (de Reuille et al., 2006; Heisler et al., 2005). This means that the change in the polarity field needed to generate a centre of convergence differs in the two cases, which could imply a different underlying mechanism. Future work should address whether the ICP-based model can account for the PIN1 polarity reorientations seen during phyllotaxis in addition to those seen in *kan1kan2* leaves.

4.3.4 Polarity reorientations are a common feature of outgrowth development

Previous studies have shown a strong correlation between PIN1 polarity reorientations, the generation of auxin maxima, and the development of new shoot and root primordia (Benkova et al., 2003; Heisler et al., 2005; Reinhardt et al., 2003). Here, I show that centres of PIN1 polarity convergence and auxin accumulation predict sites of ectopic outgrowths in mutant leaf tissue. The correlations observed during outgrowth development in WT and ectopic contexts suggest that reorientation of PIN1, and auxin accumulation, play an important role in the generation of new outgrowths, regardless of the developmental context. However, how PIN1 reorientations cause the development of new outgrowths is unclear.

One hypothesis is that PIN reorientations generate new outgrowths by locally concentrating auxin, which itself is sufficient to trigger organ outgrowth (Benkova et al., 2003; Reinhardt et al., 2000; Reinhardt et al., 2003). In support of this hypothesis, *pin1* mutants, and plants treated with the auxin transport inhibitor NPA, fail to form auxin maxima and generate naked meristems devoid of outgrowths (Reinhardt et al., 2000; Reinhardt et al., 2003). Local application of auxin to these naked meristems is sufficient to restore the formation of outgrowths, which develop from the sites of auxin application (Reinhardt et al., 2000). This suggests that the only function of PIN-mediated auxin transport is to locally concentrate auxin, which is then sufficient to generate primordia.

Another, but not mutually exclusive, hypothesis is that the reorientation of cell polarities, promotes outgrowth formation partly independently from its effect on auxin distributions, by locally reorienting the principle orientations of anisotropic growth. In this case, the polarity field marked by PIN1 would be used to direct the principle direction of growth of the tissue (Green et al., 2010; Kennaway, 2011; Kuchen et al., 2012; Sauret-Gueto et al., 2013). A local reorientation of

the polarity field during the generation of centres of PIN1 convergence would therefore cause the local direction of anisotropic growth to deviate from the principle direction of growth of the surrounding tissue, which can contribute to emergence of an outgrowth (Kennaway, 2011). This hypothesis seems contradictory to the finding that local auxin application can promote the formation of outgrowths in a *pin1* mutant background (where polarity fields may be disrupted). However, redundant mechanisms of polarity generation, which could respond to auxin application, probably exist in the *pin1* mutant background, as these mutants still develop leaves, suggesting that polar auxin transport still generates auxin maxima at the flanks of the vegetative meristem (Guenot et al., 2012). The hypothesis that growth is specified relative to an underlying polarity field is supported by a correlation between PIN1 polarity fields and the polarity fields required in models that account for experimentally observed patterns of anisotropic growth in *A.thaliana* leaf and petal primordia (Kuchen et al., 2012; Sauret-Gueto et al., 2013). In chapter 6 I will explore how changes in the PIN1 polarity field in the *kan1kan2* leaf could be linked with the specification of growth of *kan1kan2* outgrowths.

4.4 Methods

4.4.1 *A.thaliana* mutant and transgenic lines

4.4.1.1 Marker lines and their introduction into the *kan1kan2* background

All *kan1kan2* mutants carry *kan1-2* and *kan2-1* alleles in the Landsberg (Ler) background, as described by Eshed et al., 2001. All marker lines were originally in the Col-0 background and were described previously (*PIN1::PIN1:GFP* (Heisler et al., 2005); *DR5::GFP* (Benkova et al., 2003); *LAX1::GUS* (Bainbridge et al., 2008); *YUCCA1::GUS* (Cheng et al., 2006)). The *AUX1::AUX1:YFP* line corresponds to the *AUX1-YFP116* construct described by (Swarup et al., 2004). The plasma-membrane RFP marker is a fusion between plasma-membrane localised aquaporin, PIP2A, and

the mCherry fluorescent protein (Nelson et al., 2007). All images of marker construct expression in WT were obtained using the original marker lines in the Col-0 background.

In contrast to single *kan1* and *kan2* mutants, *kan1kan2* double mutants are sterile. To generate stocks of seeds that could be used in experiments to analyse marker constructs in the *kan1kan2* background, all reporter constructs were introduced into the *kan1kan2+/-* background by crossing (*kan1kan2+/-* plants are fertile). The offspring of these *kan1kan2+/-* plants segregated for *kan1kan2* double mutants with the reporter constructs which could be selected and used in experiments.

To generate *kan1kan2+/-* plants with the desired reporter constructs, the original reporter lines (in the Col-0 background) were crossed with *kan1kan2+/-* mutants. F1 offspring of this cross were selfed, and from F2s, *kan1kan2+/-* plants with the presence of the reporter constructs were selected. Plants with the desired marker constructs were identified by sowing F2s on plates containing antibiotics (*PIN1::PIN1:GFP*, *LAX1::GUS*, *YUCCA1::GUS* and *AUX1::AUX1:YFP* confer resistance to Kanamycin, and were selected for by growing on plates containing 50 µg/ ml Kanamycin) and through screening for the presence of markers using confocal microscopy. Plants with the desired markers were transferred to soil and those that were *kan1kan2+/-* mutants were identified based on their fruit phenotype, which is intermediate between *kan1* and *kan1kan2* mutants and displays abnormally shaped siliques with ectopic outgrowths (Eshed et al., 2001). In the offspring of *kan1kan2+/-* plants with the desired marker constructs, *kan1kan2* seedlings were identified based on their upwardly curled cotyledon phenotype and those with the presence of desired marker constructs were selected for experiments.

4.4.1.2 Introduction of aux/lax mutant alleles into the kan1kan2 background and quantification of outgrowth number in kan1kan2aux/lax mutants

To generate *kan1kan2aux1lax1*, *kan1kan2aux1lax1lax2* and *kan1kan2aux1lax1lax2lax3* mutants, *aux1lax1lax2lax3* mutants in the Col-0 background (Bainbridge et al., 2008) were crossed with *kan1kan2+/-* mutants in the Ler background. This generated an F1 in which plants were either heterozygous for all 6 genes, or homozygous for WT copies of *KAN2* and heterozygous for the other 5 genes. F1 plants were selfed and F2 progenies, which segregated for all alleles, were used to identify plants that had the following genotypes: *kan1kan2+/-aux1lax1*; *kan1kan2+/-aux1lax1lax2*; *kan1kan2+/-aux1lax1lax2lax3* and *kan1kan2+/-aux1lax1+/-lax2lax3* (the screening method is described below). The former three lines were then selfed, and their offspring (the F3 from the original cross) were sown on soil (see plant growth conditions (4.4.3)) and screened for the following genotypes: *kan1kan2aux1lax1*, *kan1kan2aux1lax1lax2* and *kan1kan2aux1lax1lax2lax3*. For at least 10 plants of each of these genotypes, the number of outgrowths per leaf was counted for all the rosette leaves (at least 10) using a Leica M205C stereomicroscope.

The *kan1kan2+/-aux1lax1+/-lax2lax3* plants identified from the F2 were used to determine whether the loss of outgrowths in *kan1kan2aux1lax1lax2lax3* mutants segregated with a loss of *AUX/LAX* gene function (rather than with an unknown modifier from the Col-0 background). The selfed progeny of these plants segregated for mutations in *kan2* and *lax1*, but were homozygous for mutant alleles of *KAN1*, *AUX1*, *LAX2* and *LAX3*. In this family, which was grown on soil, I identified 156 *kan1kan2* double mutants, based on their overall leaf and flower phenotypes (Eshed et al., 2004). I then classified these plants into those that developed many outgrowths (120) and those which had a reduced number and size of outgrowths (36). To check whether the reduction in the number of outgrowths segregated with the *lax1* mutation, I used PCR-based

genotyping to determine the *LAX1* genotype of the 36 plants with few outgrowths and 40 of their siblings that had many outgrowths.

4.4.1.3 Screening for aux/lax mutants

Mutant alleles of *aux1* were selected for by growing plants on plates containing 0.1 μ M 2,4-D (SIGMA) and screening for seedlings with auxin resistant root growth (Marchant and Bennett, 1998). *lax1*, *lax2* and *lax3* alleles were screened for by PCR-based genotyping to detect the presence or absence of the dSpm T-DNA insertion in each gene, as described by Bainbridge et al., 2008. The primers used are detailed below in Table 4.2:

Allele detected	Forward primer (5' -3')	Reverse primer (5' -3')
<i>LAX1</i>	LAX1 FWD: ATATGGTTGCAGGTGGCACA	LAX1 RVS: GTAACCGGCAAAAGCTGCA
<i>lax1</i>	LAX1 FWD	SPM RVS: AAGCACGACGGCTGTAGAATAG
<i>LAX2</i>	LAX2 FWD: ATGGAGAACGGTGAGAAAGCAGC	LAX2 RVS: CGCAGAAGGCAGCGTTAGCG
<i>lax2</i>	LAX2 FWD	SPM RVS
<i>LAX3</i>	LAX3 FWD: TACTCACCGGAGGCCACCA	LAX3 RVS: TGATTGGTCCGAAAAAGG
<i>lax3</i>	LAX3 FWD	SPM RVS

Table 4.2. Primers used to detect the presence of WT and mutant alleles of *LAX1*, *LAX2* and *LAX3*.

4.4.2 Genotyping

DNA was extracted by placing a piece of leaf tissue of approximately 1cm² in an Eppendorf tube and disrupting the tissue manually using a micropesle. 500µl of DNA extraction buffer (200mM Tris HCl pH 7.5; 150 mM NaCl; 25mM EDTA pH8; 0.5% SDS) was added to the disrupted tissue and samples were then centrifuged for 5 minutes at 14, 000 g. 400 µl of supernatant was removed into a new tube, 400 µl of propanol was added to the supernatant and samples were mixed by inverting several times. Samples were incubated at room temperature for 20 minutes. The samples were then centrifuged for 20 minutes at 14, 000 g. After this step, a white DNA pellet was visible, and the supernatant was discarded. The DNA pellet was washed by adding 500 µl of 70% (v/v) ethanol, which was left in Eppendorf tubes for 2 minutes and then removed and discarded. DNA pellets were left to air dry for approximately 20 minutes until all the ethanol had evaporated. DNA pellets were then re-suspended in 25 µl of Buffer EB elution buffer (Quiagen) and stored at -20°C until required for use.

PCRs were performed using Taq PCR core kit (Qiagen). Each PCR was performed in a volume of 10 µl, with 5.7 µl of water, 1 µl 10x PCR Buffer, 1 µl 1mM dNTPs, 0.6 µl 5µM forward primer, 0.6 µl 5 µM reverse primer, 0.1 µl Taq polymerase (5 units/ µl) and 1 µl DNA extracted as described above.

PCR reactions were performed in a thermocycler using the following conditions: 5 minutes at 94°C, followed by 35 cycles of: 30 seconds at 94°C, 30 seconds at 55°C and 1 minute at 72°C; followed by 5 minutes at 72°C.

4.4.3 Plant growth conditions

Prior to sowing for confocal imaging experiments, *A.thaliana* seeds were sterilised in eppendorfs using 1 ml 2.5 % (v/v) sodium hypochlorite for 4 minutes, followed by 1 ml 70 % (v/v) ethanol for 1 min. Seeds were then rinsed 4 times with 1 ml sterile water and sown on plates containing MS agar medium (0.8 % (w/v) agar, 1x Murashige and Skoog salt mixture, 1 % (w/v) sucrose, 100 μ g/ml inositol, 1 μ g / ml thiamine, 0.5 μ g / ml pyridoxin, 0.5 μ g / ml nicotinic acid, 0.5 μ g/ ml MES (2-(*N*-morpholino)ethanesulfonic acid), pH 5.7). The seeds were stratified in the dark at 4°C for 72 hours and were then transferred to a growth room and grown at 20°C with 16 hr light, 8hr dark cycles.

kan1kan2 plants carrying *aux/lax* mutant alleles were sown on soil prior to characterisation of their phenotype. Seeds were stratified directly (without sterilisation) and then sown in John Innes Centre *A.thaliana* Soil Mix (Levington F2 compost with Intercept and grit at a 6:1 ratio) and were grown under long-day conditions (16 h light and 8 h dark) in a glasshouse, supplemented with artificial light, at approximately 22°C.

4.4.4 Confocal imaging of fluorescent markers

4.4.4.1 Tracking

For tracking experiments using *kan1kan2* mutants, seedlings were first grown on plates until 4 days after stratification. Seven seedlings were then transferred into a tracking chamber (Sauret-Gueto et al., 2012) where they were kept for the duration of the imaging experiment. During this period, there was a constant flow of liquid media (1/4 strength Murashige and Skoog, 0.75 % sucrose, 1.1 μ g / ml MES, pH 5.8) at 1 μ l / s through the growth chamber. Seedlings in the chamber were imaged using a Zeiss EXCITER Laser Confocal Microscope every 6 to 12 hours (times are

provided for specific experiments in figure legends). To image GFP and YFP markers, a 488-nm line of an argon ion laser was used. Emitted light was filtered through a 500-550-nm band-pass filter. To image RFP markers, a 543 nm helium-neon laser was used and emitted light was filtered using a 560-615-nm band-pass filter. A 40x oil objective was used for all experiments. Between imaging, the chamber containing seedlings was kept at 20°C, with 16 hr light, 8hr dark cycles.

Confocal z-stacks were converted into individual PNG images using Bioformats converter (<http://cmpdartsrv3.cmp.uea.ac.uk/wiki/BanghamLab/index.php/BioformatsConverter>). Z-stacks of PNG images were then rendered in 3D using Volviewer (<http://cmpdartsrv3.cmp.uea.ac.uk/wiki/BanghamLab/index.php/VolViewer#Download>). All snapshots shown in figures were taken from Volviewer.

4.4.4.2 Confocal snapshots

In confocal imaging experiments that were performed without tracking, seedlings were mounted in water on microscope slides and a coverslip was placed on top of samples. Confocal images were obtained and processed as described above.

4.4.5 GUS staining

Before GUS staining, seedlings were grown on plates as described in 4.4.3.

4.4.5.1 GUS staining with wax embedding

Seedlings between 5 and 12 DAS were removed from plates and pre-fixed by introducing them into 20ml glass vials containing 90% (v/v) ice cold acetone. Samples were incubated on ice for 20 minutes, the acetone was removed and samples were washed by adding 50mM phosphate buffer for 5 minutes. The phosphate buffer was then replaced by GUS staining solution [(Sessions et al., 1999), 50mM Sodium Phosphate buffer, 10mM potassium ferrocyanide, 10mM potassium

ferricyanide, 0.2% Triton X-100, 1 mM X-Gluc] which was vacuum infiltrated into samples for 5 minutes. Samples were then incubated overnight at 37°C in the dark. GUS staining solution was removed, and samples were passed through an ethanol series, with 30 minutes each in 20%, 35% and 50% (v/v) ethanol. Samples were incubated for 30 minutes in FAA in 70% ethanol (10% (v/v) formaldehyde, 70% (v/v) ethanol, 5% (v/v) acetic acid). Samples were then washed in 70% (v/v) ethanol, and washed twice for 10 minutes in 90% (v/v) ethanol. Samples were incubated in 0.1% (w/v) Eosin in 100% ethanol for 2 hours at room temperature, followed by overnight incubation at 4°C. Eosin solution was removed, and samples were washed twice for 1.5 hours in 100% ethanol. Samples were then incubated in the following solutions: 2 x 20 minutes in 25% (v/v) HistoClear, 75% ethanol; 2 x 20 minutes in 50% (v/v) HistoClear, 50% ethanol; 2x 20 minutes in 75% (v/v) HistoClear, 25% ethanol; 4 x 15 minutes in 100% HistoClear.

Samples were embedded for 3.5 hours in 50% (v/v) melted paraplast, 50% HistoClear at 60°C (in glass vials), then transferred to 100% paraplast and left overnight at 60°C. Paraplast wax was changed 5 times, at 60°C. Samples were mounted in paraffin blocks using a Tissue-Tek TEC 5 embedding console from Sakura. Samples were sectioned, (12 μ m sections) and sections were mounted and affixed to poly-L-lysine sides (Thermo Scientific). Slides were washed 3 times for 3 minutes with histoclear and then Entellan and a coverslip were used to mount samples. The Entellan was left to dry overnight and then samples were imaged using a Leica M205C stereo microscope.

4.4.5.2 GUS staining without wax embedding

Seedlings between 5 and 12 DAS were removed from plates, and added to GUS staining solution [50mM Sodium Phosphate buffer; 3mM potassium ferrocyanide; 3mM potassium ferricyanide; 0.2% Triton X-100; 1 mM X-Gluc]. The solution was vacuum infiltrated for 5 minutes, and then

samples were incubated at 37 °C in the dark overnight. Then samples were passed through an ethanol series of 20%, 30%, 50%, 70%, (v/v) ethanol. Samples were mounted on slides (in 70% (v/v) ethanol) and imaged using a Leica M205C stereo microscope.

Where indicated in figure legends, samples were treated with chloral hydrate [50% w/v chloral hydrate in 40% glycerol] overnight at room temperature before imaging. In this case, samples were washed in water after the GUS staining step and then chloral hydrate solution was added. Following the overnight incubation, samples were mounted in chloral hydrate.

4.4.6 Propidium iodide (PI) staining of *kan1kan2* leaves.

Leaves were removed from plants and placed into 10% (v/v) acetic acid, 50% (v/v) methanol solution and kept at 4°C overnight. The acetic acid /methanol solution was removed and the samples were washed twice with water. The samples were dehydrated with two washes each in 40% (v/v) ethanol, 60% (v/v) ethanol and then 80% (v/v) ethanol. The samples were then boiled in 80% (v/v) ethanol at 80°C for 2-10 minutes in a water bath. Samples were then rehydrated with two washes each in 60% (v/v) ethanol, 40% (v/v) ethanol, 20% (v/v) ethanol, and water. Samples were left in water for 10 minutes and then treated with alfa-amylase [3 mg of alpha-amylase (SIGMA) in 10 ml of 20mM phosphate buffer (pH 7), 2 mM NaCl, 0.25 mM Ca₂Cl] overnight at 37°C. The next day, samples were washed three times with water and then treated with 1% periodic acid [1% in solution from SIGMA] (an oxidising agent) for 40 minutes at room temperature. The periodic acid was removed and samples were washed twice with water. PI staining solution [333 mM sodium metabisulphite, 0.5M HCl, 148 µM PI] was added and incubated for 1-2 hours at room temperature until the material appeared pink in colour. PI staining solution was then removed and the samples were washed twice with water. Samples were then imaged using OPT.

4.4.7 OPT imaging

OPT imaging was performed as described by Lee et al., 2006 and Sharpe et al., 2002. Following PI staining, plants were embedded in 1% low melting point agarose and embedded samples were kept in methanol overnight to dehydrate. To clear the agarose before scanning, the methanol was replaced with 2 parts (v/v) Benzyl Benzoate, 1 part Benzyl Alcohol and samples were left for 12 hours until almost transparent. A prototype OPT device was used to image embedded leaves (Lee et al., 2006; Sharpe et al., 2002). A 20-W halogen lamp connected to the OPT device was used to collect visible light transmission images. Images were reconstructed into png slices and visualised in 3D using *VolViewer*.

4.4.8 Computational models

Computational models were implemented essentially as described previously (in chapter 2 for the indirect cell-cell coupling model, and in chapter 3 for the up-the-gradient model). However, in this chapter I use square rather than hexagonal cell geometries and, in the indirect cell-cell coupling model, I introduce an explicit representation of PIN which was not included in previously described implementations. I describe the details of these differences below and, for each simulation described in the main text, I provide parameter values and any specific implementation details.

4.4.8.1 *Indirect cell-cell coupling*

In all simulations of indirect cell-cell coupling in this chapter, rectangular cells with regular geometries are used. In these simulations, each long edge of the cell is 17.3 μm , and each short edge of the cell is 15 μm . There are 6 membrane and cell wall compartments for each long edge, each with an associated length of 2.89 μm , and there are 5 membrane and cell wall compartments for each short edge, each with an associated length of 3 μm . The area of each

cytoplasmic compartment is $260 \mu\text{m}^2$. Apart from these differences in geometry, the cell wall graph used to simulate intracellular partitioning is as described in chapter 2. Unless stated below, all equations and parameter values were the same as described in chapter 2 (Table 2.1).

In the simulations presented in this chapter, I explicitly represent PIN and assume that PIN is produced and degraded in cytoplasmic compartments, and is recruited to the membrane by the A^* polarity component. The rate of auxin efflux from the cytoplasm into a cell wall compartment is assumed to depend on the concentration of PIN in the intervening membrane compartment. The system is initialised with a default concentration of PIN in the cytoplasmic compartment of all cells

$$\text{PIN}(t = 0) = c_{\text{PIN}} \quad (4.1)$$

where $\text{PIN}(t=0)$ is the initial concentration of PIN in each cytoplasmic compartment and c_{PIN} is the default initial concentration of PIN, both with units of $\text{A}_u/\mu\text{m}^2$. In all simulations, c_{PIN} is $0.003 \text{ A}_u/\mu\text{m}^2$.

The rate of change of PIN concentration in a given membrane compartment depends on default binding of PIN from the cytoplasm to the membrane, plus default unbinding from the membrane into the cytoplasm. It is also assumed that A^* in a given membrane compartment promotes the binding of PIN to that membrane compartment and that PIN1 can diffuse between adjacent membrane compartments of the same cell. The equation describing the rate of change of PIN concentration in a given membrane compartment is:

$$\frac{\partial \text{PIN}}{\partial t} = (\rho_{\text{PIN}} + \tau A^*) \text{PIN}_c - \mu_{\text{PIN}} \text{PIN} + D_{\text{PIN}} \nabla^2 \text{PIN} \quad (4.2)$$

where PIN is the concentration of PIN in the focal membrane compartment, with units of $A_u/\mu\text{m}$ and PIN_{1c} is the concentration of PIN in the cytoplasmic compartment of the same cell as the focal membrane compartment, with units of $A_u/\mu\text{m}^2$. ρ_{PIN} is the default binding rate of PIN to the membrane, with units of $\mu\text{m}/\text{s}$, and τ is a constant describing the rate at which membrane-bound A^* promotes the binding of PIN to the membrane, with units of $\mu\text{m}^2/A_u\cdot\text{s}$. A^* is the concentration of the A^* polarity component in the focal membrane compartment, with units of $A_u/\mu\text{m}$. μ_{PIN} is the default unbinding rate of PIN from the membrane into the adjacent cytoplasmic compartment, with units of $/\text{s}$. D_{PIN} is the diffusion constant of PIN in the membrane, with units of $\mu\text{m}^2/\text{s}$.

In all simulations where PIN is explicitly represented, ρ_{PIN} is $0.03\ \mu\text{m}/\text{s}$, τ is $2\ \mu\text{m}^2/A_u\cdot\text{s}$, μ_{PIN} is $0.004\ /\text{s}$ and D_{PIN} is $0.1\ \mu\text{m}^2/\text{s}$ (the same as the diffusion rate for A^* and B^* polarity components in the membrane).

The corresponding equation describing the rate of change of PIN concentration for a given cytoplasmic compartment is:

$$\frac{\partial PIN_c}{\partial t} = \frac{-1}{R_c} \sum_{n \in N(c)} l_n ((\rho_{PIN} + \tau A^*_{n}) PIN_c - \mu_{PIN} PIN_n) \quad (4.3)$$

Where PIN_c is the concentration of PIN in the focal cytoplasmic node and PIN_n is the concentration of PIN in the membrane compartment n , in the neighbourhood of the cell c ($N(c)$). R_c is the area of the cytoplasmic compartment and l_n is the length of the n th membrane compartment. ρ_{PIN} , τ and μ_{PIN} are as described above in equation (4.2). A^*_{n} is the concentration of A^* in the membrane compartment n .

In all simulations with an explicit representation of PIN, the export of auxin from a cytoplasmic compartment to a wall compartment depends on the concentration of PIN in the intervening membrane compartment. This is in contrast to indirect cell-cell coupling models which do not have an explicit representation of PIN and where the export of auxin depends only on the concentration of A^* in the membrane. Therefore, equations 2.15 and 2.16, describing the rates of change of auxin concentrations in cytoplasmic and wall compartments respectively, are changed so that equation 2.15, describing the rate of change of auxin in cytoplasmic compartments becomes:

$$\frac{\partial Aux}{\partial t} = \rho_{Aux} - \mu_{Aux} Aux + \frac{1}{R_c} l_w \sum_{n \in N(c)} (v_{in} Aux_w - v_{out} Aux - \psi_{PIN} PIN_n Aux) \quad (4.4)$$

Where all symbols are as described for equation 2.15, except ψ_{PIN} , which is the rate of PIN-dependent active efflux of auxin from the cytoplasm into the wall with units of $\mu\text{m}^2/\text{A}_u\text{s}$. PIN_n is the concentration of PIN in the membrane compartment n , in the neighbourhood of the cell c ($N(c)$).

And equation 2.16, describing the rate of change of auxin in wall compartments, becomes:

$$\frac{\partial Aux_w}{\partial t} = -\frac{1}{R_w} l_w \sum_{n \in N(w)} (v_{in} Aux_w - v_{out} Aux_c - \psi_{PIN} PIN_n Aux_c) + D_{Aux} \nabla^2 Aux_w \quad (4.5)$$

Where all symbols are as described for equation 2.16, except ψ_{PIN} , which is as described above. PIN_{1n} is the concentration of PIN in the membrane neighbor, n , in the neighbourhood of the wall compartment w ($(N(w))$). In all simulations, ψ_{PIN} is $25 \mu\text{m}^2/\text{A}_u\text{s}$. All PIN-related parameter values used in simulations are provided in Table 4.3.

Symbol	description	unit	value
c_{PIN}	default initial concentrations of PIN1 in cytoplasmic compartments	$A_u/\mu\text{m}^2$	0.003
ρ_{PIN}	PIN1 default membrane binding rate	$\mu\text{m}/\text{s}$	0.03
τ	A^* -dependent promotion of PIN binding	$\mu\text{m}^2/A_u\cdot\text{s}$	2
μ_{PIN}	PIN1 default membrane unbinding rate	/s	0.004
D_{PIN}	PIN1 diffusion in cell membrane	$\mu\text{m}^2/\text{s}$	0.1
ψ_{PIN}	PIN-dependent active auxin efflux rate	$\mu\text{m}^2/A_u\cdot\text{s}$	25

Table 4.3 PIN-related parameter values used in the indirect cell-cell coupling model.

All other parameter values are as described in Table 2.1 or in the text below.

Other changes from the models presented in chapter 2, and specific features of each model used for simulations, are listed below for each figure in turn:

Fig. 4.11. Generation of a proximo-distal polarity field in an indirect cell-cell coupling model with an explicit representation of PIN. In the simulations used to generate both panels (A and B), ε , the limit for noise addition to A^* and B^* at the start of the simulation, is 0 and γ_{Aux} , the rate of auxin-independent promotion of A^* to A conversion is $0.5 \mu\text{m}^2/A_u\cdot\text{s}$. Also, in cells apart from those in the proximal and distal-most rows, the production rate of auxin, $\rho_{Aux} = 4 \times 10^{-4} A_u/\mu\text{m}^2\cdot\text{s}$ and the degradation rate of auxin, $\mu_{Aux} = 0.01 /s$. In both simulations, in the proximal-most row of cells, $\rho_{Aux} = 5.5 \times 10^{-4} A_u/\mu\text{m}^2\cdot\text{s}$. In the simulation used to generate A, in the distal-most row of cells, $\mu_{Aux} =$

0.04 /s. In the simulation used to generate B, in the distal most row of cells, $\mu_{Aux} = 0.01$ /s (the same as in all other cells in the array) and the inwards permeability of cells to auxin (v_{in}) is increased four-fold to 3 $\mu\text{m}/\text{s}$.

Fig. 4.12 Formation of centres of polarity convergence in an indirect cell-cell coupling model. In the simulation used to generate panel A, parameter values are as described for Fig. 4.11, except that, ρ_{Aux} , the production rate of auxin = 4.5×10^{-4} $\text{A}_u/\mu\text{m}^2.\text{s}$ in all cells except those in the proximal-most row, in which $\rho_{Aux} = 5.5 \times 10^{-4}$ $\text{A}_u/\mu\text{m}^2.\text{s}$. Also, the degradation rate of auxin, $\mu_{Aux} = 0.003$ /s in all cells. As in Fig. 4.11B, cells in the distal-most row of cells have an inwards permeability (v_{in}) of 3 $\mu\text{m}/\text{s}$. After 6 000s of the simulation, a proximo-distal polarity field has been established and a cell with elevated inwards permeability of auxin (which represents elevated auxin import) is added. In this cell, $v_{in} = 7.5$ $\mu\text{m}/\text{s}$ (this is a 10-fold increase in inward permeation compared with the background rate).

In the simulation used to generate panel B, parameter values are as described for Fig. 4.11. After 6 000 s of the simulation a proximo-distal polarity field has been established and a cell with elevated inwards permeability of auxin (elevated auxin import) and elevated degradation of auxin is added. In this cell, $v_{in} = 7.5$ $\mu\text{m}/\text{s}$ and $\mu_{Aux} = 0.07$ /s (this is a 10-fold increase in inward permeation compared with the background rate and a 23-fold increase in the auxin degradation rate).

Fig. 4.20 A. The effect of a band of cells with elevated auxin synthesis distal to a cell with elevated import in the indirect cell-cell coupling model. This simulation was performed as described for Fig. 4.12B, except that, after 6 000s of the simulation, as well as adding elevated auxin degradation and inwards permeability to one cell, I also add an elevated auxin production rate to three cells on

the distal side of the cell with elevated import and degradation. In these cells (shown in red in Fig.

4.20A), the auxin production rate, $\rho_{Aux} = 1.1 \times 10^{-3} \text{ A}_u / \mu\text{m}^2 \cdot \text{s}$.

4.4.8.2 Up the gradient model.

The up-the-gradient model is simulated as described in Chapter 3, except in this chapter, square cells are used. The length of each edge and associated with each edge compartment, is $5 \mu\text{m}$. The area of each cell, and associated with each cytoplasmic compartment, is $25 \mu\text{m}^2$. The parameter values used for all simulations are given in Table 4.4 and any additional details associated with each simulation are listed below.

Symbol and units	C_A Au/ μm^2	ε	C_{PIN}edge Au/ μm	ε_{PIN}	PIN_i Au/ μm	b	σ /s	H Au/ μm^2	R μm^2	I μm	μ /s	D $\mu\text{m}/\text{s}$	T $\mu\text{m}^2/\text{A}\text{u}\cdot\text{s}$
Fig: 4.9, 4.10	0.01	0	0.0	0	0.1	6	0.0	0.0	25	5	0.000	32.4	51.9
4.16 A, B 4.17	0.01	0	0.0	0	0.1	6	0.01	0.1	25	5	0.000	32.4	51.9
4.16C	0.01	0	0.0	0	0.1	6	0.01	0.1	25	5	0.0001	32.4	51.9
4.19	0.01	0	0.0	0	0.1	6	0.00	0.0	25	5	0.0001	32.4	51.9

4.20	0.01	0	0.0	0	0.1	6	0.00 1	0.1	25	5	0.000	32.4	51.9
-------------	------	---	-----	---	-----	---	-----------	-----	----	---	-------	------	------

Table 4.4. Parameter values used in up-the-gradient simulations.

C_A is the default initial concentration of auxin in cytoplasmic compartments, ε is the limit for noise addition to C_A , $C_{PINedge}$ is the default initial concentration of PIN at each cell edge, ε_{PIN} is the limit for noise addition to $C_{PINedge}$, PIN_i is the total amount for PIN available for binding to the membrane in cell i , b is the exponentiation base for PIN allocation to the membrane, σ is the auxin production rate, H is the target auxin concentration, R is the area of cytoplasmic compartments, l is the length of cell edge compartments, μ is the auxin degradation rate, D is the passive permeability of auxin and T is the rate of PIN-mediated auxin transport.

Fig. 4.9 Generation of a proximo-distal polarity field in an up-the-gradient model. In the simulation used to generate panel A, auxin is not produced or degraded (as stated in Table 4.4), except in the distal-most row of cells, where auxin is produced ($\sigma = 1.2 /s$ and the target auxin concentration, $H = 0.1 \text{ Au}/\mu\text{m}^2$) and in the proximal-most row of cells where auxin is degraded ($\mu = 0.05 /s$). The simulation used to generate panel B is the same as that used to generate panel A, except that elevated auxin degradation in the proximal-most row of cells is removed, and all cells degrade auxin at a background rate ($\mu = 0.005 /s$ in all cells, including the proximal-most file of cells).

Fig. 4.10 Formation of centres of polarity convergence in an up-the-gradient model. The simulations used to generate panels A and B are implemented as for Fig. 4.9A, but with addition of an elevated auxin production rate, σ , of $2.4 /s$ to one cell (in the case of panel A), or four cells (in the case of panel B) after 15s of the simulation (the elevated auxin production remains for the rest of the simulation).

In the simulation used to generate panel C (where a transient local increase in auxin concentration causes the formation of a centre of convergence), all cells except those in the distal-most row (but including the proximal-most row), produce and degrade auxin at a

background rate ($\sigma = 0.004 /s$ and $\mu = 0.0001 /s$). In the distal-most row of cells, $\sigma = 1.2 /s$ and $\mu = 0.0001 /s$. In all cells, the target auxin concentration, $H_t = 0.1 \text{ Au}/\mu\text{m}^2$. Between 15s and 50s in the simulation, the auxin concentration of a single cell (indicated in red in Fig. 4.10 C) is held at $0.1 \text{ Au}/\mu\text{m}^2$. After this time period, a centre of convergence with high auxin remains.

Fig.4.16 Generation of a proximo-distal polarity field in an up-the-gradient model with elevated auxin import in the distal minus organiser. In the simulation used to generate panel A, polarity is established according to the parameters shown in Table 4.4, except that, as in the simulation used to generate a proximo-distal polarity field in Fig.4.9A, in the proximal-most row of cells, the auxin degradation rate, $\mu = 0.05 /s$, and in the distal-most file of cells, the auxin production rate, $\sigma = 1.2 /s$. Also, in this simulation, an elevated rate of auxin import is added to cells in the distal-most row (which affects auxin flux between cells as described in equation 3.5). In all cells except those in the distal-most row, $I=0$. In cells in the distal-most row, $I= 20 \mu\text{m} / s$. The simulation used to generate panel B is the same as that used to generate panel A, except all cells (including those in the distal-most row) have the same rate of auxin production ($\sigma = 0.01 /s$ in all cells). The simulation used to generate panel C is the same as that used to generate B, except in the proximal-most row of cells (and in all other cells of the array), auxin degradation occurs at a background level ($\mu = 0.0001 /s$).

Fig. 4.17 Generation of centres of convergence in an up-the-gradient model with elevated auxin import in minus organisers. The simulations used to generate this figure are as described above for Fig 4.16B, except that, after 50 s of the simulation, elevated auxin import is added to one cell (panel A), two cells (panel B) or four cells (panel C) within the array. In this cell, $I = 20 \mu\text{m} / s$. In all other cells, $I = 0 \mu\text{m} / s$.

Fig. 4.19 The effect of auxin production in proximal regions of tissue in an up-the-gradient model.

In this simulation, all parameters as shown in Table 4.4, except the proximal-most file of cells has an elevated auxin production rate, σ , of 5 /s and a target auxin concentration, H , of 0.01 $\text{Au}/\mu\text{m}^2$. Also, cells in the distal most row have an elevated rate of auxin import, $I = 10 \mu\text{m} / \text{s}$, in all other cells, $I=0 \mu\text{m} / \text{s}$.

Fig. 4.20 B The effect of a band of cells with elevated auxin synthesis distal to a cell with elevated import in the up-the-gradient model. This simulation was performed as for Fig.4.17 B but the auxin production rate (σ) in all cells = 0.001 /s (parameter values are shown in Table 4.4). Also, at the same time elevated auxin import is added to two cells in the array, three cells with elevated auxin production are added on the distal side of the high-import cells. In these three cells, the auxin production rate, $\sigma = 10 /s$. Additionally, in the high import cells, $I = 2 \mu\text{m} / \text{s}$. In all other cells, $I=0 \mu\text{m} / \text{s}$.

5 The role of *CUC2* in polarity reorientations

5.1 Introduction

As described in the previous chapter, ectopic outgrowths develop within the proximal half of the first leaf of *kan1kan2* seedlings. The precise position and number of outgrowths varies between leaves, suggesting that their positioning is non-deterministic. Here, I consider mechanisms that could position the outgrowths.

One hypothesis is that ectopic outgrowths are positioned randomly within a certain zone of the leaf, due to the stochastic formation of ectopic boundaries between adaxial and abaxial cell identity. In *kan1kan2* leaves, which lack proper specification of abaxial identity (due to loss of two abaxial-specific *KANADI* transcription factors), patches of cells in the abaxial half of the leaf may stochastically express elevated levels of adaxial-specific transcription factors. Antagonistic interactions between adaxial transcription factors, and the remaining abaxial-specific transcription factors (Emery et al., 2003; Yamaguchi et al., 2012), could cause the formation of ectopic boundaries between adaxial and abaxial identity. Indeed, the *YABBY* transcription factor, *FIL*, has been proposed to be expressed in response to adaxial-abaxial boundary formation (Husbands et al., 2009), is locally up-regulated in *kan1kan2* outgrowths, and together with another *YABBY* gene, *YAB3*, is required for outgrowth development (Eshed et al., 2004). Support for a role for adaxial-abaxial juxtaposition in generating outgrowths also comes from studies of *phantastica* mutants of *Antirrhinum majus*, which carry a mutation in a gene required for adaxial identity. In these mutants, ectopic leaf outgrowths develop at ectopic boundaries between adaxial and abaxial cell types (Waites and Hudson, 1995) on the adaxial leaf surface.

In the previous chapter, I show that ectopic centres of PIN1 polarity convergence form early in *kan1kan2* leaf development and predict the positions of new outgrowths. Therefore, an

alternative hypothesis for outgrowth positioning is that it depends on a mechanism that positions centres of PIN1 polarity convergence, independently from the formation of local adaxial-abaxial boundaries. How the ectopic centres of polarity convergence are positioned in *kan1kan2* leaves is unclear, but a similar phenomenon is observed during leaf serration development, where the formation of centres of PIN1 convergence in the leaf margin positions the sites of new serrations (Bilsborough et al., 2011; Hay et al., 2006). The *CUC2* transcription factor is important for this process, since *cuc2* mutants do not form serrations or centres of PIN1 polarity convergence in the leaf margin (Bilsborough et al., 2011; Nikovics et al., 2006). In WT leaves, centres of PIN1 polarity convergence and auxin maxima (indicated by *DR5* activity) become interspersed with regions of elevated *CUC2* expression (Bilsborough et al., 2011). This has been proposed to be due to the formation of centres of PIN1 convergence within a broad *CUC2* expression domain, followed by down-regulation of *CUC2* by elevated auxin at the centre of convergence (Bilsborough et al., 2011). In support of this, auxin application to leaves has been shown to inhibit *CUC2* expression.

A computational model has been proposed for how *CUC2* and auxin-regulated PIN1 polarity interact to position sites of new serrations (Bilsborough et al., 2011). This model hypothesises that PIN1 polarity is controlled by an up-the-gradient mechanism. *CUC2* is proposed to be required for PIN1 to be reoriented within cells. In this model, the presence of *CUC2* is therefore required for cells to become polarised, and to reorient their PIN1 polarity, in response to intercellular auxin gradients. *CUC2* is assumed to be down-regulated in the presence of elevated auxin levels found at centres of polarity convergence. This stabilises the positions of new centres of PIN1 polarity convergence as, in the absence of *CUC2*, polarity cannot change. With rules about how auxin and *CUC2* influence growth rates, the model can capture the dynamics and pattern of serration development in the *A. thaliana* leaf margin.

Here, I investigate the role of *CUC2* in positioning *kan1kan2* outgrowths. I present and test new hypotheses for how *CUC2* may interact with up-the-gradient or indirect cell-cell coupling mechanisms to account for the positioning of ectopic centres of PIN1 convergence in *kan1kan2* leaves. I then discuss possible relationships between *CUC2*-regulated polarity and adaxial-abaxial boundary formation.

5.2 Results

5.2.1 *CUC2* is required for the development of *kan1kan2* outgrowths and ectopic centres of PIN1 polarity convergence

To test whether *CUC2* is required for the generation of *kan1kan2* outgrowths, I generated a *kan1kan2cuc2* mutant. Supporting a role of *CUC2* in outgrowth development, leaves of this mutant did not develop ectopic outgrowths (Fig. 5.1).

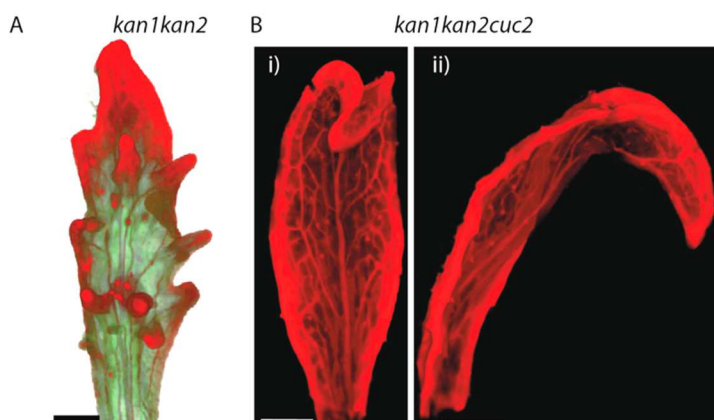


Fig. 5.1 Loss of ectopic outgrowths in a *kan1kan2cuc2* background.

A) 3D-Optical projection tomography image of the abaxial surface of a *kan1kan2* leaf, showing ectopic outgrowths. The image is artificially coloured to emphasise the 3D shape. **B)** OPT image of the abaxial surface (i), and side view (ii) of a *kan1kan2cuc2* leaf, showing a loss of ectopic outgrowths. Scale bars = 500 μ m

To test whether the lack of ectopic outgrowths in *kan1kan2cuc2* mutants is correlated with a lack of PIN1 polarity convergence formation, I imaged the *PIN1::PIN1:GFP* reporter in the first leaf of

mutant seedlings, over a period of three days (at the stage when centres of PIN1 convergence were observed to form in *kan1kan2* leaves, chapter 4). Centres of PIN1 polarity convergence were never observed to form in the *kan1kan2cuc2* background (I performed time lapse imaging on 3 leaves, and snapshot imaging of 20 leaves, and did not observe centres of PIN1 convergence, Fig. 5.2). Similar to young leaf primordia of WT and *kan1kan2* seedlings (chapter 4), in young *kan1kan2cuc2* leaf primordia of around 65 μm in width, *PIN1::PIN1:GFP* expression was approximately equal in all cells of the leaf and PIN1 polarities were oriented along the proximo-distal axis (Fig. 5.2i). At later stages of development, *PIN1::PIN1:GFP* signal was lost in most cells, but could still be detected in small groups of cells in the proximal half of the leaf (Fig. 5.2ii to v). These groups of cells did not appear to have organised polarity patterns: PIN1:GFP signal appeared equal on all edges of most cells and appeared to be polarised along the proximo-distal axis in small numbers of cells (Fig. 5.2). The reduction in *PIN1::PIN1:GFP* expression throughout most of the leaf in *kan1kan2cuc2* mutants is similar to observations of WT leaves (Fig. 4.5), but contrasts with *kan1kan2* leaves which maintained more wide-spread expression of *PIN1::PIN1:GFP* in leaves between 95 and 160 μm in width (Fig.4.3 and also see Fig. 5.3 in the next section).

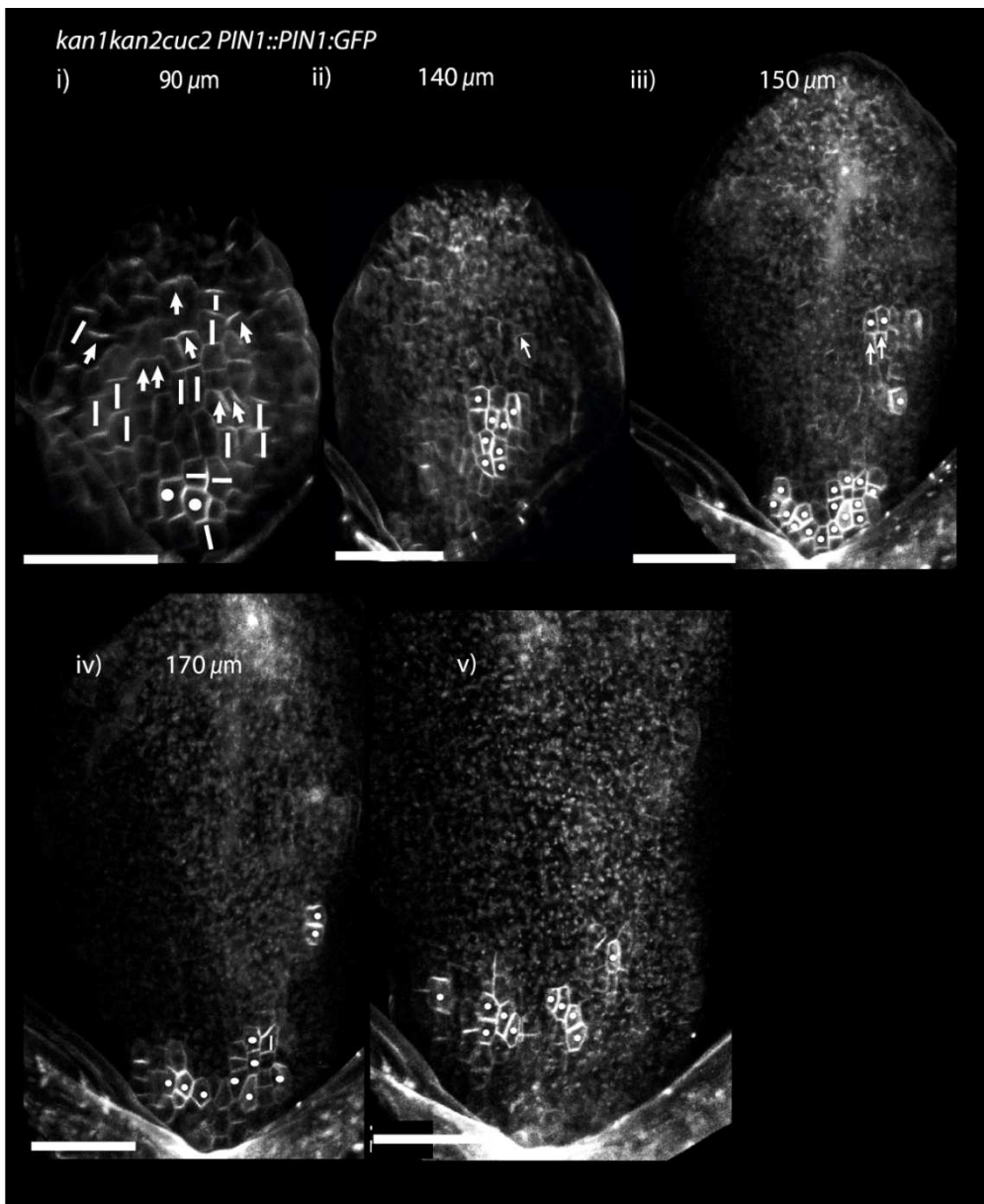


Fig. 5.2 PIN1::PIN1::GFP in leaf one of the kan1kan2cuc2 mutant.

i) to v) show confocal images of the same leaf imaged at successive time points. Leaf widths are given above each image. Times from beginning of experiments at which images were taken are i) =0hrs, ii)=24hrs, ii)36hrs, iv)48hrs, v)72hrs. White dots indicate cells that have approximately equal PIN1:GFP signal at all edges, white lines and arrows indicate inferred axes and polarities of the PIN1:GFP distribution. The data set shown here is representative of that obtained by tracking three *kan1kan2cuc2PIN1::PIN1::GFP* leaves (from three different seedlings), and of snapshot images of *kan1kan2cuc2* leaf primordia taken at each of the developmental stages shown. Scale bars = 50 μ m.

5.2.2 *CUC2::RFP* is initially expressed in the proximal half of the leaf and then its expression becomes more restricted.

To further investigate the role of *CUC2* in the formation of ectopic outgrowths, I imaged *PIN1::PIN1:GFP* and *CUC2::RFP* reporters in the abaxial side of the first leaf of *kan1kan2* seedlings. Leaves were tracked over four to five days to allow the dynamics of *PIN1* expression and polarity to be related to *CUC2::RFP* expression dynamics. Tracking experiments were initiated when leaves were approximately 50 μm in width, approximately two days before *kan1kan2* outgrowths were observed to form. To obtain information about expression patterns at earlier stages, for which tracking is difficult, snapshot images from single time points were used.

At the earliest stages imaged, *CUC2::RFP* was expressed throughout the proximal half of the lamina but absent from the distal half (Fig. 5.3 Bi). At this early stage, *PIN1::PIN1:GFP* was expressed in all cells of the abaxial epidermis (Fig. 5.3 Ai, Ci). In slightly older leaves, and approximately two days before outgrowth emergence, the expression of *CUC2::RFP* remained similar but *PIN1::PIN1:GFP* expression was weaker in the distal half of the leaf compared with in the proximal half (Fig. 5.3 Aii, Bii, Cii). At even later stages, one to two days prior to outgrowth emergence, expression of *PIN1::PIN1:GFP* became restricted to a band of cells, through loss of expression in cells at the leaf base (Fig. 5.3 Aiii). At this stage, *CUC2::RFP* expression also became restricted to a band of cells within the distal half of the *PIN1::PIN1:GFP* expression domain (Fig. 5.3 Bi and iv, Ciii and iv). When outgrowths were first seen to emerge, *PIN1* expression was maintained in groups of cells at the tips of emerging outgrowths, but lost from surrounding cells (Fig. 5.3 A v, blue and yellow arrows). By this stage, expression of *CUC2::RFP* was restricted to cells on the distal edge of the groups which maintained elevated *PIN1::PIN1:GFP* expression (Fig. 5.3 B v and C v).

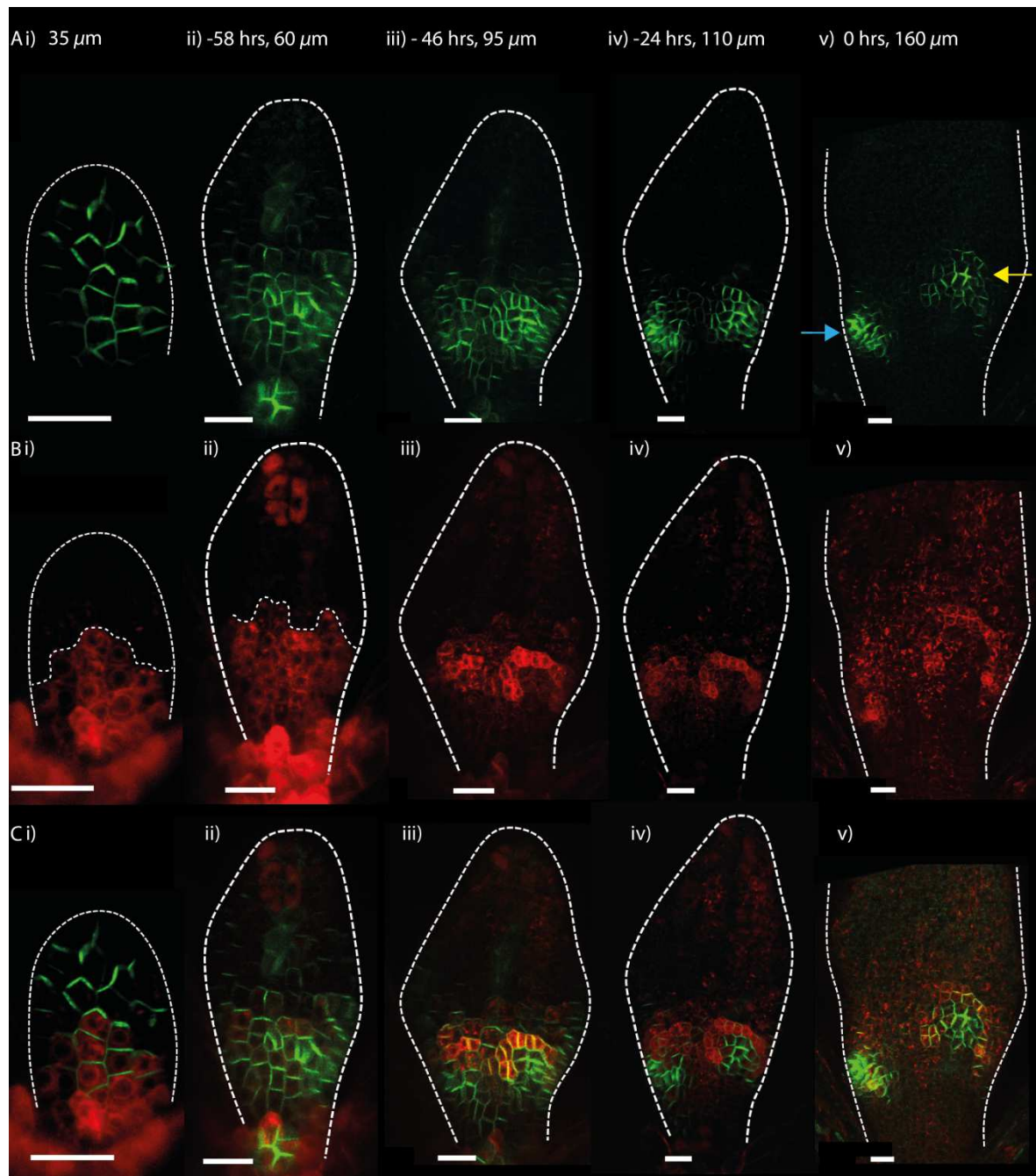


Fig. 5.3 Expression of *CUC2::RFP* and *PIN1::PIN1:GFP* in *kan1kan2* leaves during the development of ectopic centres of polarity convergence.

A) Confocal images of the expression pattern of a *PIN1::PIN1:GFP* reporter in a *kan1kan2* leaf. Times relative to outgrowth emergence, and leaf widths, are given above each image. **B)** Confocal images of the expression pattern of a *CUC2::RFP* reporter in the same leaf. Dotted lines in i) and ii) show the distal edge of the *CUC2::RFP* expression domain. The *CUC2::RFP* reporter has an ER-targeting motif fused to the RFP, therefore any non-ER localised signal (such as that at the tip of the leaf) is considered to be due to auto-fluorescence. **C)** Combined confocal channels, showing *PIN1::PIN1:GFP* (green) and *CUC2::RFP* (red). Ai), Bi) and Ci) show a leaf primordium that was imaged at a single time point. Aii)- v), Bii)- v) and Cii) to v) show time-lapse images from a leaf of another individual, imaged over 58 hours prior to outgrowth emergence. Blue and yellow arrows

indicate centres of PIN1 polarity convergence at the tips of emerging outgrowths. The data shown here are representative of that obtained by tracking 5 *kan1kan2 PIN1::PIN1:GFP CUC2::RFP* leaves. Scale bars = 20 μ m.

5.2.3 Centres of PIN1 polarity convergence form within the proximal domain of *CUC2::RFP* expression.

As described in chapter 4, PIN1 polarities are initially oriented distally in young *kan1kan2* leaf primordia (Fig. 4.4). Prior to outgrowth formation, polarities reorient in local regions of the leaf to generate centres of polarity convergence (Fig.4.3). These centres of polarity convergence predict the positions of new outgrowths, and as outgrowths emerge from the leaf, centres of convergence are located at their tips (Fig. 5.3 A v, blue and yellow arrows, Fig. 5.4 A iv). To investigate when these centres of PIN1 convergence first form in relation to the expression patterns of *CUC2*, I tracked back the cell identities and polarities of the tip cells to earlier time points (cells marked with yellow dots and arrows in Fig. 5.4 i to iii). At the earliest stages of *kan1kan2* leaf development, when PIN1 polarities point distally throughout the leaf, *CUC2* expression was present throughout the proximal half of the lamina (Fig. 5.3 Ai, Bi, Ci). Tracing cell lineages in the time-lapse data revealed that cells at the centre of polarity convergence descended from a single cell that was at a centre of polarity reorientation within the *CUC2::RFP* expression region (Fig. 5.4 A i, Bi, Ci). This cell had high levels of *PIN1::PIN1:GFP* signal from the earliest stage when a polarity reorientation could be detected. These data suggest that centres of convergence start to form from an initial proximo-distal PIN1 polarity field, within a broad proximal domain of *CUC2::RFP* expression.

The locations of early centres of PIN1 polarity convergence within the *CUC2::RFP* expression domain were variable. For example, in the leaf shown in Fig. 5.3 and Fig. 5.4, in one case the centre of convergence was located one cell back from the distal edge of domain with elevated

CUC2::RFP expression (Fig. 5.4 Ai, Bi, Ci, yellow dot). In another case, a centre of convergence was tracked back to a cell that was four cells back from the distal edge of the *CUC2::RFP* expression domain (marked with blue dot in Fig. 5.4 Ai, Bi, Ci, and blue arrow in Fig. 5.3 A v). Besides the variable position of centres of convergence along the proximo-distal axis, variation was also observed in the position of polarity convergences along the medio-lateral axis.

At later stages, expression of *CUC2::RFP* was not detected in the cells close to the centre of PIN1 polarity convergence (Fig. 5.4 B ii-iv, C ii-iv). Instead, expression of *CUC2::RFP* was maintained in a horse-shoe shaped band of cells that flanked the distal side of the centre of convergence. Expression of *CUC2::RFP* in this domain remained until outgrowth emergence (Fig. 5.4 B iv and C iv), but at later stages it became undetectable (not shown).

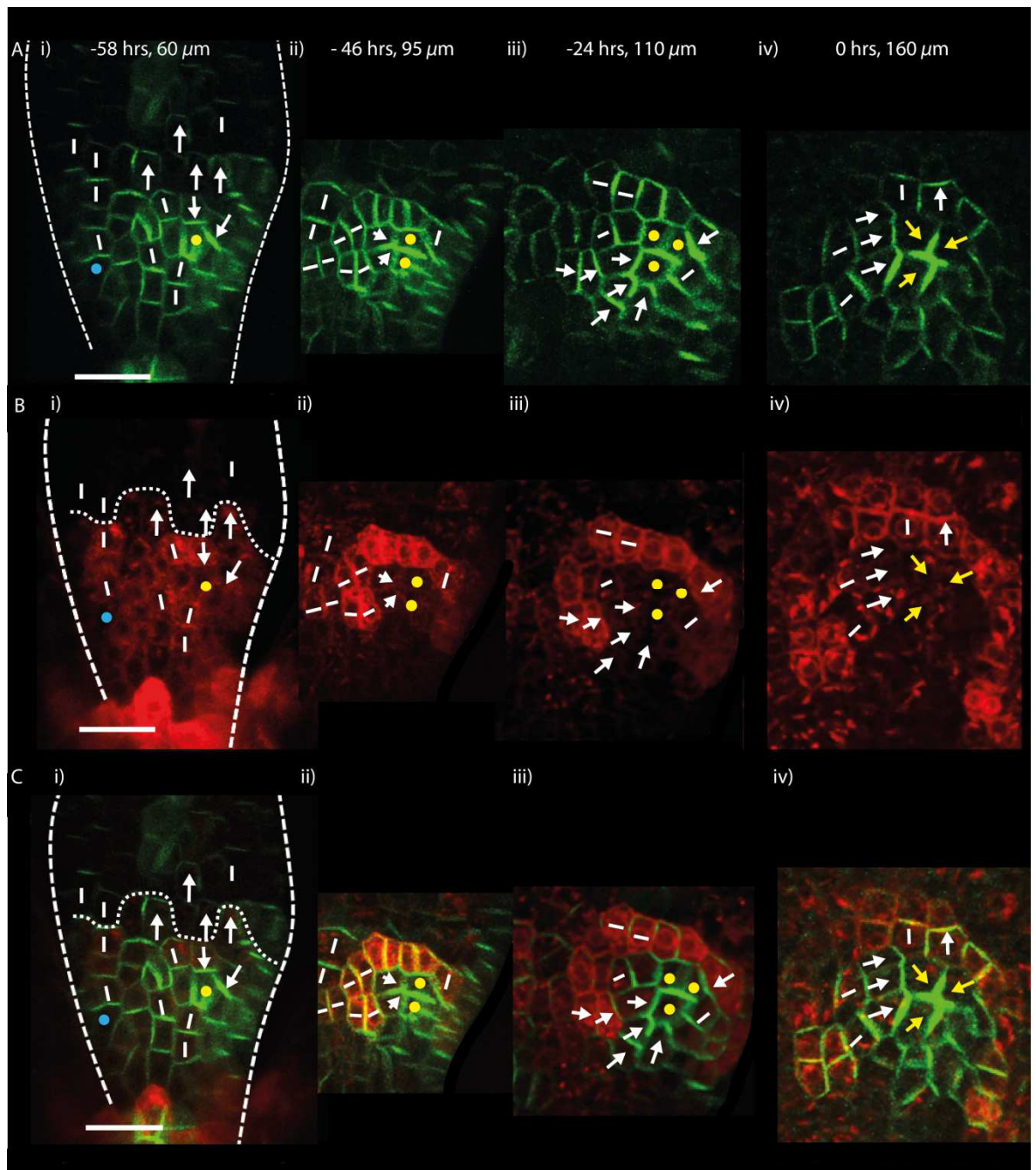


Fig. 5.4 Formation of a centre of PIN1 polarity convergence in relation to expression of *CUC2::RFP*.

A) Confocal images of the *PIN1::PIN1:GFP* reporter in a *kan1kan2* leaf imaged over 58 hours prior to outgrowth development. Images are zoomed in versions of those shown in Fig. 5.3 (outgrowth indicated by the yellow arrow in Fig. 5.3 Av). Times relative to outgrowth emergence, and leaf widths are given above each image. **B)** Confocal images of the expression pattern of *CUC2::RFP* in the same leaf as shown in A. Dotted line in i) shows the distal edge of the *CUC2::RFP* expression domain. **C)** Combined confocal channels, showing *PIN1::PIN1:GFP* (green) and *CUC2::RFP* (red). Yellow symbols mark the cells at the centre of polarity convergence (panels iv) and their ancestors. White lines indicate the inferred axiality of the *PIN1::PIN1:GFP* distribution, and arrows indicate inferred polarities. The blue dots in panels i) indicate the cell which gave rise to another.

PIN1 polarity convergence on the left of the leaf (blue arrow in Fig. 5.3 panels v). The data shown here is consistent with patterns of *PIN1::PIN1:GFP* and *CUC2::RFP* signal obtained by tracking four out of four other centres of polarity convergence. Scale bars = 20 μ m.

5.2.4 *CUC2::RFP* expression is restricted to the base of WT leaves.

As shown in chapter four, WT leaves do not form centres of PIN1 convergence in the lamina. In young WT leaves of around 50 μ m in width, *PIN1::PIN1:GFP* was expressed in all cells, similar to what was observed in young *kan1kan2* primordia (Fig. 5.5 Ai). However, as WT leaves grew from approximately 70 μ m to 100 μ m in width, the expression of *PIN1::PIN1:GFP* became almost undetectable (Fig. 5.5 Aii, iii), and no GFP signal could be detected in the lamina at subsequent stages of development (Fig. 5.5 Aiv) . This contrasts with *kan1kan2* leaves, which maintained elevated *PIN1::PIN1:GFP* expression in groups of cells in the lamina until they were more than 200 μ m wide (Fig. 5.3 Av). WT leaves also lacked *CUC2::RFP* expression in the lamina: expression of this reporter was only detected at the base of young WT leaves (Fig. 5.5 Bi-iv, Ci-iv). Expression extending throughout the proximal half of the lamina, or in a band running across the lamina, as seen in *kan1kan2*, was not observed in WT. This suggests that the elevated expression of *PIN1* and *CUC2* in the proximal half of the *kan1kan2* lamina is an ectopic feature of this mutant background.

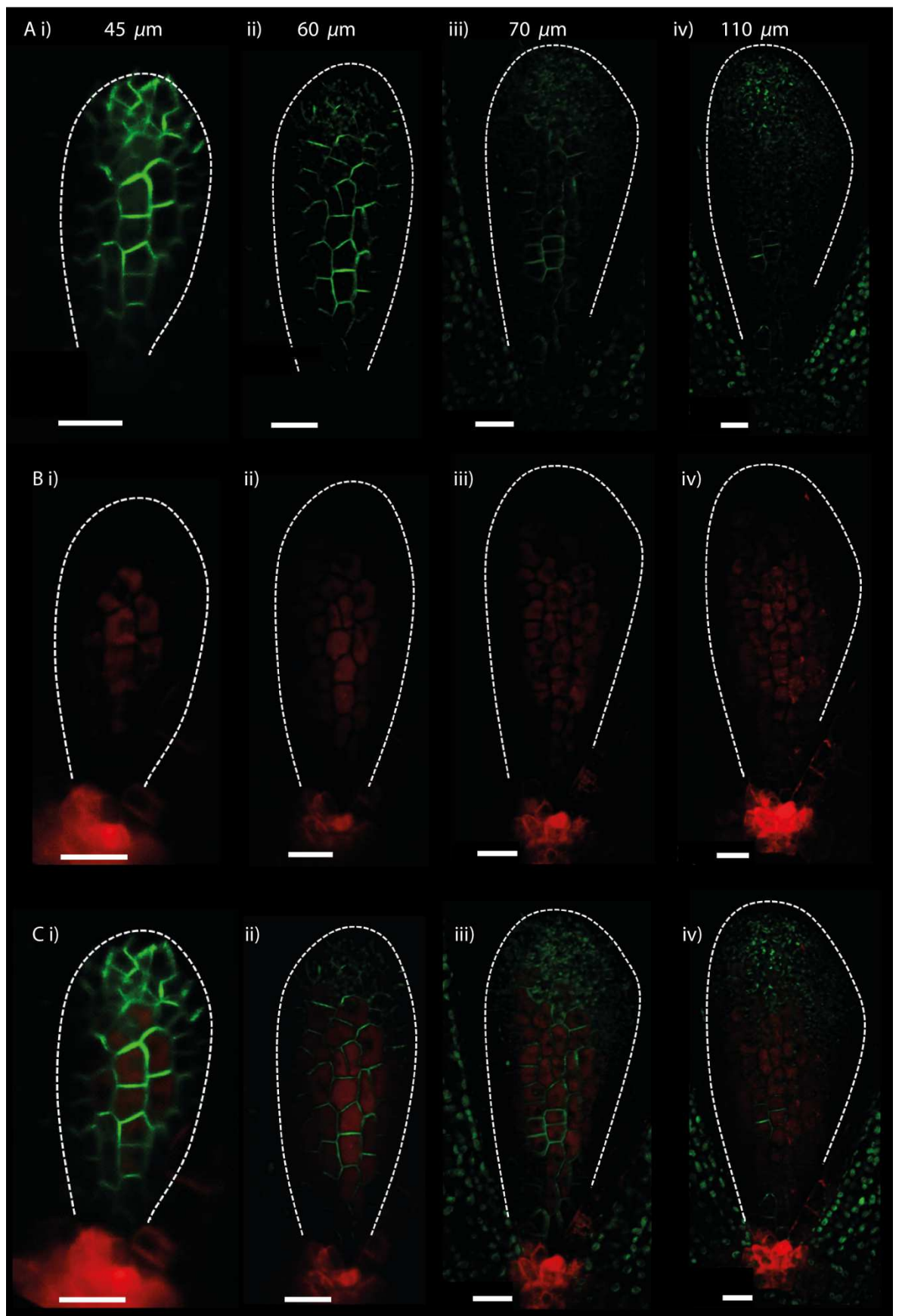


Fig. 5.5 Expression patterns of *CUC2::RFP* and *PIN1::PIN1::GFP* in WT leaves.

A) Confocal images of *PIN1::PIN1::GFP* reporter in the first leaf of a WT seedling. Leaf widths are given above each image. **B)** Confocal images of *CUC2::RFP* in the same leaf. **C)** Combined confocal channels, showing *PIN1::PIN1::GFP* (green) and *CUC2::RFP* (red). Panels i-iv show the same leaf, imaged at successive time points. Times since the beginning of the experiment are i) 0hrs, ii) 24 hrs, iii), 33.5 hrs, iv) 47.5 hrs. Scale bars = 20 μ m. Images shown are representative of those obtained by tracking four leaves from four seedlings. Leaf margins, which were previously reported to express *CUC2* (Nikovics et al., 2006), are not in focus in these images.

5.2.5 *kan1kan2* leaves that do not generate centres of PIN1 convergence have elevated expression of *CUC2::RFP* in proximal regions of the lamina.

As shown in chapter 4, some *kan1kan2* leaves do not form outgrowths in live imaging experiments and this is correlated with a lack of ectopic centres of PIN1 polarity convergence. In these leaves, the initial expression patterns of *PIN1::PIN1::GFP* and *CUC2::RFP* were similar to those seen in *kan1kan2* leaves that formed ectopic outgrowths. In young primordia of around 50-60 μ m in width, *CUC2::RFP* was expressed throughout the proximal half of the lamina and *PIN1::PIN1::GFP* expression was elevated in the proximal half of the leaf relative to the distal half (Fig. 5.6 Ai, Bi, Ci). At later stages, as observed in *kan1kan2* leaves that made outgrowths, the expression of both transgenes became restricted to a band within the proximal half of the leaf (due to loss of expression in cells towards the leaf base (Fig. 5.6 panels ii-iii)). However, when centres of PIN1 convergence did not form, *CUC2::RFP* expression was not observed in distinct horse-shoe shapes with high levels of *PIN1::PIN1::GFP* expression at their centre. These observations suggest that *CUC2::RFP* expression may be restricted to a band in the proximal half of the leaf, independently from the formation of PIN1 centres of convergence. However, the formation of well-defined horseshoe-like bands of *CUC2::RFP* is likely to be related to the formation of centres of PIN1 polarity convergence.

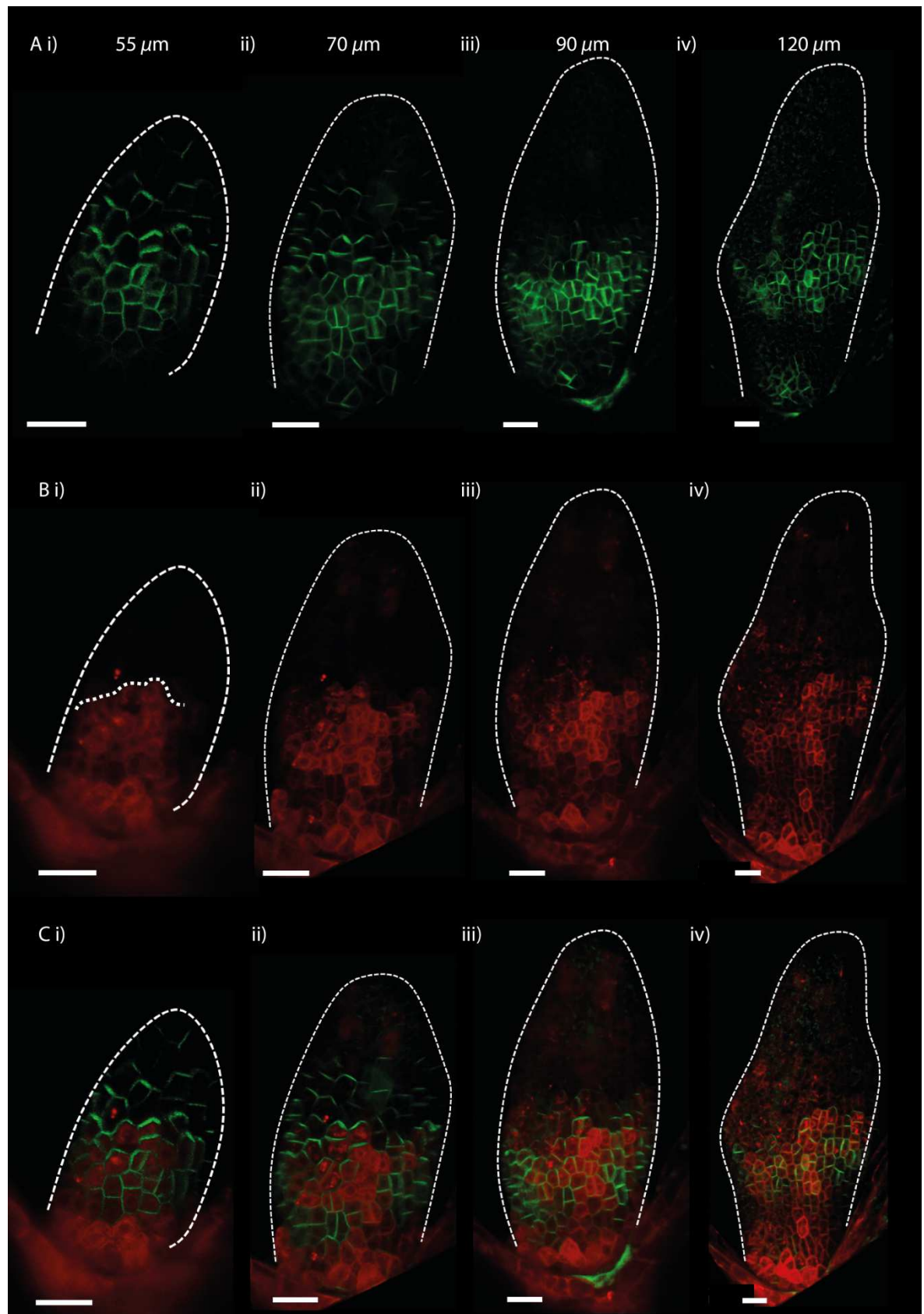


Fig. 5.6 Expression of *PIN1::PIN1:GFP* and *CUC2::RFP* in a *kan1kan2* leaf that did not develop an ectopic outgrowth.

A) Confocal images of the *PIN1::PIN1:GFP* reporter in the first leaf of a *kan1kan2* seedling. Leaf widths are given above each image. **B)** Confocal images of *CUC2::RFP* in the same leaf. Dashed white line shows the distal boundary of the domain with elevated *CUC2::RFP* expression. **C)** Combined confocal channels, showing *PIN1::PIN1:GFP* (green) and *CUC2::RFP* (red). Panels i-iv show the same leaf, imaged at successive time points. Times since the beginning of the experiment are i) 0 hrs, ii) 13 hrs, iii), 36 hrs, iv) 59.5 hrs. The images shown here are representative of those obtained by tracking eight *kan1kan2CUC2::RFP PIN1::PIN1:GFP* leaves that did not generate outgrowths. Scale bars = 20 μ m.

In summary, several aspects of *CUC2::RFP* expression are different between leaf one of WT and *kan1kan2* seedlings. Whereas in WT expression of *CUC2::RFP* is restricted to the base of the lamina, in *kan1kan2* leaves, expression occurs throughout the proximal half of the leaf. The *CUC2::RFP* expression pattern changes during the development of centres of PIN1 convergence, forming a horseshoe-like shape around each PIN1 convergence. I hypothesise that these ectopic patterns of *CUC2::RFP* expression might be related to the mechanism that positions outgrowths, which I explore with modelling in the next section.

5.2.6 Models of positioning centres of PIN1 polarity convergence

I explore possible roles for *CUC2* in the positioning of centres of convergence in both up-the-gradient and indirect cell-cell coupling models. I test the ability of different models to account for four main aspects of the data presented above:

- Centres of *PIN1* convergence should be positioned in the proximal half of the lamina and should arise from an initial proximo-distal polarity field. In chapter 4, this was achieved in models by specifying points of minus organiser activity within the proximal half of the tissue. Here, I investigate how centres of convergence may arise from rules that operate in all cells, without specifying the precise location of minus organisers of polarity.

- The centres of convergence should initially be generated within a broad domain of *CUC2* expression.
- *CUC2* expression should then be cleared from centres of convergence after their initial formation.
- Elevated levels of *PIN1* expression should be present in the proximal half of the lamina, with especially high levels at centres of *PIN1* polarity convergence.

The apparent incompatibility of the up-the-gradient model with the pattern of auxin biosynthesis in WT leaves, discussed in the previous chapter, will initially be ignored.

5.2.6.1 An up-the-gradient model of leaf serration development can account for some aspects of *PIN1::PIN1:GFP* and *CUC2::RFP* behaviour.

Initially, I explore to what extent a published up-the-gradient model of serration development (Bilsborough et al., 2011) can account for the observations listed above. In this model, the *CUC2* concentration of a cell must exceed a threshold level for the cell to change its PIN localisation. In the presence of high auxin, *CUC2* expression is repressed, and cells can no-longer reorient PIN.

In the published model, the leaf margin is represented by a 1D file of cells, folded to generate a leaf outline. The central-most cells of the file represent the leaf tip, and the two ends represent the base. It is assumed that the leaf base acts as an auxin sink (with a fixed auxin concentration of zero). In the initial state of the simulation, *CUC2* is assumed to be present in all cells. As *CUC2* is required for PIN localisation to change, this assumption is necessary for proximo-distal PIN polarity to be established. The observation that *CUC2::RFP* expression is restricted to the base of young WT leaf primordia (Fig. 5.5) raises the question of whether this assumption is valid. However, it is possible that at stages earlier than those imaged here, *CUC2* is expressed throughout the leaf.

With these assumptions, for a small leaf, with seven margin cells on each side, a PIN polarity convergence forms at the leaf tip (in the centre of margin). As the leaf grows, PIN polarity reversals occur within its distal half, generating a centre of convergence at either side of the leaf tip. In the model, elevation of the auxin concentration at centres of polarity convergence causes the down-regulation of CUC2, locally preventing further polarity changes.

To account for the positioning of new *kan1kan2* outgrowths, I first extend this 1D model into 2D, using a grid of cells to represent the *kan1kan2* abaxial epidermis (Fig.5.7 A and B). As in the published serration model, I assume that the proximal region of the leaf acts as an auxin sink with a fixed auxin concentration of zero (blue cells in Fig.5.7 Ai). I also assume that CUC2 is initially present in all cells (magenta cells in (Fig.5.7 Ai), must exceed a threshold level for cells to reorient PIN, and is down-regulated by auxin. Finally, to generate a distally-oriented polarity field, I add the assumption that auxin is fixed at a relatively high level at the distal end of the array (Fig.5.7 Ai).

With these assumptions, for a small array, all cells have a distally oriented polarity. As a consequence of high auxin at the distal end of the array, CUC2 is down-regulated (Fig.5.7 Aiii). However, with the same assumptions, but in a larger array of cells, centres of polarity convergence form in the distal half of the array (Fig.5.7 B ii, iii). The centres of PIN polarity convergence and the tip of the leaf have elevated auxin (Fig.5.7 B ii and iv) and therefore low levels of CUC2 (white cells in Fig.5.7 B iii).

These centres of polarity convergence form because, before convergence formation, the auxin gradient in the distal half of the array becomes shallow (Fig.5.7 C). As a result of the shallow auxin gradient, some cells have similar concentrations of auxin in all their neighbours and therefore localise PINs equally to all their edges (Fig.5.7 Di). Since all cells synthesise auxin at background

rate, this reduction in PIN polarity causes an increase in the auxin concentration of the weakly polarised cells (local regions of unpolarised cells do not transport auxin away as efficiently as regions of polarised cells). Thus, neighbouring cells reorient their polarity to point towards the weakly polarised cells, and a centre of convergence is generated (Fig.5.7 B).

In this 2D simulation, convergence formation is influenced by boundary effects. The open left and right boundaries of the tissue bias the polarity of cells at these edges to orient inwards (because they have no neighbours on the outside). When the proximo-distal auxin gradient becomes shallow, it is not sufficiently strong to overcome the boundary effects and thus left and right boundary cells orient their PIN inwards, which contributes to convergence formation. Thus, a weak proximo-distal auxin gradient may cause the formation of centres of convergence even without the loss of polarity described above. However, in the 1D serration model, these boundary effects are absent and polarity reorientations occur only according to the mechanism described above (through a loss of polarity in cells exposed to a weak intercellular auxin gradient). In the future, the 2D simulation presented here should be run with periodic boundary conditions across the left and right borders to eliminate boundary effects.

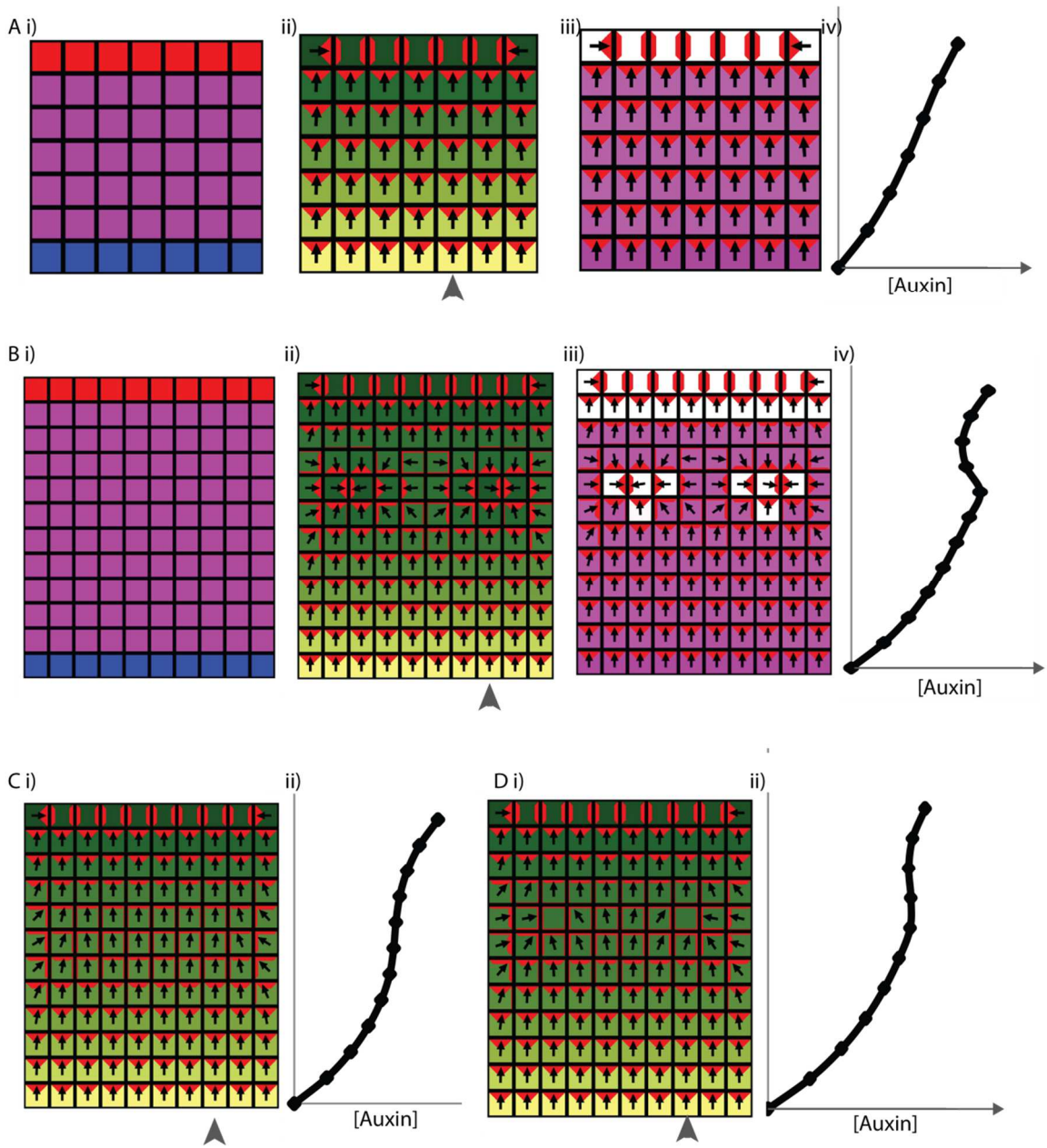


Fig.5.7 Positioning of centres of convergence in an up-the-gradient model with CUC2.

A) Generation of proximo-distal polarity in a small array of cells by fixing auxin concentrations at the proximal and distal boundaries. i) Initial state of the simulation. The base acts as a strong auxin sink with a fixed auxin concentration of 0 (dark blue cells). The distal end of the tissue has a fixed high auxin concentration (red cells). All cells, including the most proximal and distal rows, start with the same levels of CUC2 (magenta cells). ii) Resulting pattern of PIN1 polarisation and auxin concentrations. PIN localisation is shown in red (thicker red lines indicate a higher concentration at the cell edge). Arrows point to the region of the cell with the highest PIN concentration. Auxin concentration is shown in green (dark green indicates high concentration, light green indicates low concentration). iii) Effect of resulting auxin distribution on the levels of CUC2. CUC2 is repressed at the distal end of the tissue which has high auxin (white cells lack CUC2). iv) Graph showing auxin concentrations for the column of cells marked by the grey arrow

head in ii). Note the relatively steep inter-cellular auxin gradient across the entire array. **B)** Same simulation as in A), but with a larger array of cells. ii) Because the array is longer, centres of convergence form towards the distal end of the tissue. iii) CUC2 is cleared from the centres of convergence and from the distal rows of cells. iv) Graph showing concentrations of auxin, for the column of cells marked by the grey arrow head in ii). **C)** and **D)** Auxin distributions and PIN polarity at earlier time points of the simulation shown in B). C) i) At the beginning of the simulation, cells point proximo-distally. ii) The auxin gradient is shallow in the distal half of the array. D) i) As a consequence of the shallow auxin gradient, some cells lose their PIN polarity. ii) Cells with a loss of a polarity undergo an increase in auxin concentration.

To account for the observation that PIN1 polarity reversals occur in the proximal, rather than distal, half of the *kan1kan2* lamina, it is necessary to add a further assumption to this model. Based on the *CUC2::RFP* data (Fig. 5.3), one possibility is that, after establishment of the proximo-distal polarity field, the distribution of CUC2 changes and becomes restricted to the proximal half of the leaf, restricting PIN1 reorientations to this region. To model this, I use the same boundary conditions as for the model described above. I assume that initially all cells have CUC2, which is necessary to establish a proximo-distal polarity field. CUC2 is then removed from the distal half of the leaf, before a polarity convergence forms (Fig 5.8 Ai). This restriction of CUC2 to the proximal half of the array prevents the formation of polarity convergences in the distal half. However, this further assumption is not sufficient to cause the formation of centres of convergence in the proximal half (all polarities remain proximo-distal) (Fig 5.8 Aii and iii). This is because the strong sink at the base of the tissue, combined with a background rate of auxin production in every cell, creates a relatively steep auxin gradient in this region of the leaf (Fig 5.8 A iv). Polarities align with this auxin gradient rather than forming a centre of convergence. To form centres of convergence, a further assumption is necessary: for example, that the auxin sink at the base of the leaf is made weaker after CUC2 is restricted to the proximal half of the array (Fig 5.8 B). This disrupts the initial proximo-distal polarity field, causing a centre of convergence to form within the proximal CUC2 domain.

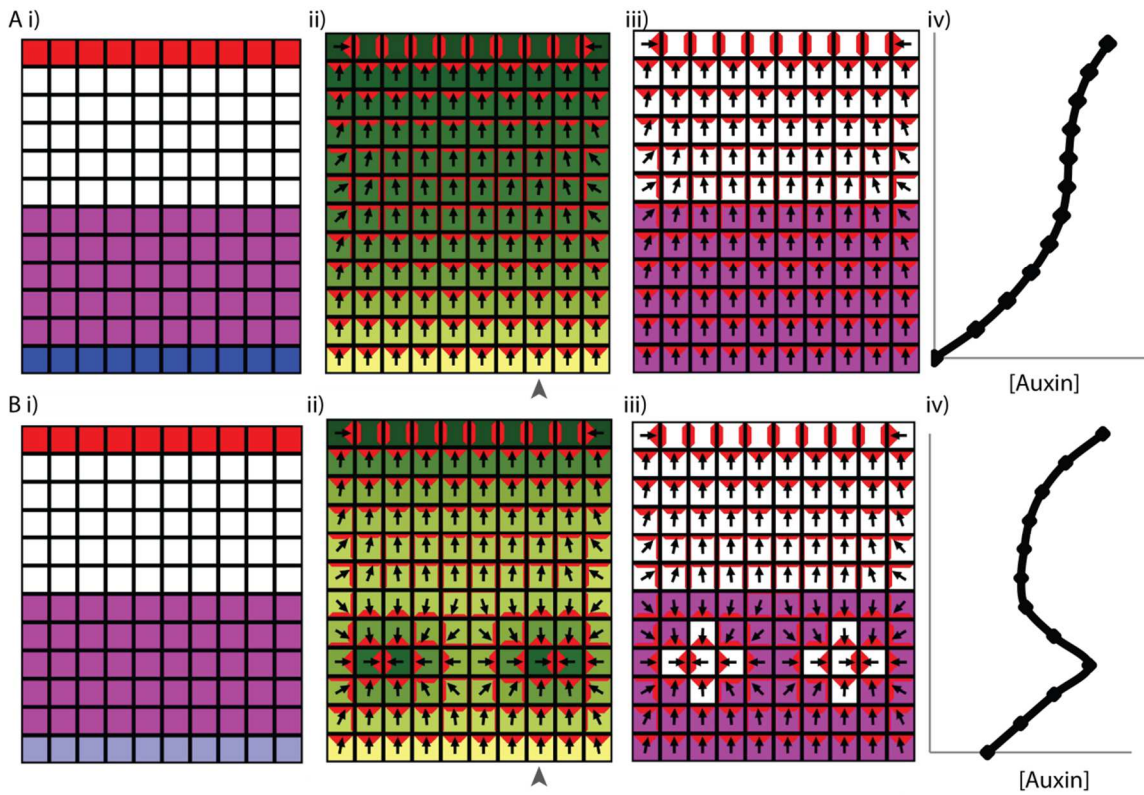


Fig 5.8 Positioning centres of convergence in the proximal half of the lamina in an up-the-gradient model with CUC2.

A) A proximo-distal polarity field is established through the presence of an auxin sink (with an auxin concentration of 0, blue cells in i) at the base of the array, and a row of cells with elevated auxin concentration (red cells) at the distal end. Initially, CUC2 is present in all cells, to allow polarity to be established, but then CUC2 (and therefore the ability to reorient PIN) is restricted to the proximal half of the tissue (magenta cells). ii) A polarity reorientation does not occur and CUC2 remains throughout the proximal half (iii). iv) Graph of auxin concentration for the column of cells marked by the grey arrow head in ii). Note that the proximal half of the tissue has a relatively steep proximo-distal auxin gradient. **B)** Same as A), but once CUC2 is restricted to the proximal half, the strength of the auxin sink at the base of the tissue is reduced (light blue cells in i). ii) As a consequence of the weak auxin sink at the base of the tissue, a centre of polarity convergence with high auxin forms in the proximal half of the tissue. iii) CUC2 expression is cleared from the centre of polarity convergence because of high auxin levels in this region. iv) Graph showing auxin concentrations for the column of cells marked by the grey arrow head in ii).

It is therefore possible to extend the Bilsborough et al., 2011 model of leaf serrations to account for the formation of a PIN1 polarity convergence in a proximal domain with elevated CUC2 expression by adding two extra assumptions: 1) that CUC2 becomes restricted to the proximal half of the leaf once a proximo-distal polarity field is generated, and 2) that an auxin sink at the base of the leaf gets weaker over time. However, this model does not account for some other experimentally observed features of PIN1 convergence formation. It does not capture the elevated expression of PIN1 in the proximal half of the lamina because no assumptions are made about how the expression of PIN1 is regulated. The model also does not take into account the observation that similarly to CUC2, the auxin biosynthesis enzyme, YUC1, is expressed throughout the proximal region of young *kan1kan2* primordia (Fig. 4.18). Finally, elevated expression of auxin importers at the tips of leaves and of *kan1kan2* outgrowths (Fig. 4.13) was not included in the model. Next, I generate an up-the-gradient model which captures these aspects of the data, but maintains the assumption that the role of CUC2 is to control the ability (or plasticity) of cells to reorient PIN. I will refer to this model as the “up-the-gradient CUC2 plasticity” model.

5.2.6.2 An up-the-gradient CUC2-plasticity model can capture all aspects of PIN1 convergence formation

To generate an initial proximo-distal polarity field, I incorporate an elevated rate of auxin import at the distal end of the tissue (Fig. 5.9 A i, cells with yellow outline), which is consistent with *LAX1::GUS* expression in this region (Fig. 4.13). I also assume that all cells have equal background rates of auxin production, and that the base of the leaf has an elevated rate of auxin degradation and therefore acts as an auxin sink (Fig. 5.9 A i, blue cells) (these assumption are not consistent with patterns of *YUC1::GUS* expression in young leaf primordia but are required to generate a proximo-distal polarity field). To allow polarity establishment across the whole tissue, CUC2 is

assumed to be present in all cells (Fig. 5.9 A, magenta). The proximo-distal polarity field generated is stable, since all cells experience a proximo-distal inter-cellular auxin gradient (Fig. 5.9 A iii).

After this initial phase of the simulation, I restrict the CUC2 domain to the proximal half of the array to match the experimentally observed expression pattern of *CUC2::RFP* (Fig. 5.9 B i). This restricts the ability of cells to reorient PINs to the proximal region. I also introduce the new assumption that auxin synthesis begins to occur at an elevated rate throughout the proximal half of the array (Fig. 5.9 B ii), consistent with expression of *YUC1::GUS* in this region. This region of elevated auxin biosynthesis may be regulated by CUC2, but, in the model shown, I assume that it is independent of CUC2. Finally, I remove the elevated rate of auxin removal from the base of the leaf. These assumptions make the auxin gradient in the proximal half of the array weak enough to generate a polarity reorientation in this region (Fig. 5.9 Ci). To capture the elevated levels of PIN1 expression at the base of *kan1kan2* leaves, I add the assumption that the total level of PIN in each cell increases with increasing auxin concentration (Fig. 5.9 Biii). And, to capture the observed expression of auxin importers at sites of polarity convergence, I assume that auxin concentrations above a threshold level induce elevated auxin import.

Together, these assumptions capture the elevated levels of PIN1 expression within the proximal domain of the leaf, and the formation of a polarity convergence in this region (Fig. 5.9 C i). Auxin importer expression (yellow outlines in (Fig. 5.9 C ii and iii) is induced in cells at the centre of polarity convergences as a consequence of auxin accumulation in these regions. As observed experimentally, CUC2 expression is cleared from the centres of convergence (Fig. 5.9 C iii), which is not specified directly in the model but occurs as a consequence of auxin accumulation in these regions (Fig. 5.9 C).

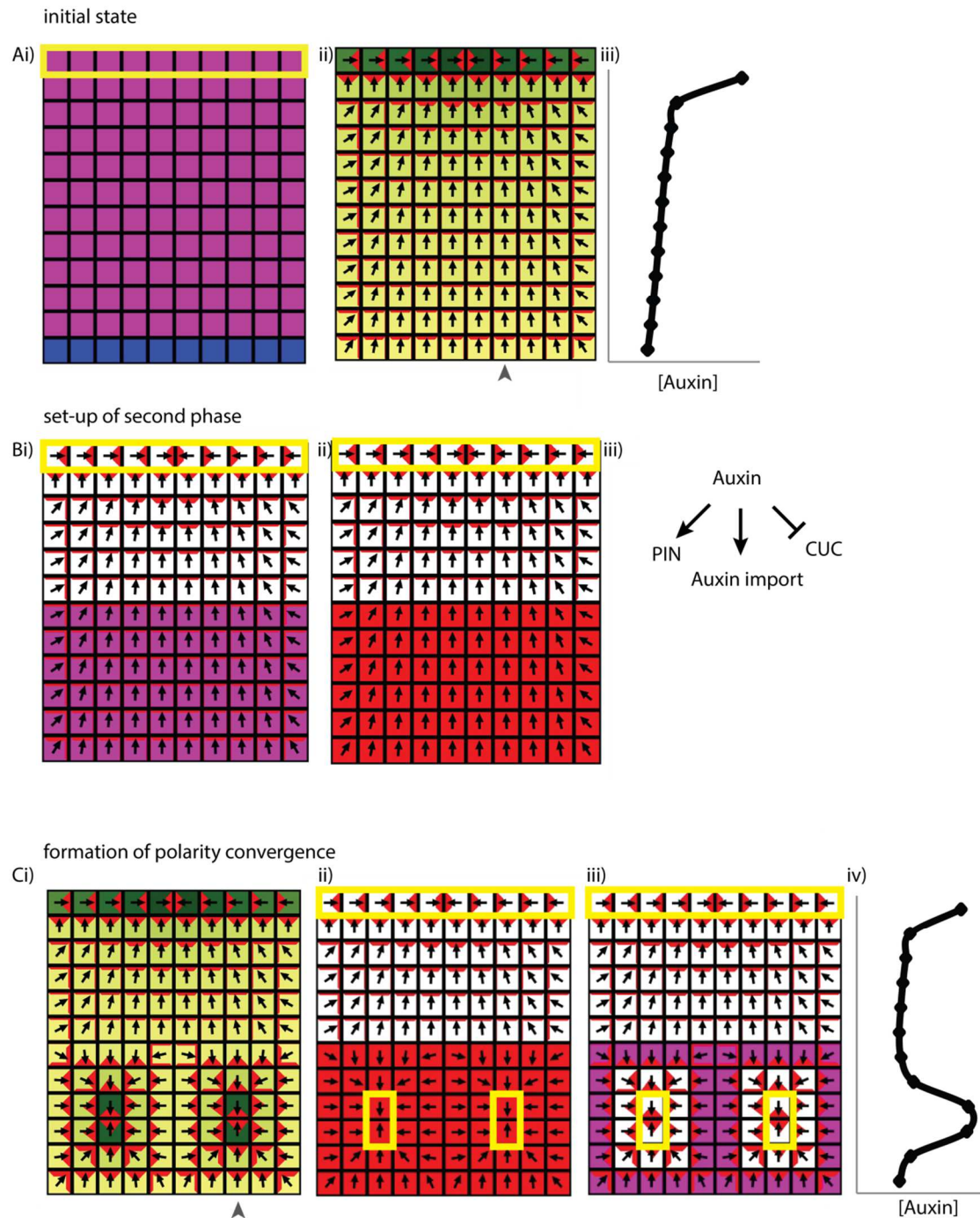


Fig. 5.9 An up-the-gradient CUC2-plasticity model for positioning centres of convergence in *kan1kan2* leaves.

A) i) Initial set up of the simulation. CUC2 is present in all cells (so PIN reorientation can occur throughout the array), the base has an elevated rate of auxin degradation (blue cells) and the distal-most row of cells has an elevated rate of auxin import (yellow outline). All cells have the same background rate of auxin production. ii) Auxin concentrations and PIN distributions at the end of the first phase of the simulation, before the CUC2 pattern changes. Polarity points distally and auxin accumulates at the leaf tip. iii) Graph showing auxin concentrations in the file of cells

marked by the grey arrow head in ii). **B)** Specified CUC and organiser pattern for the second phase of the simulation. i) CUC2 (magenta) is restricted to the proximal half of the array. ii) An elevated rate of auxin biosynthesis is also added to the proximal half of the array (red cells) and auxin degradation is removed from cells at the base. iii) From this point onwards in the simulation, it is assumed that the total level of PIN in each cell increases with increasing auxin concentration. It is also assumed that when auxin exceeds a threshold, auxin import is increased and that auxin inhibits CUC2 expression. **C)** Outcome of the second phase of the simulation. i) Auxin and PIN distributions. A PIN polarity convergence forms in the proximal region of the tissue. As a consequence of auxin promoting the levels of PIN in each cell, cells in the proximal half of the tissue have increased levels of PIN at their edges. ii) Auxin biosynthesis and import distributions. Elevated auxin biosynthesis (red cells) remains throughout the proximal half of the array. Cells at the centre of the polarity convergence have elevated rates of auxin import (yellow outlines). iii) CUC2 distribution. CUC2 is cleared from the centre of convergence as a consequence of elevated auxin concentrations in this region. iv) Graph showing concentrations of auxin for the column of cells marked by the grey arrow head in i).

In this model, the presence of elevated auxin biosynthesis in the proximal region of the tissue is required for convergence formation (when it is removed from the model presented above, a centre of convergence does not form). It is therefore possible that, an up-the-gradient mechanism generates polarity in the *kan1kan2* leaf, and that CUC2 in the proximal half of the leaf promotes auxin biosynthesis, causing the formation of centres of convergence. This raises the question of whether CUC2 regulation of plasticity (the ability of cells to reorient PIN) is required for the up-the-gradient model to capture *kan1kan2* convergence formation (perhaps the role of CUC2 is only to regulate auxin biosynthesis). If the requirement of CUC2 for polarity reorientation is removed from this model, then cells in the proximal half of the tissue still generate polarity convergences due to the presence of elevated auxin synthesis in this region (Fig. 5.10). However, the position of the centres of convergence is shifted slightly distally, and cells in the distal half of the array have polarities oriented proximally, towards the centres of convergence. Thus, the inclusion of CUC2-regulation of plasticity is therefore important to capture the restricted domain of the polarity reorientation seen in *kan1kan2* leaves.

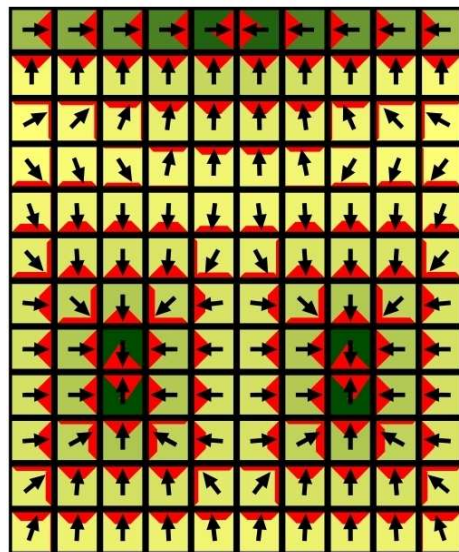


Fig. 5.10 Consequence of CUC2-independent polarity reorientation in the up-the-gradient CUC2 plasticity model.

Auxin and PIN distributions for the up-the-gradient model presented in Fig. 5.9, but with CUC-independent reorientation of polarity. Note that the centres of polarity convergence are shifted distally compared with Fig. 5.9 Ci and that cells in the distal half of the tissue have proximally oriented polarities.

In summary, the new up-the-gradient CUC2 plasticity model presented here is able to position centres of convergence in the proximal half of the tissue, taking into account the expression patterns of *CUC2*, *YUC1* and *LAX1* at the time of *kan1kan2* convergence formation. The model makes the following assumptions:

- 1) Polarity is established according to an up-the-gradient mechanism and *CUC2* is required for PIN1 polarity reorientation.
- 2) In an initial phase of the simulation, *CUC2* is present in all cells to allow establishment of a proximo-distal polarity field.
- 3) Also in this initial phase, all cells have equal rates of auxin production, auxin is degraded at an elevated rate in cells at the base of the leaf, and auxin import rates are elevated in at the distal end of the tissue.
- 4) In a second phase of the simulation, *CUC2* expression becomes restricted to the proximal half of the leaf.
- 5) In this second phase, auxin production becomes elevated in the proximal half of the leaf, and the auxin sink at the base of the leaf is removed.

6) Intracellular auxin up-regulates levels of PIN and auxin importers and down-regulates *CUC2*.

Assumptions 1-5 are required to account for the *kan1kan2* PIN1 polarity pattern, however, assumptions listed in 6 are required only to account for the expression pattern of *PIN1*, *LAX1* and *CUC2*, and are not required to account for observed polarity fields.

Although the assumptions of this model, and its outcomes, are consistent with the patterns of *PIN1*, *CUC2*, *YUC1* and *LAX1* expression at the time of convergence formation, some assumptions required to establish the initial proximo-distal polarity field are not consistent with experimental observations. The assumption that the base of the leaf acts as an auxin sink, and all cells in the tissue produce auxin at the same background rate is not consistent with the observation of *YUC1::GUS* expression at in the proximal half of young *kan1kan2* leaf primordia (Fig. 4.18). Also, it is unclear whether *CUC2* is expressed throughout very young leaf primordia.

5.2.6.3 Indirect cell-cell coupling model with regulation of auxin production by *CUC2*

I next investigate the assumptions that are required for the indirect cell-cell coupling model to account for the positioning of centres of polarity convergence in the proximal half of the *kan1kan2* lamina. A simple hypothesis is that, similarly to the up-the-gradient model presented above, the presence of *YUC1*-mediated auxin biosynthesis causes the formation of centres of convergence in the proximal half of the lamina.

As shown in chapter 4, with the indirect cell-cell coupling model, a proximo-distal polarity field may be generated in the presence of a plus organiser with elevated auxin biosynthesis at the base of the array, and a minus organiser with elevated auxin import rates at the distal end (Fig. 5.11 A). In this scenario, the intracellular auxin concentration is low and relatively uniform throughout the

array of cells, but elevated in minus organiser cells at the distal end (Fig. 5.11 A iii). If, from the beginning of the simulation, auxin biosynthesis is extended from the plus organiser at the base, throughout the proximal half of the array, a proximo-distal polarity field is still established (Fig. 5.11 B i-ii). With this new assumption, however, the profile of intracellular auxin concentrations is altered so that a second peak is present within the proximal domain with elevated auxin synthesis (Fig. 5.11 B iii, arrow). In the absence of any PIN-mediated auxin transport, this pattern of auxin biosynthesis would create a second peak in auxin concentration in the proximal-most row of cells. However, distally oriented auxin transport throughout the tissue shifts the second peak distally, so that it is positioned towards the distal side of the domain with elevated auxin biosynthesis.

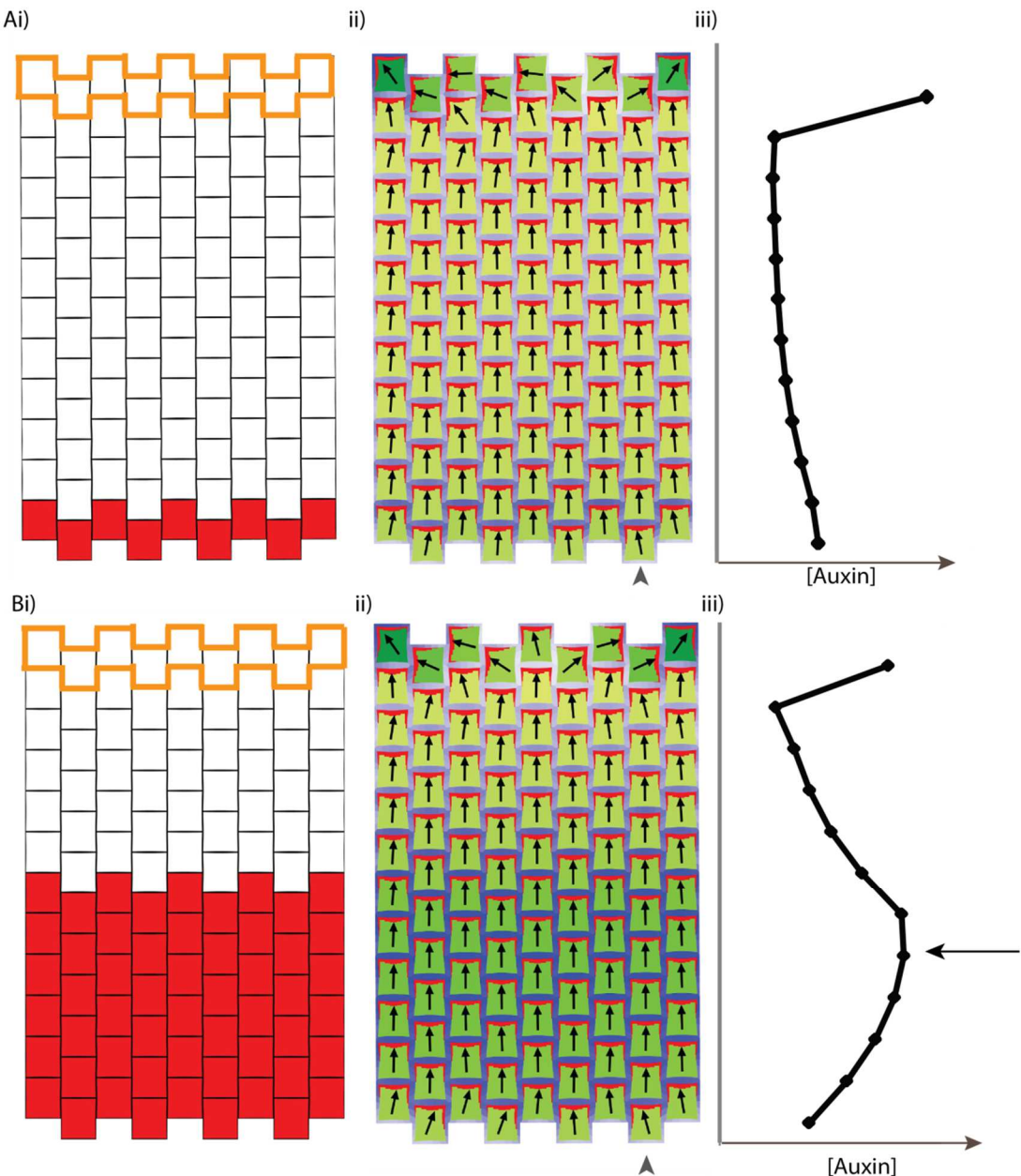


Fig. 5.11 Effect of a proximal domain with elevated auxin production rates on the intracellular auxin concentration profile in an indirect cell-cell coupling model.

A) i) Generation of a proximo-distal polarity field through elevated auxin production in the proximal-most file of cells (red cells), and elevated auxin import in the distal-most file of cells (cells with orange outline). ii) Effect on PIN polarity and auxin concentration distributions. PIN localisation is shown in red (thicker red lines indicate a higher concentration of PIN in the membrane). Arrows point to the region of the cell with the highest PIN concentration. Auxin concentration is shown in green (darkest green indicates highest concentration, light green indicates low concentration). iii) Graph of auxin distribution for the file of cells marked with the grey arrow in ii). **B**) Same as A, but with elevated auxin production in the proximal half of the tissue (red cells in i). Note the peak in auxin concentration in the proximal region of the tissue (black arrow in iii) in addition to the peak at the distal end of the array.

Given this auxin concentration profile, it is possible to induce the presence of minus organisers of polarity within the proximal domain, by assuming that intracellular auxin concentrations above a threshold level cause elevated levels of auxin import and removal (Fig. 5.12 A). If this rule is applied at a time point after the establishment of a proximo-distal polarity field according to the model in Fig. 5.11 B, all cells towards the distal half of the auxin biosynthesis domain simultaneously activate auxin import and removal (as they all have similar auxin concentrations). For individual cells within this region to acquire elevated auxin import and removal before others (generating single-celled minus organisers), some cells must acquire auxin concentrations above the threshold before others. To achieve this, I add noise in auxin concentrations throughout the simulation. I also assume that, in an initial phase of the simulation, a proximo-distal polarity field is established in the presence of elevated rates of auxin synthesis in the proximal half of the array. I then define a second phase of the simulation, in which the rate of auxin synthesis in the proximal domain gradually increases further. If a cell's auxin concentration exceeds a threshold during or after this time, it acquires elevated rates of auxin import and removal.

This causes some cells in the proximal half of the array to activate elevated auxin import and removal before others, forming minus organisers of polarity. These cells deplete auxin from the surrounding area, preventing neighbouring cells from also becoming minus organisers. Therefore, centres of polarity convergence become spaced from each other as a consequence of the changes in auxin distribution which accompany minus organiser formation (Fig. 5.12 A ii-iv).

To account for the observed differences in PIN1 expression across the *kan1kan2* leaf (Fig. 5.3), I added the rule that the production rate of PIN is proportional to the concentration of intracellular auxin. The cells at centres of polarity convergence, which have the highest auxin concentration,

have elevated levels of PIN in the membrane (Fig. 5.12 Bi and iii), similar to what was observed experimentally. Also, cells in the proximal half of the array have higher total levels of PIN in the membrane than cells in the distal half (Fig. 5.12 Bii), with the exception of cells in the distal-most row. As a consequence of their elevated auxin import rates, these distal cells have elevated intracellular auxin and elevated PIN levels compared with surrounding cells (Fig. 5.12 Bi).

In this model, the polarity reorientations are restricted to a few cells around each minus organiser. It is therefore not necessary to prevent a polarity reorientation in the distal half of the tissue by adding the assumption, which was needed in the up-the-gradient CUC2 plasticity model, that polarity reorientation is dependent on CUC2. An alternative hypothesis for the role of CUC2 in the indirect cell-cell coupling model is that it promotes the ectopic expression of *YUCCA1* throughout the proximal domain. This was incorporated into the model by assuming that CUC2 is present throughout the proximal region (red domain in Fig. 5.12) and promotes elevated auxin biosynthesis.

Clearance of CUC2 from centres of polarity convergence may be captured by assuming that when the auxin concentration exceeds a threshold level, CUC2 is removed from cells. Minus organisers have elevated auxin concentrations as a consequence of their elevated import rates and transport of auxin towards them (Fig. 5.12 Aiv, Biii), and therefore lose expression of CUC2 (Fig. 5.12 Ci, magenta cells). Because of the loss of CUC2 expression, elevated rates of auxin biosynthesis are also lost from minus organisers (Fig. 5.12 Cii, red cells). Similar to this model where CUC2 regulates auxin biosynthesis, expression of both *CUC2::RFP* and *YUC1::GUS* is absent at the tips of outgrowths where centres of convergence are present (Fig. 5.3 and Fig. 4.18).

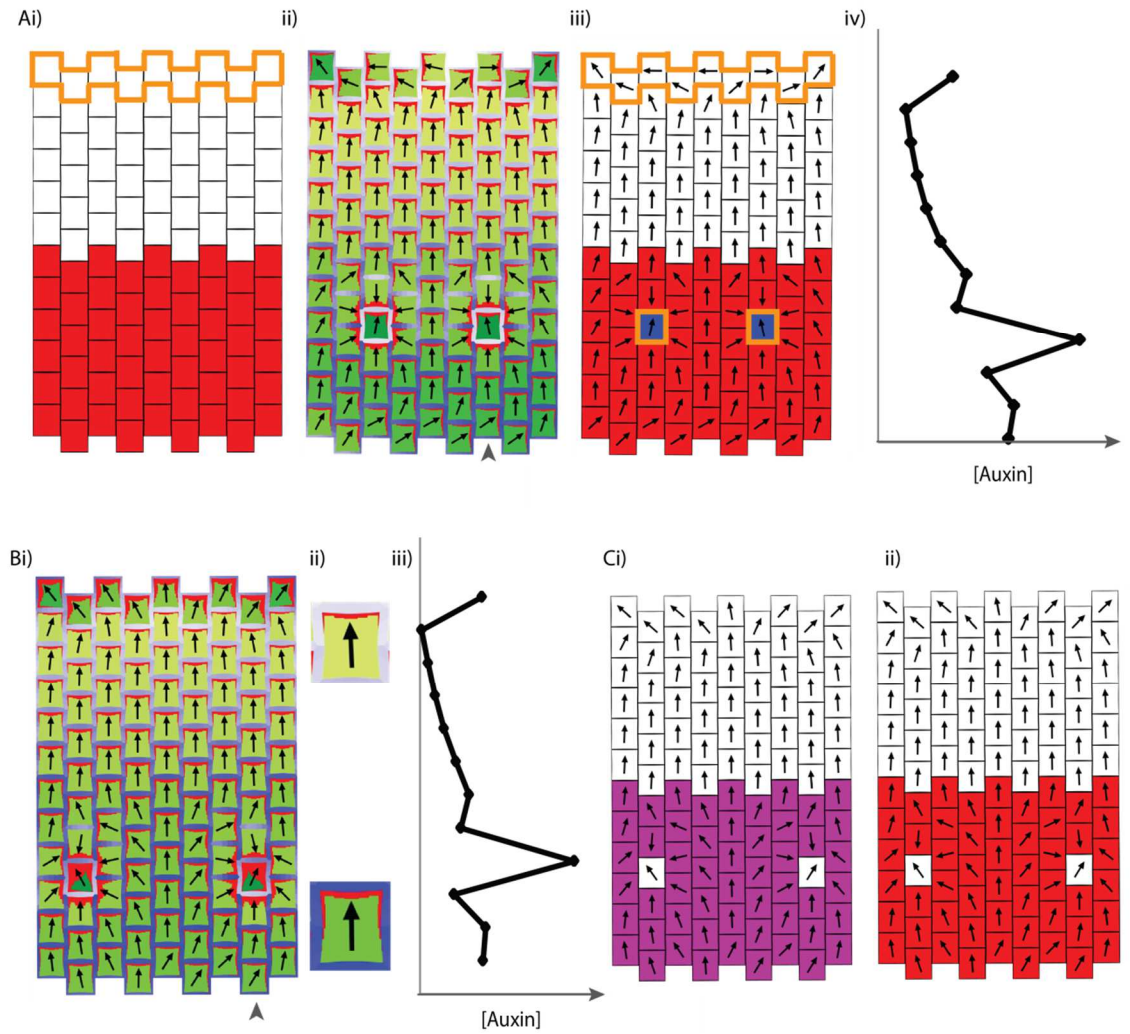


Fig. 5.12 Positioning centres of convergence in an indirect cell-cell coupling model where CUC2 promotes auxin biosynthesis.

A) i) In the first phase of the simulation, a proximo-distal polarity field is generated due to the presence of elevated auxin synthesis throughout the proximal half of the array (red cells), and elevated auxin import at the tip (cells with orange outline). In a second phase, auxin biosynthesis rates in the proximal domain gradually increase. When auxin exceeds a threshold level, elevated auxin import and removal rates are activated. ii) This causes minus organisers of polarity, and centres of polarity convergence, to be induced in the proximal half of the array. iii) Scheme showing patterns of auxin biosynthesis (red cells), auxin degradation (blue cells), and import (cells with orange outlines) following induction of the minus organisers. iv) Graph showing the concentrations of intracellular auxin for the column of cells marked by the grey arrow head in ii).

B) Same as A, but with promotion of PIN production by intracellular auxin concentration. ii) shows zoomed in images of cells from the proximal (bottom) and distal (top) of the array. **C)** For the model shown in B), CUC2 (i) and auxin biosynthesis patterns (ii) at the end of the simulation. It is assumed that intracellular auxin above a threshold represses CUC2, and that CUC2 is required to promote auxin biosynthesis.

In summary, this model includes the following assumptions:

- 1) Polarity is established according to an indirect cell-cell coupling mechanism.
- 2) *CUC2* is not required for *PIN1* polarity reorientation but promotes auxin biosynthesis.
- 3) *CUC2*, and therefore elevated rates of auxin biosynthesis, are present in the proximal half of the lamina.
- 4) Elevated intracellular auxin activates elevated rates of auxin import and removal (minus organisers), represses *CUC2*, and promotes the expression of *PIN1*. The activation of minus organisers is required to position the centres of convergence, but the promotion of *PIN1* expression and repression of *CUC2* are required only to capture the expression patterns of these genes, not for the centres of convergence to form.

This model can account for the positioning of centres of *PIN1* convergence within the proximal half of the *kan1kan2* leaf, and for their elevated levels of *LAX1::GUS* and *PIN1::PIN1::GFP* expression. The model also captures the absence of *CUC2::RFP* and *YUC1::GUS* expression at centres of convergence.

A major difference between the up-the-gradient *CUC2*-plasticity model and the indirect cell-cell coupling model is the set of assumptions required to account for the initial proximo-distal polarity field. The indirect cell-cell coupling model assumes that the proximo-distal polarity field is established in the presence of *CUC2*, and therefore elevated auxin biosynthesis, in the proximal half of the tissue. However, the up-the-gradient *CUC2*-plasticity model assumes that *CUC2* is initially expressed throughout the tissue, which has equal, and relatively low, rates of auxin biosynthesis. Only at later stages of this model are *CUC2* and elevated rates of auxin biosynthesis present in the proximal region of the tissue. The models also make different predictions about the role of elevated auxin import: in the up-the-gradient *CUC2*-plasticity model, elevated auxin import

is not required for convergence formation, but, to account for *LAX1::GUS* expression patterns, is induced at centres of convergence by high auxin. In the indirect cell-cell coupling model, elevated auxin import is induced before convergence formation and is required for PIN1 polarity reorientations.

In the up-the-gradient model, CUC2-dependent regulation of the ability of cells to reorient PIN is required to account for *kan1kan2* PIN1 polarity patterns, but CUC2 may also promote auxin biosynthesis in the proximal half of the array (which is required in this model for the centre of convergence to form). The indirect cell-cell coupling model predicts that CUC2 regulates polarity by promotion of auxin biosynthesis but does not require CUC2-dependent regulation of the ability of cells to reorient.

5.2.7 *CUC2* is required for ectopic expression of *YUC1* in *kan1kan2* leaves

To test the prediction that *CUC2* promotes auxin biosynthesis, I generated a *kan1kan2cuc2* mutant line carrying the *YUC1::GUS* reporter. In contrast to young *kan1kan2* leaf primordia, which have expression of *YUC1::GUS* throughout the proximal third of the lamina of the first leaf (Fig. 5.13 Ai), *kan1kan2cuc2* leaves of approximately the same width have a more restricted domain of *YUC1::GUS* expression at the leaf base (Fig. 5.13 Bi). As described in chapter 4, in slightly older *kan1kan2* primordia, *YUC1::GUS* is expressed in a stripe across the leaf (Fig. 5.13 Aii) and, as outgrowths emerge, expression is present at their base, on the distal side of the outgrowth (Fig. 5.13 Aiii). In contrast, similar to WT leaves (Fig. 5.13 C), *kan1kan2cuc2* mutants did not have detectable expression of *YUC1::GUS* in the lamina (Fig. 5.13 Bi-ii). This supports the hypothesis that *CUC2* promotes *YUC1*-mediated auxin biosynthesis in the leaf lamina.

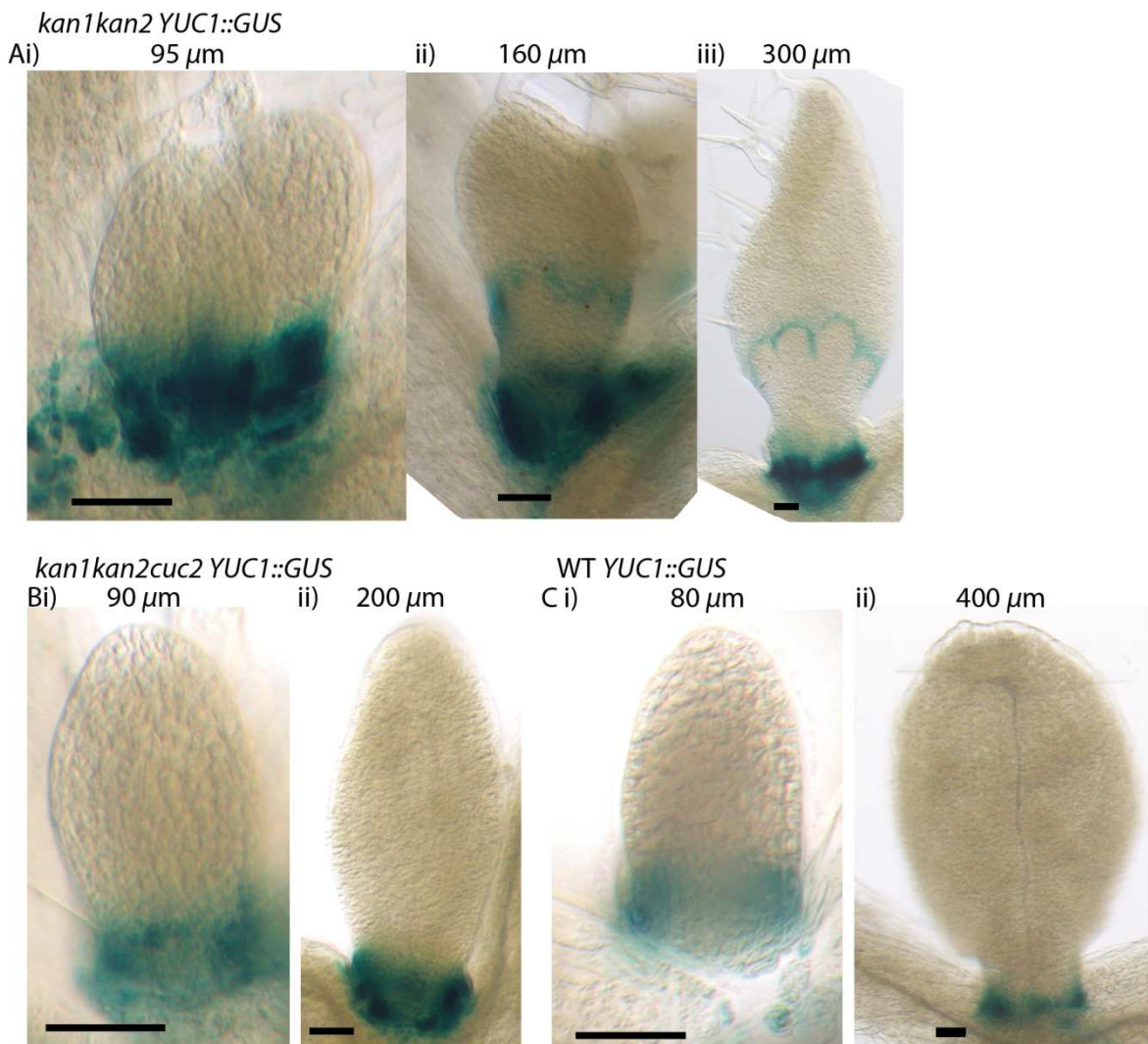


Fig. 5.13 Expression of *YUC1::GUS* in *kan1kan2* and *kan1kan2cuc2* leaf primordia.

A) *YUC1::GUS* expression in the first leaf of *kan1kan2* seedlings, showing leaves at different development stages. **B)** As for A), but for *kan1kan2cuc2* seedlings. **C)** As for A), but for WT seedlings. Each image is representative of those obtained for at least 6 seedlings with leaves at the developmental stages shown. Scale bars =50 μ m.

5.2.8 *CUC2* and *YUC* genes are required for the generation of ectopic sites of *LAX1::GUS* expression.

To test the prediction made by both models that *YUC*-driven auxin biosynthesis is required for the induction of cells with elevated auxin import, I generated *kan1kan2yuc4 LAX1::GUS* plants that

were segregating for *yuc1*. One quarter of these plants (which I assume were *kan1kan2yuc1yuc4* mutants) completely lacked ectopic outgrowths in leaf one and two, and did not have detectable points of *LAX1::GUS* activity within the lamina or leaf margin (Fig. 5.14 A, which is representative of 12 out of 48 *kan1kan2yuc4 LAX1::GUS* seedlings segregating for *yuc1*). This is in comparison to the remainder of the *kan1kan2yuc4LAX1::GUS* plants segregating for *yuc1*, and to *kan1kan2* plants, in which all observed seedlings had points of ectopic *LAX1::GUS* expression in the lamina or margin of leaf one or two (Fig. 5.14 B (n=30 WT leaves)). *kan1kan2yuc1LAX1::GUS* seedlings, with WT copies of *YUC4*, also generated ectopic outgrowths associated with *LAX1::GUS* expression. These findings suggest that *YUC1* and *YUC4*-driven auxin biosynthesis is required for ectopic expression of the auxin importer, *LAX1*, in the *kan1kan2* lamina. *LAX1::GUS* expression was also found to be dependent on *CUC2*, as *kan1kan2cuc2* mutants lacked points of elevated *LAX1::GUS* expression in the lamina (Fig. 5.14 C).

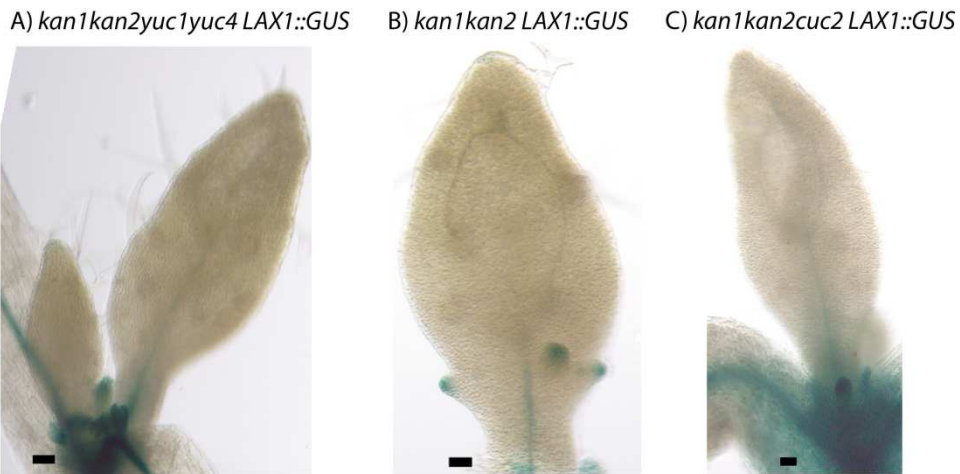


Fig. 5.14 Expression of *LAX1::GUS* in *kan1kan2yuc1yuc4*, *kan1kan2* and *kan1kan2cuc2* backgrounds.

A) *LAX1::GUS* expression in leaf one and two of a *kan1kan2yuc1yuc4* seedling. **B)** As for A), but showing leaf one of a *kan1kan2* seedling. **C)** As for A), but showing leaf one of a *kan1kan2cuc2* seedling. Images are representative of those obtained for at least 10 seedlings of each genotype, with leaves at the developmental stages shown. Scale bars =50 μ m.

5.3 Discussion

5.3.1 *CUC2* promotes outgrowth formation by up-regulating *YUC1*-mediated auxin synthesis

I show in this chapter that *CUC2* has an important role in *kan1kan2* outgrowth development, which involves up-regulation of auxin biosynthesis. Centres of PIN1 polarity convergence form within a broad domain of *CUC2* promoter activity in the proximal half of the leaf and *kan1kan2cuc2* mutants fail to generate both centres of PIN1 convergence and ectopic outgrowths (Fig. 5.1, Fig. 5.2, Fig. 5.3). Similar to *CUC2*, *YUC1* expression is elevated in the proximal region of the *kan1kan2* abaxial lamina (Fig. 4.18) and *YUC*-mediated auxin biosynthesis is required for the development of ectopic outgrowths (Wang et al., 2011 and Fig. 5.14). The ectopic expression of *YUC1* is lost in the *kan1kan2cuc2* mutant background, indicating that *CUC2* promotes outgrowth development at least partly through its effects on *YUC1* expression (Fig. 5.13).

It should be noted that the patterns of *CUC2* promoter activity revealed here using the *CUC2::RFP* reporter (Fig. 5.3 and Fig. 5.4) may not precisely reflect the activity of the *CUC2* protein since *CUC2* is post-transcriptionally regulated by a miRNA (miR164) (Nikovics et al., 2006). However, *YUC1::GUS*, which I show is expressed down-stream of *CUC2*, shows a similar expression pattern to the *CUC2::RFP* reporter, suggesting that this reporter reflects *CUC2* protein activity relatively well.

The role of *CUC2* in influencing auxin biosynthesis rates has important implications for *CUC2*-regulation of polarity but was not included in a previous model of this process (Bilsborough et al., 2011). The models presented in this chapter offer two alternative hypotheses for how elevated *YUC1*-mediated auxin biosynthesis in the proximal half of the *kan1kan2* abaxial lamina could position centres of convergence in this region. One possibility is that an up-the-gradient mechanism controls PIN1 polarity (Fig. 5.9). In this scenario, addition of elevated auxin

biosynthesis to the proximal region of an array of cells with a proximo-distal polarity field may cause a reduction in the steepness of the proximo-distal auxin gradient. This causes a transient loss of polarity, local auxin accumulation and a local polarity reorientation (Fig. 5.9). Elevated auxin importer activity, which is observed at outgrowth tips, is not required for the polarity reorientation but may be captured if import is induced by elevated auxin at the centre of convergence.

Another possibility is that an indirect cell-cell coupling mechanism controls polarity (Fig. 5.11 and Fig. 5.12). In this scenario, elevated auxin biosynthesis in the proximal half of the leaf causes a peak in intracellular auxin concentration within this region, which may locally induce elevated rates of auxin import and auxin removal. Cells with elevated rates of import and removal act as minus organisers of polarity and cause the formation of centres of PIN1 polarity convergence.

5.3.2 Distinguishing between up-the-gradient and indirect cell-cell coupling models

Although the up-the-gradient model correctly predicts the formation of centres of convergence in the presence of elevated auxin biosynthesis in the proximal half of the leaf, unrealistic assumptions are required to account for the proximo-distal polarity field which precedes outgrowth development. As discussed in the previous chapter, to account for a proximo-distal polarity field (which is present in WT leaves and in *kan1kan2* leaves prior to formation of centres of convergence), the up-the-gradient model requires the base of the leaf to act as an auxin sink. However, this is not consistent with the expression of *YUC1::GUS* at the base of young WT leaves, and throughout a broad proximal region of young *kan1kan2* leaves. These regions of elevated auxin biosynthesis at the base of young leaves are however compatible with the indirect cell-cell coupling model.

The two models also make different predictions about the role of auxin import in the generation of *kan1kan2* outgrowths. The indirect cell-cell coupling model predicts that sites of minus organiser activity, with elevated expression of auxin importers, are required for polarity reorientations. Therefore, auxin importers need to be activated prior to the formation of centres of convergence. The finding that *kan1kan2aux1lax1lax2lax3* mutants have a large reduction in the number of outgrowths (Fig 4.15) supports an important role of auxin import in outgrowth development. In contrast, with an up-the-gradient polarity mechanism, regions with elevated expression of auxin importers are not required for the formation of the polarity convergence. Importer expression may therefore be activated before or after the polarity convergence forms because locally elevated auxin levels are present at both times and could induce importer expression. In support of the assumption of both models that auxin induces elevated auxin import, expression of *LAX1::GUS* in roots was found to increase upon auxin application (Peret et al., 2012).

Time-lapse confocal imaging of *PIN1::PIN1:GFP* and a *LAX1* fluorescent reporter could help to distinguish between models, since the appearance of *LAX1* expression after formation of a polarity convergence would favour the up-the-gradient model. The two models could also be distinguished by investigating whether centres of *PIN1* polarity convergence form in a *kan1kan2aux1lax1lax2lax3* background (according to the indirect cell-cell coupling model, *PIN1* convergence formation should be disrupted, but according to the up-the-gradient model, convergences should still form).

In the up-the-gradient model of positioning centres of polarity convergence, it is necessary that only cells in the proximal half of the leaf are able to reorient *PIN*, otherwise *PIN1* reorientation may spread to the distal half of the leaf (Fig. 5.10), which is not observed experimentally. One way this can be done, is by including the experimentally observed expression of *CUC2* in the proximal

half of the leaf, and the rule that PIN polarities can only reorient in the presence of *CUC2*. The finding presented here, that *CUC2* promotes *YUC1*-mediated auxin biosynthesis, does not rule out a direct role for *CUC2* in regulating cells' ability to reorient PIN1 and is therefore compatible with the up-the-gradient model presented. Consistent with a role of *CUC2* in regulating plasticity of cells to reorient PIN1, a *CUC2::CUC2:VENUS* reporter is expressed throughout the shoot apical meristem where PIN1 polarities continuously reorient, but absent from regions of developing lateral organs which tend to maintain a fixed polarity orientation (Heisler et al., 2005; Nikovics et al., 2006).

5.3.3 The role of *CUC2* as a boundary gene

The *CUC* family of transcription factors is important for the correct establishment of organ boundaries. Expression of these transcription factors is elevated at cotyledon and floral organ boundaries and *cuc1cuc2* mutants have fused organs (Aida et al., 1997; Heisler et al., 2005; Takada et al., 2001). *CUC2* and *CUC3* are also involved in the development of serrations and are expressed in their distal indentation region, at the boundary between the serration and the main lamina (Hasson et al., 2011; Nikovics et al., 2006). Consistent with the role of *CUC2* as a boundary gene during *kan1kan2* outgrowth development, here I show that, after the initial formation of centres of PIN1 polarity convergence, *CUC2* expression is restricted to the distal side of the convergence, which will later form a boundary between the developing outgrowth and the main lamina.

It has been hypothesised that *CUC* genes contribute to boundary formation by repressing growth (Nikovics et al., 2006). The finding that *CUC2* likely influences auxin production, offers another potential explanation. In the indirect cell-cell coupling model, regions with elevated auxin biosynthesis act as plus organisers of polarity. Expression of *CUC* genes at the boundary between

organs or regions of tissue should therefore cause polarity orientations to diverge away from that boundary. *CUC* genes could therefore be involved in specifying separate polarity fields in neighbouring regions of tissue, which in turn could specify orientations of growth, as has already been proposed (Green et al., 2010; Kuchen et al., 2012; Sauret-Gueto et al., 2013). The divergent polarity fields around regions of *CUC2* expression could thus ensure that separate organs or regions of tissue maintain different orientations of growth. This could be tested by quantifying growth rates, and the principle directions of growth, around domains of *CUC2* expression (for example during the development of WT leaf serrations or *kan1kan2* outgrowths).

5.3.4 CUC-regulated polarity and adaxial-abaxial juxtaposition

There is evidence that the formation of boundaries between adaxial and abaxial cell fate could be important for outgrowth positioning and generation. The transcription factors *WOX1* and *PRS* (*WOX3*) are expressed at the adaxial-abaxial boundary in WT leaves, downstream of adaxial and abaxial identity genes (Nakata et al., 2012). *WOX1* and *PRS* are required for *kan1kan2* outgrowth development, since *kan1kan2wox1prs* mutants lack ectopic outgrowths (Nakata et al., 2012). Furthermore, ectopic expression of *WOX1* under the abaxial-specific promoter, *FIL*, is sufficient to cause the development of ectopic *kan1kan2*-like outgrowths from WT leaves (Nakata et al., 2012). One potential explanation for these findings is that when expressed in the epidermis, *WOX1* and *PRS* cause the expression of *CUC2*. In support of this hypothesis, *CUC2* is expressed at the margin of WT leaves (Nikovics et al., 2006) where adaxial and abaxial identities are juxtaposed and *WOX1* and *PRS* are expressed (Nakata et al., 2012). Also, *kan1kan2* leaves, which have ectopic expression of *CUC2* in the proximal region of the abaxial epidermis (Fig. 5.3), also ectopically express *WOX1* and *PRS* in this region (Nakata et al., 2012). It is possible that a broad domain of *WOX1* and *PRS* expression in the *kan1kan2* abaxial epidermis specifies the *CUC2* expression

domain and thus the region that is competent to form the observed centres of PIN1 polarity convergence according to the models presented here.

A second possibility is that boundary identities are present more locally within the ectopic *CUC2* expression domain of *kan1kan2* leaves. Local boundaries of adaxial and abaxial cell identity may form spontaneously and specify the precise positions of new centres of convergence. To do this, such boundaries may specify regions where minus organisers of polarity form. For an indirect cell-cell coupling system, this could involve the formation of sub-epidermal strands of *PIN1* expression which remove auxin from the epidermis, or sites of elevated epidermal *LAX1* expression, at positions of ectopic boundaries. In an up-the-gradient model, this may involve the presence of cells with elevated auxin production or import at ectopic boundary regions (as described in chapter 4). In these scenarios, *CUC2*-regulated auxin biosynthesis may be required for the generation of centres of convergence, but not influence their position.

A third hypothesis is that *CUC2*-dependent formation of centres of polarity convergence positions new adaxial-abaxial boundaries. This could explain the observation that *kan1kan2* outgrowths have elevated expression of the *YABBY* gene *FIL*, which is thought to be expressed in response to adaxial-abaxial boundary formation (Eshed et al., 2004). In support of the hypothesis that adaxial-abaxial identities are specified down-stream of centres of convergence, in the shoot apical meristem, centres of PIN1 polarity convergence and sub-epidermal strands of *PIN1* expression are found at the boundary between adaxial and abaxial identities. Importantly, it appears that the formation of centres of PIN1 convergence precedes the expression of adaxial and abaxial genes in the incipient primordium (Heisler et al., 2005).

These models could be tested by monitoring the expression of adaxial and abaxial specific genes during the development of ectopic centres of convergence in *kan1kan2* leaves. In the case of the

second hypothesis (that boundaries position centres of convergence), local boundaries of adaxial and abaxial gene expression would precede outgrowth development and predict the positions of outgrowths. In the cases of the first and third hypotheses, local boundaries that provide a pre-pattern for convergence formation would not precede outgrowth development. A more detailed analysis of the expression of *WOX1* and *PRS* prior to, and during *kan1kan2* outgrowth development could also help to clarify this issue as published data does not show whether these genes are expressed broadly or more locally in the abaxial side of *kan1kan2* leaves (Nakata et al., 2012).

The anatomical features of *kan1kan2* outgrowths argue against a role for local adaxial-abaxial boundaries in outgrowth development. Ectopic outgrowths are radially symmetric, with no obvious adaxial-abaxial tissue polarity, and have vascular tissue arranged so that a ring of phloem tissue surrounds a central region of xylem tissue (in contrast to WT leaves which have a polarised arrangement of these tissues)(Eshed et al., 2004). These vascular arrangements were also observed in the radialised leaves of *phan* mutants of *Antirrhinum majus* which have a loss of adaxial identity (Waites and Hudson, 1995). This suggests that the outgrowths do not have a clear adaxial-abaxial boundary and is most consistent with the first hypothesis, that a broad region with boundary identity (*WOX1* and *PRS* expression) functions only to define the domain with elevated *CUC2* expression.

The different hypotheses could be tested by inducing ectopic sectors of *CUC2* or adaxial or abaxial gene expression in wild-type leaves and testing their sufficiency to generate outgrowths. If ectopic expression of *CUC2* is sufficient to generate outgrowths, it would be interesting to investigate whether this involves a local change in adaxial-abaxial identity. Likewise, if ectopic expression of an adaxial gene in the abaxial side of the leaf is sufficient to generate an outgrowth,

it would be interesting to investigate whether this involves changes in PIN1 polarity and whether *CUC2* is involved in this process.

It would also be useful to investigate the role of *CUC2* in the generation of ectopic outgrowths in the *FIL::WOX1* background. Whether these outgrowths are *CUC2*-dependent is unknown. If ectopic *CUC2* expression is induced by *FIL::WOX1*, and if the outgrowths in this background are *CUC2* dependent, this would suggest that the ectopic presence of an adaxial-abaxial boundary identity functions up-stream of *CUC2* in the generation of outgrowths. However, if *CUC2* is not required for *FIL::WOX1* ectopic outgrowths, this would suggest that in *kan1kan2* leaves, *CUC2*-dependent polarity convergences may function upstream of the specification of ectopic adaxial-abaxial boundaries.

5.3.5 *kan1kan2* outgrowths and serration development

The findings presented in this and in the previous chapter provide new evidence that the formation of *kan1kan2* outgrowths occurs via similar mechanisms to leaf serration development. In both cases, centres of PIN1 polarity convergence predict sites of new outgrowths and first form within a broad domain of *CUC2* promoter activity in a *cuc2*- and *yuc*-dependent manner (Fig. 5.1, Fig. 5.2, Fig. 5.3, Bilsborough et al., 2011, Wang et al., 2011). Also, *LAX1* expression is elevated at the tips of both types of outgrowth (Fig. 4.13). Finally, when serrations and *kan1kan2* outgrowths emerge, the expression of *CUC2* and *YUC1* is restricted to their distal side (Fig. 4.18, Fig. 5.3, Nikovics et al., 2006; Wang et al., 2011). The finding that *kan1kan2* outgrowth development is similar to serration development is consistent with a previous report that ectopic outgrowths have margin-like cell shapes and express an enhancer trap reporter which, in WT leaves, is only expressed in the margin (Eshed et al., 2004).

However, there are likely to be important differences associated with the development of these two types of outgrowths. Serrations form at the adaxial-abaxial boundary that is specified when new primordia form at the shoot apical meristem (Heisler et al., 2005). They therefore share a middle identity domain with the rest of the leaf and grow in the same plane as the rest of the leaf. However, *kan1kan2* outgrowths grow out of the main plane of the leaf and have their own central identity region with strands of vascular tissue which are perpendicular to central domain of the main lamina (Eshed et al., 2004). How this central vascular region is established in *kan1kan2* outgrowths, and how their growth is specified to occur out of the main plane of the leaf will be addressed in the following two chapters.

5.4 Methods

5.4.1 Imaging procedures

OPT imaging, confocal imaging, including time-lapse confocal imaging, and GUS staining were performed as described in Chapter 4.

5.4.2 *A.thaliana* mutant and transgenic lines

5.4.2.1 Reporter lines

The *CUC2::RFP* marker was provided by Patrick Laufs. This marker is in the Col-0 background and confers Hygromycin resistance to plants. The *PIN1::PIN1:GFP*, *LAX1::GUS* and *YUC1::GUS* markers are as described in chapter 4. All reporter constructs were introduced into the *kan1kan2* background by crossing as described in chapter 4.

5.4.2.2 Generation of *kan1kan2cuc2* mutants

kan1kan2cuc2 mutants were generated by crossing *kan1kan2+/-* plants with *cuc2-3* mutants which were obtained from the Syngenta Arabidopsis Insertion Library collection (Sessions et al., 2002). In the F2 of this cross, *kan1kan2+/- cuc2* individuals were identified by screening for the *kan1kan2+/-* fruit phenotype, and by PCR-based screening for *cuc2-3* homozygous individuals. The presence of a T-DNA insertion in the *CUC2* locus was detected by using a forward primer, which binds to the T-DNA: 5'-TCCATAACCAATCTCGATACAC-3' and a reverse primer which binds within the *CUC2* locus downstream of the T-DNA insertion (referred to as CUC2-R): 5'-GGAGGCTAAAGAAGTACCATTC-3'. The presence of a WT copy of *CUC2* was detected using a forward primer CUC2-F: 5'-AATATCCATCCACATTATTACCAC-3', which binds to *CUC2* upstream of the site of the T-DNA insertion in *cuc2-3*, along with CUC2-R. One quarter of the offspring of *kan1+/- kan2 cuc2* individuals were *kan1kan2cuc2* mutants, and could be identified at the seedling stage (and therefore selected for experiments) based on the upwardly curled cotyledon phenotype of *kan1kan2* mutants.

kan1kan2cuc2PIN1::PIN1:GFP, *kan1kan2cuc2YUC1::GUS* and *kan1kan2cuc2LAX1::GUS* lines were generated by crossing *kan1kan2+/-cuc2* plants with *kan1kan2+/-* plants carrying the reporters of interest and selecting plants with the desired alleles and reporters from F2s.

5.4.2.3 Generation of *kan1kan2yuc1yuc4 LAX1::GUS* plants

The *kan1kan2+/- yuc1+/- yuc4* mutants used are as described in (Cheng et al., 2006; Wang et al., 2011). *kan1kan2+/-yuc1+/-yuc4 LAX1::GUS* plants were selected in an F2 of a cross between *kan1kan2+/- yuc1+/- yuc4* plants and *LAX1::GUS* plants. F2 seedlings with the *LAX1::GUS* construct were by selected for sowing seeds on plates containing 50 µg/ ml Kanamycin. Those that were *kan1kan2+/-* mutants were identified based on their fruit phenotype and the presence of the

yuc1+/-yuc4 genotype was selected for by PCR-based genotyping. The *yuc1* and *yuc4* alleles have T-DNA insertions, and mutant alleles were screened for using the following primers for *yuc1*: LBb1: 5'-GCGTGGACCGCTTGCTGCAAC-3' and YUC1-R: 5'-CCTGAAGCCAAGTAGGCACGTT-3' and the following primers for *yuc4*: LBb1: 5'-GCGTGGACCGCTTGCTGCAAC-3' and YUC4-R: 5'-GCCCAACGTAGAATTAGCAAG-3'. WT copies of *YUC1* were screened for using YUC1-F: 5'-GGTCATGTGTTCCAAGGG-3' and YUC1-R and WT copies of *YUC4* were screened for using YUC4-F 5'-CCCTTCTTAGACCTACTCTAC-3' and YUC4-R. To analyse the expression of *LAX1::GUS* in *kan1kan2yuc1yuc4* mutants, the offspring of *kan1kan2+/-yuc1+/-yuc4 LAX1::GUS* or *kan1kan2+/yuc1+/-yuc4 LAX1::GUS+/-* plants were sown on plates containing 50 µg/ ml Kanamycin (to select against any plants without a copy of the *LAX1::GUS* transgene), and seedlings with a *kan1kan2* phenotype were selected and stained to reveal GUS activity. Of these seedlings, one quarter did not have outgrowths, and were therefore assumed to be *kan1kan2yuc1yuc4* mutants (since *kan1kan2* seedlings were consistently observed to develop outgrowths from their first two leaves).

5.4.3 Model descriptions

5.4.3.1 Up-the-gradient model

The simulations of the up-the-gradient model used to generate Figs. 5.7, 5.8, 5.9 and 5.10 were all implemented as described in Chapter 3 (equations 3.1 to 3.5). However, in the simulations presented in this chapter, CUC2 is represented in the model and its production, decay and effect on PIN polarisation are simulated as described by Bilsborough et al., 2011.

The system is initialised with a default concentration of CUC in all cytoplasmic compartments.

$$CUC(t = 0) = c_{CUC} \quad (5.1),$$

Where CUC ($t= 0$) is the concentration of CUC at the initial time point of the simulation, and c_{CUC} is the default initial concentration of CUC in cytoplasmic compartments, with units of $A_u/\mu\text{m}^2$. In all simulations, $c_{CUC} = 0.02 A_u/\mu\text{m}^2$.

At each time step of the simulation, the production and decay of CUC are simulated in each cell. Auxin inhibits the production of CUC, and promotes its degradation. The equation describing the rate of change of CUC concentration for a cytoplasmic compartment is:

$$\frac{\partial CUC}{\partial t} = \frac{\rho_{CUC}}{1 + \kappa_{CUC} A} \cdot CUC - (\nu + \nu_A A) CUC \quad (5.2)$$

Where CUC is the concentration of CUC in the given cytoplasmic compartment, ρ_{CUC} is the production rate of CUC, with units of $A_u / \mu\text{m}^2 \cdot \text{s}$, κ_{CUC} is a dimensionless constant describing the sensitivity of CUC production to being down-regulated by auxin, A is the concentration of auxin in the given cytoplasmic compartment, ν is the default degradation rate of CUC, with units of $/ \text{s}$ and ν_A is the rate of auxin-dependent CUC degradation, with units of $\mu\text{m}^2 / A_u \cdot \text{s}$.

In all simulations, $\rho_{CUC} = 0.63 A_u / \mu\text{m}^2 \cdot \text{s}$, $\nu = 3.6 / \text{s}$ and $\nu_A = 0.18 \mu\text{m}^2 / A_u \cdot \text{s}$.

In the simulations used to generate Fig. 5.7 and Fig. 5.8, $\kappa_{CUC} = 1.6$. In the simulation used to generate Fig. 5.9 and 5.10, $\kappa_{CUC} = 1.8$.

It is assumed that the CUC concentration cannot exceed a maximum value, CUC_{MAX} . In all simulations, $CUC_{MAX} = 0.05 A_u / \mu\text{m}^2$.

The effect of CUC on the ability of cells to reorient PIN proteins is implemented by assuming that when a cell's CUC concentration is below a threshold, T_{CUC} , the concentration of PIN at all the edges of the cell remain constant. In all simulations, $T_{CUC} = 0.01 A_u / \mu\text{m}^2$. When the concentration

of CUC exceeds this threshold, the concentration of PIN at the edges of a cell is calculated according to equation 3.3.

Details regarding the implementation of each simulation are described below.

Fig 5.7. Positioning of centres of convergence in an up-the-gradient model with CUC2. To generate A, B and C), simulations are implemented as described above, with non-CUC related parameter values detailed in Table 5.1. In the distal most file of cells, the auxin concentration is set to $0.12 A_u / \mu\text{m}^2$ throughout the simulation, and in the proximal most file of cells, the auxin concentration is set to 0.

Fig 5.8 Positioning of centres of convergence in the proximal half of the lamina in the up the gradient model with CUC2. To generate A), where CUC2 is restricted to the proximal half of the tissue following establishment of polarity, the model is implemented as for Fig. 5.7, except that after 3.9 s of the simulation, the concentration of CUC2 in the distal half of the tissue is fixed to 0. The simulation used to generate B) is implemented as described for A), but after 100s of the simulation, the concentration of auxin in the proximal-most file of cells is raised from 0 to $0.08 A_u / \mu\text{m}^2$ (the sink becomes weaker).

Fig 5.9 An up-the-gradient CUC2-plasticity model for positioning centres of convergence in kan1kan2 leaves. In the initial phase of the simulation, the distal-most file of cells has an elevated auxin import rate ($I = 0.2 \mu\text{m} / \text{s}$ in the distal most file, in all other cells, $I = 0 \mu\text{m} / \text{s}$) and the proximal most file of cells has an elevated rate of auxin degradation ($\mu = 0.05 / \text{s}$ in the proximal most file, but $\mu = 0.001 / \text{s}$ in all other cells). These boundary conditions allow the establishment of a proximo-distal polarity field.

After the establishment of the proximo-distal polarity field, after 400s of the simulation, the concentration of CUC in the distal-most half of the tissue is set to 0. Also, the auxin production rate (σ) in the proximal half of the tissue is elevated to 0.05/s (compared with 0.01 in all other cells). Additionally, the elevated auxin degradation rate in the proximal-most file of cells is removed, so that $\mu = 0.001 /s$ in all cells.

After 400s of the simulation (in its second phase), if the auxin concentration of a cell exceeds a threshold level, $\text{Thresh}_{\text{import}}$, the auxin import rate, I , of the cell is set to $0.2 \mu\text{m}/\text{s}$. $\text{Thresh}_{\text{import}} = 0.13 \text{ A}_u / \mu\text{m}^2$. Also, the total concentration of PIN in the cell available for binding to cell edges (PIN_i) is allowed to vary between cells depending on their auxin concentration. At each time step of the simulation, PIN_i is calculated for a given cell, cell i , as follows:

$$\text{PIN}_i = d\text{PIN} + \gamma A_i \quad (5.3)$$

Where $d\text{PIN}$ is the default concentration of PIN available for binding to a cell edge, with units of $\text{A}_u/\mu\text{m}$, γ is a constant describing the extent to which auxin in the cytoplasmic compartment promotes the level of PIN available for binding to a cell edge, with units of μm , and A_i is the auxin concentration in cell i . $d\text{PIN} = 0.1 \text{ A}_u / \mu\text{m}$ and $\gamma = 0.6 \mu\text{m}$.

Fig 5.10 Consequence of CUC2-independent polarity reorientation in the up-the-gradient CUC2 plasticity model. The simulation is implemented as described for Fig. 5.9, except the concentration of PIN at a cell edge does not remain fixed once the concentration of CUC drops below T_{CUC} (the allocation of PIN to the edges of each cell is calculated independently of the concentration of CUC in the cell).

Fig	C_A Au/ μm^2	ϵ	$C_{PINedge}$ Au/ μm	ϵ_{PIN}	PIN_i Au/ μm	b	σ /s	H Au/ μm^2	R μm^2	l μm	μ /s	D $\mu\text{m/s}$	T $\mu\text{m}^2/\text{Au.s}$
5.7, 5.8	0.01	0	0.025	0	0.1	6	0.4	0.1	25	5	0.005	32.4	51.9
5.9, 5.10	0.01	0	0.025	0	0.1 for first part of simulation, see text	6	0.01	0.1	25	5	0.001	32.4	51.9

Table 5.1. Parameter values used in up-the-gradient simulations.

C_A is the default initial concentration of auxin in cytoplasmic compartments, ϵ is the limit for noise addition to C_A , $C_{PINedge}$ is the default initial concentration of PIN at each cell edge, ϵ_{PIN} is the limit for noise addition to $C_{PINedge}$, PIN_i is the total amount for PIN available for binding to the membrane in cell i , b is the exponentiation base for PIN allocation to the membrane, σ is the auxin production rate, H is the target auxin concentration, R is the area of cytoplasmic compartments, l is the length of cell edge compartments, μ is the auxin degradation rate, D is the passive permeability of auxin and T is the rate of PIN-mediated auxin transport. Parameter values related to the production and degradation of CUC are described in the main text.

5.4.3.2 *Indirect cell-cell coupling model*

Unless otherwise stated below, simulations of the indirect cell-cell coupling model are implemented as described in Chapter 4. All PIN-related parameter values are as described in Table 4.3, except ψ_{PIN} , the PIN-dependent auxin efflux rate, =30 $\mu\text{m}^2/\text{A.u.s}$. All other (non-PIN related) parameter values are as described in Table 2.1, except ϵ , the limit for noise addition to the initial concentrations of polarity components in the membrane = 0.0083, ρ_{Aux} , the production rate of auxin, = 1×10^{-4} $\text{A.u}/\mu\text{m}^2\text{s}$ and μ_{Aux} , the rate of auxin degradation, = 0.01 /s. The system is initialised with an auxin concentration in each cell of 0.001 $\text{A.u}/\mu\text{m}^2$.

Fig 5.11 Effect of a proximal domain with elevated auxin production rates on the intracellular auxin concentration profile in an indirect cell-cell coupling model. In the simulation used to generate A), in the proximal-most file of cells, there is an elevated auxin production rate (p_{Aux}) of $7 \times 10^{-4} \text{ A}_u / \mu\text{m}^2 \cdot \text{s}$ and in the distal-most file of cells, the inwards permeability of auxin, $v_{in} = 2.25 \mu\text{m} / \text{s}$ (three-fold elevated compared with in other cells). The simulation shown in B) is implemented as for A), except, in the proximal-most file of cells, $p_{Aux} = 9 \times 10^{-4} \text{ A}_u / \mu\text{m}^2 \cdot \text{s}$, and in the other cells in the proximal half of the canvas, $p_{Aux} = 5 \times 10^{-4} \text{ A}_u / \mu\text{m}^2 \cdot \text{s}$.

Fig. 5.12 Positioning centres of convergence in an indirect cell-cell coupling model where CUC2 promotes auxin biosynthesis. The simulation shown in A) is implemented as for Fig. 5.11 B, except in the first 6500 seconds of the simulation, the production rate of auxin, p_{Aux} , in the proximal-most file of cells, $= 7 \times 10^{-4} \text{ A}_u / \mu\text{m}^2 \cdot \text{s}$. In this first phase of the simulation, the production rate of auxin in all other cells in the proximal half of the array is $5 \times 10^{-4} \text{ A}_u / \mu\text{m}^2 \cdot \text{s}$. Then, between 6500 and 10 000 s of the simulation, the auxin production rate of all cells in the proximal half of the array (including those in the proximal-most file) is increased at every time step of the simulation:

$$\frac{d\rho_{Aux}}{dt} = \alpha_{Aux} \quad (5.4)$$

Where p_{Aux} is the auxin production rate of a given cell and α_{Aux} is a constant describing the rate of increase of the auxin production rate, with units of $\text{A}_u / \mu\text{m}^2 \cdot \text{s}^2$ ($\alpha_{Aux} = 2 \times 10^{-7} \text{ A}_u / \mu\text{m}^2 \cdot \text{s}^2$). As a consequence of this increase in the auxin production rate, after 10 000 s of the simulation, in the proximal-most file of cells, $p_{Aux} = 1.4 \times 10^{-3} \text{ A}_u / \mu\text{m}^2 \cdot \text{s}$, and in the other cells in the proximal-most half of the leaf, $p_{Aux} = 1.2 \times 10^{-3} \text{ A}_u / \mu\text{m}^2 \cdot \text{s}$.

After 6 500 s of the simulation, if the auxin concentration of a cell exceeds a threshold, T_{import} , the inwards permeability of the cell to auxin is increased 15-fold ($v_{in} = 11.25 \mu\text{m/s}$) and the auxin degradation of the cell is increased 12-fold so that $\mu_{\text{Aux}} = 0.12 /s$. $T_{\text{import}} = 0.085 \text{ A}_u/\mu\text{m}^2$.

Noise is added to the concentrations of auxin every 0.1s of the simulation, according to the following equation:

$$Aux_n = Aux + (\theta_{\text{Aux}} * \sqrt{Aux}) \quad (5.5),$$

where Aux_n is the concentration of auxin in a given cytoplasmic compartment after the addition of noise with units of $\text{A}_u/\mu\text{m}^2$, Aux is the concentration of auxin in that compartment before the addition of noise (with the same units), θ_{Aux} is a random number drawn from a normal distribution, with mean 0, and standard deviation 1×10^{-6} . Noise is added to the concentration of auxin in proportion to the square root of the auxin concentration.

The simulation used to generate Fig. 5.12 B is performed as for Fig. 5.12 A, except that PIN is produced and degraded in all cells, with a production rate that is dependent on the auxin concentration of the cell. Equation 4.3, describing the rate of change of PIN concentration in the cytoplasm is therefore modified to become:

$$\frac{\partial PIN_c}{\partial t} = \alpha_{PIN} Aux - \beta_{PIN} PIN_c - \frac{1}{R_c} \sum_{n \in N(c)} l_n ((\rho_{PIN} + \tau A^* n) PIN_c - \mu_{PIN} PIN_n) \quad (5.6)$$

Where PIN_c is the concentration of PIN in the given cytoplasmic compartment, α_{PIN} is the rate of auxin-dependent PIN production, with units of $/s$ and β_{PIN} is the rate of PIN degradation, with units of $/s$. The second half of the equation describes PIN binding and unbinding from the edges of

the cell and is as described for Equation 4.3. In the simulation used to generate 5.12 B, $\alpha_{PIN} = 2 \times 10^{-5} /s$ and $\beta_{PIN} = 4 \times 10^{-3} /s$.

In this simulation, c_{PIN} , the default initial concentration of PIN in cytoplasmic compartments = $0.0015 \text{ A}_u/\mu\text{m}^2$. The simulation also differs from that used to generate Fig 5.12 A because the rates of auxin import and degradation are higher in cells at the distal end of the tissue, so that in these cells, the auxin degradation rate, $\mu_{Aux} = 0.012 /s$ and the inwards permeability of the cell to auxin, $v_{in} = 3 \mu\text{m} /s$. Also, to simulate repression of CUC2, and therefore of auxin biosynthesis, by elevated auxin, when the auxin concentration of a cell exceeds a threshold (the same threshold used to regulate auxin import, T_{import}) the auxin production rate of this cell, ρ_{Aux} is set to $1 \times 10^{-4} \text{ A}_u/\mu\text{m}^2 \cdot s$ (the same as cells in the distal half of the array).

6 Integration of polarity in the epidermis and sub-epidermis through indirect cell-cell coupling

6.1 Introduction

So far, I have focussed on the generation of polarity patterns in the epidermis of *kan1kan2* leaves. However, changes in epidermal PIN1 polarity are often linked with the development of specific patterns of PIN1 localisation in sub-epidermal tissue. For example, in shoot apical meristems of *A.thaliana* and tomato, at early stages of the formation of epidermal centres of PIN1 convergence, sub-epidermal cells below the convergence localise PIN1 apically, towards the epidermis (Bayer et al., 2009). As primordia begin to emerge, cells at the centre of the epidermal polarity convergence have basally localised PIN1 and are connected to a strand of sub-epidermal cells which also localise PIN1 basally (Bayer et al., 2009; Benkova et al., 2003; Reinhardt et al., 2003). Sub-epidermal cells adjacent to this strand have oblique and lateral polarities oriented towards it (Bayer et al., 2009). Such sub-epidermal strands of basally localised PIN1 specify the site of the leaf midvein (I therefore sometimes refer to them as pro-vascular strands). Similar to cells at the epidermal centre of convergence, cells in the sub-epidermal PIN strand have elevated expression of the auxin-responsive reporter *DR5::GFP* (Scarpella et al., 2006).

During the formation of the leaf midvein, the sub-epidermal strand with elevated PIN1 expression appears to propagate away from the site of epidermal polarity convergence towards existing vascular tissue in the stem (Bayer et al., 2009). In this case, the strand of cells with elevated PIN1 levels therefore propagates in the same direction as the PIN1 polarity (forwards propagation, Fig. 6.1). However, there is evidence, from observations of leaf vascular development and from experiments on pea epicotyls, that strands of cells with elevated levels of PIN1 may also

propagate backwards, in the opposite direction to the PIN1 polarity, away from an auxin sink (Sauer et al., 2006; Scarpella et al., 2006) (backwards propagation, Fig. 6.1).

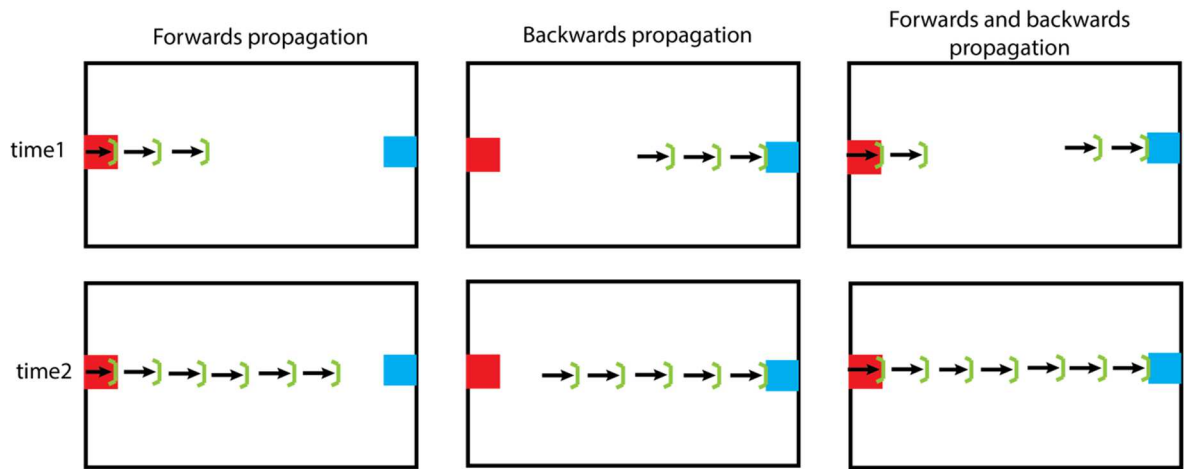


Fig. 6.1 Forwards and backwards propagation of sub-epidermal PIN1 strands.

Two subsequent time points are illustrated for each mode of propagation. Red squares indicate auxin sources, blue squares indicate auxin sinks. Green lines indicate high levels of PIN1 and arrows show directions of PIN1 polarities. With forwards propagation (which appears to occur during the development of the leaf midvein (Bayer et al., 2009)), elevated levels of PIN1 occur first near an auxin source, and then propagate, along the direction of polarity, away from the source. With backwards propagation (which appears to occur during the development of some leaf vascular strands (Scarpella et al., 2006)), elevated levels of PIN1 occur first near an auxin sink, and then propagate, in the opposite direction to the polarity, away from the auxin sink towards an auxin source. To generate connected strands with elevated PIN1, forwards and backwards propagating strands must connect.

Experiments in pea involved ectopic application of auxin to the side of epicotyls that had recently been wounded above the site of auxin application (Sauer et al., 2006). In this scenario, one day after auxin application, cells with ectopic PIN1 expression were observed close to the central vascular tissue and these cells had polarity oriented away from the ectopic auxin source. Three days after application of auxin, ectopic PIN1 expression extended through the epicotyl spanning the region between the central vascular tissue and the point of auxin application in the epidermis.

It therefore appears that the elevated levels of PIN1 propagate backwards from an auxin sink (the vascular tissue) to the auxin source, whilst maintaining polarity oriented towards the sink.

Propagation of strands with elevated expression of PIN1 also appears to occur in the opposite direction to PIN1 polarity during the formation of second order vein loops in the *A.thaliana* leaf (Scarpella et al., 2006). These loops form in two phases, after the central pro-vascular strand of the future mid-vein has developed. First, the lower part of the loop forms through PIN strand propagation between an epidermal convergence in the leaf margin and the existing pro-vascular strand of the midvein. Secondly, the upper part of the loop appears to propagate distally (towards the leaf tip) from the lower part of the loop. During this process of distal-wards strand propagation, cells in the developing strand have polarities oriented proximally, towards the lower part of the loop, suggesting that the PIN1 strand propagates in the opposite direction to the polarity. Models of sub-epidermal PIN1 strand formation should therefore be assessed for their ability to capture both forwards and backwards propagation of PIN strands. To generate connections between vascular strands, forwards and backwards propagating strands most-likely connect with each other (forwards and backwards propagation, Fig. 6.1) and this feature should also be captured by models of pro-vascular strand formation. The flux-based model is currently the most successful at capturing features of leaf vascular development, including forwards and backwards propagation of sub-epidermal PIN strands (Feugier et al., 2005; Rolland-Lagan and Prusinkiewicz, 2005).

Several models have been proposed for how epidermal centres of convergence may be coupled with sub-epidermal PIN1 strands. One hypothesis is that the up-the-gradient model generates both types of polarity pattern. With this model, if intracellular auxin promotes the expression of PIN, travelling waves of high auxin, which cause the formation of strands of cells with high PIN expression, may develop (Merks et al., 2007). Given an epidermal cell which has an elevated level

of auxin, underlying sub-epidermal cells will initially orient their polarity up-the-gradient, towards this epidermal cell. With specific boundary conditions used in the model of Merks et al., 2007, the epidermal cell orients its polarity basally, towards sub-epidermal cells. Elevated auxin in the epidermal cell causes it to express high levels of PIN, which lowers its auxin concentration (due to a higher rate of efflux) but raises the auxin concentration of a cell below. The cell below will orient its polarity away from the epidermal cell which now has a low auxin concentration. This sub-epidermal cell will acquire high levels of PIN, passing auxin to the cell below. The next cell below will then orient its polarity basally, allowing the strand to further propagate in the same way. This model requires the auxin concentration at the centre of convergence to decrease as the sub-epidermal strand of PIN develops. This is problematic because *DR5::GFP* expression suggests high auxin concentrations are maintained at the tips of primordia during sub-epidermal PIN strand formation (Heisler et al., 2005; Scarpella et al., 2006)

An alternative hypothesis is that a flux-based model underlies the formation of both the epidermal centre of convergence and the sub-epidermal PIN strand. A computational model based on this hypothesis can account for the coupled formation of both types of polarity pattern and the spacing between successive primordia in the shoot apical meristem (Stoma et al., 2008). This model assumes that PIN1 allocation to the membrane increases linearly with increasing auxin flux in the epidermis but increases quadratically with auxin flux in sub-epidermal tissue. It is also assumed that, due to elevated auxin import in epidermal cells, auxin is not exchanged between the epidermis and sub-epidermis except at sites of incipient primordia. When the auxin concentration in the epidermis reaches a threshold level (at a distance from existing primordia), auxin movement between the epidermis and sub-epidermis may occur. This triggers the formation of a sub-epidermal strand of PIN which, in turn, creates a local depletion of auxin in the epidermis, triggering the formation of a centre of convergence. This model has been criticized because, like the up-the-gradient model presented above, it predicts a transient auxin minimum

in the epidermis which has not been observed experimentally (Bayer et al., 2009). Also, although the model includes a role for auxin import in the epidermis, it does not include or account for experimental observations of higher epidermal auxin importer expression at sites of incipient primordia (Bainbridge et al., 2008; Reinhardt et al., 2003).

A third hypothesis is that both up-the-gradient and flux-based polarisation underlie the formation of epidermal centres of convergence and sub-epidermal PIN strands (Bayer et al., 2009). A computational model based on this hypothesis can accurately capture all aspects of the PIN polarity pattern and auxin distribution associated with developing leaf primordia. The model assumes that all cells may polarise according to a with-the-flux or up-the-gradient mechanism, and that which mechanism is used depends on the auxin concentration of the cell. At lower auxin concentrations (which initially exist in the epidermis), cells polarise according to the up-the-gradient model. This generates an epidermal centre of convergence with high auxin. At high auxin concentrations, which occur close to the centre of convergence, the flux-based mechanism controls polarisation and leads to sub-epidermal strand formation.

In this chapter, I show that similar to leaf primordia, *kan1kan2* outgrowths are marked by epidermal centres of convergence that, from early stages of outgrowth development, are coupled with sub-epidermal strands with elevated PIN1 levels. I compare the abilities of the indirect cell-cell coupling and flux-based models to account for the generation of sub-epidermal PIN1 strands. Using an indirect cell-cell coupling model of PIN1 strand formation, I address the role of auxin-induced auxin import in the generation of epidermal and sub-epidermal PIN1 patterns. I show that the polarity patterns seen in *kan1kan2* outgrowths can be accounted for with an indirect cell-cell coupling model that doesn't require a dip in epidermal auxin concentration prior to outgrowth development.

6.2 Results

6.2.1 In *kan1kan2* leaves, new epidermal centres of convergence are coupled with sub-epidermal PIN1 strands

To characterise the PIN1 polarity pattern in sub-epidermal tissue prior to the emergence of ectopic *kan1kan2* outgrowths, I performed immuno-localisation of PIN1 in transverse cross-sections of *kan1kan2* leaves. At early stages of leaf development, prior to outgrowth emergence, sub-epidermal strands of PIN1 expression were present and extended from an epidermal PIN1 convergence to the centre of the leaf (Fig. 6.2 A). Strands with elevated PIN1 expression were approximately two to three cells wide, similar to previous observations in the shoot apical meristem (Bayer et al., 2009). Cells closest to the centre of the strands tended to have the highest PIN1 expression and had PIN1 polarities oriented away from the epidermis, towards the centre of the leaf. Some cells on the outside of the strands had polarities pointing towards the centre of the strands.

Following the emergence of *kan1kan2* outgrowths, sub-epidermal strands of elevated PIN1 expression were present at the centre of each outgrowth, below epidermal centres of convergence (Fig. 6.2 B). The strands extended from sub-epidermal cells immediately below the epidermis, to the central vascular tissue of the leaf, where PIN1 strands from several outgrowths converged (Fig. 6.2 Bii). Thus, during the development of new *kan1kan2* outgrowths, new centres of epidermal convergence were connected to sub-epidermal PIN1 strands, which, in turn, connected with the auxin-transport network of the existing leaf.

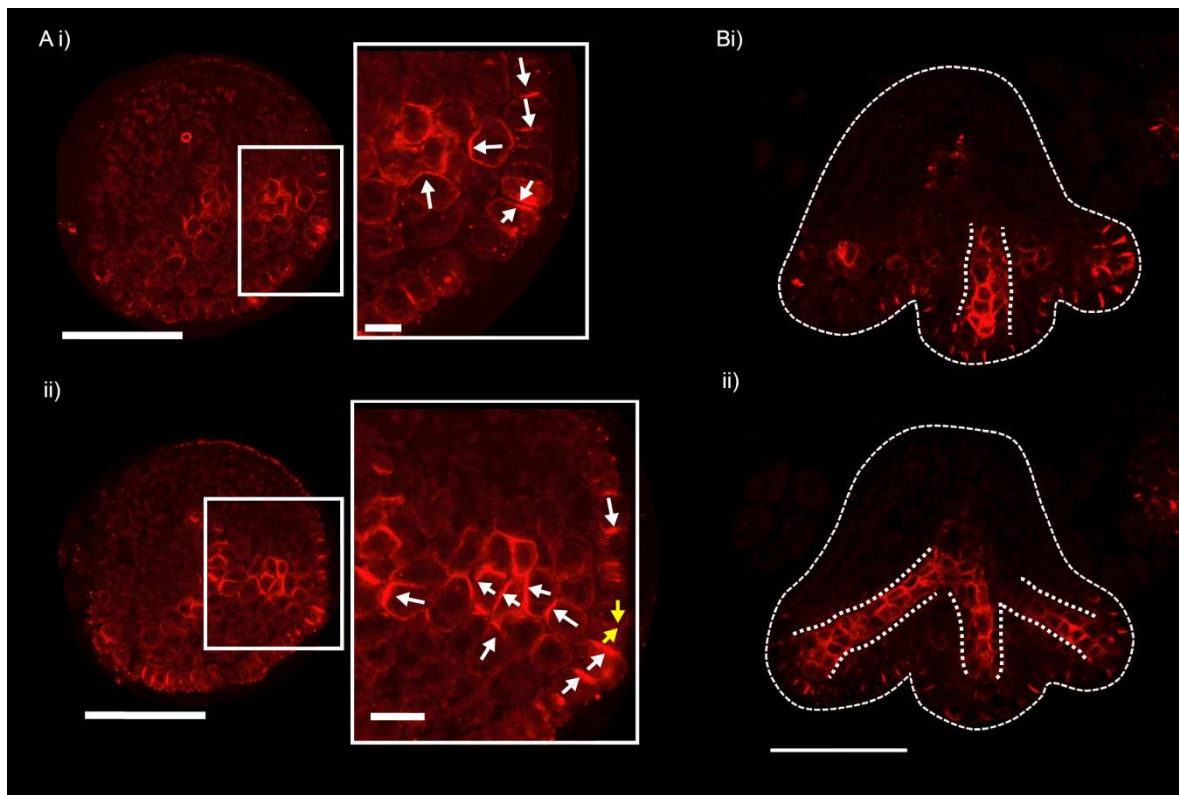


Fig. 6.2 PIN1 immuno-localisation in transverse cross-sections of *kan1kan2* leaves.

A) PIN1 immuno-localisation in a *kan1kan2* leaf before outgrowth emergence. i) and ii) are consecutive sections across the tissue (each section is 8 μ m thick). A centre of PIN1 polarity convergence can be seen in i) and the site of this convergence is shown with yellow arrows in ii). Arrows show the direction of PIN1 polarity. The adaxial side of the leaf is at the top of the image. **B)** PIN1 immuno-localisation in a *kan1kan2* leaf in which outgrowths have begun to emerge. Dotted white lines indicate the strands of cells with elevated levels of PIN1. Each image is representative of those obtained from four different seedlings. All scale bars = 50 μ m, except those in the zoomed in panels, which are 10 μ m.

I next explore how such sub-epidermal strands of cells with elevated levels of PIN1 could emerge in an indirect cell-cell coupling model, which, as I have shown in previous chapters, can account for the generation of epidermal centres of convergence. To do this, I run previously published simulations of the flux-based model (Rolland-Lagan and Prusinkiewicz, 2005) (which is currently the most successful model for vascular strand formation) and explore how PIN strands arise through forwards and backwards propagation this model. I investigate whether the principles

involved in strand propagation in the flux-based model may also cause strand formation in the indirect cell-cell coupling model, which I have previously shown behaves similarly to the flux-based model in a number of scenarios (chapter 3).

6.2.2 Forwards propagation of PIN strands in indirect cell-cell coupling and flux-based models

6.2.2.1 *Forwards propagation from an auxin source in the flux-based model*

First, I consider how PIN1 strands emerge through forwards propagation, away from an auxin source, in the flux-based model. In a version of this model where the rate of PIN allocation to cell edges increases quadratically with increasing auxin efflux, PIN strands arise spontaneously given local auxin sources (Fig. 6.3) (Rolland-Lagan and Prusinkiewicz, 2005). This is because cells in a region of tissue with higher flux will tend to have higher levels of PIN in the membrane. Consider a system that is initialised with a gradient of auxin from left to right, in addition to elevated auxin production in the file of cells on the left and an auxin sink in the file of cells on the right. If one cell in the left-most file is given an elevated rate of auxin production (higher than in other source cells), then initially this strong source cell has a higher auxin concentration than its surrounding neighbours (Fig. 6.3B i). As a consequence, there will be an elevated rate of auxin efflux across its right-most cell edge which results in allocation of an elevated level of PIN to this edge (Fig. 6.3B ii). As a consequence of right-wards auxin flux from the source cell, its right neighbour acquires an increased auxin concentration, increasing its efflux towards the sink, and therefore elevating PIN concentration at its right-most edge (Fig. 6.3B ii-iii). In this way, a strand of cells with elevated PIN levels spreads from a strong source of auxin to a sink (Fig. 6.3B iv and A).

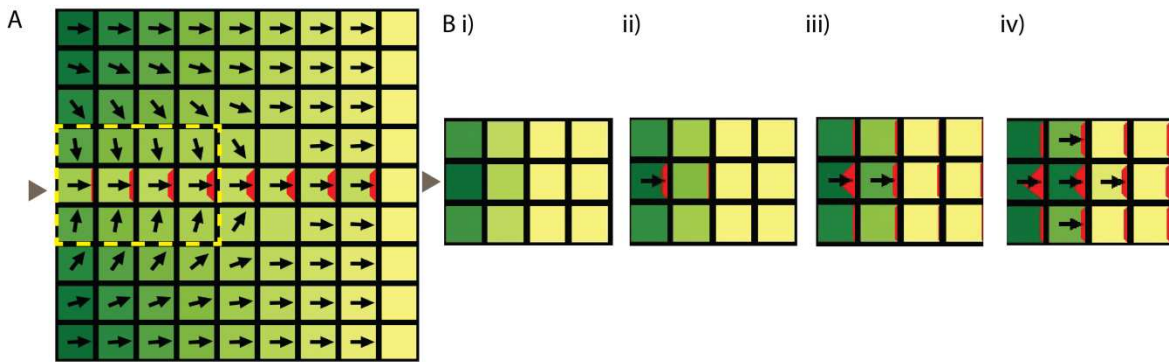


Fig. 6.3 Forwards propagation of a PIN strand from an auxin source in the flux-based model.

A) Final state of a simulation of the flux-based model where PIN allocation to the membrane increases quadratically with increasing auxin flux (adapted from Rolland-Lagan and Prusinkiewicz, 2005). At the beginning of the simulation, an auxin gradient is imposed from left to right across the tissue, the left file of cells has an elevated rate of auxin production, and the right file has a fixed auxin concentration of 0. The cell marked with the grey triangle has an elevated auxin production rate compared with other source cells. This causes a strand of cells with elevated PIN1 expression to propagate from the strong source cell to the sink. Neighbouring cells orient their PIN proteins towards the strand with elevated PIN1 levels. Intensity of green indicates the concentration of auxin (dark green indicates highest auxin concentration, yellow indicates low auxin concentration). The thickness of the red line indicates the concentration of PIN in the membrane (all cells with arrows have some PIN but in most cells the amount of PIN is much lower than in the central strand, therefore their PIN is not drawn). **B)** Initial events in the simulation for the cells marked by the dashed yellow outline in A). i) Grey triangle indicates the source cell, which initially has a higher auxin concentration than surrounding cells. ii) As a consequence of auxin efflux across its right-most edge, the source cell allocates PIN to this edge. This raises the auxin concentration of the right neighbour of the source cell. iii) The right neighbour of the source cell allocates PIN to its right edge, causing propagation of auxin to its right neighbour (iv). To enable differences in auxin concentration to be visualised in B), the colour scale differs from that used in A).

An outcome of this model is that cells neighbouring the central PIN strand allocate their PIN proteins towards it, which is compatible with observed PIN1 polarities in *kan1kan2* outgrowths (Fig. 6.2). This happens because high PIN-mediated flux along the strand causes a drop in the auxin concentration of the strand cells, which results in passive auxin influx from adjacent cells to the strand cells (Fig. 6.3 A). This causes the lateral neighbours of the strand (those at the top and bottom of the strand in Fig. 6.3) to preferentially allocate PIN, in the direction of this flux, towards the high PIN strand.

6.2.2.2 Forwards propagation from an auxin source in an indirect cell-cell coupling model with auxin-induced PIN expression

Similar to the flux-based model, with an indirect cell-cell coupling system, cells polarise in the direction of auxin flux. However, unlike the flux-based model, with the basic indirect cell-cell coupling mechanism, the amount of PIN allocated to a membrane is not proportional to the rate of efflux across that membrane. Instead, PIN is allocated to the membrane in proportion to the concentration of the A* intracellular partitioning component, which is not directly influenced by the rate of auxin efflux. If it is assumed that all cells express equal levels of PIN, all cells will therefore tend to allocate similar total amounts of PIN to the membrane. As a consequence, files of cells with elevated levels of PIN1 in the membrane do not arise spontaneously in this model and, to account for such strands, extra assumptions must be added.

One hypothesis is that strands with elevated PIN levels are caused by intracellular auxin promoting the expression of PIN1, an assumption which is supported by experimental observations (Vieten et al., 2005). To model this scenario, I begin with an array of cells, with a file of cells with elevated auxin synthesis at the left (plus organiser), and a file of cells with elevated auxin removal at the right (minus organiser). As a consequence of this pattern of organisers, polarities point from left to the right across the array (Fig. 6.4 A). Once this coordinated pattern of polarity is established, an elevated rate of auxin production is added to a cell at the left of the array (Fig. 6.4 B, arrow). As a consequence of auxin transport from the strong source cell, its right neighbour acquires elevated intracellular auxin and elevated levels of PIN. With the same parameter values for the basic auxin transport parameters as those used in previous simulations (i.e. in chapters 4 and 5), a broad region of PIN expression is induced at the right of the source cell, in which polarities are oriented slightly outwards, away from the centre of the strand (Fig. 6.4 B).

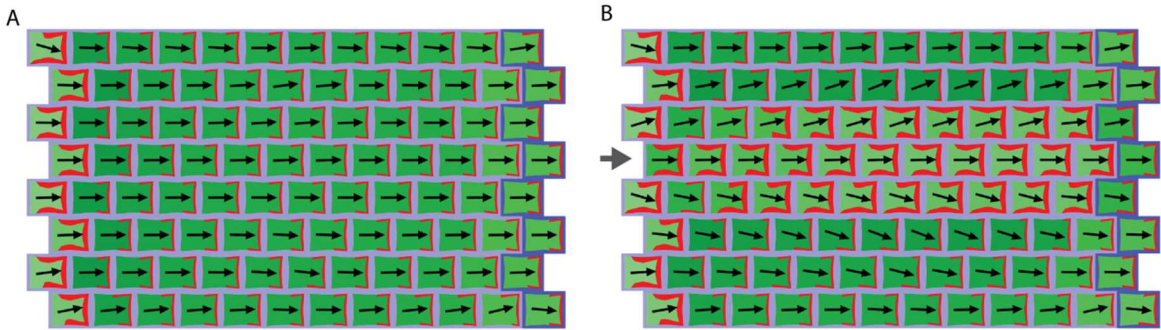


Fig. 6.4 Forwards propagation of a PIN strand in an indirect cell-cell coupling system with auxin promotion of PIN.

A) End of the first phase of the simulation, during which the file of cells at the left of the array has an elevated rate of auxin production and an elevated level of PIN (plus organiser), and a file of cells at the right has an elevated rate of auxin import and degradation (minus organiser), causing coordination of polarity across the tissue. All cells express a basal level of PIN proteins (shown in red) to allow cell-cell coupling to operate. Arrows point towards membrane regions with highest concentrations of PIN. The intensity of blue surrounding cells indicates their level of auxin import. Dark blue indicates a high rate of auxin import, light blue indicates a lower rate. **B)** End of the second phase of the simulation in which feedback between intracellular auxin and PIN expression operates. When the intracellular auxin concentration exceeds a threshold level, synthesis of PIN is promoted (in proportion to the auxin concentration) until the levels of PIN reach a maximum level. There is no degradation of PIN (so the auxin-induced increase in PIN expression is irreversible). A seed cell with higher auxin production than other plus organiser cells is positioned at the location marked with the grey arrow. A broad, diverging region of cells with high levels of PIN and high levels in the membrane (shown by thick red lines) propagates away from the source.

6.2.2.3 Assumptions about auxin movement between cells affect polarities surrounding the PIN strand

The orientation of polarities away from the PIN strand in this model contrasts with the orientation of polarities towards the strand in the flux-based model. This may be considered surprising since, in chapter 3, I show that these two models behave similarly in several scenarios. The difference in the models' behaviour may be partly because they make different assumptions about how auxin moves passively from cell to cell. Whereas the indirect cell-cell coupling model incorporates biologically relevant properties of auxin movement across the cell wall, the flux-based model does not. In particular, the indirect cell-cell coupling model assumes that to move from one cell to

another, auxin must pass through a cell wall, where it can diffuse laterally along the wall's length. Also, the indirect cell-cell coupling model assumes that the outwards permeability of cells to auxin is lower than their inwards permeability, an assumption based on differences in pH between the cytoplasm and the cell wall. Because the latter is more acidic, auxin (a weak acid) can permeate passively into cells. However, in the cytoplasm, auxin tends to be predominantly in an ionised form which cannot move passively thorough the membrane (Rubery and Sheldrake, 1973; Steinacher et al., 2012). These assumptions are not incorporated into published implementations of the flux based model, including the one that I present here (Rolland-Lagan and Prusinkiewicz, 2005; Stoma et al., 2008). Instead, these models assume that auxin can move directly from cell to cell (they do not model lateral diffusion of auxin in the wall) and that the inwards and outwards permeabilities of cells to auxin are equal.

As a consequence of the representation of the cell wall in the indirect cell-cell coupling model, if a cell has elevated levels of PIN at its right-most end, the auxin exported at this end will diffuse along the length of the cell wall. This causes extracellular auxin from the PIN-rich end of the cell to spread to its top and bottom walls, causing its lateral neighbours to orient their polarity away. Also, in the flux-based model, one way that a PIN strand cell with low auxin can cause neighbours to orient towards it, is that compared with neighbouring cells, this cell has a reduced rate of passive auxin efflux. In the indirect cell-cell coupling model, this effect could reduce extracellular auxin levels at the lateral edges of PIN strand cells, encouraging neighbours to orient polarity towards the strand. However, since the rate of passive auxin efflux is assumed to be low in the indirect cell-cell coupling model, reducing the intracellular auxin concentration of a cell has little effect on the amount of auxin leaving the cell through passive permeation.

If the assumptions about auxin movement between cells in the indirect cell-cell coupling model are made more similar to those in the published implementations of the flux-based models (i.e.,

auxin has an equal rate of inwards and outwards permeability, and does not diffuse along the length of the cell wall), a PIN strand with very slightly inwardly oriented polarities of neighbouring cells is generated (Fig. 6.5). Thus, these assumptions do have an impact on the polarity orientations of cells neighbouring the strand, but changing these assumptions alone in the indirect cell-cell coupling model is not sufficient to generate a PIN strand with inwardly oriented polarities such as those which may emerge from the flux based model (Fig. 6.3). This is likely because other differences exist between the two models, such as how tightly localised PIN is to one end of the cell, and affect this behaviour (I do not explore this further).

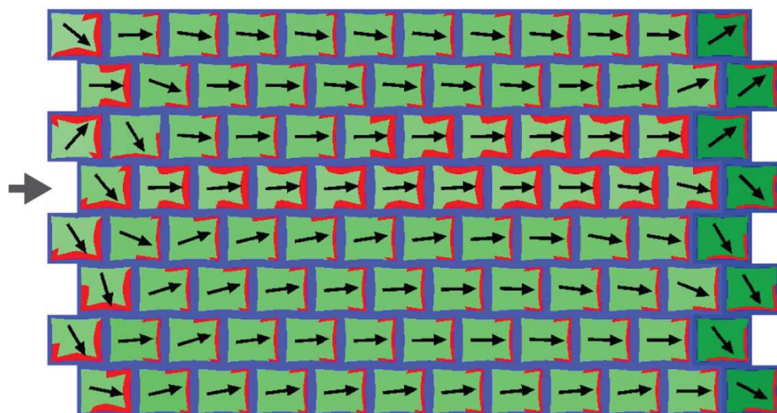


Fig. 6.5 PIN strand formation by forwards propagation in an indirect cell-cell coupling system with altered assumptions about auxin movement

End of the second phase of a simulation in which high intracellular auxin promotes PIN levels (as described for Fig. 6.4 B). The first phase of the simulation involved polarity establishment, as described for Fig. 6.4 A. Throughout the simulation, it is assumed that auxin has an equal rate of inwards and outwards permeability, and that no diffusion of auxin occurs along the length of the cell wall. A cell with high auxin production is present on the left of the array (grey arrow). A strand with high PIN propagates away from the source cell.

6.2.2.4 Forwards propagation in an indirect cell-cell coupling model with auxin-regulated expression of PIN and auxin importers

I next explore whether a narrow strand of cells with elevated PIN levels and neighbouring cells oriented towards it may be generated if elevated auxin not only induces elevated PIN levels, but also causes elevated rates of auxin import (Fig. 6.6). I use the original assumptions about the passive movement of auxin between cells and assume that intracellular auxin above a certain threshold causes an elevated rate of auxin import. I assume that intracellular auxin above a second, higher threshold, causes an increased rate of PIN production, until the total amount of PIN in the cell reaches a maximum value. With these assumptions, a cell acquires an elevated auxin import rate before acquiring an elevated rate of PIN expression. In a simulation where a strong source cell is present at the left of the array, three cells on the right of the source cell acquire an elevated rate of auxin import and PIN1 expression. However, in the next file of cells, the cell on the right of the source cell acquires an elevated intracellular auxin concentration, and an elevated rate of auxin import, before its top and bottom neighbours. The elevated auxin import in this cell depletes auxin from its top and bottom neighbours, tending to prevent their intracellular auxin concentration reaching the thresholds required to induce elevated import and PIN expression. As a consequence, a narrow and non-diverging strand of elevated PIN propagates between the source cell and the minus organiser on the right of the array (Fig. 6.6). Also, because of the elevated auxin import rates in the PIN strand, neighbouring cells orient their polarity towards it. Therefore, within an indirect cell-cell coupling system, the formation of non-diverging sub-epidermal PIN strands can be accounted for with feedback between intracellular auxin levels, auxin import rates, and PIN expression.

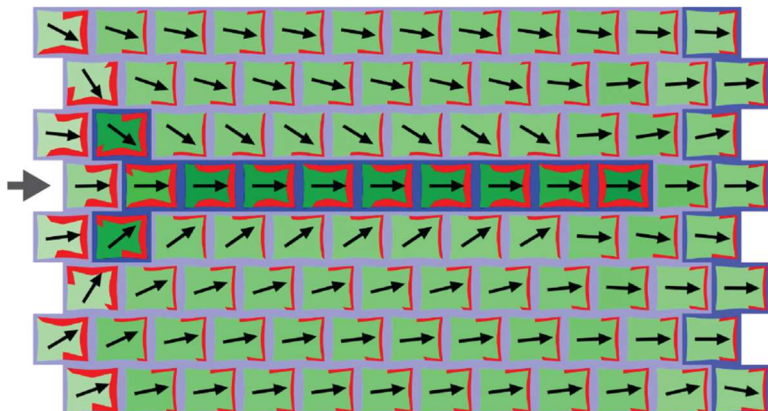


Fig. 6.6 Forwards propagation of a PIN strand in an indirect cell-cell coupling system where high auxin promotes auxin import and PIN.

End state of the second phase of a simulation in which there is feedback between intracellular auxin and the expression of both auxin importers and PIN. The first phase of the simulation involved polarity establishment as described for Fig. 6.4 A. In the second phase, when the intracellular auxin concentration exceeds an initial threshold level, T_1 , the rate of auxin import in the cell is irreversibly increased up to a maximum level. When intracellular auxin concentration exceeds a second, higher threshold level, T_2 , synthesis of PIN is promoted with the same assumptions as in Fig. 6.4 B). A cell with high auxin production is present on the left (grey arrow). This leads to the formation of a narrow strand with high PIN and high auxin importer expression, which propagates away from the source cell.

6.2.3 Backwards propagation of PIN strands in indirect cell-cell coupling and flux-based models.

In the models considered so far, PIN strands propagate away from auxin sources, in the direction of the polarity. However, in the flux-based model, PIN strands may also propagate backwards, in the opposite direction to the polarity, away from a local auxin sink (Rolland-Lagan and Prusinkiewicz, 2005). Here, I show a simulation of how this happens in the flux-based model and then present an indirect cell-cell coupling model for back propagation.

6.2.3.1 Backwards propagation from a sink in the flux-based model

With the flux based model, for a 2D array with a broad auxin source on the left of the tissue, and a single cell auxin sink on the right, the left neighbour of the sink (cell A in Fig. 6.7 B) acquires an

elevated auxin flux into the sink and therefore orients PIN towards the sink (Fig. 6.7 Bi, ii). The reduction in the auxin concentration of cell A causes its left neighbour to establish a high rate of auxin flux into it, thus causing a leftwards propagation of the PIN strand (Fig. 6.7 Biii and iv). In this case, cell polarities are oriented to the right, but the strand propagates to the left. Therefore, in the flux based model, elevated PIN expression may be propagated from a sink, in the opposite direction to the polarity that is being established.

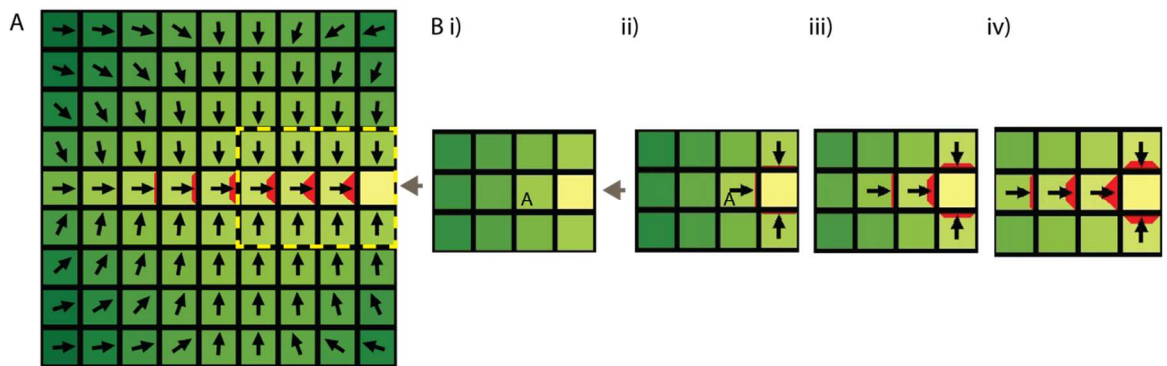


Fig. 6.7 Backwards propagation of a strand with elevated PIN from a sink cell in a flux-based model.

A) Final state of a simulation of the flux-based model with a point sink (Rolland-Lagan and Prusinkiewicz, 2005). At the beginning of the simulation, an auxin gradient is imposed from left to right across the tissue, the left file of cells has an elevated rate of auxin production, and a single cell on the right (marked with grey arrow) acts as an auxin sink and has its auxin concentration fixed to 0. This causes a strand of cells with elevated PIN levels to propagate from the sink cell towards the source. Neighbouring cells orient their PIN proteins towards the strand with elevated PIN levels. All cells with arrows have low levels of PIN which are not shown. **B)** Initial events in the simulation for the cells marked by the dashed yellow outline in A). i) Grey arrow indicates the sink cell. ii) As a consequence of auxin efflux (initially due to passive permeation) across its right-most edge, the left neighbour of the sink cell (cell A) allocates PIN to its right edge. This lowers the auxin concentration of cell A. iii) The reduction in auxin concentration of cell A causes a flux, due to passive permeation, from the left neighbour of cell A towards it. The left neighbour of cell A therefore allocates PIN to its right cell edge. (iv) The strand continues to propagate left-wards as cells establish right-wardly oriented polarity. To enable differences in auxin concentration to be visualised in B), the colour scale is not the same as in A).

6.2.3.2 Backwards propagation from a sink in the indirect cell-cell coupling model requires different assumptions from forwards propagation

The flux-based model, with exactly the same parameter values and assumptions, may generate forwards or backwards propagating strands depending on the pattern of auxin sources and sinks. However, in the indirect cell-cell coupling model presented above, where strands are induced by high auxin, strands with elevated import and PIN can only propagate forwards, in the same direction as the polarity. This is because, during strand propagation, for a cell to establish elevated auxin import and PIN expression, it must acquire an elevated auxin concentration through auxin transport from one of its neighbours. Auxin propagates from cell to cell along the direction of PIN polarity, therefore the strand can only propagate in the direction of this polarity. A cell adjacent to a point sink will orient its polarity towards the sink, therefore if this cell acquired high auxin and high PIN, it would not be able to propagate the strand away from the sink.

However, with alternative rules for strand propagation, the indirect cell-cell coupling may capture the propagation of strands away from a sink, in the opposite direction to the polarity (Fig. 6.8). This occurs if auxin import and PIN levels become elevated in cells that have low levels of extracellular auxin. Specifically, I assume that when the total level of extracellular auxin surrounding a cell drops below a threshold level, the cell acquires an elevated rate of auxin import. This elevated auxin import causes a further drop in extracellular auxin levels surrounding the cell. I assume that an elevated rate of PIN production is induced when extracellular auxin levels drop below a second, lower threshold. With these rules, in the presence of a file of cells with elevated auxin production on the left of the tissue, and a point sink on the right, extracellular auxin is lowest near the sink, causing cells near the sink to have elevated auxin import and PIN (Fig. 6.8i). For a cell with rightwards polarity, an increase in its auxin import rate and level of PIN reduces the extracellular auxin concentration at its left end. This reduction in extracellular auxin

causes the left neighbour to acquire elevated auxin import and PIN, causing propagation of the strand in the opposite direction to the polarity (Fig. 6.8 ii, iii). The strand does not connect with the source at the left of the array (as was observed experimentally in pea epicotyls (Sauer et al., 2006)) since extracellular auxin levels are relatively high in this region.

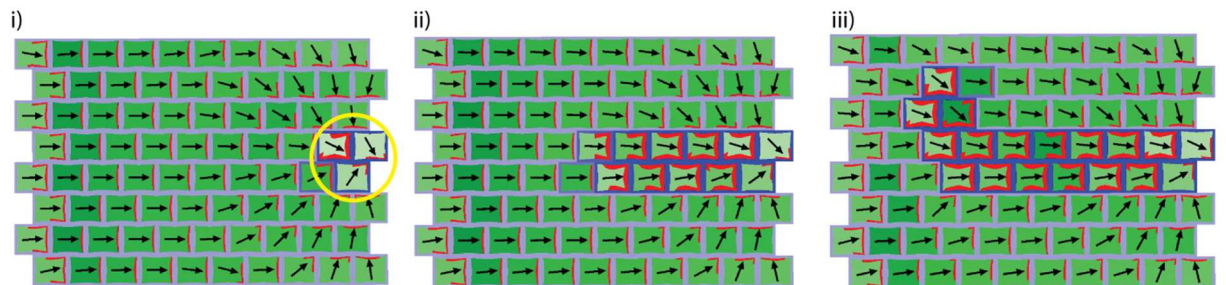


Fig. 6.8 Backwards propagation of a PIN strand in an indirect cell-cell coupling model where low extracellular auxin promotes auxin import and PIN.

In an initial phase of the simulation, the file of cells on the left has an elevated rate of auxin production, and three cells on the right have elevated rates of auxin degradation and import (indicated by yellow circle in i). After a coordinated polarity field is established, in the second phase of the simulation, a cell acquires an elevated rate of auxin import if the total level of extracellular auxin surrounding it drops below a threshold. If the total amount of extracellular auxin drops below a second, lower threshold, the cell's rate of PIN production irreversibly increases until the total level of PIN in the cell reaches a maximum level. This causes the propagation of a strand of cells with elevated auxin import, and PIN, away from the sink, in the opposite direction to the polarity. i) to iii) show snapshots from this second phase of the simulation.

6.2.4 Connecting forward and backward propagating PIN strands

6.2.4.1 *Forwards and backwards propagating strands connect in the flux-based model*

In the flux-based model, a strand propagating forwards along the direction of polarity may connect with a strand propagating backwards, in the opposite direction to the polarity (Fig. 6.9). I implement this by introducing a strong point auxin source at the left of the tissue, as in the simulation of forwards propagation (Fig. 6.3), and a strong point auxin sink at the right of the tissue, as in the simulation of backwards propagation (Fig. 6.7). The strands meet because the cell

at the front of a forwards propagating strand will have elevated auxin, and the cell at the back of a backwards propagating strand will have low auxin. When the two ends of the strands approach each other, there will be a high auxin flux between them, causing intervening cells to allocate high levels of PIN away from the forwards propagating strand, towards the backwards propagating strand (thus in the same direction as the polarity of the existing strands). In this way the two initially separate strands become connected to form one continuous strand (Fig. 6.9).

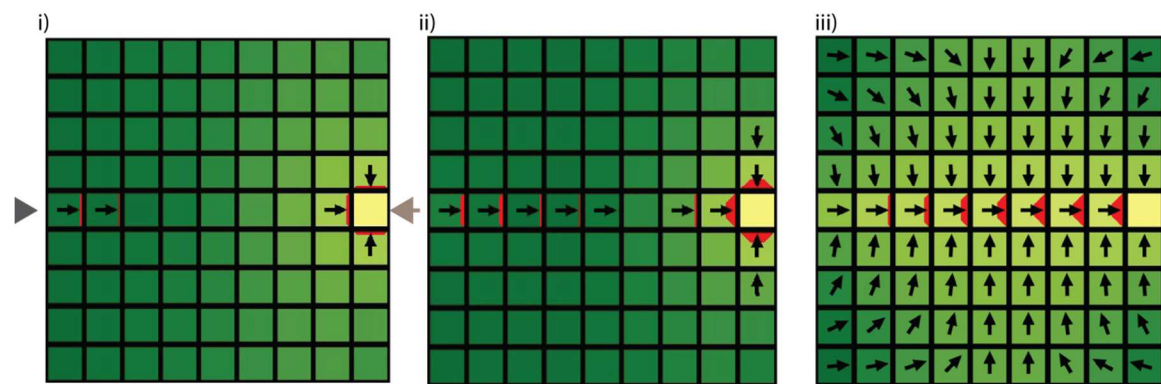


Fig. 6.9 Connection of PIN strands propagating forwards from a point source and backwards from a point sink in a flux-based model.

At the beginning of the simulation, an auxin gradient is present from left to right across the tissue. The file of cells at the left of the tissue has an elevated rate of auxin production and the cell marked with an arrow on the right acts as an auxin sink. The cell on the left marked with the triangle has a higher auxin production rate than other cells on the left. i) to iii) show snapshots at increasing times in the simulation. i) and ii) Strands of cells with elevated levels of PIN simultaneously propagate backwards, away from the sink, and forwards, away from the source, and then connect (iii). PIN levels are drawn using different scales in the three images (to enable PIN to be seen at early stages in the simulation when the levels in the membrane are lower).

6.2.4.2 Forwards and backwards propagating strands do not readily connect in the indirect cell-cell coupling model

To test whether PIN strands propagating forwards from a source (as in Fig. 6.6) and backwards from a sink (as in Fig. 6.8) may connect with the indirect coupling model, I combined both models

of strand propagation in a single simulation. At the start of the simulation, I assume that the file of cells on the left of the tissue has an elevated rate of auxin production, and that two cells on the right (marked by the yellow ellipse in Fig. 6.10 i) have an elevated rate of auxin degradation and import. After the establishment of a coordinated polarity field, two cells on the left are given a higher rate of auxin production than surrounding cells. I further assume that if a cell has either high intracellular auxin levels or low extracellular auxin levels surrounding it, its auxin import rate increases, and if a cell has either very high intracellular auxin levels or very low extracellular auxin levels surrounding it, this induces elevated production of PIN. These rules cause two strands of cells with elevated auxin import and PIN to propagate forwards, away from the point source, and backwards, away from the sink (Fig. 6.10 i, ii). However, the two strands do not connect to each other (Fig. 6.10 iii). This is because cells between the two strands have intermediate intracellular and extracellular auxin levels, due to a high rate of auxin transport towards them from the forwards propagating strand, and due to a high rate of auxin import into the backwards propagating strand. Thus, these cells do not meet any of the thresholds for induction of elevated levels of auxin import and PIN. In order to account for the connection of forwards and backwards propagating strands, additional assumptions would have to be added to the indirect cell-cell coupling model, which I have not explored further.

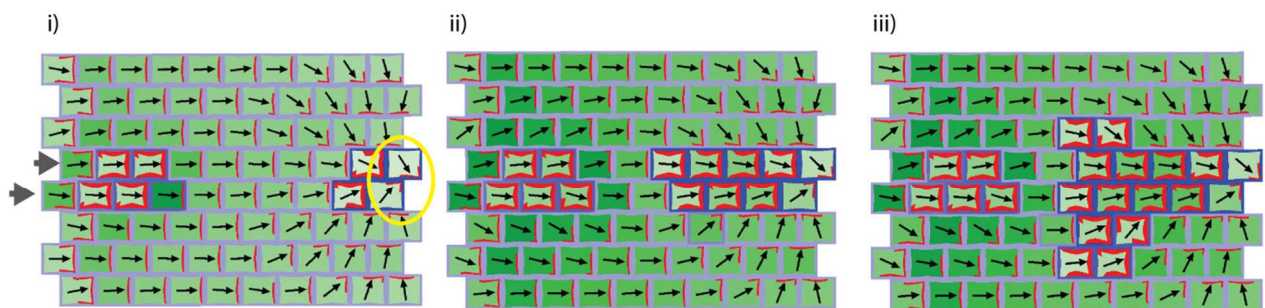


Fig. 6.10 Combination of forwards and backwards strand propagation rules in an indirect cell-cell coupling model.

In a first phase of the simulation, the file of cells on the left of the tissue has an elevated rate of auxin production, and the two cells on the left marked by the yellow ellipse in i) have an elevated rate of auxin degradation and import. In a second phase, the cells marked by the grey arrows on the left of the tissue have a higher auxin production rate than other cells on the left. The rules for forwards (Fig. 6.6) and backwards (Fig. 6.8) propagation of PIN strands are combined so that high intracellular auxin, or low extracellular auxin, induces elevated levels of auxin import and PIN. i) to iii) show snapshots of the simulation taken at successive time points.

In summary, when a flux-based mechanism controls polarity generation, strands of cells with elevated levels of PIN are readily accounted for. With this single model, and with no changes in parameter values or assumptions, PIN strands may either propagate forwards, away from an auxin source, or backwards, away from auxin sink, or in both directions, depending on the patterns of auxin production and decay. However, in an indirect cell-cell coupling model, PIN strands are less easily accounted for, and do not arise spontaneously without the addition of extra assumptions. However, by assuming that feedback exists between intracellular or extracellular auxin levels, and the expression of auxin importers and PIN proteins, this model may capture forwards and backwards propagation of PIN strands, although connection of these strands could not be readily achieved.

6.2.5 Integrating epidermal and sub-epidermal polarity patterns in *kan1kan2* leaves

Next, I use the indirect cell-cell coupling model for forwards propagation of PIN strands (Fig. 6.6) to generate hypotheses for how the coupled epidermal centres of convergence and sub-epidermal PIN strands seen in *kan1kan2* outgrowths may develop. To model the polarity patterns seen in outgrowths, it is necessary to consider the polarity context in which they form. Prior to the polarity reorientations that precede *kan1kan2* outgrowths, the polarity pattern of the *kan1kan2* leaf primordium is similar to that of WT leaves: in the epidermis, polarities are oriented distally, towards the leaf tip, and in sub-epidermal tissue, polarities are oriented proximally,

towards the leaf base (Fig. 6.11 A). At early stages of *kan1kan2* leaf development, cells in the proximal half of the abaxial epidermis undergo a polarity orientation to generate a centre of polarity convergence (Fig. 6.11 B, red arrows). This centre of convergence is coupled to a sub-epidermal strand of cells with elevated PIN1 expression, in which polarities are oriented away from the epidermis. As an outgrowth develops, the epidermal centre of convergence is localised at its tip and the sub-epidermal strand of cells with elevated PIN1 expression runs along its centre, connecting with pro-vascular cells in the centre of the leaf (Fig. 6.11 C, red arrows). Therefore, *kan1kan2* outgrowth development involves the insertion of a new leaf-like pattern of PIN polarity into the existing polarity pattern of the leaf.

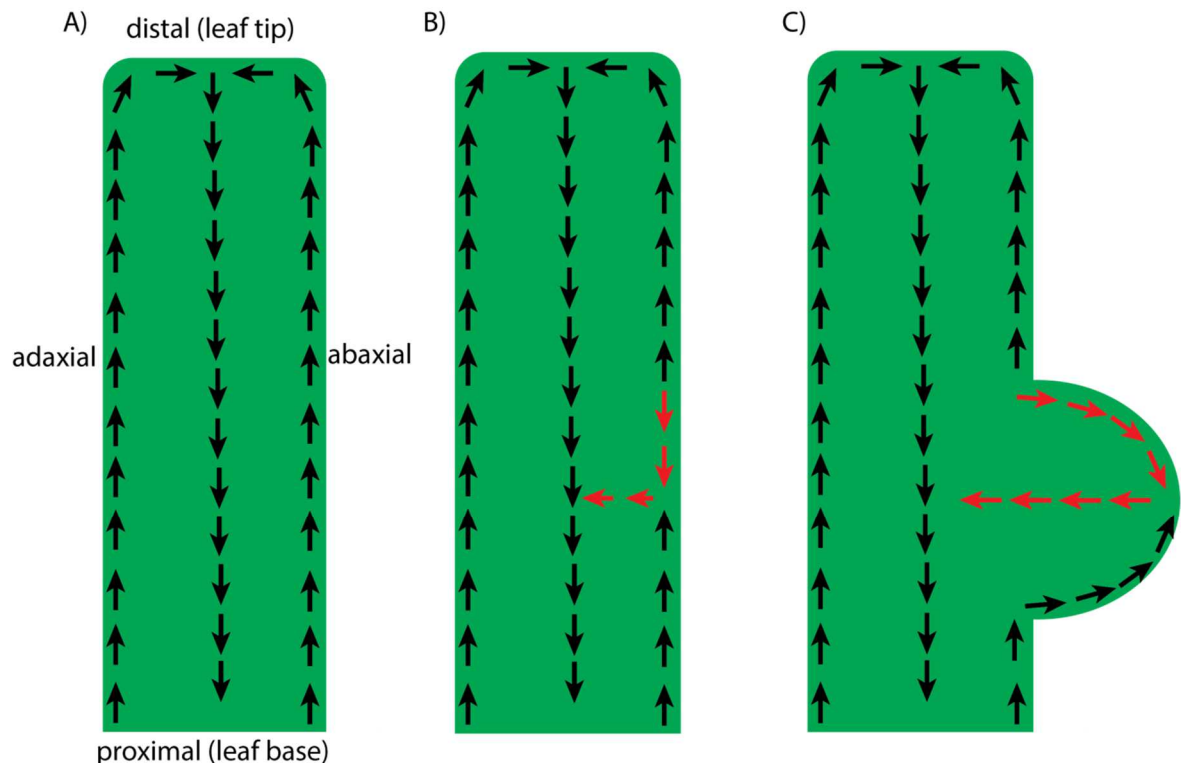


Fig. 6.11 Schematics of the polarity patterns in the longitudinal cross-sectional plane of *kan1kan2* leaves.

Arrows indicate PIN1 polarity patterns inferred from Fig. 4.4 and Fig. 4.3 (epidermis) and Fig. 6.2 (sub-epidermis). Red arrows show changes in the polarity field relative to the WT leaf. **A)** Polarity pattern in the longitudinal cross-sectional plane of WT leaf primordia (Scarpella et al., 2006) and in *kan1kan2* leaf primordia prior to polarity reorientations associated with outgrowths. In the epidermis, polarities are oriented distally, towards the leaf tip, and in pro-vascular cells of sub-

epidermal tissue, polarities are oriented proximally, towards the leaf base. **B)** Polarity reorientations that precede outgrowths. A polarity reorientation in the abaxial epidermis (red arrows) generates an epidermal centre of polarity convergence, which is coupled to a sub-epidermal strand of cells with elevated PIN, linking the epidermis with the central pro-vascular tissue of the leaf. **C)** As an outgrowth develops, the epidermal centre of convergence is localised at its tip. The sub-epidermal strand of cells with elevated PIN1 expression runs along the centre of the outgrowth and connects with pro-vascular cells in the centre of the leaf.

To model this, first I use a pre-pattern of auxin biosynthesis, import, and degradation that generates the polarity pattern seen in the longitudinal cross-sectional plane of WT leaves, and in *kan1kan2* leaves prior to outgrowth-related polarity reorientations (Fig. 6.11 A). I then address how, in the context of this polarity pattern, new identity regions can emerge and form a new epidermal centre of convergence and sub-epidermal PIN strand (Fig. 6.11 B).

6.2.5.1 *Generation of a leaf-like auxin transport pattern through a pre-pattern of organisers*

To capture the polarity pattern seen in WT, and in young *kan1kan2* leaf primordia, I incorporate the following assumptions into the initial state of an indirect cell-cell coupling simulation of the longitudinal cross-sectional plane of the leaf:

- 1) Cells in the array have different identities, to match plant tissue layers (known as L1, L2 and L3). The outer-most cells of the array, except those in the bottom row, are assumed to be epidermal (L1) cells (Fig. 6.12 A, orange cells); the cells in the inner-most file have L3 identity (Fig. 6.12 A, green cells); all other cells have L2 identity.
- 2) Auxin is synthesised at an elevated rate in epidermal cells at the base of the leaf (Fig. 6.12 B, red cells marked A). This is consistent with observations of *YUC1::GUS* expression in epidermal tissue at the base of leaves (Fig. 4.18 and (Wang et al., 2011)).

- 3) Auxin is removed at an elevated rate from L3 cells at the base of the leaf (Fig. 6.12 B, blue cell marked B). This represents removal of auxin into pre-existing vascular tissue at the leaf base.
- 4) There is an elevated rate of auxin import at the leaf tip (Fig. 6.12 B, cells with purple outline, marked C). This is consistent with the observed expression pattern of *LAX1* expression at the tips of young leaf primordia (Fig. 4.13 and (Bainbridge et al., 2008)
- 5) There is an elevated rate of auxin import in L3 cells running from the leaf tip to the leaf base (Fig. 6.12 B, cells with dark blue outline, marked D). This is consistent with expression of *LAX1::GUS* and *LAX2::GUS* in developing vascular tissue (Bainbridge et al., 2008).
- 6) At a later stage of the simulation, I add an elevated rate of auxin synthesis to the distal-most L3 cell (Fig. 6.12 B, red cell marked E). This assumption is supported by experimental observations of *YUC4::GFP* expression in sub-epidermal cells at the leaf tip (Fig. 6.12 E).

With these assumptions, epidermal (L1) cells in the left and right-most files of the array acquire distally oriented polarities, which point away from the auxin source at the base of the leaf and towards the region with elevated auxin import at the tip (Fig. 6.12 C). At the tip of the model leaf, epidermal cells' polarities converge towards a central cell which has an inwardly oriented polarity, pointing towards the vascular L3 file with elevated auxin import. After the establishment of this epidermal centre of convergence, an elevated rate of auxin synthesis is added to the distal-most L3 cell. Together with the auxin sink present at the base of this L3 file, this causes L3 cells to establish proximally oriented polarities. In cells between the epidermis and the L3 file, polarities are oriented inwards, away from the epidermis towards the L3 file (Fig. 6.12 C).

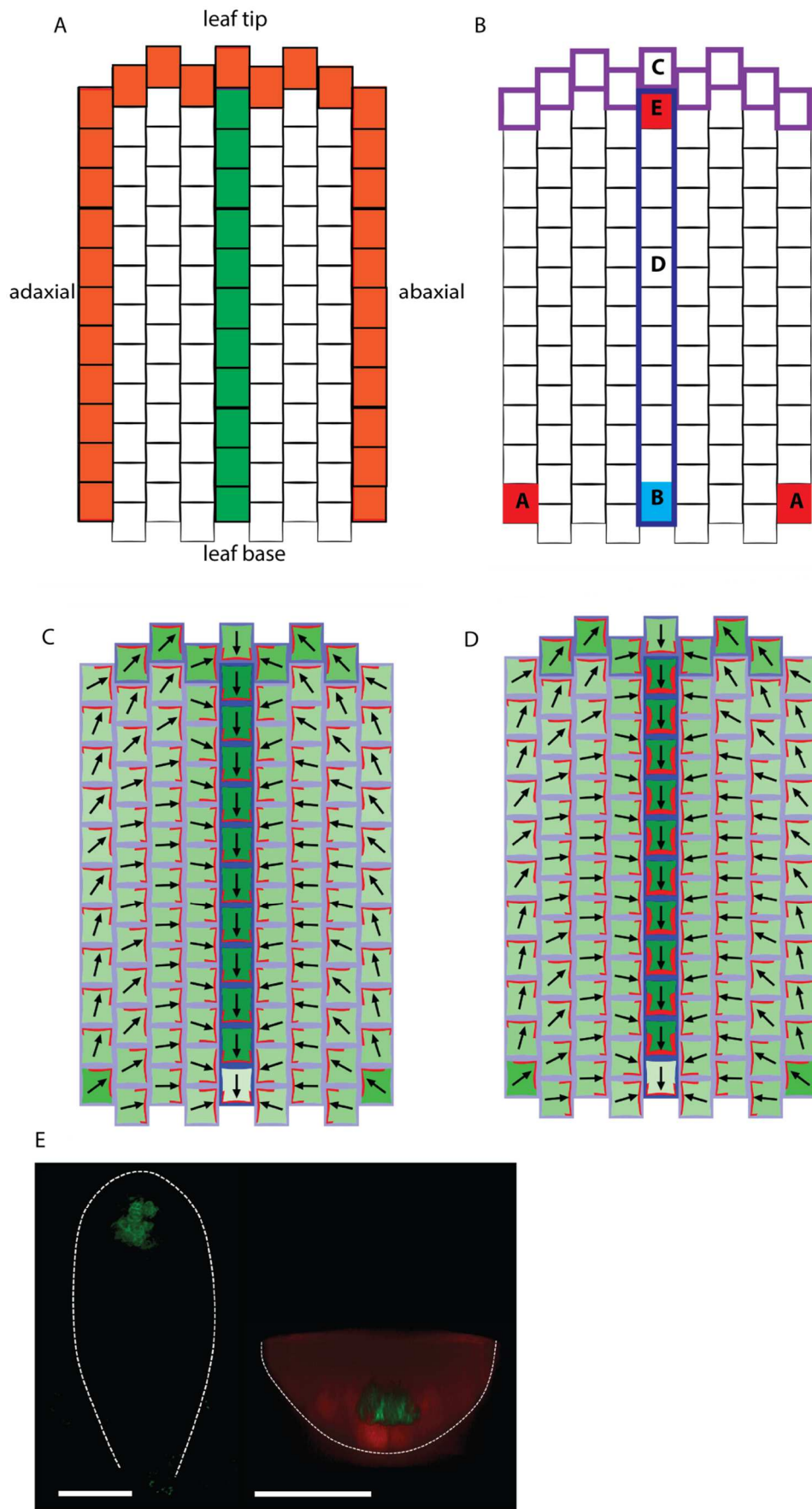


Fig. 6.12 Generation of the PIN1 polarity pattern in the longitudinal cross-sectional plane of the leaf through a pre-pattern of auxin production, degradation and import.

A) Cell identities in a canvas used to simulate the longitudinal cross-sectional plane of the leaf. Orange cells represent epidermal (L1) cells and green cells represent central provascular (L3) tissue. All other cells represent L2 tissue. **B)** Specified patterns of auxin production, degradation and import. Red indicates an elevated rate of auxin production. Regions A to D are present from the start of the simulation, region E is added at a later time. Cells marked A have elevated auxin production rates; the blue cell marked B has an elevated rate of auxin degradation; cells surrounded by the purple outline (marked C) have an elevated rate of auxin import and cells surrounded by the dark blue outline (marked D) also have an elevated rate of auxin import (higher than cells marked C). An elevated auxin production rate is added to the cell marked E once convergent polarities are established in the epidermis. **C)** Polarity pattern emerging as a consequence of the pre-pattern of organiser regions shown in B. The darkness of blue surrounding cells indicates their rate of auxin import (darkest blue is highest import). **D)** Same as C), but with rules for forwards propagation of PIN strands as described for Fig. 6.6. This causes the central most file of cells to acquire even higher rates of auxin import and elevated levels of PIN (indicated by thick red lines). **E)** Confocal image of a WT (Col-0) *A.thaliana* leaf expressing a *YUC4::GFP* marker, showing expression towards the tip of the leaf (left). Right image shows an optical transverse section through the tip of the leaf in the region with *YUC4::GFP* expression. The red channel shows auto-fluorescence, and the green channel shows GFP signal. Note that *YUC4::GFP* expression is in sub-epidermal tissue. Scale bar = 50 μ m.

If the assumptions used for forwards propagation of PIN strands (high intracellular auxin promotes auxin import and very high intracellular auxin promotes PIN levels) are assumed to operate in all L2 and L3 cells, then cells in the central L3 file establish even higher levels of auxin import and elevated levels of PIN1 expression (Fig. 6.12 D). This occurs because cells in this file have elevated auxin levels due both to pre-specified elevated auxin import rates and because the emergent polarity pattern involves neighbouring cells orienting their polarity towards the L3 file. With this model, auxin levels are elevated at the leaf tip and in the L3 file of cells with elevated import and PIN1 expression, similar to experimentally observed patterns *DR5::GFP* expression (Scarpella et al., 2006).

In this model, the PIN polarity pattern and the auxin distribution are emergent features arising as a consequence of the effects of the pre-specified pattern of auxin production, degradation, and import on the indirect cell-cell coupling system. All the identity regions in the model that modulate auxin distributions (regions A-E in Fig. 6.12 B) and therefore influence the polarity

pattern are pre-specified. I next address how new identity regions may emerge within the resulting polarity field and be used to generate new centres of polarity convergence and sub-epidermal PIN strands. To do this, I use the model presented above as the first phase of a simulation, and in a second phase, add rules similar to those that I have previously shown (in separate simulations) are sufficient to generate epidermal centres of convergence and sub-epidermal PIN strands.

6.2.5.2 Coupled formation of ectopic epidermal centres of convergence and sub-epidermal PIN strands

To combine the separate models of epidermal PIN1 convergence formation (Fig. 5.12) and forwards propagation of sub-epidermal PIN strands (Fig. 6.6), to generate a coupled epidermal convergence and sub-epidermal PIN strand, I found the following assumptions necessary:

- As in the model of epidermal convergence formation presented in chapter 5, cells in the proximal half of the abaxial epidermis have an elevated rate of auxin biosynthesis (representing ectopic *CUC2* and *YUCCA1* activity) (Fig. 6.13 A, double headed arrow).
- In all cells, intracellular auxin concentrations above an initial threshold promote an elevated rate of auxin import, and intracellular auxin concentrations above a second, higher threshold promote expression of PIN.
- I assume that the maximum expression of PIN1 is higher in sub-epidermal tissue (L2 and L3) than in the epidermis (L1), and that the maximum levels of import are higher in the epidermis compared with the sub-epidermis. This promotes the formation of centres of convergence in regions of the epidermis that have high auxin but also allows strand propagation in the neighbouring regions of the sub-epidermis.

- I also assume that the auxin concentrations required for the induction of import and PIN in the sub-epidermis are lower than in the epidermis (this allows propagation of import and PIN expression from the epidermis to the sub-epidermis).
- To allow auxin accumulation at the epidermal centre of convergence to trigger the formation of a PIN strand below, I assume that elevated auxin import induced by high auxin is only present on anti-clinal edges of the epidermal cells (brown arrows in Fig.6.13 B).

Combining these assumptions leads to the induction of a region with elevated auxin import within the domain of ectopic epidermal auxin biosynthesis (Fig.6.13 B). This causes a centre of convergence to form in the epidermis (Fig.6.13 C-E, orange arrow). As the polarity convergence forms, a strand of elevated PIN1 expression, which links the epidermis with the central-most L3 file of cells, forms below (Fig.6.13 C-E). Therefore, an ectopic region of auxin biosynthesis in the abaxial epidermis alone, can allow the formation of both an epidermal centre of convergence and a sub-epidermal PIN strand in a system with feedback between intracellular auxin, auxin import rates and PIN expression. New identity regions as well as new polarity patterns are emergent features of this model (black and pink outlines in Fig.6.13 F): regions of the epidermis and sub-epidermis with elevated auxin import and PIN were not pre-specified. In this model, because the epidermal convergence is generated through a region with elevated auxin import, there is no drop in epidermal auxin concentrations prior to convergence formation.

Relatively high levels of PIN must be induced in sub-epidermal cells for the stand with elevated PIN expression to connect with the L3 file in the centre of the leaf. As a consequence of high PIN levels in the sub-epidermal strand, neighbouring cells' polarities orient away from it, rather towards it. However, it is possible that with changes in parameter values, a sub-epidermal PIN strand with neighbouring polarities oriented towards it could be generated.

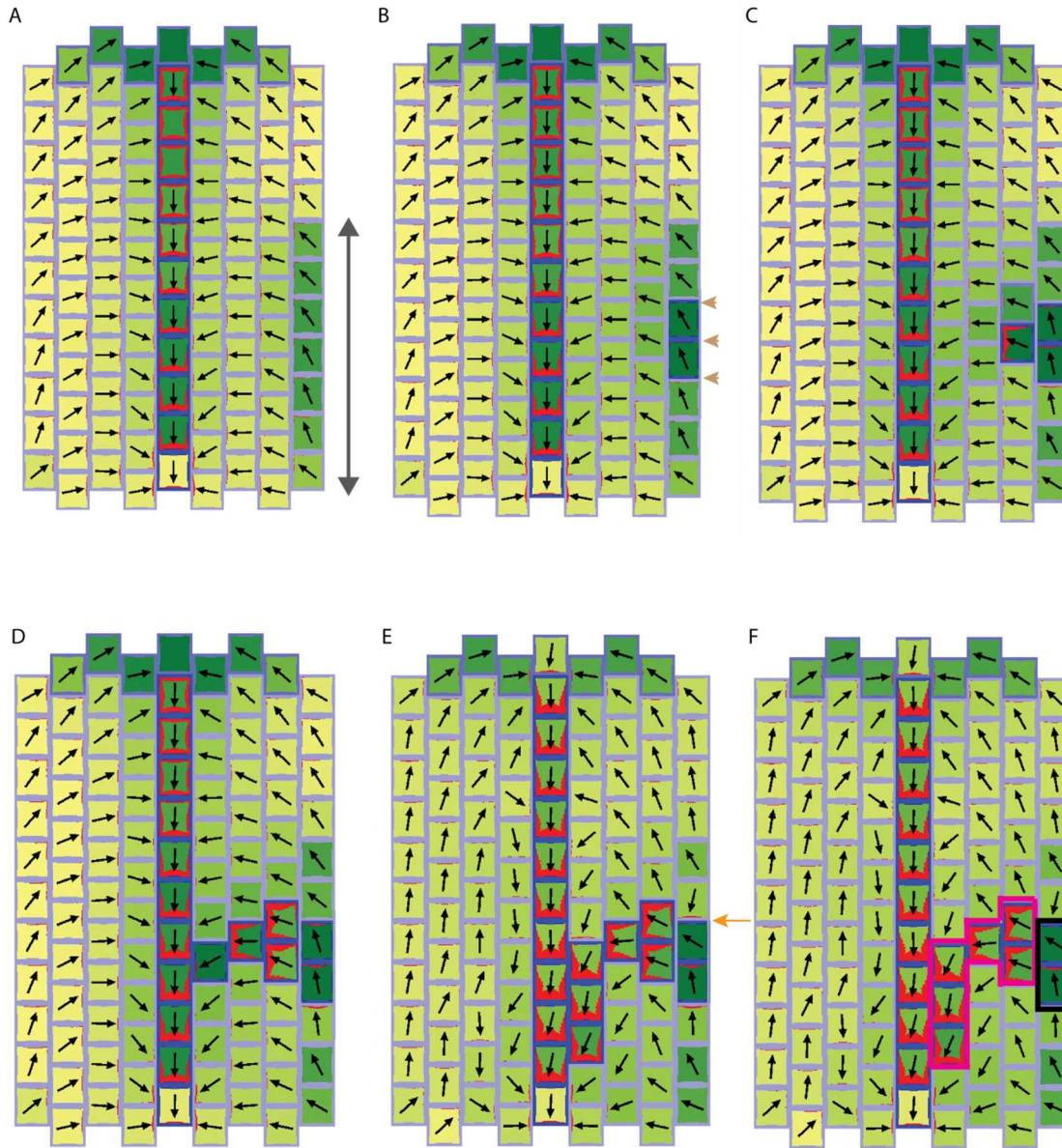


Fig.6.13 Indirect cell-cell coupling model for the formation of a coupled epidermal centre of convergence and sub-epidermal PIN strand.

The model represents the longitudinal cross-sectional plane of the *kan1kan2* leaf. In the first phase of the simulation, the pattern of organisers and identities is as described for Fig. 6.12. Throughout the simulation, in epidermal cells, intracellular auxin above a threshold concentration induces an elevated rate of auxin import on anti-clinal walls (indicated by brown arrows in B). PIN expression is also increased in epidermal cells with elevated auxin. In sub-epidermal cells, intracellular auxin above an initial threshold concentration induces an elevated rate of auxin import on all cell walls and auxin above a second, higher, threshold induces elevated PIN expression. The maximum level of PIN1 expression in the epidermis is lower than in the sub-epidermis, and the maximum rate of auxin import is higher in the epidermis than in the sub-epidermis. **A)** In the second phase of the simulation, abaxial epidermal cells (indicated with double-headed arrow) are given an elevated rate of auxin production. **B)** This causes induction of elevated auxin import rates on anticalinal walls of epidermal cells. **C-E)** An epidermal centre of

convergence (orange arrow in E) forms in the epidermis and a sub-epidermal PIN strand propagates away from the epidermis. **F**) New identity regions emerging from the model. Black and pink outlines show new identity regions, in the epidermis and sub-epidermis respectively, which are composed of cells with elevated auxin import and PIN. In all images, intensity of green indicates auxin concentrations. Note that there is no dip in auxin concentration prior to convergence formation. Intensity of blue surrounding cells indicates the level of auxin import (darkest blue indicates highest auxin import rate). Arrows point to regions with highest PIN and in cells with the highest levels of PIN, PIN distributions are shown in red.

6.3 Discussion

6.3.1 An indirect cell-cell coupling model for epidermal centres of convergence and sub-epidermal PIN strands

Here, I show that the indirect cell-cell coupling model can capture the generation of epidermal centres of polarity convergence, which are coupled to sub-epidermal strands of cells with elevated PIN expression and basally localised PIN. Unlike the published flux-based model of epidermal convergences and sub-epidermal strands, the model presented here does not involve a local drop in epidermal intracellular auxin concentration prior to convergence formation (Stoma et al., 2008). This is because the indirect cell-cell coupling model uses elevated auxin import, which is induced by elevated auxin concentrations, to generate centres of convergence. A cell with elevated auxin import locally depletes extracellular auxin, causing neighbouring cells to orient towards it, but also locally concentrates intracellular auxin. Restricting elevated auxin import to anti-clinal walls of epidermal cells means that walls in contact with the sub-epidermis may still have a high net efflux of auxin. This allows auxin to be transported towards sub-epidermal cells, raising their intracellular auxin concentration and causing induction of elevated levels of auxin import and PIN. Since the flux-based model behaves similarly to the indirect cell-cell coupling model in a number of scenarios (chapter 3), it is possible that the problem of a dip in auxin concentration during convergence formation in the flux-based model of epidermal and

sub-epidermal polarity patterns (Stoma et al., 2008) could be addressed by incorporating a role of auxin import in generating centres of convergence.

As discussed in Chapter 4, a role of auxin import in generating centres of convergence is supported by the expression of *LAX1::GUS* at sites in the *kan1kan2* lamina prior to outgrowth emergence. In the shoot apical meristem, expression of *AUX1* and *LAX1* importers is locally elevated in the epidermis at sites of incipient and developing primordia (Bainbridge et al., 2008; Reinhardt et al., 2003). This appears to be consistent with expression of auxin importers being up-regulated in new primordia, rather than being constitutively expressed in the epidermis as has previously been assumed (Stoma et al., 2008).

In the indirect cell-cell coupling model, localisation of elevated auxin import specifically to anti-clinal walls of the epidermis helps auxin to propagate from the epidermis into sub-epidermal cells at centres of convergence (otherwise high auxin at the centre of convergence remains in L1 cells and tends not to propagate into cells below). A previous study reported that *AUX1* appeared to be localised specifically to anti-clinal walls of epidermal cells, but also suggested a polar localisation of *AUX1* in these cells, which was not incorporated in the model presented here (Reinhardt et al., 2003). The sub-cellular localisation of *LAX1* in the epidermis has not been characterised. Future work should therefore include a more detailed investigation into the sub-cellular localisation of these proteins during the formation of epidermal centres of convergence. As discussed in chapter 4, the ability of *aux1lax1lax2lax3* and *kan1kan2aux1lax1lax2lax3* mutants to generate new outgrowths suggests that if elevated auxin import is involved in generating centres of convergence, *AUX/LAX* genes may function redundantly with other mechanisms (such as reduced expression of efflux carriers) which control the permeability of cells to auxin. Whether these mechanisms increase permeability specifically on anti-clinal walls should be investigated.

The model of epidermal polarity convergence and sub-epidermal PIN strand formation presented here requires different transcriptional responses to auxin by epidermal and sub-epidermal cells. In sub-epidermal cells, the level of PIN expression induced by auxin is assumed to be higher than the level induced in epidermal cells. This assumption of different transcriptional responses in different tissue layers is supported by findings in the shoot apical meristem that some Aux/IAA transcriptional regulators, which are degraded by auxin, are differentially expressed between the epidermis and sub-epidermal pro-vascular tissue (Vernoux et al., 2011).

The indirect cell-cell coupling model of epidermal polarity convergence and sub-epidermal PIN strand formation captures the general features of PIN strand formation, but not the details of the experimentally observed polarity pattern changes in the shoot apical meristem. In particular, in meristems of *Arabidopsis* and tomato, there is a transient polarisation of sub-epidermal cells towards the epidermis at early stages of epidermal convergence formation (Bayer et al., 2009), a feature which is not captured by the model. This polarity pattern was not observed in *kan1kan2* outgrowths, but this could be because too few leaves were imaged to capture this transient state and time-lapse data is not available for the cross-sectional plane. Whether this transient polarity pattern occurs in *kan1kan2* outgrowths, and whether it can be captured by the indirect cell-cell coupling model should be investigated in the future.

The model also fails to capture oblique polarity orientations, towards the sub-epidermal PIN strand, in the cells adjacent to it. This is because the forming PIN strand expresses high levels of PIN, resulting in high extracellular auxin. Thus, neighbouring cells orient away from it. If the levels of PIN in the strand are lower, compared with auxin import rates, then the strand does not propagate sufficiently to connect with the main PIN strand in the centre of the leaf. Future work should address what extra assumptions must be added to the model to more accurately capture

the experimentally observed PIN patterns and these assumptions, along with those already incorporated, should be tested experimentally.

Here, I have shown how the new epidermal centre of convergence and sub-epidermal PIN strand associated with *kan1kan2* outgrowths may be positioned and generated within a pre-existing leaf-like pattern of PIN polarity. In this model, the combination of the pre-existing distally-oriented polarity in the abaxial epidermis, along with ectopic elevated auxin biosynthesis in this region, positions a new identity domain in the epidermis due to the rule that elevated intracellular auxin promotes auxin import and PIN expression. The new identity region with elevated auxin import in the abaxial epidermis then causes a change in polarity. Thus, there is feedback between the polarity system and the identity of specific regions of the tissue that act as organisers of polarity. Such a feedback mechanism between polarity and identity may operate in the shoot apical meristem to establish the pattern of organisers needed to generate the leaf polarity pattern. Future modelling work should address how this could occur.

6.3.2 Mechanisms of PIN strand formation differ between flux and indirect cell-cell coupling models.

Although comparisons of the flux and indirect cell-cell coupling models presented in chapter 3 showed that these models behave similarly in a number of scenarios, here I show that the two models have different requirements for the establishment of sub-epidermal PIN strands. These strands arise readily from the flux-based model and may propagate forwards from an auxin source or backwards from an auxin sink without addition of extra assumptions to the model. However, a number of extra assumptions must be added to the indirect cell-cell coupling model to capture these behaviours.

The flux based model can readily connect forwards and backwards propagating PIN strands, whereas strands propagating according to the forwards and backwards mechanisms in the indirect cell-cell coupling model may approach each other but do not connect. One possible solution to this problem of connection would be to introduce a diffusible vein-inducing factor into the indirect cell-cell coupling model. If the factor was produced by vein cells with elevated auxin import and PIN and, at high levels, promoted vein identity (elevated auxin import and PIN), cells in between forwards and backwards propagating strands would have high levels of this signal and acquire vein identity, allowing the strands to be connected. A similar factor was proposed by Bayer et al., 2009, in the combined up-the-gradient and flux-based model used to account for the formation of coupled centres of convergence and sub-epidermal PIN strands. In this published model, the factor was required to enable a propagating PIN strand to connect with a sink.

One reason for some of the differences in behaviour of the flux and indirect cell-cell coupling model may be the assumptions that the two models make about the passive movement of auxin between cells. It is possible that, as I show for the indirect cell-cell coupling model, the flux-based model may not generate polarities oriented towards the centre of PIN strands if it is implemented with a more detailed description of auxin movement between cells. Whether the flux-based model still generates lateral polarities oriented towards PIN strands in the presence of realistic auxin diffusion rates in cell walls and different rates of inwards and outwards permeability of cells to auxin should be tested. If it does not, then it may be necessary for the PIN strands induced in the flux-based model to have elevated auxin import rates, similar to what was assumed for the indirect cell-cell coupling model. If this is the case, then the requirement for auxin import to account for the PIN1 polarity patterns in pro-vascular strands may be a prediction of both flux and indirect cell-cell coupling models.

6.3.3 The indirect cell-cell coupling and flux-based models make testable predictions about the formation of sub-epidermal PIN strands

The prediction that auxin import plays an important role in vascular strand formation may be tested experimentally. In the indirect cell-cell coupling model, strands with elevated PIN levels can still form through forwards propagation in the absence of auxin import (if elevated intracellular auxin promotes PIN expression), although the cells neighbouring the strands have polarities oriented away from the strand, and the strand has low auxin (Fig. 6.4). A similar prediction would possibly be made by a detailed flux-based model. The expression of *LAX1::GUS* and *LAX2::GUS* markers in developing vascular tissue, and the disruption of cotyledon vascular development in *lax2* mutants supports a role of auxin import in the development of sub-epidermal PIN strands (Bainbridge et al., 2008; Peret et al., 2012). However, a more detailed analysis of PIN1 polarities in *aux/lax* mutants should be performed in the future to investigate whether PIN1 polarities are altered in ways predicted by the models.

In the indirect cell-cell coupling model, for different regions of the tissue to have different levels of PIN in the membrane, they must have different levels of PIN expression. To account for PIN strand propagation, PIN expression may be regulated by intracellular or extracellular auxin. This model therefore gives rise to the prediction that mutants that are defective in auxin regulation of PIN transcription may have defects in PIN strand formation and vascular patterning. In support of these predictions, the auxin-responsive transcription factor, *MONOPTEROUS (MP)* is expressed in response to auxin, and is required to induce the expression of PIN1 during vascular patterning (Wenzel et al., 2007). Also, *mp* mutants have severe defects in vascular patterning (Wenzel et al., 2007). In contrast, in the flux-based model, strands of cells with elevated levels of PIN in the membrane form independently of auxin-regulated PIN expression. However, the finding that auxin-regulated PIN1 transcription plays a role in vascular development is not incompatible with

the flux-based model because auxin may be required to induce a background level of PIN expression which is then polarised according to the flux-based mechanism.

Whilst the flux-based model can account for the forwards (along the polarity) and backwards (in the opposite direction to the polarity) propagation of PIN strands using a single simple mechanism, the indirect cell-cell coupling model requires two different rules for forwards and backwards propagation. With indirect cell-cell coupling, the expression of auxin importers and PIN is either promoted by high intracellular auxin, leading to forwards propagation, or by low extracellular auxin, causing backwards propagation. Thus, the indirect cell-cell coupling model predicts that specific mutations affecting intracellular or extracellular perception might affect only one of the propagation mechanisms. For example, if mutants were found which could form the lower part of closed vein loops in leaves (which form due to forwards propagation), but not the upper part of loops (which appear to form due to back propagation) (Scarpella et al., 2006) this would provide support for separate mechanisms being involved in forwards and backwards propagation.

To better evaluate models for PIN strand formation, time-lapse imaging of the development of PIN1 strands during leaf vascular patterning is required. This is because, as far as I am aware, all descriptions of pro-vascular strand development currently available are based on snapshots of PIN1 taken from different individual plants at different time points. It is therefore possible, in the case of leaf vascular development, that some of the apparent back-propagation of PIN strands may be due to growth and division of existing PIN-expressing cells rather than due to cell to cell signalling. To unambiguously demonstrate back-propagation, and to determine whether different forwards and/or backwards propagating strands connect, it will be necessary to perform time-lapse imaging to monitor the same developing PIN strands over time.

Time-lapse imaging could also be used to investigate the roles of local auxin sources, and regions of elevated auxin import, in the dynamics of leaf vascular development. In the leaf, it is possible that local regions of elevated auxin biosynthesis may be present which allow the development of closed vein loops through forwards, rather than back propagation. It is therefore important to know the locations of auxin biosynthesis relative to the dynamic patterns of PIN1 localisation. Also, the dynamics of auxin importer expression relative to PIN expression and polarity patterns during the development of pro-vascular tissue should be investigated using time-lapse imaging. Furthermore, although *aux/lax* quadruple mutants have not been reported to have severe defects in vascular patterning, their leaf PIN1 polarity dynamics have not yet been reported. An analysis of this could help to test the prediction of the indirect cell-cell coupling model that without elevated auxin import, PIN1 strands are wider and have outwardly oriented polarities in neighbouring cells.

6.4 Methods

Confocal imaging and plant growth conditions were as described in Chapter 4. The *YUC4::GFP* line was in the Col-0 background and was provided by Yunde Zhao (University of California San Diego). *kan1kan2* mutants are as described in Chapter 4.

6.4.1 Immuno-localisation of PIN1

13 days after sowing, whole seedlings were fixed in ice cold FAA (50 % (v/v) EtOH, 3.7% formaldehyde, 5% (v/v) acetic acid, 0.5% (v/v) Triton x-100, 1% (v/v) DMSO). The fixative was vacuum infiltrated for 5 minutes on ice and then left over night at 4°C. Samples were dehydrated through ethanol (50% (v/v) ethanol for 2 hours, followed by two incubations in 70% (v/v) ethanol for 4 hours), embedded in Paraplast, and then sectioned (8 μ m sections). Sections were affixed to poly-L-lysine slides (Thermo Scientific) and then dewaxed in Histoclear (two 10 minute

incubations). Samples were then rehydrated to water by passing through a decreasing ethanol series (100% ethanol was used for 10 minutes, followed by two minutes each in 100%, 95%, 85%, 70% and 50% (v/v) ethanol, followed by 10 minutes in 30% (v/v) ethanol and 2 x 2 minutes in ddH₂O. Slides were then boiled for 10 minutes in an antigen retrieval solution of 10mM citrate (pH 6.0) and cooled for 10 minutes at room temperature. Slides were rinsed twice with ddH₂O, then incubated in blocking buffer (5% [w/v] nonfat dry milk, 0.3% (v/v) Triton x-100, 0.9% [w/v] NaCl, 10 mM Na phosphate, pH 7.4). Detergent was washed off in PBS (0.9% [w/v] NaCl, 10 mM Na phosphate, pH 7.4), slides were then drained and sections were incubated over night at 4°C with a commercially available goat anti-PIN1 (aP-20) polyclonal primary antibody (Santa Cruz Biotechnology) diluted 1:300 in blocking buffer without detergent (5% [w/v] nonfat dry milk, 0.9% [w/v] NaCl, 10 mM Na phosphate, pH 7.4). Slides were then washed three times for 15 minutes in 0.3% (v/v) Triton x-100, in PBS. Detergent was then removed by washing in PBS. Slides were drained, and then incubated for three hours at room temperature with a Cy3 conjugated rabbit anti-goat secondary antibody (Jackson ImmunoResearch), diluted 1 in 300 in blocking buffer without detergent. Slides were then washed three times for 10 minutes in 0.3% (v/v) Triton x-100, in PBS, washed once for 10 minutes in PBS, drained, and mounted in 1% (w/v) DABCO in glycerol. Fluorescent signal was observed using confocal microscopy (as described in chapter 4 for detection of RFP).

6.4.2 Model Descriptions

6.4.2.1 Flux-based models

Flux based models were implemented as described in Chapter 3. The simulations used to generate Fig. 6.3 and Fig. 6.7 are described in Rolland-Lagan and Prusinkiewicz et al., 2005, and that used to generate Fig. 6.9 is based on these. The model assumes that PIN allocation to each cell edge

increases in proportion to the flux across that edge squared, and that there is a non-limited pool of PIN in each cell (equations 3.8, 3.9b, 3.13, 3.14). Parameter values are given in Table 6.1.

In the simulations used to generate Fig. 6.3, Fig. 6.7 and Fig. 6.9 the system is initialised with a gradient of auxin concentrations from the left to the right of the array. This gradient is created by setting each cell's auxin concentration as follows:

$$A = \frac{F(c-1)}{T} \quad (6.1)$$

Where A is the auxin concentration of the cell, F is a constant (with a value of 15), c is the column number of the cell (1 is the right column, 10 is the left-most column) and T is a constant with a value of 0.325.

In the simulation used to generate Fig. 6.3, cells in the left-most column (except the central cell of this column) produce auxin throughout the simulation at a rate of $0.15 \text{ A}_u / \mu\text{m}^2 \cdot \text{s}$. The central-most cell of this column produces auxin at an elevated rate of $0.5 \text{ A}_u / \mu\text{m}^2 \cdot \text{s}$. All cells in the right-most column have their auxin concentration fixed to 0.

In the simulation used to generate Fig. 6.7, all cells in the left-most column produce auxin throughout the simulation at a rate of $0.15 \text{ A}_u / \mu\text{m}^2 \cdot \text{s}$. In the right most column, the central cell has its auxin concentration fixed to 0 throughout the simulation.

In the simulation used to generate Fig. 6.9, cells in the left-most column (except the central cell of this column) produce auxin throughout the simulation at a rate of $0.15 \text{ A}_u / \mu\text{m}^2 \cdot \text{s}$. The central-most cell of this column produces auxin at an elevated rate of $0.3 \text{ A}_u / \mu\text{m}^2 \cdot \text{s}$. In the right most column, the central cell has its auxin concentration fixed to 0 throughout the simulation.

In all three simulations, PIN concentrations at cell edges are truncated at a maximum value P_{max} , of $0.7 \text{ A}_u / \mu\text{m}$.

Symbol and units	μ /s	D $\mu\text{m/s}$	T $\mu\text{m}^2 / \text{A}_u \cdot \text{s}$	γ /s	α $\text{A}_u / \mu\text{m} \cdot \text{s}$	ρ $\text{A}_u / \mu\text{m}^2 \cdot \text{s}$
Fig: 6.2, 6.5, 6.7	0	4.2	1.30	0.05	1×10^{-6}	0

Table 6.1 Parameter values used in flux-based simulations.

μ is the auxin degradation rate, D is the passive permeability of auxin and T is the rate of PIN-mediated auxin transport. γ is the rate of PIN unbinding from the membrane, α is a constant parameter determining the extent to which flux promotes PIN allocation to cell edges, ρ is the auxin production rate.

6.4.2.2 *Indirect cell-cell coupling models.*

Apart from where differences are described below, models presented were implemented according to the description of indirect cell-cell coupling presented in chapter 2, and with an explicit representation of PIN, as described in chapter 4. Unless detailed below, all relevant parameter values are given in Table 2.1 and in Table 4.3.

6.4.2.2.1 *Forwards propagation of PIN strands in an indirect cell-cell coupling system*

Fig. 6.4 Forwards propagation of a PIN strand in an indirect cell-cell coupling system with auxin promotion of PIN. In the first phase of the simulation (shown in A), in all cells except those in the left-most file, the auxin production rate, $\rho_{Aux} = 2 \times 10^{-4} \text{ A}_u / \mu\text{m}^2 \cdot \text{s}$ and in all cells except those in the right-most file, the auxin degradation rate, $\mu_{Aux} = 0.02 / \text{s}$. In the file of cells on the left of the array,

$\rho_{Aux} = 3 \times 10^{-4} \text{ A}_u / \mu\text{m}^2 \cdot \text{s}$ and in the file of cells on the right, $\mu_{Aux} = 0.05 / \text{s}$. Also, the file of cells on the right of the array has an elevated rate of inwards auxin permeation (representing increased auxin import), in these cells, $v_{in} = 1.5 \mu\text{m} / \text{s}$. The system is initialised as described previously, except c_{PIN} , the initial concentration of PIN in cytoplasmic compartments, $= 0.002 \text{ A}_u / \mu\text{m}^2$ in all cells except the file of cells on the left of the tissue, where $c_{PIN} = 0.005 \text{ A}_u / \mu\text{m}^2$. Also, the initial concentration of auxin in all cytoplasmic compartments $= 0.5 \text{ A}_u / \mu\text{m}^2$. τ , the rate of A^* -dependent PIN binding to the membrane $= 1.5 \mu\text{m}^2 / \text{A}_u \cdot \text{s}$ and ρ_{PIN} , the default binding rate of PIN $= 0.01 \mu\text{m} / \text{s}$. In the second phase of the simulation (the end of which is shown in B), at time $= 2000\text{s}$, one of the cells (indicated in Fig. 6.4B) in the left-most file is given an elevated auxin production rate ($\rho_{Aux} = 6 \times 10^{-4} \text{ A}_u / \mu\text{m}^2 \cdot \text{s}$).

After 3000s of the simulation, when the auxin concentration of a cell exceeds a threshold level, PIN is produced in that cell (in proportion to its auxin concentration squared) until the total level of PIN reaches a maximum value. Once the maximum value of PIN is reached, the total level of PIN in the cell remains constant, irrespective of the concentration of auxin in the cell. This can be expressed as:

if $Aux_c > T_{AP}$ and $PIN_{total} < PIN_{max}$:

$$\frac{\partial PIN_c}{\partial t} = \alpha_{PIN} Aux_c^2 - \frac{1}{R_c} \sum_{n \in N(c)} l_n (\rho_{PIN} + \tau A^* n) PIN_c - \mu_{PIN} PIN_n \quad (6.2a)$$

otherwise

$$\frac{\partial PIN_c}{\partial t} = \frac{-1}{R_c} \sum_{n \in N(c)} l_n (\rho_{PIN} + \tau A^* n) PIN_c - \mu_{PIN} PIN_n \quad (6.2b)$$

Where Aux_c is the concentration of auxin in the given cell, with units of $\text{A}_u / \mu\text{m}^2$, T_{AP} is the threshold auxin concentration at which auxin promotes the expression of PIN, $\text{PIN}_{\text{total}}$ is the total amount of PIN in the membrane and in the cytoplasm of the cell (with units of A_u), and PIN_{max} is the maximum total amount of PIN per cell. α_{PIN} is the rate at which auxin promotes PIN expression, with units of $\mu\text{m}^2 / \text{A}_u \cdot \text{s}$. All other terms are as described for equation 4.3 and are related to PIN binding and unbinding from the membrane.

In the simulation used to generate Fig.6.4 B, $T_{AP} = 0.0126 \text{ A}_u / \mu\text{m}^2$, $\text{PIN}_{\text{max}} = 2 \text{ A}_u$ and $\alpha_{PIN} = 1 \mu\text{m}^2 / \text{A}_u \cdot \text{s}$.

Fig. 6.5 PIN strand formation by forwards propagation in an indirect cell-cell coupling system with altered assumptions about auxin movement The simulation is implemented as described above for Fig. 6.4B, except that the rates of outwards and inwards permeation are higher and equal : $v_{in} = v_{out} = 1.5 \mu\text{m} / \text{s}$. Also, D_{Aux} , the diffusion constant of auxin in the cell wall = $0 \mu\text{m}^2/\text{s}$. Also, in the file of cells on the right of the tissue, the auxin degradation rate, $\mu_{Aux} = 0.025 / \text{s}$. Additionally, $T_{AP} = 0.0107 \text{ A}_u / \mu\text{m}^2$, $\text{PIN}_{\text{max}} = 5 \text{ A}_u$ and $\alpha_{PIN} = 5 \mu\text{m}^2 / \text{A}_u \cdot \text{s}$.

Fig. 6.6 Forwards propagation of a PIN strand in an indirect cell-cell coupling system where high auxin promotes auxin import and PIN. The simulation is implemented as described for Fig 6.4 B, except that as well as the total amount of PIN per cell being increased by auxin, the rate of auxin permeation into the cell (representing auxin import) is also influenced by intracellular auxin concentrations.

I assume that when the auxin concentration of the cell reaches an initial threshold, the inwards permeability of the cell to auxin (v_{in}) increases until it reaches a maximum level. This can be stated as:

if ($Aux_c > T_{AI}$ and $v_{in} < v_{inmax}$):

$$\frac{\partial v_{in}}{\partial t} = \alpha_I Aux_c^2 \quad (6.3a)$$

otherwise

$$\frac{\partial v_{in}}{\partial t} = 0 \quad (6.3b)$$

Where Aux_c is the concentration of auxin in the cell, T_{AI} is the threshold auxin concentration at which auxin promotes v_{in} , α_I is the rate at which auxin promotes the inwards permeability of the cell, with units of $\mu m^5 / A_u^2 \cdot s^2$ and v_{inmax} is the maximum rate of inwards permeability.

In the simulation used to generate Fig.6.6, $T_{AI} = 0.0125 A_u / \mu m^2$, $v_{inmax} = 5 \mu m / s$ and $\alpha_I = 600 \mu m^5 / A_u^2 \cdot s^2$.

As described for Fig 6.4 B (equations 6.2a and b) I also assume that when the auxin concentration reaches a threshold, the total rate of PIN production in the cell increases. In this case, $T_{AP} = 0.019 A_u / \mu m^2$ (which is higher than T_{AI}) therefore the rate of inwards permeability of the cell will tend to increase before the level of PIN in the cell increases.

6.4.2.2.2 Backwards propagation of PIN strands in an indirect cell-cell coupling system

Fig. 6.8 Backwards propagation of a PIN strand in an indirect cell-cell coupling model where low extracellular auxin promotes auxin import and PIN. The first phase of the simulation is initialised as described for Fig. 6.4A, except, that auxin degradation and inwards permeability are only elevated in three cells at the right hand side of the array (rather than in the all cells in the right-

most file). In these cells, the rate of auxin degradation, μ_{Aux} , = 0.2 /s and the inwards permeability of auxin, v_{in} , = 3 $\mu\text{m}/\text{s}$.

In the second phase of the simulation, to achieve propagation of a strand of cells with elevated levels of auxin import and PIN away from the auxin sink, after 2 500s of the simulation, it is assumed that when the total level of extracellular auxin surrounding a cell drops below a threshold, the rate of inwards permeability of that cell to auxin increases until the inwards permeation reaches a maximum rate. When the total level of extracellular auxin surrounding a cell drops below a second, lower threshold, PIN is produced in that cell until the concentration of PIN reaches a maximum value. Once the maximum value of PIN or inwards permeation is reached, the total level of PIN or the rate of inwards permeation of the cell remains constant, irrespective of the concentration of auxin in the cell. The effect on auxin inward permeability rates may be expressed as:

if ($Aux_e < T_{EAi}$ and $v_{in} < v_{inmax}$):

$$\frac{\partial v_{in}}{\partial t} = \alpha \quad (6.4a)$$

otherwise

$$\frac{\partial v_{in}}{\partial t} = 0 \quad (6.4b)$$

Where Aux_e is the total amount of extracellular auxin surrounding a cell (with units of A_u), T_{EAi} is a threshold total amount of extracellular auxin, below which v_{in} increases (also with units of A_u). α is the rate at which the inwards permeability of the cell increases, with units of $\mu\text{m}/\text{s}^2$ and v_{inmax} is the maximum rate of inwards permeability.

In the simulation used to generate Fig.6.8, $T_{EAi} = 0.14 A_u$, $v_{inmax} = 3.3 \mu\text{m}/\text{s}$ and $\alpha = 6 \times 10^{-4} \mu\text{m}/\text{s}^2$.

The effect of low extracellular auxin on PIN levels may be expressed as:

if $\text{Aux}_e < T_{\text{EAP}}$ and $\text{PIN}_{\text{total}} < \text{PIN}_{\text{max}}$:

$$\frac{\partial \text{PIN}_c}{\partial t} = \beta - \frac{1}{R_c} \sum_{n \in N(c)} l_n (\rho_{\text{PIN}} + \tau A^* n) \text{PIN}_c - \mu_{\text{PIN}} \text{PIN}_n \quad (6.5a)$$

otherwise

$$\frac{\partial \text{PIN}_c}{\partial t} = \frac{-1}{R_c} \sum_{n \in N(c)} l_n (\rho_{\text{PIN}} + \tau A^* n) \text{PIN}_c - \mu_{\text{PIN}} \text{PIN}_n \quad (6.5b)$$

Where Aux_e is the total level of extracellular auxin surrounding a cell (with units of A_u), T_{EAP} is the threshold total amount of extracellular auxin, below which the rate of PIN production increases (also with units of A_u), $\text{PIN}_{\text{total}}$ is the total amount of PIN in the cell (with units of A_u), and PIN_{max} is the maximum total amount of PIN per cell. β is the rate of PIN production in the presence of low extracellular auxin, with units of $\text{A}_u/\mu\text{m}^2\text{s}$. All other terms are as described for equation 4.3 and are related to PIN binding and unbinding from the membrane.

In the simulation used to generate Fig.6.8, $T_{\text{EAP}} = 0.12 \text{ A}_u$, $\text{PIN}_{\text{max}} = 1.5 \text{ A}_u$ and $\beta = 1 \times 10^{-4} \text{ A}_u/\mu\text{m}^2\text{s}$.

6.4.2.2.3 Combined forwards and backwards propagation models

Fig. 6.10 Combination of forwards and backwards strand propagation rules in an indirect cell-cell coupling model. The system is initialised as described above for Fig.6.8, with an elevated auxin production rate in the file of cells at the left of the array, and an auxin sink localised in two cells at the right of the array. After 2 400s of the simulation (at the beginning of its second phase), two of the source cells in the left file (indicated in Fig. 6.10) are given an elevated rate of auxin production, so that their auxin production rate, $\rho_{\text{Aux}} = 9 \times 10^{-4} \text{ A}_u/\mu\text{m}^2\text{s}$.

In this simulation, rules for forwards and backwards propagation of PIN strands are combined so that the inwards permeability of a cell to auxin increases if the cell's intracellular auxin concentration exceeds a threshold level, or if the total level of extracellular auxin surrounding the cell decreases below a threshold level. In both scenarios, I assume that the rate of auxin import increases at a constant rate that is not dependent on the auxin concentration of the cell (as for equation 6.4 a). The same rules apply to the level of PIN in the cell. Thus, the levels of PIN in the cell and the rate of inwards permeability of auxin are governed by the following rules:

if $v_{in} < v_{inmax}$ and ($Aux_e < T_{EA}$ or $Aux_c > T_{AI}$):

$$\frac{\partial v_{in}}{\partial t} = \alpha \quad (6.6a)$$

otherwise

$$\frac{\partial v_{in}}{\partial t} = 0 \quad (6.6b)$$

and

if $PIN_{total} < PIN_{max}$ and ($Aux_e < T_{EAP}$ or $Aux_c > T_{AP}$):

$$\frac{\partial PIN_c}{\partial t} = \beta - \frac{1}{R_c} \sum_{n \in N(c)} l_n ((\rho_{PIN} + \tau A^* n) PIN_c - \mu_{PIN} PIN_n) \quad (6.7a)$$

otherwise

$$\frac{\partial PIN_c}{\partial t} = \frac{-1}{R_c} \sum_{n \in N(c)} l_n ((\rho_{PIN} + \tau A^* n) PIN_c - \mu_{PIN} PIN_n) \quad (6.7b)$$

Where all terms and symbols are as described above for equations 6.2-6.5. In the simulation used to generate Fig. 6.10, $T_{EAI} = 0.143 \text{ A}_u$, $T_{AI} = 0.015 \text{ A}_u/\mu\text{m}^2$, $v_{inmax} = 3.5 \mu\text{m}/\text{s}$ and $\alpha = 6 \times 10^{-4} \mu\text{m}/\text{s}^2$. $T_{EAP} = 0.12 \text{ A}_u$, $T_{AP} = 0.021 \text{ A}_u/\mu\text{m}^2$, $\text{PINmax} = 1.5 \text{ A}_u$ and $\beta = 5 \times 10^{-3} \text{ A}_u/\mu\text{m}^2\cdot\text{s}$.

6.4.2.2.4 Indirect cell-cell coupling models of the longitudinal cross-sectional planes of WT and *kan1kan2* leaves.

Fig. 6.12 Generation of the PIN1 polarity pattern in the longitudinal cross-sectional plane of the leaf through a pre-pattern of auxin production, degradation and import.

In the simulation used to generate panel C, all parameters values are as described in Table 2.1 and Table 4.3 except that τ , the rate of A^* dependent promotion of PIN binding to the membrane = $1 \mu\text{m}^2/\text{A}_u\cdot\text{s}$ and ψ_{PIN} , the rate of PIN-dependent auxin efflux = $10 \mu\text{m}^2/\text{A}_u\cdot\text{s}$. The system is initialised as described in chapter 2, except that the initial concentration of auxin in every cell = $0.005 \text{ A}_u/\mu\text{m}^2$ and the c_{PIN} , the initial concentration of PIN in cytoplasmic compartments, = $0.002 \text{ A}_u/\mu\text{m}^2$. In all cells, unless otherwise stated below, ρ_{Aux} , the production rate of auxin = $1.2 \times 10^{-4} \text{ A}_u/\mu\text{m}^2\cdot\text{s}$ and μ_{Aux} , the degradation rate of auxin = $0.005/\text{s}$. Also, unless otherwise stated below, the inwards permeability of auxin, $v_{in} = 0.75 \mu\text{m}/\text{s}$.

In the red cells marked A in Fig. 6.12 B, $\rho_{Aux} = 6 \times 10^{-4} \text{ A}_u/\mu\text{m}^2\cdot\text{s}$.

In the blue cell marked B in Fig. 6.12 B, $\mu_{Aux} = 0.15/\text{s}$ and $v_{in} = 3 \mu\text{m}/\text{s}$.

In the cells marked with a purple outline (C) in Fig. 6.12 B, $v_{in} = 1.125 \mu\text{m}/\text{s}$.

In the cells enclosed by the dark blue outline (D) in Fig. 6.12 B, $v_{in} = 2.625 \mu\text{m}/\text{s}$.

After 1000s of the simulation, the red cell marked E in Fig. 6.12 B is given an elevated rate of auxin production ($\rho_{\text{Aux}} = 1.8 \times 10^{-3} \text{ A}_u / \mu\text{m}^2 \cdot \text{s}$).

The simulation used to generate Fig. 6.12 D is implemented as described above, with feedback between intracellular auxin concentrations and the production of PIN and the rate of inwards permeability to auxin (as described for Fig. 6.6). In this simulation, $T_{\text{AP}} = 0.05 \text{ A}_u / \mu\text{m}^2$, $\text{PIN}_{\text{max}} = 0.5 \text{ A}_u$ and $\alpha_{\text{PIN}} = 0.05 \mu\text{m}^2 / \text{A}_u \cdot \text{s}$. $T_{\text{AI}} = 0.04 \text{ A}_u / \mu\text{m}^2$, $v_{\text{inmax}} = 7 \mu\text{m} / \text{s}$ and $\alpha_I = 600 \mu\text{m}^5 / \text{A}_u^2 \cdot \text{s}^2$.

Fig. 6.13 Indirect cell-cell coupling model for the formation of a coupled epidermal centre of convergence and sub-epidermal PIN strand.

The first phase of the model is implemented as described for Fig. 6.12, except for some changes in parameter values. μ , the default unbinding rate of membrane bound polarity components = 0.003 /s, μ_{PIN} , the default unbinding rate of PIN from the membrane = 0.008/s, γ_{Aux} , the rate of auxin-dependent promotion of A^* to A conversion = $0.6 \mu\text{m}^2 / \text{A}_u \cdot \text{s}$ and ψ_{PIN} , the rate of PIN-dependent auxin export = $30 \mu\text{m}^2 / \text{A}_u \cdot \text{s}$. In all cells, unless otherwise stated below, ρ_{Aux} , the production rate of auxin = $1.5 \times 10^{-4} \text{ A}_u / \mu\text{m}^2 \cdot \text{s}$ and μ_{Aux} , the degradation rate of auxin = 0.005 /s. Also, unless otherwise stated below, the inwards permeability of auxin, $v_{\text{in}} = 0.75 \mu\text{m} / \text{s}$.

In the red cells marker A in Fig. 6.12 B, $\rho_{\text{Aux}} = 6 \times 10^{-4} \text{ A}_u / \mu\text{m}^2 \cdot \text{s}$.

In the blue cell marked B in Fig. 6.12 B, $\mu_{\text{Aux}} = 0.2 / \text{s}$ and $v_{\text{in}} = 3 \mu\text{m} / \text{s}$.

In the cells marked with a purple outline (C) in Fig. 6.12 B, $v_{\text{in}} = 1.125 \mu\text{m} / \text{s}$.

In the cells enclosed by the dark blue outline (D) in Fig. 6.12 B, $v_{\text{in}} = 2.25 \mu\text{m} / \text{s}$.

After 2000s of the simulation, the red cell marked E in Fig. 6.12 B is given an elevated rate of auxin production ($\rho_{Aux} = 3 \times 10^{-4} \text{ A}_u / \mu\text{m}^2 \cdot \text{s}$).

After 2500 steps of the simulation, the cells in the right-most column (abaxial L1) marked with the double-headed arrow in Fig. 613 A, are given an elevated rate of auxin production ($\rho_{Aux} = 9.6 \times 10^{-4} \text{ A}_u / \mu\text{m}^2 \cdot \text{s}$).

There is feedback between intracellular auxin concentrations and the production of PIN and rate of inwards permeability to auxin (as described for Fig. 6.4), with different parameters for L1 cells and L2 cells.

In L1 cells, except those in the distal-most array which I assume have fixed levels of auxin import and PIN, $T_{AP} = 0.07 \text{ A}_u / \mu\text{m}^2$, $PIN_{max} = 0.2 \text{ A}_u$ and $\alpha_{PIN} = 0.0025 \mu\text{m}^2 / \text{A}_u \cdot \text{s}$. $T_{AI} = 0.057 \text{ A}_u / \mu\text{m}^2$, $v_{inmax} = 8 \mu\text{m} / \text{s}$ and $\alpha_I = 600 \mu\text{m}^5 / \text{A}_u^2 \cdot \text{s}^2$.

In L2 cells, $T_{AP} = 0.06 \text{ A}_u / \mu\text{m}^2$, $PIN_{max} = 0.9 \text{ A}_u$ and $\alpha_{PIN} = 0.005 \mu\text{m}^2 / \text{A}_u \cdot \text{s}$. $T_{AI} = 0.047 \text{ A}_u / \mu\text{m}^2$, $v_{inmax} = 3 \mu\text{m} / \text{s}$ and $\alpha_I = 600 \mu\text{m}^5 / \text{A}_u^2 \cdot \text{s}^2$.

7 Hypothesis for the role of polarity fields in the generation of new 3D outgrowths

7.1 Introduction

To understand the development of *kan1kan2* outgrowths, it is necessary to understand how changes in the PIN1 polarity fields described in previous chapters are linked to changes in 3D growth. During *kan1kan2* outgrowth development, two orthogonal planes of the leaf must be deformed by growth (Fig. 7.1). Firstly, there must be deformation within the plane of the abaxial epidermis as a local bulge forms from the abaxial leaf surface (Fig. 7.1 B). The appearance of this bulge is similar to leaf primordium initiation in the shoot apical meristem, where indeed an increased rate of isotropic growth in the plane of the epidermis correlates with outgrowth emergence (Kwiatkowska and Dumais, 2003). Secondly, the deformation within the plane of the abaxial epidermis must be accompanied by increased growth perpendicular to plane of the epidermis (Fig. 7.1 C). How this increased growth perpendicular to the plane of the epidermis is coordinated with changes in growth within the plane of the epidermis, to generate a 3D outgrowth, is unknown.

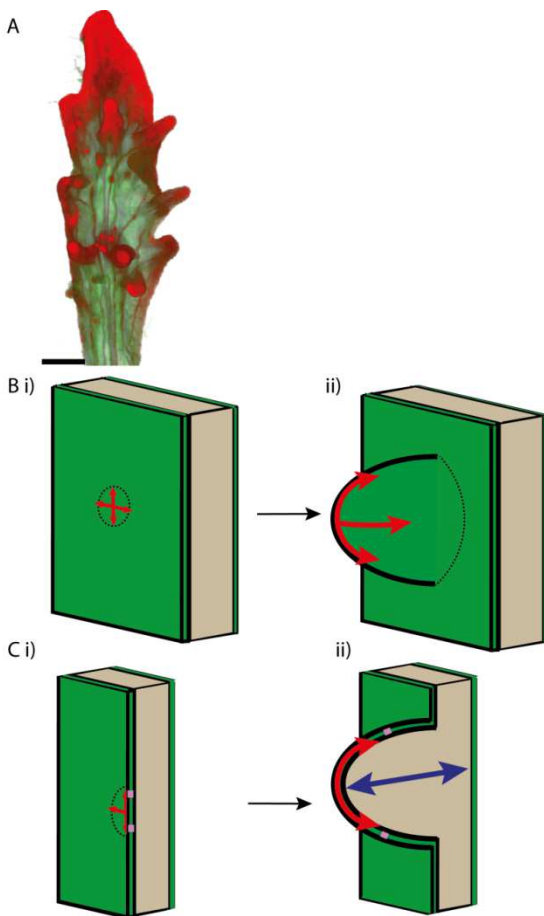


Fig. 7.1. Growth within two orthogonal planes during the generation of a 3D outgrowth.

A) 3D Optical projection tomography image of a *kan1kan2* leaf, showing abaxial surface with ectopic outgrowths. **B)** Deformation of the plane of the epidermis during the development of a 3D outgrowth.

In the example shown, the tissue within the circle marked in i) acquires a high rate of isotropic growth, causing the tissue to buckle out of the plane to produce the outgrowth in ii).

C) To generate a solid 3D outgrowth, an increased rate of growth perpendicular to the plane of the epidermis (blue arrow) must occur simultaneously with the change in growth within the plane of the epidermis (red arrow).

Computational models have been used to generate hypotheses for how genetically-determined patterns of gene expression and polarity fields may control the growth of tissues such as petals and leaves of *A.thaliana* (Green et al., 2010; Kennaway, 2011; Kuchen et al., 2012; Sauret-Gueto et al., 2013). These models use a 2D sheet to represent developing tissue and provide hypotheses for how growth within the plane of this sheet may be specified. Such computational models are useful as they allow predictions to be made about how specified growth (that is, the growth which an infinitesimally small region would undergo if it was isolated from the tissue) interacts with the mechanical constraints of a tissue to generate experimentally observed shapes and growth patterns. However, these models of leaves and petals do not consider how growth perpendicular to the main plane of the tissue might be specified. Therefore, the existing model of leaf development cannot be readily extended to account for *kan1kan2* outgrowth development.

Here, I present a tissue-level model for how growth in the cross-sectional plane of the wild-type leaf may be specified. Next, I present a hypothesis for how the changes in PIN1 patterns observed in *kan1kan2* mutants may be related to a change in the growth of the cross-sectional plane (as illustrated in Fig. 7.1 C) during the development of ectopic outgrowths. I then present quantifications of growth parameters for the abaxial epidermis of *kan1kan2* leaves and relate the findings to possible models of growth.

7.2 Results

7.2.1 Role of an outer-inner polarity field in the growth of the transverse cross-sectional plane of the leaf

The WT leaf grows anisotropically in the transverse cross-sectional plane, from an initial D-shaped primordium, to an elongated ellipse-like shape (Fig. 7.2 A). For this anisotropic growth to be specified, there must be a source of axial information in the cross-sectional plane of the leaf. However, the proximo-distal polarity field hypothesised to be present in the plane of the leaf (Kuchen *et al.*, 2012) does not provide axial information in the cross-sectional plane. I therefore hypothesise that a second, outer-inner polarity field exists in addition to the polarity field in the main plane of the leaf.

To model this outer-inner polarity field and its role in growth, I use the growing polarised tissue (GPT) framework (Kennaway *et al.*, 2010). As the starting shape of the model, I use a circular canvas, which provides a simplified representation of the cross-sectional plane of a young WT leaf primordium. I incorporate known patterns of tissue identity into the model by adding an adaxial identity (ID_ADAXIAL) to the top half of the canvas and an abaxial identity (ID_ABAXIAL) to the bottom half (Fig. 7.2Bi). I further add an epidermal identity around the edge of the canvas (ID_L1) and assume that a mid-plane identity (ID_MIDPLANE) is specified at the adaxial-abaxial boundary

in a region of overlap between ID_{ADAXIAL} and ID_{ABAXIAL} where ID_{L1} is absent (Fig. 7.2 Bii).

This choice of specified regions is based on described expression domains of adaxial-specific transcription factors such as PHABULOSA, of abaxial specific transcription factors including those belonging to *KANADI* and *YABBY* familys, and of *WOX1* and *PRS*, which are expressed at the adaxial-abaxial boundary (Nakata et al., 2012; Yamaguchi et al., 2012).

The outer-inner polarity field is generated by assuming that ID_{L1} acts as a plus organiser, and therefore causes polarity to point away from it, and that ID_{MIDPLANE} acts as a minus organiser, causing polarity to point towards it (Fig. 7.2 B iii). As a consequence of this pattern of organisers, the polarity field is oriented vertically, along the adaxial-abaxial leaf axis, throughout most of the leaf (Fig. 7.2 B iii). The basic shape transformation of the transverse cross-sectional plane of the WT leaf can be accounted for if growth occurs at a higher rate perpendicular to this outer – inner polarity field than parallel to it (Fig. 7.2 C).

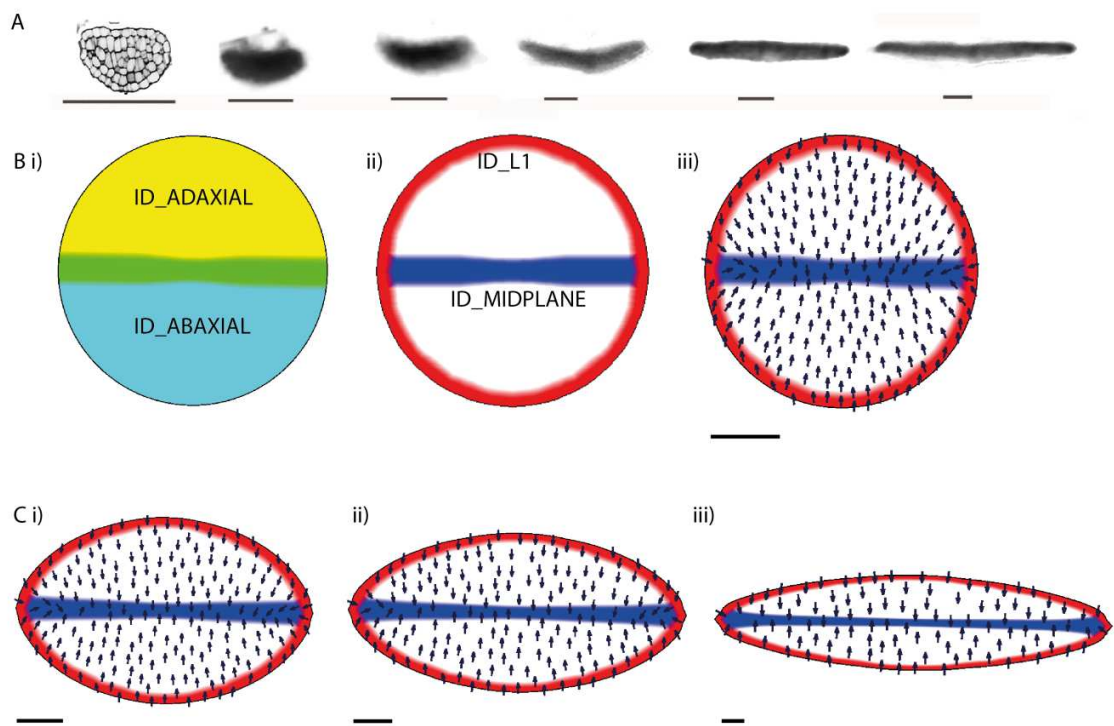


Fig. 7.2 Model for the growth of the transverse cross-sectional plane of the WT leaf.

A) Optical transverse cross-sections of a propidium iodide-stained WT leaf imaged with confocal microscopy (left-most image) and OPT images of non propidium-iodide stained WT leaves at increasing developmental stages. Scale bars = 100 μ m. These images were obtained and provided by Karen Lee. **B)** Identity regions specified for a basic GPT-framework model for the growth of the transverse cross-sectional plane of the WT leaf from a circle to an ellipse. i) The upper half of the leaf is given an adaxial identity (yellow, ID_ADAXIAL) and the bottom half is given an abaxial identity (blue, ID_ABAXIAL). ii) ID_L1 (red) is present at the edge of the canvas. ID_MIDDLE (blue) is present where ID_ADAXIAL and ID_ABAXIAL overlap (green in i) and where ID_L1 is absent. iii) ID_L1 acts as a plus organiser of an outer-inner polarity field and ID_MIDDLE acts as a minus organiser of this polarity field. The direction of the polarity field is shown by arrows. Growth is specified to occur at a higher rate parallel to the polarity field than perpendicular. **C)** Resultant shape changes at successive stages (i - iii) of the model. Scale bars all represent one space unit in the model (the model is not scaled to represent the leaf dimensions).

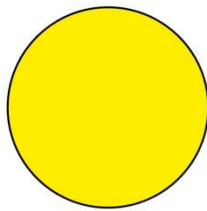
Given this model, one way that an outgrowth can be generated is through a reorientation of the outer-inner polarity field. This may occur if a minus organiser of polarity is ectopically positioned

so that it extends from below the abaxial epidermis to the ID_MIDPLANE domain (Fig. 7.3 Bii). In this scenario, the outer-inner polarity field locally reorients to point laterally, rather than vertically, around the ectopic minus organiser (Fig. 7.3 Bii-vi). Keeping the assumption that growth occurs at a higher rate perpendicular to this polarity field than parallel to it, an outgrowth is generated that is centred on the ectopic minus organiser (Fig. 7.3 B vi).

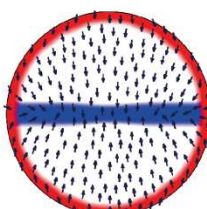
Despite the fact that equal growth rates were specified throughout the leaf (Fig. 7.3 A), because of the change in the polarity field in the abaxial side of the canvas, this side grows less along the horizontal direction than the adaxial side, causing the canvas to bend downwards (Fig. 7.3 B vi). This downwardly bent shape generated by the model contrasts with mature *kan1kan2* leaves, which bend upwards in the transverse cross-sectional plane (Fig. 7.3 C). I hypothesise that this shape of *kan1kan2* leaves could be due to higher growth rates perpendicular to the polarity field in the abaxial side compared with the adaxial side. Indeed, if ID_ABAXIAL promotes growth perpendicular to the polarity field (Fig. 7.3 D), then, depending on the strength of growth promotion, the final shape of the canvas is flat or bent upwards (Fig. 7.3 Eii-vi), better resembling the transverse cross-sectional plane of a mature *kan1kan2* leaf (Fig. 7.3 C).

In this model, the position of the ectopic minus organiser is equivalent to the position of ectopic sub-epidermal strands of PIN1 expression observed in *kan1kan2* leaf primordia. In this context, these PIN1 strands run from the epidermis towards the centre of the leaf prior to outgrowth development (Fig. 6.2 A), and are found along the centres of developing outgrowths (Fig. 6.2 B). Therefore, one hypothesis for how increased growth perpendicular to the plane of the abaxial epidermis is specified in *kan1kan2* outgrowths is that the sub-epidermal strand with elevated PIN1 expression acts as a minus organiser of an outer-inner polarity field.

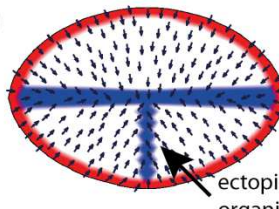
A



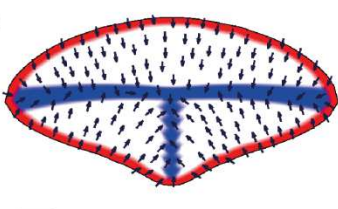
B i)



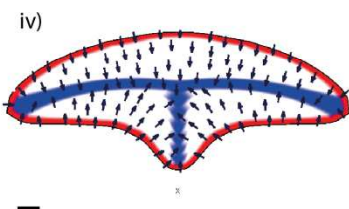
ii)



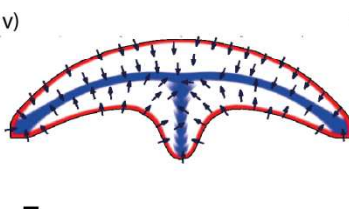
iii)



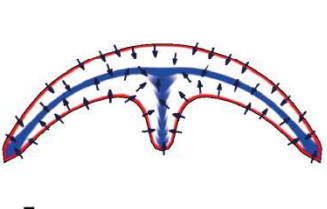
iv)



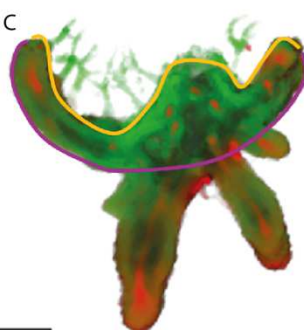
v)



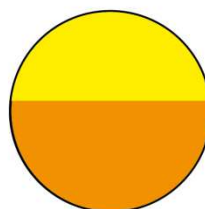
vi)



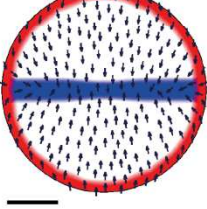
C



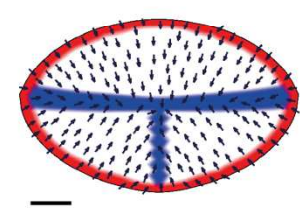
D



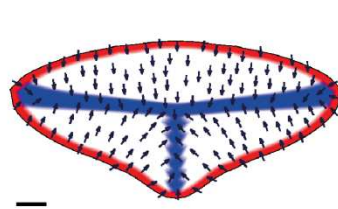
E i)



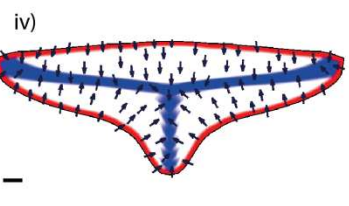
ii)



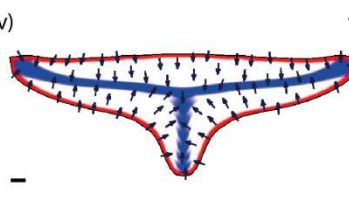
iii)



iv)



v)



vi)

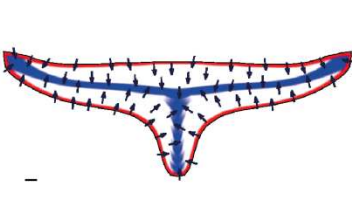


Fig. 7.3 A polarity reorientation-based model for growth of the transverse cross-sectional plane of the *kan1kan2* leaf.

A) and B) Growth is initially specified as for the WT leaf. A) The canvas has a uniform distribution of specified growth rates perpendicular to the outer-inner polarity field. B) Polarity pattern and resultant shape changes for successive changes of the model i) The polarity field is initially specified as for the WT leaf. ii) After an initial growth phase, the expression of ID_MIDPLANE is extended ectopically in a line between the abaxial ID_L1 and the adaxial-abaxial boundary. This causes a polarity reorientation around the ectopic line of ID_MIDPLANE so that the polarity field is oriented laterally in this region. iii)- vi) Since growth occurs a higher rate perpendicular to the polarity than parallel to it, the lateral polarity field causes the formation of an outgrowth. The change in the principle direction of growth in the region around the ectopic organiser means this region has a reduction in growth rate along the horizontal direction. This causes the canvas to bend downwards (v- vi). **C)** Transverse optical section through an OPT image of a mature *kan1kan2* leaf. Yellow and purple lines mark the lamina from which ectopic outgrowths protrude. The yellow line marks the adaxial side of the lamina, and the purple line marks the abaxial side. **D) and E)** Same as A) and B), but ID_ABAXIAL promotes growth perpendicular to the polarity field. D) Specified pattern of growth rates perpendicular to the outer-inner polarity field. Orange indicates highest rate. **E)** The pattern of growth rates causes an upwards bending of the canvas.

To test whether PIN1 marks the predicted region of minus organiser activity within WT leaves, immuno-localisation of PIN1 was performed on transverse cross-sections through WT leaf primordia. Consistent with the hypothesis that PIN1 marks minus organisers of an outer-inner polarity field, PIN1 expression was found to be elevated throughout a central plane in the WT leaf, where the midplane minus organiser is hypothesised to be (Fig. 7.4). To my knowledge, this is the first time that immunolocalisation of PIN1 has been reported for transverse leaf cross-sections. The broad expression domain observed here is similar to the expression domain of *WOX1* and *PRS* transcription factors at the adaxial-abaxial boundary (Nakata et al., 2012) and contrasts with confocal images of sub-epidermal PIN1:GFP expression in whole leaves where only the strongest regions of expression, in vascular strands, are detected (Scarpella et al., 2006).

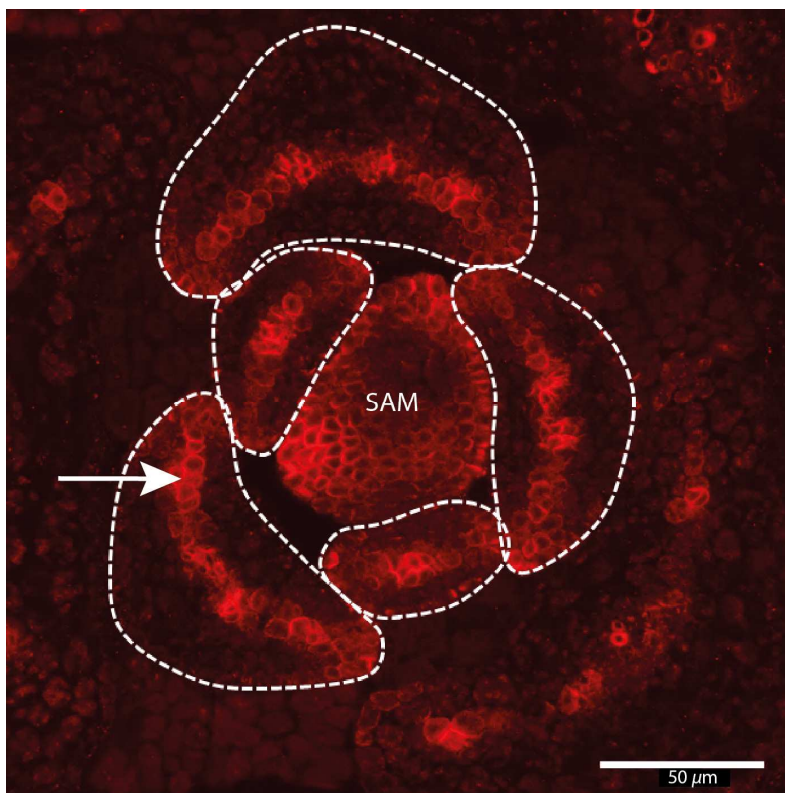


Fig. 7.4 PIN1 expression marks a middle plane identity region in WT leaf primordia.
 Immuno-localisation of PIN1 in a transverse cross-section of a WT (Ler) seedling. Dashed white lines show the outlines of primordia. White arrow indicates elevated PIN1 expression at the midplane. The central tissue is the vegetative shoot apical meristem.

7.2.2 Quantification of growth of the *kan1kan2* abaxial epidermis

Due to current limitations of imaging techniques, it is not possible to readily obtain growth parameters for the cross-sectional plane of leaves. Therefore, whether growth orientations in this plane are similar to those in the model presented above, cannot currently be tested. However, growth parameters can be obtained for the abaxial epidermis of the leaf (Kuchen et al., 2012). If changes in growth of the cross-sectional plane of the leaf occur according to the model presented above, this would most likely have an effect on growth within the plane of the abaxial epidermis which can be measured experimentally.

To obtain a description of growth of the *kan1kan2* abaxial epidermis prior to outgrowth emergence, I used cell vertices marked by a fluorescent plasma-membrane marker as landmarks that were tracked over time to obtain local growth parameters. By measuring the displacements

of cell vertices relative to each other, for a series of successive time points prior to outgrowth emergence, it was possible to calculate the principle orientations of growth and growth rates for local regions of the abaxial epidermis. Growth parameters were calculated both for *kan1kan2* leaves that went on to develop outgrowths, and for those that didn't.

One leaf that made an outgrowth, and two that didn't, were tracked using a constitutively expressed plasma-membrane RFP marker, which allowed growth parameters to be obtained for whole leaves (Fig. 7.5). Growth parameters for regions that gave rise to outgrowths were also obtained using a *PIN1::PIN1:GFP* marker for four other leaves that made outgrowths. In this case, only cells around the centre of convergence could be tracked, however the results obtained for this restricted region were consistent with those obtained using the plasma-membrane marker.

In leaves that developed ectopic outgrowths, local differences in principle orientations of growth preceded outgrowth development (Fig. 7.5 A). One to two days prior to outgrowth emergence, cells in the distal-most two-thirds of the leaf grew preferentially along the proximo-distal axis (Fig. 7.5 A i). In contrast, a group of cells within the proximal-most third of the leaf grew preferentially along the medio-lateral leaf axis, orthogonal to the principle orientation of growth in more distal regions (Fig. 7.5 A i, double headed arrow). Cells in the proximal region continued to grow along the medio-lateral axis until at least 13 hours prior to outgrowth development (Fig. 7.5 A ii). Tracking cell fates revealed that cells at the tips of emerging outgrowths descended from the proximal region that had medio-lateral growth prior outgrowth emergence (Fig. 7.5 A, red cell outlines).

In *kan1kan2* leaves that did not generate outgrowths, proximal regions showed only transient differences in growth orientations compared with distal regions (Fig. 7.5 B). In both tracked leaves, when the leaf widths were less than 100 μm , groups of cells in their proximal half grew

preferentially along the medio-lateral axis (Fig. 7.5 B i). However, at a later stage, the majority of cells in both proximal and distal regions of the leaves grew preferentially along the proximo-distal axis (Fig. 7.5 B ii). This is contrast with the leaves that developed outgrowths, where preferential growth along the medio-lateral leaf axis in proximal regions was sustained when leaves were greater than $100\mu\text{m}$ in width (compare Fig. 7.5 Aii and B ii). This suggests that locally sustained growth along the medio-lateral leaf axis is associated specifically with outgrowth development, rather than being a general feature of the *kan1kan2* background.

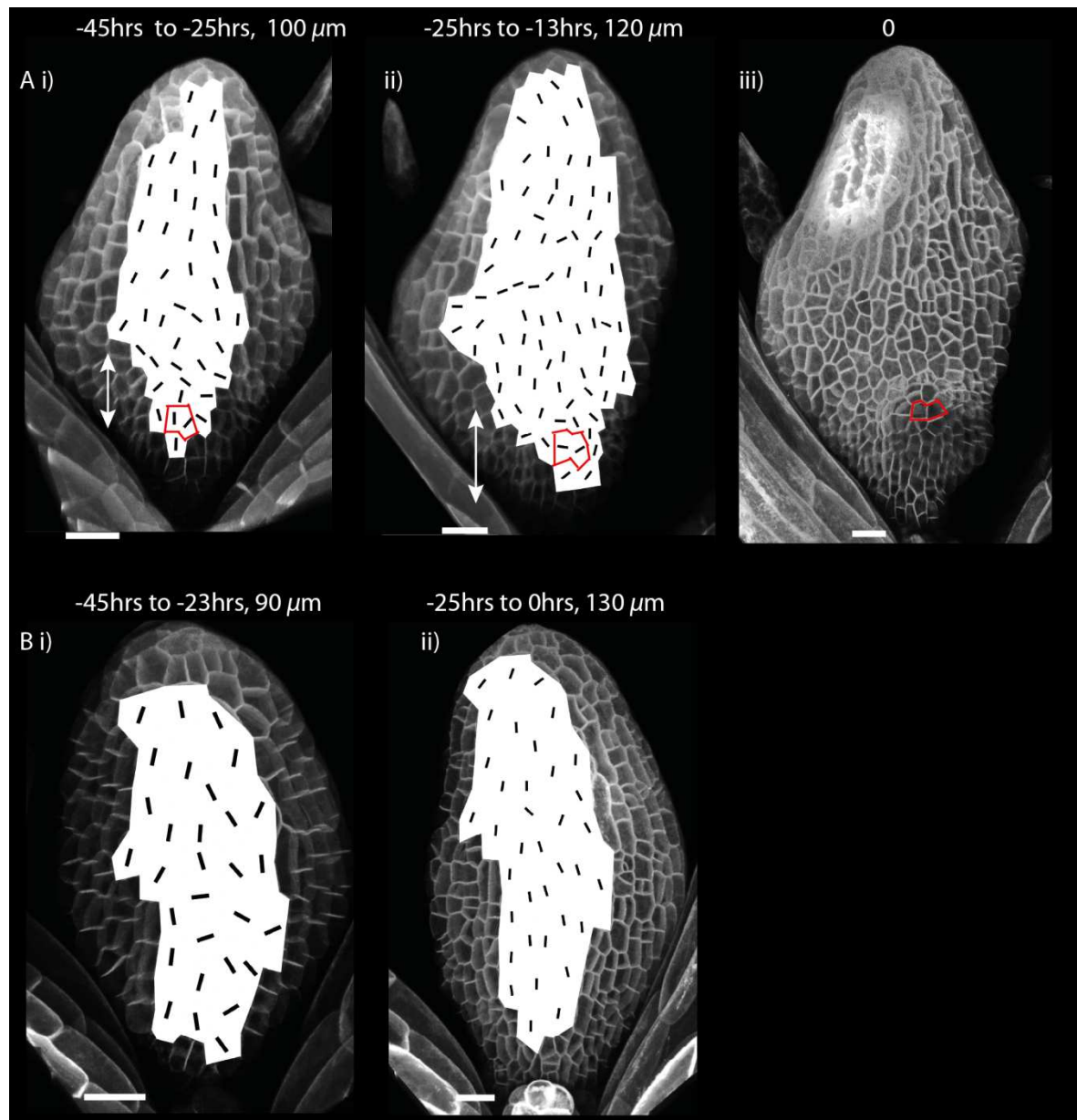


Fig. 7.5 Principle directions of growth in *kan1kan2* leaves prior to outgrowth development

A) Principle directions of growth in a *kan1kan2* leaf that generated an ectopic outgrowth. A i) and A ii) show the principle orientations of growth in the periods 45 to 25 and 25 to 13 hours prior to outgrowth emergence. Widths of the leaf at the end of the growth period are given above the images. Lines are drawn to show the principle growth orientation of a local region when its total anisotropy for the period of growth was greater than 5%. Double headed arrows show regions with growth oriented along the medio-lateral axis. A iii) shows the leaf when the outgrowth has begun to emerge. Cells outlined in red give rise to the tip of outgrowth. **B)** Growth parameters of a representative *kan1kan2* first leaf which did not generate an ectopic outgrowth. Times relative to the end of the experiment, and leaf widths at the end of each growth interval, are given above images. Scale bars = 20 μ m

A characteristic pattern of growth rates was also found to precede outgrowth development. Within the proximal region of leaves that gave rise to outgrowths, a band of cells running across the leaf had a locally reduced areal growth rate (growth rate in area) between one to two days prior to outgrowth emergence (black cell outlines in Fig. 7.6 Ai). This band of cells was located distal to the cells which eventually gave rise to the outgrowth tip (which are outlined in brown in Fig. 7.6). In the day preceding outgrowth emergence, growth rates were generally higher in the proximal region of the leaf compared with in the distal region (Fig. 7.6 Aii), which is similar to what is observed for the WT leaf (Kuchen et al., 2012).

The areal growth rate can be decomposed into growth rates parallel or perpendicular to the midline of the leaf (the line running along the centre of the leaf from the base of the leaf to the tip). Plotting these two components revealed that cells within the band with low areal growth rates had comparatively low growth rates along the midline between one to two days prior to outgrowth emergence (low Kmidline, Fig. 7.6 B i). However, this region had similar growth rates to surrounding cells in the direction perpendicular to the midline (Fig. 7.6 C i). In the last day prior to outgrowth emergence, the reduction in Kmidline in these cells could no-longer be detected (Fig. 7.6 B ii).

The proximal band of cells with reduced Kmidline was not clearly evident in leaves that did not generate outgrowths. At early stages of development, these leaves had more uniform patterns of areal growth rates and growth rates along the midline than those that developed outgrowths (Fig. 7.6 Di, Ei). Similar to WT leaves, and to *kan1kan2* leaves that gave rise to outgrowths, at later stages, a clear proximo-distal gradient in growth parallel to the midline was present, with cells nearest the base of the leaf growing at higher rates parallel to the midline than cells near the tip (Fig. 7.6 D ii, Eii, Fii).

In summary, these findings suggest that, within the plane of the abaxial epidermis, a reorientation of the principle directions of growth, and a local modulation of growth rates, is associated with outgrowth development.

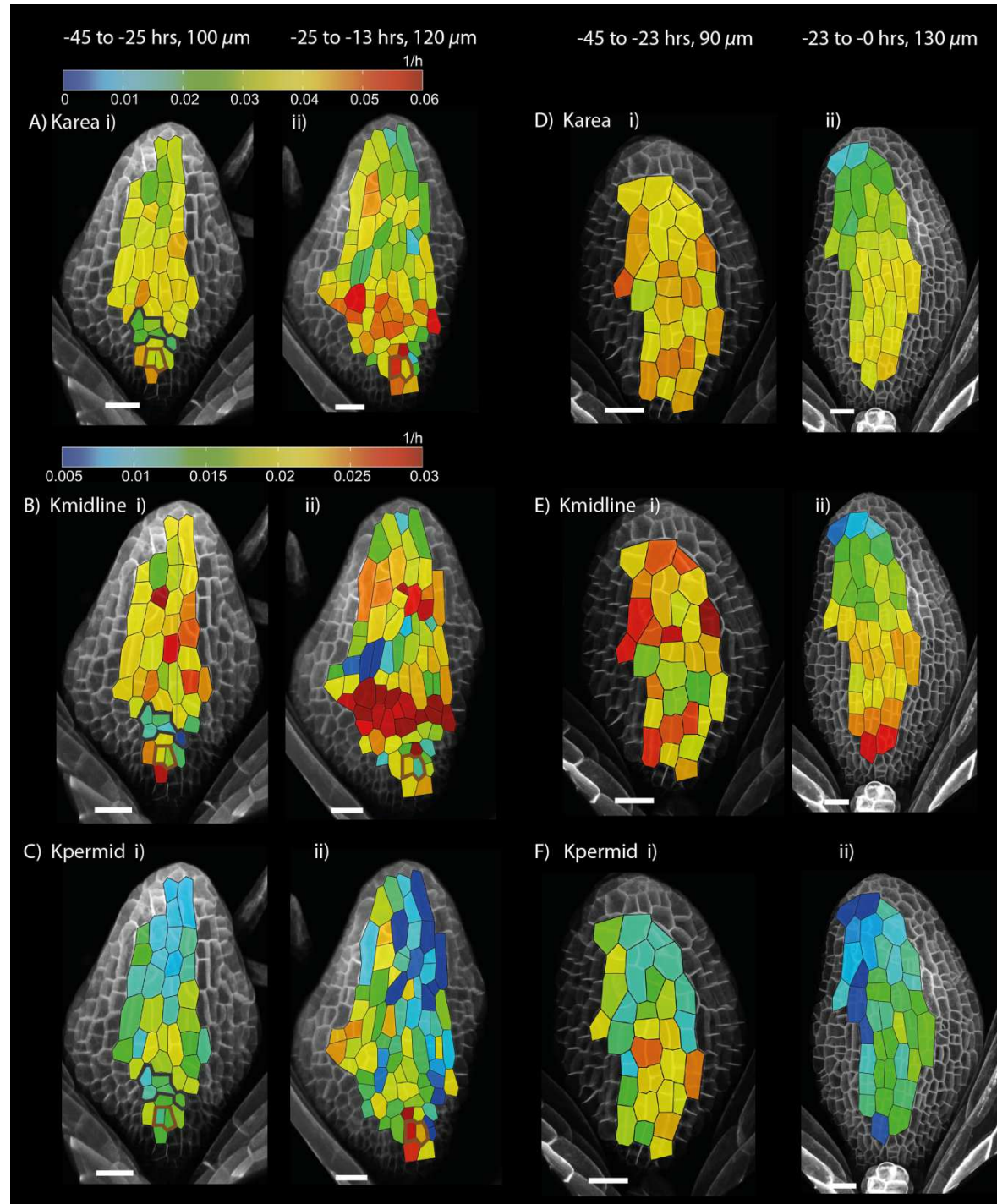


Fig. 7.6 Growth rates of *kan1kan2* leaves prior to outgrowth development

A)–C) Growth rates of the abaxial epidermis of a *kan1kan2* leaf that generated an ectopic outgrowth. **A)** Growth rates in area in the periods 45 to 25 and 25 to 13 hours prior to outgrowth emergence (time intervals, and leaf widths at the end of each time interval, are shown above images). Cells outlined in brown in A–C gave rise to the tip of the outgrowth. Cells outlined in black in panels i) have low growth parallel to the midline 45 to 25 hours prior to outgrowth development. **B)** Growth rates parallel to the midline. **C)** Growth rates perpendicular to the midline. **D)–F)** Growth rates of the abaxial epidermis of a *kan1kan2* leaf that did not generate an ectopic outgrowth. Time intervals relative to the end of the experiment, and leaf widths at the end of each time interval for which growth was calculated, are given above each image. **D)** Growth rate in area. **E)** Growth rate parallel to the midline. **F)** Growth rate perpendicular to the midline. The colour bar above A applies to all areal growth rates (A and D), and the colour bar above B applies to all growth rates parallel or perpendicular to the midline (B, C, E, F). Scale bars = 20 μ m.

7.3 Discussion

7.3.1 Coordination of growth between orthogonal planes of the leaf

Here, I hypothesise that reorientation of an outer-inner polarity field causes local changes in growth orientation in the cross-sectional plane of the leaf during the development of *kan1kan2* outgrowths. I assume that the outer-inner polarity field is normally oriented along the adaxial-abaxial leaf axis and that growth is specified to occur at a higher rate perpendicular to the polarity field than parallel to it. A local reorientation of the outer-inner polarity field in the abaxial half of the leaf, so that it is oriented along the medio-lateral axis, causes a local increase in growth perpendicular to the abaxial epidermis. I hypothesise that sub-epidermal PIN strands that precede *kan1kan2* outgrowths, and are later found at their centres, mark minus organisers of the outer-inner polarity field that cause its reorientation.

In plants, growth rates are known to be controlled by the strength of the cell wall (Cosgrove, 2005). Therefore, to affect growth, the change in the polarity field in the model I propose must cause changes in the cell wall strength in the cross-sectional plane of the leaf. The model predicts

that, in WT leaves, cell walls orthogonal to the epidermis (and parallel to the outer-inner polarity field) are more highly reinforced than walls parallel to the epidermis. At sites of *kan1kan2* outgrowths, reorientation of the outer-inner polarity field is expected to cause a switch in the walls that are preferentially reinforced, so that walls parallel to the leaf surface are more reinforced than walls perpendicular to the surface. This prediction could be tested by directly measuring the strengths of different cell walls in emerging outgrowths and surrounding tissue (Peaucelle, 2014).

There are several hypotheses for how deformation of the plane of the abaxial epidermis could be coordinated with deformation perpendicular to this plane during outgrowth development: this could involve local changes in the orientation of specified growth in both orthogonal planes, or only in one of the planes.

The first hypothesis, that changes in specified growth occur both in the plane of the abaxial epidermis and in the plane perpendicular to it, might occur through the coupled formation of epidermal centres of polarity convergence and sub-epidermal PIN1 strands. The change in PIN1 polarity in the *kan1kan2* abaxial epidermis may correlate with a change in a polarity field that is used to specify growth orientations within the abaxial epidermis. Simultaneously, the sub-epidermal PIN strand below the centre of convergence may cause a reorientation of a second, outer-inner polarity field, causing a reorientation of specified growth perpendicular to the main plane of the leaf.

Another hypothesis is that specified growth is only reoriented within the cross-sectional plane of the leaf, and that this reorientation of growth within a single plane causes resultant (observed) growth orientations to change in both the cross-sectional plane, and within the plane of the abaxial epidermis, due to the mechanical constraints of the tissue. For example, it may be possible

for an outgrowth to develop due to a change in the orientation of specified growth only in the cross-sectional plane, possibly combined with a local region with an elevated rate of isotropic growth within the plane of the abaxial epidermis. Because of tissue connectedness, a change in growth orientation in the cross-sectional plane would most likely cause a deformation within the plane of the abaxial epidermis.

A final hypothesis is that reorientations of specified growth only occur within the plane of the abaxial epidermis and not perpendicular to this plane. Although growth of 2D cross-sections of the leaf cannot easily be accounted for without changes in the inner-outer polarity field, 2D models do not incorporate possible interactions with growth in the orthogonal plane.

In conclusion, given the possible interactions between growth in the orthogonal planes of the leaf, it is difficult to draw conclusions about how growth is specified from the observed changes in resultant growth orientation in the abaxial epidermis shown in Fig. 7.5. This is because the changes in growth orientation in the abaxial epidermis could be a result of changes in specified growth within the plane of the abaxial epidermis, and / or changes in specified growth perpendicular to this plane. To distinguish between the different hypotheses for how growth within and perpendicular to the plane of the abaxial epidermis is coordinated, it will be necessary to implement them in a 3D modelling framework. This will allow more accurate predictions to be made about the effects of interactions between specified growth in the two orthogonal planes of tissue, allowing more meaningful comparisons with experimental data.

7.3.2 Candidate molecules involved in the outer-inner polarity field

The model of growth in the cross-sectional plane of the leaf predicts the existence of an outer-inner polarity field. However, the identity of molecular components that could be involved in this outer-inner polarity field is unknown. To my knowledge, there are no cases where PIN proteins

have been observed to be polarised along this axis. However, expression of PIN1 and PIN2 in sub-epidermal tissue other than developing vascular tissue is very weak (Fig. 7.4 and Guenot et al., 2012) and it is possible that a polar distribution of these proteins exists but cannot be detected given experimental limitations. Another possibility is that a graded signal other than auxin is present along the adaxial-abaxial leaf axis and either directly provides axial information for growth or orients a second polarity system. Candidate molecules that could provide this graded signal are tasiR-ARFs, small trans-acting RNAs that are produced at the adaxial side of the leaf and move intercellularly to generate a graded distribution across the adaxial-abaxial leaf axis (Chitwood et al., 2009). However, mutants that cannot generate tasiR-ARFs are still able to grow anisotropically in the cross-sectional plane, which argues against these small RNAs being the only source of axial information in the cross-sectional plane (Garcia et al., 2006).

7.3.3 Roles of adaxial- abaxial juxtaposition for anisotropic growth of the leaf

The model of the growth of the cross-sectional plane of the WT leaf (Fig. 7.2) makes several predictions that can be tested experimentally. In this model, it is necessary to have a minus organiser in the central plane of the leaf to establish an outer-inner polarity field. This polarity field runs along the adaxial-abaxial axis throughout most of the cross-sectional plane. Given this, if growth is specified to occur at a higher rate perpendicular to the polarity field than parallel to it, the resultant growth is anisotropic and an ellipse-like shape (similar to the mature WT leaf) is generated. Positioning of the minus organiser in the central plane depends on the presence of an adaxial-abaxial boundary, and therefore a loss of adaxial or abaxial identity is predicted to cause a loss of the midplane minus organiser, or possibly its restriction to the central-most region of the leaf. If this occurs, the outer-inner polarity field will be oriented radially, from the L1 towards the centre of the leaf. Even if growth is specified to occur at a higher rate perpendicular to this radial polarity field than parallel, the resultant shape change will be isotropic and an initial circular

primordium will remain radially symmetrical. This prediction of the model is consistent with the phenotypes of mutants that have a loss of adaxial or abaxial leaf identity. For example, gain of function mutations in the normally adaxially expressed transcription factor, *PHABULOSA*, cause a loss of abaxial identity and the development of radially symmetrical leaves (McConnell and Barton, 1998; McConnell et al., 2001).

7.3.4 A system for investigating the role of CUC in regulating growth rates

The measurements of growth of the abaxial epidermis presented here suggest the existence of a band of cells with reduced growth rates parallel to the midline, located on the distal side of cells that will form the tip of an ectopic outgrowth. The position of this band is similar to the position of *CUC2* and *YUCCA1* expression preceding outgrowth development (Fig. 4.18 and Fig. 5.3), suggesting that the expression of these genes may be responsible for the change in growth rates. It has previously been suggested that *CUC2* represses growth in the sinus of serrations (Nikovics et al., 2006). However, direct measurements of growth rates have not been made in *CUC2* expressing tissue and neighbouring non-expressing tissue. Since developing *kan1kan2* outgrowths are more accessible for time-lapse imaging than the leaf margin, *kan1kan2* leaves could provide a good system to directly test the role of *CUC2* in modulating growth rates in the leaf. Also, whether *CUC2* represses growth through promotion of *YUCCA1* expression, or independently of auxin biosynthesis is unknown. This could be tested by tracking the growth of the abaxial epidermis of *kan1kan2yuc1yuc4* mutants that do not develop ectopic outgrowths. If these mutants still have a band of cells with reduced growth, it would suggest that *CUC2* represses growth independently of its effect on auxin biosynthesis.

7.4 Methods

OPT imaging of WT leaves was performed by Karen Lee as described in chapter 4. Immunolocalisation of PIN1 was performed on wild-type (Ler) seedlings at 13 days after sowing on plates, as described in chapter 6. Images were obtained using confocal microscopy, as described in chapter 4.

7.4.1 Growth analysis

kan1kan2 plants carrying a plasma-membrane RFP marker (chapter 4) were grown on plates until 4 days after sowing, and then imaged approximately every 12 hours according to the time-lapse imaging protocol described in chapter 4. Images were processed as described in Chapter 4.

The growth tensor field for the epidermis was calculated using software called *Point Tracker*, written by Pierre Barbier de Reuille. *Point Tracker* is written in Python and uses the NumPy and SciPy packages for the data analysis and PyQt4 (<http://www.riverbankcomputing.co.uk/software/pyqt>) for the user interface (Kuchen et al., 2012). Individual cell vertices were manually tracked over time by placing points on corresponding vertices in successive images. Points were linked to form closed polygonal regions (which did not necessarily correspond with cells). Growth tensors were estimated for each closed region (described in Kuchen et al., 2013) and areal growth rates and principle orientations of growth were extracted from the growth tensor fields.

7.4.2 Computational models of growth

Finite element models of growth were generated using the growing polarised tissue framework that is implemented as a MATLAB application called GFtbox and described in detail in Kennaway et al., 2011 and available to download from <http://cmpdartsrv3.cmp.uea.ac.uk/wiki/BanghamLab/index.php/GFtbox>. The models used here

are provided on the attached CD (a single script is used to specify the three models, the model to be run can be chosen by changing the parameter value on line 38 of the interaction function, see comments within the script). An initial circular canvas, which is composed of 1538 finite elements, is deformed by growth. Growth is specified by a distribution of factors across the canvas. The finite element mesh is not sub-divided during growth. Factors have one value for each segment or vertex of the canvas and are denoted by capital letters in the text.

The models are intended to be conceptual and provide proof of principle that an outer-inner polarity field may be used to approximately capture the overall shape changes of the wild-type and *kan1kan2* leaves. Therefore, the models are not scaled to match biological scales and parameter values are not given units.

There is an initial set up phase at the beginning of all simulations where a distribution of factors across the canvas (shown in Fig. 7.2) is established prior to simulation of growth. In the simulation of *kan1kan2* outgrowths, which involves an ectopic region of ID_MIDPLANE identity, after 20 steps of the simulation, ID_MIDPLANE is also positioned in a line extending between the domain of ID_L1 and the domain of ID_MID_PLANE in the wild-type model.

After 10 steps of the simulation, the outer-inner polarity field is established and growth is simulated. It is assumed that the polarity field is specified by the gradient of a diffusible factor, polariser (P). The rate of change of P concentration at a given vertex of the canvas is given by:

$$\frac{\partial P}{\partial t} = ID_{L1} - 20 * ID_MIDPLANE * P + D_P \nabla^2 P$$

Where D_P is the diffusion constant of polariser, which has a value of 2 in all simulations. Each factor has a value of either 0 or 1 at each vertex, depending on its presence or absence.

Growth rates parallel and perpendicular to the polarity field are specified so that K_{par} , the growth rate parallel to the polarity field, is lower than K_{per} , the growth rate perpendicular. In the simulation of the wild-type leaf, and in the simulation of the *kan1kan2* leaf where growth occurs at equal rates on the adaxial and abaxial sides of the canvas, $K_{\text{par}} = 0.001$, and $K_{\text{per}} = 0.5$. In the simulation where ID_ABAXIAL promotes growth, $K_{\text{per}} = 0.5 + 0.1 * \text{ID_ABAXIAL}$.

The step size of the simulation is 0.1.

8 General Discussion

8.1 A new indirect cell-cell coupling model for plant polarity

Here I presented a new model for plant polarity which, unlike all other models, is based on an intracellular partitioning system that establishes cell polarity independently from the pre-existence or creation of auxin gradients. I also presented a simple molecular hypothesis for how auxin may indirectly couple polarities of neighbouring cells. Polarities may be locally coordinated if PIN proteins are recruited to the A* intracellular partitioning component, and if elevated extracellular auxin favours the presence of the other polarity component, B* (either by inhibition of A* by extracellular auxin, or through stronger promotion of B* compared with A*). With this system, regions of the tissue which modulate extracellular auxin levels can act as organisers of polarity, causing polarity to point towards (minus organisers) or away (plus organisers) from them.

The model can capture various polarity fields observed in plants, including the proximo-distal polarity field seen in the leaf epidermis, epidermal centres of polarity convergence, and mixed polarity fields such as those seen in the longitudinal cross-sectional plane of the leaf. With feedback between auxin levels and the expression of PIN proteins and auxin importers, the model can also capture the positioning of new centres of convergence in *kan1kan2* leaves and account for the development of pro-vascular strands with elevated levels of PIN.

Other models of plant polarity can also capture some or all aspects of the polarity patterns seen in plants. Up-the-gradient and stress-based models can account for the generation of centres of polarity convergence (Heisler et al., 2010; Jönsson et al., 2006; Smith et al., 2006), and the up-the-gradient model can account for coordinated polarity fields and the development of sub-epidermal strands of cells with elevated PIN (Merks et al., 2007). The flux-based model can also account for

these patterns (Rolland-Lagan and Prusinkiewicz, 2005; Stoma et al., 2008). Additionally, a wall-gradient based model can account for the development of sub-epidermal pro-vascular strands and epidermal centres of convergence (Wabnik et al., 2010; Wabnik et al., 2013). However, unlike these other models, an attractive feature of the indirect cell-cell coupling model is that it provides an explicit molecular mechanism for polarisation, which does not require measurements of auxin concentrations in neighbours, measurements of flux or auxin gradients across the width of the cell wall, measurements of stress, or differences in stress across the thickness of a cell wall.

Comparisons of model behaviours presented here suggest that the indirect cell-cell coupling model behaves similarly to the flux-based model in a number of scenarios, and that both behave differently to the up-the-gradient model. In the absence of biasing cues, the former two models tend to align cell polarities in tandem, hence I refer to them as tandem coupling models, whilst the up-the-gradient model tends to generate centres of polarity convergence (Jönsson et al., 2006; Smith et al., 2006). Also, tandem coupling models generate cell polarities that align down auxin gradients (polarities point towards auxin sinks), whilst the up-the-gradient model generates cell polarities that orient up auxin gradients, (polarities point towards auxin sources). These differences in behaviour between tandem coupling and up-the-gradient models allow the two classes to be distinguished experimentally.

8.2 Tandem coupling models are most compatible with locations of auxin biosynthesis

I have shown that when patterns of auxin biosynthesis are taken into consideration, tandem coupling models are more compatible with generation of leaf polarity patterns than the up-the-

gradient model. This is because, to account for the proximo-distal polarity pattern of the leaf, tandem coupling models predict that the base of the leaf acts as an auxin source, whilst the up-the-gradient model predicts that the base of the leaf acts as an auxin sink. Consistent with tandem coupling models, but not with the up-the-gradient model, expression of the auxin biosynthesis enzyme, *YUC1*, and the *CUC2* transcription factor which promotes *YUC1* expression, is elevated at the leaf base (Nikovics et al., 2006; Wang et al., 2011). PIN1 polarities were also oriented away from ectopic sites of *CUC2* and *YUC1* expression during the development of ectopic centres of polarity convergence in *kan1kan2* leaves. By contrast, in an up-the-gradient model, polarities are predicted to be oriented towards these regions with elevated auxin biosynthesis.

Since *CUC2* is expressed at the boundaries of leaf primordia from early stages of their development in the shoot apical meristem (Heisler et al., 2005), it appears likely that auxin biosynthesis is elevated in these regions. Whether this is the case should be determined experimentally, but if auxin synthesis is elevated in boundary domains of the meristem, it is unclear whether the up-the-gradient model could still account for polarity patterns seen during phyllotaxis. This is because, in the presence of elevated auxin synthesis in boundary domains, polarities would tend to orient towards these regions (Fig. 4.20 B), rather than away from them as is observed experimentally (Heisler et al., 2005). Thus, the findings presented here suggest that when patterns of auxin biosynthesis are taken into account, the up-the-gradient model may not be compatible with phyllotactic patterning. Future work should involve characterisation of the expression patterns of all known auxin biosynthetic genes in the shoot apical meristem and a computational assessment of whether these patterns of auxin biosynthesis are compatible with different models of phyllotaxis.

In support of tandem coupling models, cell polarities are frequently oriented away from regions of elevated auxin biosynthesis during plant development. In addition to the observations of the

WT and *kan1kan2* leaf epidermis described above, in sub-epidermal leaf tissue, polarities of pro-vascular cells are oriented proximally (Scarpella et al., 2006), away from a region of elevated *YUC4* expression in sub-epidermal cells at the leaf tip (Wang et al., 2011 and Fig. 6.12 E). Like the leaf, petals have distally oriented PIN1 polarities (Sauret-Gueto et al., 2013) and elevated expression of *YUC1* and *YUC4* at their base (Cheng et al., 2006). Additionally, during early embryogenesis, PIN7 is apically localised, oriented away from the suspensor at the base of the pro-embryo, which has elevated expression of *YUC3*, *YUC4* and *YUC9* (Friml et al., 2003; Robert et al., 2013).

There is also more direct evidence that local auxin sources influence PIN polarity orientations. At globular stages of embryogenesis, *TAA1* and *YUC* auxin biosynthesis enzymes begin to be expressed in the apical-most cells of the embryo. The onset of their expression coincides with, and is required for, the polarisation of PIN1 which switches from having a non-polar distribution to point basally, away from sites of elevated auxin biosynthesis (Robert et al., 2013). Consistent with these observations, ectopic application of auxin to wounded stems is sufficient to cause up-regulation of PIN expression and its polarisation away from the site of auxin application (Sauer et al., 2006). The effect of dynamic auxin sources during embryogenesis on PIN polarisation can be captured by the model of Wabnik et al., 2010, which has behaviours of both tandem coupling and up-the-gradient models (Wabnik et al., 2013). However, the experimental data appears to be consistent with tandem coupling models and provides strong support for the prediction of these models that polarities become oriented away from local auxin sources.

8.3 Auxin import has an important role in tandem coupling models

As well as localised regions of auxin biosynthesis, local modulation of auxin import rates plays an important role in both flux-based and indirect cell-cell coupling models of polarity. I have shown that both models require regions of locally elevated auxin import to account for the formation of

centres of polarity convergence with sustained elevated levels of intracellular auxin. In both models, centres of convergence, such as those generated in the shoot apical meristem or in *kan1kan2* leaves, may be generated in the absence of elevated auxin import as long as auxin degradation is locally elevated (which could represent removal of auxin into internal tissue). However, without auxin import, centres of convergence tend to be less stable, and the models predict at least transient local reductions in auxin concentrations (Fig. 3.9, Stoma et al., 2008) which are not observed experimentally (Brunoud et al., 2012; Heisler et al., 2005) .

Several lines of evidence support the predicted requirement of auxin import in tandem coupling models. A loss of all functional copies of *AUX/LAX* auxin importers disrupts organ emergence from the shoot apical meristem, and in the most severely affected meristems, causes a loss of centres of *PIN1* polarity convergence (Bainbridge et al., 2008). Consistent with this, here I have shown that a loss of all *AUX/LAX* auxin importers suppresses the formation of ectopic *kan1kan2* outgrowths (Fig 4.15). As predicted by tandem coupling models, expression of *AUX1* and *LAX1* is elevated at the tips of emerging outgrowths (Bainbridge et al., 2008, Fig. 4.13, Fig. 4.14). A role for locally elevated auxin import in generating centres of *PIN1* polarity convergence is not inconsistent with the up-the-gradient model, but it does not readily arise from this model. Also more consistent with tandem coupling models, *aux1lax1lax2* mutants have weaker and broader expression domains of the auxin-responsive reporter *DR5::GFP*, with the most severely affected meristems having almost uniform expression levels of this reporter (Bainbridge et al., 2008). It is unclear how this may be reconciled with up-the-gradient models where centres of convergence with high auxin form spontaneously in the absence of auxin import (Jönsson et al., 2006; Smith et al., 2006).

In the future, the prediction of tandem coupling models that auxin import is important for the generation of *kan1kan2* centres of convergence should be more directly tested by analysing *PIN1*

polarity patterns in *kan1kan2aux1lax1lax2lax3* leaves. Also, the role of other mechanisms that might be redundant with AUX/LAX auxin importer proteins in the generation of centres of convergence should be investigated. This includes, for example, down-regulation of non-polar auxin exporters (Blakeslee et al., 2007), or auxin's effects on its own inward permeation rate due to acidification of the cell wall (Steinacher et al., 2012).

8.4 Evidence for organisers of polarity

In chapter 2, and in Abley et al., 2013, it was hypothesised that polarity becomes coordinated with respect to tissue axes (e.g. to point along the proximo-distal axis of a tissue), through the action of organiser regions located at tissue boundaries. Organiser regions are predicted to modulate the polarity generating system, causing polarities to orient away from plus organisers and towards minus organisers. The findings presented here, and others discussed above, provide support for the notion of organisers of polarity. The finding that local sites of auxin biosynthesis in leaves and embryos appear to be involved in causing PIN polarities to orient away from them provides evidence for plus organisers. Also, the finding that auxin import is locally elevated at sites of polarity convergence, and may be required for their formation, supports the prediction of minus organisers of polarity.

I've shown that, in the context of *kan1kan2* leaves, the positioning of new organisers of polarity can be influenced by existing polarity fields. The proximo-distal polarity field of the leaf influences where peaks in auxin concentration will form in the presence of a broad domain with elevated auxin biosynthesis in the proximal half of the leaf (driven by *CUC2* expression). These peaks of auxin concentration may then be used to position new minus organisers of polarity (regions with elevated auxin import and removal), causing a change in the polarity field. This type of feedback between the polarity field and the positioning of organisers could potentially be used to generate

self-organising, dynamic polarity fields such as those seen during phyllotaxis. Indeed, in a flux-based model of phyllotaxis, the pattern of polarity in the meristem determines the auxin distribution, which in turn controls sites of auxin sinks, and therefore feeds-back to change the pattern of polarity (Stoma et al., 2008).

8.5 An indirect cell-cell coupling-based hypothesis for phyllotaxis.

Whether the indirect cell-cell coupling model can also capture PIN1 polarity patterns observed during phyllotaxis has not yet been tested. The *CUC2*-based model of *kan1kan2* outgrowth positioning presented here cannot be applied directly to the meristem. This is because, in the shoot apical meristem, expression of the *CUC2* transcription factor, which promotes auxin biosynthesis in the *kan1kan2* leaf, is weak in regions of incipient primordia (Heisler et al., 2005). This suggests that, in this context, the domain in which new centres of convergence form may not be determined by elevated auxin production.

However, the flux based model of phyllotaxis (Stoma et al., 2008), combined with the presence of elevated auxin import in new primordia (Bainbridge et al., 2008), suggest an alternative way that the indirect cell-cell coupling model could account for phyllotaxis. If it is assumed that all cells in the meristem synthesise auxin at a background rate, and primordia act as strong auxin sinks (due to high auxin import and removal into internal tissues), then auxin levels may be highest at the maximum distance from existing primordia. In the flux-based model the accumulation of auxin at a distance from existing primordia is most likely enhanced by a reduction in the strength of polarisation in these regions (due to weak auxin fluxes far away from auxin sinks). A similar effect may occur in an indirect cell-cell coupling system. With strong feedback between extracellular auxin and the intracellular partitioning system, regions with slightly elevated auxin could cause a reduction in polarity, further enhancing the accumulation of auxin due to a reduction in its

transport. If elevated auxin import is induced in cells with an elevated intracellular auxin concentration, this would cause the formation of a centre of convergence at the maximum distance from existing centres of convergence. Because this model would use elevated auxin import to position the centre of convergence, unlike the current flux-based model of phyllotaxis (Stoma et al., 2008), it would not require a reduction in auxin concentration prior to convergence formation.

8.6 Future work to further evaluate models

8.6.1 Growth and indirect cell-cell coupling

To investigate whether the indirect cell-cell coupling model of phyllotaxis conceived above is feasible, it will be necessary to implement it on a growing array of cells representing the shoot apical meristem. However, whether the indirect cell-cell coupling system is robust to growth and cell division has not been thoroughly investigated. Since plant polarity must be established and maintained in growing tissues, future work should involve investigating the effects of growth on the behaviour of the indirect cell-cell coupling model in the scenarios that have been investigated here using static tissues. The finding that indirect cell-cell coupling can coordinate polarities for arrays of cells with irregular geometries (which may arise during growth) suggests that the polarity mechanism will be robust enough to account for the polarity patterns of growing tissues.

It will also be interesting to use the cellular-level models of polarity described here to drive growth in mechanically realistic models of morphogenesis. Polarity fields such as the PIN1 polarity field seen in the epidermis of leaves and petals are hypothesised to specify the principle orientations of tissue growth (Green et al., 2010; Kennaway, 2011; Kuchen et al., 2012; Sauret-Gueto et al., 2013). However, so far, models of growth have included simple polarity fields generated by graded diffusible factors and have not included cellular-level mechanistic models of

polarity. It will be interesting to implement current models of growth using the cellular level models of polarity explored here to specify the principle directions of growth. This will allow the effects of feedback between polarity fields and growth to be investigated and compared for different polarity models (such as the up-the-gradient, flux-based and indirect cell-cell coupling models), perhaps revealing further testable differences in polarity model behaviours when growth is taken into account.

8.6.2 Testing candidate intracellular partitioning components

Another way to further distinguish between models is to investigate whether an auxin-gradient independent intracellular partitioning system functions upstream of PIN polarity in a range of developmental contexts. The most likely candidates for A* and B* polarity components are ROP proteins (homologs of Rho GTPases), which can inter-convert between membrane bound and cytosolic forms and are homologous to proteins thought to function mutually antagonistically to generate cell polarity in a range of animal and fungal systems (Wedlich-Soldner and Li, 2003; Yang and Lavagi, 2012). ROP proteins are asymmetrically localised in cells and required to generate cell polarity in several plant developmental contexts including polar growth of pollen tubes, the polar emergence of root hairs and the development of multiple polarities in individual leaf pavement cells (Jones et al., 2002; Molendijk et al., 2001; Xu et al., 2010; Yang and Lavagi, 2012).

Similar to the indirect cell-cell coupling mechanism, there is also evidence that ROP proteins influence PIN localisations at the plasma-membrane. The presence of active ROP2 in the lobe regions of pavement cells inhibits the endocytosis of PIN1, and since PIN proteins undergo constitutive vesicle recycling to and from the plasma membrane, this reduction in endocytosis elevates PIN1 levels in regions with high levels of ROP2 (Nagawa et al., 2012). This occurs through the action of the ROP2-effector protein, RIC4 which inhibits endocytosis by stabilising actin

filaments (Nagawa et al., 2012). Also, in roots, ROP6 and its effector RIC1 inhibit clathrin-mediated endocytosis, thus promoting the presence of PIN1 and PIN2 in the plasma-membrane (Chen et al., 2012; Lin et al., 2012). Additionally, ROP1 interacts with a scaffold protein, INTERACTOR OF CONSTITUTIVELY ACTIVE ROP1 (ICR1), which is polarly localised and promotes exocytosis, thus promoting the presence of PIN1 and PIN2 proteins in specific regions of the plasma membrane (Hazak et al., 2010).

The activity of ROPs, and therefore the presence of PIN proteins in the plasma-membrane, is influenced by extracellular auxin. Auxin inhibits endocytosis, thus promoting the presence of PIN proteins in the plasma-membrane (Paciorek et al., 2005; Robert et al., 2010) . This effect of auxin on endocytosis is mediated at least in part through activation of ROPs: auxin activates ROP2 in pavement cells (thus promoting RIC4-dependent reduction in endocytosis) and its inhibition of endocytosis in roots depends on ROP6 (Chen et al., 2012; Xu et al., 2010). The activation of ROPs and inhibition of endocytosis is most likely promoted by extracellular auxin since these effects are dependent on the ABP1 auxin receptor which is localised at the cell surface (Chen et al., 2012; Jones and Herman, 1993; Robert et al., 2010).

Thus, ROP proteins are candidate intracellular partitioning (A*-B*) molecules and, consistent with indirect cell-cell coupling (where A* recruits PIN to the membrane), ROPs promote the presence of PIN proteins in the membrane. Also consistent with indirect cell-cell coupling (where extracellular auxin feeds back to influence the intracellular partitioning system), extracellular auxin most likely influences ROP activity. However, the activation of ROPs by extracellular auxin contrasts with the implementation of indirect cell-cell coupling used here, where extracellular auxin inhibits the presence of A*, and therefore PIN, in the membrane. This inconsistency in the model can be overcome if extracellular auxin promotes the presence of both A* and B* in the membrane, with stronger promotion of B* than A*. This model was tested and can capture all the

behaviours of the indirect cell-cell coupling model presented in chapter 2 (and most-likely generates the behaviours reported in other chapters, although this has not been tested). This mechanism is consistent with experimental observations in pavement cells that auxin promotes both the PIN-recruiting ROP2 (equivalent to A*) and ROP6 (equivalent to B*), but with a higher rate of activation of ROP6 (Xu et al., 2010).

Despite the experimental evidence in favour of ROP-mediated intracellular partitioning and indirect cell-cell coupling, whether polar localisations of ROPs are consistently correlated with PIN polarity patterns is unknown. Although ROPs play a role in regulating PIN polarity in roots, ROPs are not polarly localised in this context (Chen et al., 2012). Future work should involve investigating whether the cellular distributions of PIN and active ROPs correlate in different plant tissues, including the leaf epidermis and the shoot apical meristem. Also, whether ROPs are consistently required for PIN polarity in these tissues should be investigated, since previous work has shown alterations (but not complete losses) of root PIN polarity in *rop* mutant backgrounds (Lin et al., 2012). Since there are 11 ROPs in *A.thaliana*, 6 of which have been implicated in cell polarity (Yang, 2008), it is possible that multiple ROPs may function redundantly in the generation of PIN polarities, therefore multiple mutants will most likely have to be analysed. To test the indirect cell-cell coupling model and distinguish it from other models, it will be necessary to investigate whether, as predicted by this model, ROP proteins can generate cell polarity in single cells, independently from auxin gradients. It will also be useful to further investigate the role of the candidate extracellular auxin receptor, ABP1, in the coordination of PIN1 polarity fields, for example those in WT and *kan1kan2* leaves. Since *abp1* null mutants are embryonic lethal, this would require an investigation of whether a reduction in ABP1 function disrupts PIN1 polarity patterns (Shi and Yang, 2011).

8.6.3 Testing the behaviours of cells in the absence of neighbours or pre-established asymmetries

Analysis of the behaviour of cultured cells in the absence of pre-established asymmetries or polarisable neighbours is likely to be a useful way to distinguish between models. Although the up-the-gradient model can establish polarity in a single cell surrounded by non-polarisable neighbours, cells without neighbours are unlikely to be able to polarise. The same prediction is true for the stress-based polarity model. However, both models predict that groups of cells or 1D files would establish polarity and spontaneously form centres of polarity convergence. Conversely, with a flux-based model, isolated cells may be able to polarise, depending on their auxin synthesis rate and the auxin concentration of the surrounding medium. The same is true for the indirect cell-cell coupling model, whereby isolated cells would polarise, providing the auxin concentration was permissive for intracellular partitioning to occur. Both tandem coupling models predict that groups of cells would spontaneously generate swirled patterns of polarity, and that 1D files would establish coordinated polarity orientations.

Previously, a tobacco-derived BY-2 cell line expressing *AtPIN1:GFP* was used to assess the localisation of PIN1 in isolated cell files in culture. The experimental observations made did not match the predictions of any of the models outlined above. In files of cultured cells, PIN1 was preferentially localised to all membranes that were juxtaposed with neighbouring cells (Boutte et al., 2006). Each cell therefore had peaks of PIN at both of its cell ends. This observation is inconsistent with the indirect cell-cell coupling and flux-based models, which predict that cells would have a single peak of PIN1 localisation and coordinated polarities. It is also inconsistent with the up-the-gradient model, which also predicts that cells would have a single peak of PIN1 localisation and that files of cells would form convergent polarities. This suggests that either

cultured BY-2 cells do not reflect the polarisation behaviour of tissues, or that the current models of auxin-regulated polarity are limited in their capacity to account for PIN polarisation.

When protoplasts were made by removing the cell wall from BY-2 cells, or by removing the cell wall from *A.thaliana* root cells expressing PIN1:GFP or PIN2:GFP, cells lost any pre-existing asymmetry in PIN distribution and localised PIN proteins equally throughout the plasma membrane (Boutte et al., 2006; Feraru et al., 2011). This observation is consistent with up-the-gradient and stress-based models because, in the absence of neighbours, the cues for PIN polarisation (asymmetries in stress in the cell wall or in auxin concentrations in neighbours) are absent. However, the loss of polarity in protoplasts might be largely due to the requirement of the cell wall for regulation of PIN lateral diffusion at the cell surface: PIN proteins in the plasma membrane are physically attached to the cell wall, and this attachment reduces their rate of diffusion as measured by fluorescence recovery after photobleaching (FRAP) (Feraru et al., 2011). A requirement for the presence of the cell wall for polarity maintenance is not inconsistent with intracellular partitioning-based or flux-based systems and could be incorporated into these models to try to better account for the polarisation behaviour of protoplasts.

In the future, cell culture systems should be further developed and used to distinguish between models. Any system used must be known to express all the hypothesised components required for each model. For example, it should be determined whether hypothesised intracellular partitioning components (ROPs and their interactors and effectors) are expressed in the BY-2 system. The polarisation of components other than just PIN proteins should also be assessed in culture. This is because a loss of PIN polarity in protoplasts does not necessarily disprove intracellular partitioning, as intracellular partitioning components, which are proposed to function up-stream of PIN polarisation, may still be polarised. It will also be useful to assess the polarisation behaviour of 2D sheets of cultured cells to distinguish between models.

8.6.4 The role of mechanical signals in polarity and growth

Here, I've focussed on comparisons of chemical-based models of polarity, and have ignored the potential roles of mechanical cues in influencing the generation and orientation of polarity. However, mechanical cues are able to influence polarity in multiple systems (Asnacios and Hamant, 2012) and have been hypothesised to be important for the alignment of polarities in the *D.melanogaster* wing (Aigouy et al., 2010), and for the establishment of PIN1 polarities in the shoot apical meristem (Heisler et al., 2010). It is therefore important to consider how chemical- and mechanical-based models may be related.

The stress-based model of PIN1 polarity is a more explicit mechanism which could underlie the up-the-gradient model (Heisler et al., 2010). Therefore, it might be assumed that the two models make similar predictions (i.e. that polarity will align up auxin gradients). Given this assumption, if auxin is assumed to be the only regulator of stress patterns, then the stress-based model, like the up-the-gradient model, predicts that polarities would align towards regions with elevated auxin biosynthesis. This would make the stress based model incompatible with patterns of polarity and auxin biosynthesis observed in leaves. However, there may be other factors influencing stress patterns, which have not been accounted for and that may outweigh the effects of elevated auxin biosynthesis at the base of leaves and outgrowths. For example, the geometry of boundary regions between new primordia and the shoot apical meristem (arising from the increased growth of the primordium) causes the maximal direction of stress to be locally aligned along the boundary (Hamant et al., 2008). According to a stress-based polarity model, this stress pattern would cause an alignment of PIN polarities away from the boundary (towards the primordium tip, and meristem centre), possibly counteracting the effect of elevated auxin biosynthesis in this region (Heisler et al., 2010). In the future, the combined effects of geometry-dependent stress

patterns and patterns of auxin biosynthesis should be assessed in the stress-based model for phyllotaxis.

A comparison between stress and chemical-based models may be useful, since stress-based models may make testable predictions that are incompatible with chemical based models. These predictions would most likely not arise by comparing chemical-based models alone. One prediction arising from the stress-based model concerns the effects of cell ablation. If a cell is ablated from a tissue, then this is predicted to cause PIN polarities to orient away from the site of the ablation for several cell diameters (Heisler et al., 2010). In a stress-based model, this should occur even in the absence of auxin gradients or auxin transport between cells. In support of this prediction, PIN1 polarities were found to become oriented away from a site of ablation for several cell diameters, even when auxin transport was pharmacologically inhibited, and when external auxin was applied to disrupt endogenous auxin gradients (Heisler et al., 2010). It may be the case that auxin gradients were not completely disrupted in this scenario, and, depending on whether auxin is high or low at the site of ablation, the observed polarity change may be compatible with up-the-gradient, flux-based or indirect cell-cell coupling models of polarity. However, further experiments and comparisons between models are needed to distinguish between chemical- and stress-based models and to determine whether only one or both types of mechanism for polarisation exist.

The role of mechanical vs. chemical-based signals in orienting growth should also be further investigated. In relating the patterns of PIN1 polarity seen in *kan1kan2* leaves to growth, I have hypothesised that growth orientations are controlled by an underlying chemical-based polarity field, which is consistent with previous work (Green et al., 2010; Kennaway, 2011; Kuchen et al., 2012; Sauret-Gueto et al., 2013). In this scenario, the changes in PIN1 polarity observed in *kan1kan2* outgrowths may cause a change in the principle directions of growth. However, an

alternative, but not mutually exclusive hypothesis, is that growth is oriented with respect to principle orientations of mechanical stress. Concentration of auxin at ectopic centres of PIN1 convergence in *kan1kan2* leaves may locally loosen cell walls, influencing the principle orientations of mechanical stress in the surrounding tissue, and therefore influencing the orientations of growth.

This hypothesis is supported by findings that, in the epidermis of the shoot apical meristem, microtubules are aligned along the principle directions of stress predicted from the organ's shape (Hamant et al., 2008). Also, changes in the stress pattern caused by laser ablation of cells are sufficient to cause a reorientation of microtubules so that they align with the new orientations of principle stress (Hamant et al., 2008). Because the orientation of microtubule axiality determines the orientation of cellulose microfibril deposition in cell walls, alignment of microtubules with the direction of principle stress tends to reinforce walls along the direction of stress, hence promoting growth orthogonal to the principle direction of stress.

Although this stress-based model may be compatible with the emergence of primordia from the shoot apical meristem, the negative feedback between stress and growth along the direction of stress tends to stabilise existing structures. Therefore, whether this model is compatible with the radical shape deformations which occur, for example, during the development of an *Antirrhinum* flower (Green et al., 2010), is unclear. It may therefore be the case that both chemical- and mechanical-based anisotropies guide principle directions of growth, perhaps with different mechanisms dominating in different tissues and at different stages of development. In the future, it would be interesting to compare the abilities of these two classes of models to account for growth of different tissues, and to explore the effects of integrating mechanical and chemical hypotheses in a single model.

8.7 Concluding remarks

Here I have compared the ability of different models to account for new and existing experimental data on the dynamic patterns of PIN polarity, auxin biosynthetic gene expression, and auxin importer expression, during the development of PIN1 polarity patterns in leaves. This has revealed that flux-based and indirect cell-cell coupling models are more compatible with current experimental data on leaf polarity and auxin-related gene expression patterns than the up-the-gradient model. Future work should involve extending the number of models compared to include the stress-based model (Heisler et al., 2010) and the wall-gradient model (Wabnik et al., 2010). The ability of all these models to capture PIN polarity patterns within the context of experimentally observed tissue geometries and patterns of gene expression, which may influence auxin and stress distributions, should be compared. By extending the approach taken here, it will be possible to identify further differences in model behaviours and predictions that can be tested experimentally. Ultimately, this will reveal which of the current hypotheses are most consistent with *in vivo* mechanisms of polarisation, and allow further refinement of existing models.

9 References

Abley, K., De Reuille, P.B., Strutt, D., Bangham, A., Prusinkiewicz, P., Maree, A.F., Grieneisen, V.A., and Coen, E. (2013). An intracellular partitioning-based framework for tissue cell polarity in plants and animals. *Development* 140, 2061-2074.

Adler, P.N., Krasnow, R.E., and Liu, J. (1997). Tissue polarity points from cells that have higher Frizzled levels towards cells that have lower Frizzled levels. *Curr Biol* 7, 940-949.

Aida, M., Beis, D., Heidstra, R., Willemsen, V., Blilou, I., Galinha, C., Nussaume, L., Noh, Y.S., Amasino, R., and Scheres, B. (2004). The PLETHORA genes mediate patterning of the *Arabidopsis* root stem cell niche. *Cell* 119, 109-120.

Aida, M., Ishida, T., Fukaki, H., Fujisawa, H., and Tasaka, M. (1997). Genes involved in organ separation in *Arabidopsis*: an analysis of the cup-shaped cotyledon mutant. *Plant Cell* 9, 841-857.

Aida, M., and Tasaka, M. (2006). Morphogenesis and patterning at the organ boundaries in the higher plant shoot apex. *Plant Mol Biol* 60, 915-928.

Aigouy, B., Farhadifar, R., Staple, D.B., Sagner, A., Röper, J.-C., Jülicher, F., and Eaton, S. (2010). Cell flow reorients the axis of planar polarity in the wing epithelium of *Drosophila*. *Cell* 142, 773-786.

Ambegaonkar, A.A., Pan, G., Mani, M., Feng, Y., and Irvine, K.D. (2012). Propagation of Dachsous-Fat planar cell polarity. *Curr Biol* 22, 1302-1308.

Amonlirdviman, K., Khare, N.A., Tree, D.R.P., Chen, W.-S., Axelrod, J.D., and Tomlin, C.J. (2005). Mathematical modeling of planar cell polarity to understand domineering nonautonomy. *Science* 307, 423-426.

Asnacios, A., and Hamant, O. (2012). The mechanics behind cell polarity. *Trends Cell Biol* 22, 584-591.

Bainbridge, K., Guyomarc'h, S., Bayer, E., Swarup, R., Bennett, M., Mandel, T., and Kuhlemeier, C. (2008). Auxin influx carriers stabilize phyllotactic patterning. *Genes Dev* 22, 810-823.

Bayer, E.M., Smith, R.S., Mandel, T., Nakayama, N., Sauer, M., Prusinkiewicz, P., and Kuhlemeier, C. (2009). Integration of transport-based models for phyllotaxis and midvein formation. *Genes Dev* 23, 373-384.

Benkova, E., Michniewicz, M., Sauer, M., Teichmann, T., Seifertova, D., Jurgens, G., and Friml, J. (2003). Local, efflux-dependent auxin gradients as a common module for plant organ formation. *Cell* 115, 591-602.

Bennett, T., Hines, G., and Leyser, O. (2014). Canalization: what the flux? *Trends Genet* 30, 41-48.

Bilsborough, G.D., Runions, A., Barkoulas, M., Jenkins, H.W., Hasson, A., Galinha, C., Laufs, P., Hay, A., Prusinkiewicz, P., and Tsiantis, M. (2011). Model for the regulation of *Arabidopsis thaliana* leaf margin development. *Proc Natl Acad Sci U S A* 108, 3424-3429.

Blakeslee, J.J., Bandyopadhyay, A., Lee, O.R., Mravec, J., Titapiwatanakun, B., Sauer, M., Makam, S.N., Cheng, Y., Bouchard, R., Adamec, J., *et al.* (2007). Interactions among PIN-FORMED and P-glycoprotein auxin transporters in *Arabidopsis*. *Plant Cell* 19, 131-147.

Blilou, I., Xu, J., Wildwater, M., Willemsen, V., Paponov, I., Friml, J., Heidstra, R., Aida, M., Palme, K., and Scheres, B. (2005). The PIN auxin efflux facilitator network controls growth and patterning in *Arabidopsis* roots. *Nature* 433, 39-44.

Boutte, Y., Crosnier, M.T., Carraro, N., Traas, J., and Satiat-Jeunemaitre, B. (2006). The plasma membrane recycling pathway and cell polarity in plants: studies on PIN proteins. *J. cell science* 119, 1255-1265.

Brittle, A., Thomas, C., and Strutt, D. (2012). Planar polarity specification through asymmetric subcellular localization of Fat and Dachsous. *Curr Biol* 22, 907-914.

Brittle, A.L., Repiso, A., Casal, J., Lawrence, P.A., and Strutt, D. (2010). Four-jointed modulates growth and planar polarity by reducing the affinity of dachsous for fat. *Curr Biol* 20, 803-810.

Brunoud, G., Wells, D.M., Oliva, M., Larrieu, A., Mirabet, V., Burrow, A.H., Beeckman, T., Kepinski, S., Traas, J., Bennett, M.J., *et al.* (2012). A novel sensor to map auxin response and distribution at high spatio-temporal resolution. *Nature* 482, 103-106.

Burak, Y., and Shraiman, B.I. (2009). Order and stochastic dynamics in *Drosophila* planar cell polarity. *PLoS Comput Biol* 5, e1000628.

Casal, J., Lawrence, P.A., and Struhl, G. (2006). Two separate molecular systems, Dachsous/Fat and Starry night/Frizzled, act independently to confer planar cell polarity. *Development* 133, 4561-4572.

Chant, J., and Herskowitz, I. (1991). Genetic control of bud site selection in yeast by a set of gene products that constitute a morphogenetic pathway. *Cell* 65, 1203-1212.

Chen, X., Naramoto, S., Robert, S., Tejos, R., Lofke, C., Lin, D., Yang, Z., and Friml, J. (2012). ABP1 and ROP6 GTPase signaling regulate clathrin-mediated endocytosis in *Arabidopsis* roots. *Curr Biol* 22, 1326-1332.

Cheng, Y., Dai, X., and Zhao, Y. (2007). Auxin Synthesized by the YUCCA flavin monooxygenases is essential for embryogenesis and leaf formation in *Arabidopsis*. *Plant Cell* 19, 2430-2439.

Cheng, Y.F., Dai, X.H., and Zhao, Y.D. (2006). Auxin biosynthesis by the YUCCA flavin monooxygenases controls the formation of floral organs and vascular tissues in *Arabidopsis*. *Genes Dev* 20, 1790-1799.

Chitwood, D.H., Nogueira, F.T., Howell, M.D., Montgomery, T.A., Carrington, J.C., and Timmermans, M.C. (2009). Pattern formation via small RNA mobility. *Genes Dev* 23, 549-554.

Classen, A.K., Anderson, K.I., Marois, E., and Eaton, S. (2005). Hexagonal packing of *Drosophila* wing epithelial cells by the planar cell polarity pathway. *Dev Cell* 9, 805-817.

Coen, E., Rolland-Lagan, A.-G., Matthews, M., Bangham, J.A., and Prusinkiewicz, P. (2004). The genetics of geometry. *Proc Natl Acad Sci U S A* 101, 4728-4735.

Cosgrove, D.J. (2005). Growth of the plant cell wall. *Nat Rev Mol Cell Biol* 6, 850-861.

de Reuille, P.B., Bohn-Courseau, I., Ljung, K., Morin, H., Carraro, N., Godin, C., and Traas, J. (2006). Computer simulations reveal properties of the cell-cell signaling network at the shoot apex in *Arabidopsis*. *Proc Natl Acad Sci U S A* 103, 1627-1632.

Devreotes, P.N., and Zigmond, S.H. (1988). Chemotaxis in eukaryotic cells: a focus on leukocytes and Dictyostelium. *Annu Rev Cell Biol* 4, 649-686.

Drubin, D.G., and Nelson, W.J. (1996). Origins of cell polarity. *Cell* 84, 335-344.

Emery, J.F., Floyd, S.K., Alvarez, J., Eshed, Y., Hawker, N.P., Izhaki, A., Baum, S.F., and Bowman, J.L. (2003). Radial Patterning of *Arabidopsis* Shoots by Class III HD-ZIP and KANADI Genes. *Curr Biol* 13, 1768-1774.

Eshed, Y., Baum, S.F., Perea, J.V., and Bowman, J.L. (2001). Establishment of polarity in lateral organs of plants. *Curr Biol* 11, 1251-1260.

Eshed, Y., Izhaki, A., Baum, S.F., Floyd, S.K., and Bowman, J.L. (2004). Asymmetric leaf development and blade expansion in *Arabidopsis* are mediated by KANADI and YABBY activities. *Development* 131, 2997-3006.

Etienne-Manneville, S. (2008). Polarity proteins in migration and invasion. *Oncogene* 27, 6970-6980.

Feraru, E., Feraru, M.I., Kleine-Vehn, J., Martiniere, A., Mouille, G., Vanneste, S., Vernhettes, S., Runions, J., and Friml, J. (2011). PIN polarity maintenance by the cell wall in *Arabidopsis*. *Curr Biol* 21, 338-343.

Feugier, F.G., Mochizuki, A., and Iwasa, Y. (2005). Self-organization of the vascular system in plant leaves: inter-dependent dynamics of auxin flux and carrier proteins. *J Theor Biol* 236, 366-375.

Fischer, S., Houston, P., Monk, N.A., and Owen, M.R. (2013). Is a persistent global bias necessary for the establishment of planar cell polarity? *PLoS One* 8, e60064.

Friml, J., Vieten, A., Sauer, M., Weijers, D., Schwarz, H., Hamann, T., Offringa, R., and Jurgens, G. (2003). Efflux-dependent auxin gradients establish the apical-basal axis of *Arabidopsis*. *Nature* 426, 147-153.

Fu, Y., Gu, Y., Zheng, Z., Wasteneys, G., and Yang, Z. (2005). *Arabidopsis* interdigitating cell growth requires two antagonistic pathways with opposing action on cell morphogenesis. *Cell* 120, 687-700.

Gälweiler, L., Guan, C., Müller, A., Wisman, E., Mendgen, K., Yephremov, A., and Palme, K. (1998). Regulation of polar auxin transport by AtPIN1 in *Arabidopsis* vascular tissue. *Science* 282, 2226-2230.

Garcia, D., Collier, S.A., Byrne, M.E., and Martienssen, R.A. (2006). Specification of leaf polarity in *Arabidopsis* via the trans-acting siRNA pathway. *Curr Biol* 16, 933-938.

Gardiner, E.M., Pestonjamas, K.N., Bohl, B.P., Chamberlain, C., Hahn, K.M., and Bokoch, G.M. (2002). Spatial and temporal analysis of Rac activation during live neutrophil chemotaxis. *Curr Biol* 12, 2029-2034.

Garnett, P., Steinacher, A., Stepney, S., Clayton, R., and Leyser, O. (2010). Computer simulation: The imaginary friend of auxin transport biology. *Bioessays* 32, 828-835.

Geldner, N., Friml, J., Stierhof, Y.D., Jurgens, G., and Palme, K. (2001). Auxin transport inhibitors block PIN1 cycling and vesicle trafficking. *Nature* 413, 425-428.

Goodrich, L.V., and Strutt, D. (2011). Principles of planar polarity in animal development. *Development* 138, 1877-1892.

Greb, T., Clarenz, O., Schafer, E., Muller, D., Herrero, R., Schmitz, G., and Theres, K. (2003). Molecular analysis of the LATERAL SUPPRESSOR gene in *Arabidopsis* reveals a conserved control mechanism for axillary meristem formation. *Genes Dev* 17, 1175-1187.

Green, A.A., Kennaway, J.R., Hanna, A.I., Bangham, J.A., and Coen, E. (2010). Genetic control of organ shape and tissue polarity. *PLoS Biol* 8, e1000537.

Grieneisen, V.A., Berkel, K., Xu, T., Scheres, B., Hogeweg, P., Yang, Z., and Marée, A.F.M. (2014). Intracellular ROP partitioning and auxin-mediated indirect cell-cell communication can explain interdigitation of pavement cells. *Development*, submitted.

Grieneisen, V.A., and Scheres, B. (2009). Back to the future: evolution of computational models in plant morphogenesis. *Curr Opin Plant Biol* 12, 606-614.

Guenot, B., Bayer, E., Kierzkowski, D., Smith, R.S., Mandel, T., Zadnikova, P., Benkova, E., and Kuhlemeier, C. (2012). Pin1-independent leaf initiation in *Arabidopsis*. *Plant Physiol* 159, 1501-1510.

Hager, A. (2003). Role of the plasma membrane H⁺-ATPase in auxin-induced elongation growth: historical and new aspects. *J Plant Res* 116, 483-505.

Hamant, O., Heisler, M.G., Jönsson, H., Krupinski, P., Uyttewaal, M., Bokov, P., Corson, F., Sahlin, P., Boudaoud, A., Meyerowitz, E.M., et al. (2008). Developmental patterning by mechanical signals in *Arabidopsis*. *Science* 322, 1650-1655.

Hasson, A., Plessis, A., Blein, T., Adroher, B., Grigg, S., Tsiantis, M., Boudaoud, A., Damerval, C., and Laufs, P. (2011). Evolution and diverse roles of the CUP-SHAPED COTYLEDON genes in *Arabidopsis* leaf development. *Plant Cell* 23, 54-68.

Hay, A., Barkoulas, M., and Tsiantis, M. (2006). ASYMMETRIC LEAVES1 and auxin activities converge to repress BREVIPEDICELLUS expression and promote leaf development in *Arabidopsis*. *Development* 133, 3955-3961.

Hazak, O., Bloch, D., Poraty, L., Sternberg, H., Zhang, J., Friml, J., and Yalovsky, S. (2010). A Rho scaffold integrates the secretory system with feedback mechanisms in regulation of auxin distribution. *Plos Biol* 8, e1000282.

Heisler, M.G., Hamant, O., Krupinski, P., Uyttewaal, M., Ohno, C., Jonsson, H., Traas, J., and Meyerowitz, E.M. (2010). Alignment between PIN1 polarity and microtubule orientation in the

shoot apical meristem reveals a tight coupling between morphogenesis and auxin transport. PLoS Biol 8, e1000516.

Heisler, M.G., Ohno, C., Das, P., Sieber, P., Reddy, G.V., Long, J.A., and Meyerowitz, E.M. (2005). Patterns of auxin transport and gene expression during primordium development revealed by live imaging of the *Arabidopsis* inflorescence meristem. Curr Biol 15, 1899-1911.

Husbands, A.Y., Chitwood, D.H., Plavskin, Y., and Timmermans, M.C.P. (2009). Signals and prepatterns: new insights into organ polarity in plants. Genes Dev 23, 1986-1997.

Jacobs, W.P. (1952). The role of auxin in differentiation of xylem around a wound. Am J Bot 39, 301-309.

Jilkine, A., Maree, A.F., and Edelstein-Keshet, L. (2007). Mathematical model for spatial segregation of the Rho-family GTPases based on inhibitory crosstalk. Bull Math Biol 69, 1943-1978.

Johnson, J.M., Jin, M., and Lew, D.J. (2011). Symmetry breaking and the establishment of cell polarity in budding yeast. Curr Opin Genet Dev 21, 740-746.

Jones, A.M., and Herman, E.M. (1993). KDEL-Containing Auxin-Binding Protein Is Secreted to the Plasma Membrane and Cell Wall. Plant Physiol 101, 595-606.

Jones, M.A., Shen, J.-J., Fu, Y., Li, H., Yang, Z., and Grierson, C.S. (2002). The *Arabidopsis* Rop2 GTPase is a positive regulator of both root hair initiation and tip growth. Plant Cell 14, 763-776.

Jönsson, H., Heisler, M.G., Shapiro, B.E., Meyerowitz, E.M., and Mjolsness, E. (2006). An auxin-driven polarized transport model for phyllotaxis. Proc Natl Acad Sci U S A 103, 1633-1638.

Kennaway, R., Coen, E., Green, A., Bangham, A. (2011). Generation of diverse biological forms through combinatorial interactions between tissue polarity and growth. PLoS Biol 7, e1002071.

Kierzkowski, D., Lenhard, M., Smith, R., and Kuhlemeier, C. (2013). Interaction between meristem tissue layers controls phyllotaxis. Dev Cell 26, 616-628.

Kramer, E.M., Frazer, N.L., and Baskin, T.I. (2007). Measurement of diffusion within the cell wall in living roots of *Arabidopsis thaliana*. J Exp Bot 58, 3005-3015.

Krecek, P., Skupa, P., Libus, J., Naramoto, S., Tejos, R., Friml, J., and Zazimalova, E. (2009). The PIN-FORMED (PIN) protein family of auxin transporters. Genome Biol 10, 249.

Kuchen, E.E., Fox, S., de Reuille, P.B., Kennaway, R., Bensmihen, S., Avondo, J., Calder, G.M., Southam, P., Robinson, S., Bangham, A., *et al.* (2012). Generation of leaf shape through early patterns of growth and tissue polarity. Science 335, 1092-1096.

Kwiatkowska, D., and Dumais, J. (2003). Growth and morphogenesis at the vegetative shoot apex of *Anagallis arvensis* L. J Exp Bot 54, 1585-1595.

Lawrence, P.A., Casal, J., and Struhl, G. (2004). Cell interactions and planar polarity in the abdominal epidermis of *Drosophila*. Development 131, 4651-4664.

Lawrence, P.A., Struhl, G., and Casal, J. (2007). Planar cell polarity: one or two pathways? *Nat Rev Genet* 8, 555-563.

Le Garrec, J.F., Lopez, P., and Kerszberg, M. (2006). Establishment and maintenance of planar epithelial cell polarity by asymmetric cadherin bridges: a computer model. *Dev Dyn* 235, 235-246.

Lee, K., Avondo, J., Morrison, H., Blot, L., Stark, M., Sharpe, J., Bangham, A., and Coen, E. (2006). Visualizing plant development and gene expression in three dimensions using optical projection tomography. *Plant Cell* 18, 2145-2156.

Lin, D., Nagawa, S., Chen, J., Cao, L., Chen, X., Xu, T., Li, H., Dhonukshe, P., Yamamuro, C., Friml, J., et al. (2012). A ROP GTPase-dependent auxin signaling pathway regulates the subcellular distribution of PIN2 in *Arabidopsis* roots. *Curr Biol* 22, 1319-1325.

Long, R.M., Singer, R.H., Meng, X., Gonzalez, I., Nasmyth, K., and Jansen, R.P. (1997). Mating type switching in yeast controlled by asymmetric localization of ASH1 mRNA. *Science* 277, 383-387.

Ludwig-Muller, J. (2011). Auxin conjugates: their role for plant development and in the evolution of land plants. *J Exp Bot* 62, 1757-1773.

Luga, V., Zhang, L., Viloria-Petit, A.M., Ogunjimi, A.A., Inanlou, M.R., Chiu, E., Buchanan, M., Hosein, A.N., Basik, M., and Wrana, J.L. (2012). Exosomes mediate stromal mobilization of autocrine Wnt-PCP signaling in breast cancer cell migration. *Cell* 151, 1542-1556.

Ma, D., Amonlirdviman, K., Raffard, R.L., Abate, A., Tomlin, C.J., and Axelrod, J.D. (2008). Cell packing influences planar cell polarity signaling. *Proc Natl Acad Sci U S A* 105, 18800-18805.

Macara, I.G., and Mili, S. (2008). Polarity and differential inheritance--universal attributes of life? *Cell* 135, 801-812.

Majer, C., and Hochholdinger, F. (2011). Defining the boundaries: structure and function of LOB domain proteins. *Trends Plant Sci* 16, 47-52.

Marchant, A., and Bennett, M.J. (1998). The *Arabidopsis* AUX1 gene: a model system to study mRNA processing in plants. *Plant Mol Biol* 36, 463-471.

Maree, A.F., Grieneisen, V.A., and Edelstein-Keshet, L. (2012). How cells integrate complex stimuli: the effect of feedback from phosphoinositides and cell shape on cell polarization and motility. *PLoS Comput Biol* 8, e1002402.

Maree, A.F., Jilkine, A., Dawes, A., Grieneisen, V.A., and Edelstein-Keshet, L. (2006). Polarization and movement of keratocytes: a multiscale modelling approach. *Bull Math Biol* 68, 1169-1211.

Mattsson, J., Ckurdumova, W., and Berleth, T. (2003). Auxin signaling in *Arabidopsis* leaf vascular development. *Plant Physiol* 131, 1327-1339.

McConnell, J.R., and Barton, M.K. (1998). Leaf polarity and meristem formation in *Arabidopsis*. *Development* 125, 2935-2942.

McConnell, J.R., Emery, J., Eshed, Y., Bao, N., Bowman, J., and Barton, M.K. (2001). Role of PHABULOSA and PHAVOLUTA in determining radial patterning in shoots. *Nature* 411, 709-713.

Meinhardt, H. (2007). Computational modelling of epithelial patterning. *Curr Opin Genet Dev* 17, 272-280.

Merks, R.M.H., Van de Peer, Y., Inze, D., and Beemster, G.T.S. (2007). Canalization without flux sensors: a traveling-wave hypothesis. *Trends Plant Sci* 12, 384-390.

Mitchison, G. (1980). A Model for Vein Formation in Higher Plants. *Proc R Soc Lond B* 207, 79-109.

Mogilner, A., Allard, J., and Wollman, R. (2012). Cell polarity: quantitative modeling as a tool in cell biology. *Science* 336, 175-179.

Molendijk, A.J., Bischoff, F., Rajendrakumar, C.S.V., Friml, J., Braun, M., Gilroy, S., and Palme, K. (2001). *Arabidopsis thaliana* Rop GTPases are localized to tips of root hairs and control polar growth. *EMBO J* 20, 2779-2788.

Nagawa, S., Xu, T., Lin, D., Dhonukshe, P., Zhang, X., Friml, J., Scheres, B., Fu, Y., and Yang, Z. (2012). ROP GTPase-dependent actin microfilaments promote PIN1 polarization by localized inhibition of clathrin-dependent endocytosis. *PLoS Biol* 10, e1001299.

Nakata, M., Matsumoto, N., Tsugeki, R., Rikirsch, E., Laux, T., and Okada, K. (2012). Roles of the middle domain-specific WUSCHEL-RELATED HOMEOBOX genes in early development of leaves in *Arabidopsis*. *Plant Cell* 24, 519-535.

Nelson, B.K., Cai, X., and Nebenfuhr, A. (2007). A multicolored set of in vivo organelle markers for co-localization studies in *Arabidopsis* and other plants. *Plant J* 51, 1126-1136.

Nikovics, K., Blein, T., Peaucelle, A., Ishida, T., Morin, H., Aida, M., and Laufs, P. (2006). The balance between the MIR164A and CUC2 genes controls leaf margin serration in *Arabidopsis*. *Plant Cell* 18, 2929-2945.

Overvoorde, P., Fukaki, H., and Beeckman, T. (2010). Auxin control of root development. *Cold Spring Harb Perspect Biol* 2, a001537.

Paciorek, T., Zazimalova, E., Ruthardt, N., Petrasek, J., Stierhof, Y.-D., Kleine-Vehn, J., Morris, D.A., Emans, N., Jurgens, G., Geldner, N., et al. (2005). Auxin inhibits endocytosis and promotes its own efflux from cells. *Nature* 435, 1251-1256.

Parry, G., Marchant, A., May, S., Swarup, R., Swarup, K., James, N., Graham, N., Allen, T., Martucci, T., and Yemm, A., et al. (2001). Quick on the uptake: Characterization of a family of plant auxin influx carriers. *J Plant Growth Regul* 20, 217-225.

Peaucelle, A. (2014). AFM-based mapping of the elastic properties of cell walls: at tissue, cellular, and subcellular resolutions. *J Vis Exp*, e51317

Peret, B., Swarup, K., Ferguson, A., Seth, M., Yang, Y., Dhondt, S., James, N., Casimiro, I., Perry, P., Syed, A., et al. (2012). AUX/LAX genes encode a family of auxin influx transporters that perform distinct functions during *Arabidopsis* development. *Plant Cell* 24, 2874-2885.

Petrášek, J., and Friml, J. (2009). Auxin transport routes in plant development. *Development* 136, 2675-2688.

Postma, M., Bosgraaf, L., Loovers, H.M., and Van Haastert, P.J. (2004). Chemotaxis: signalling modules join hands at front and tail. *EMBO Rep* 5, 35-40.

Postma, M., and Van Haastert, P.J. (2001). A diffusion-translocation model for gradient sensing by chemotactic cells. *Biophys J* 81, 1314-1323.

Rayle, D.L., and Cleland, R.E. (1992). The acid growth theory of auxin-induced cell elongation is alive and well. *Plant Phys* 99, 1271-1274.

Reeves, G.T., Muratov, C.B., Schupbach, T., and Shvartsman, S.Y. (2006). Quantitative models of developmental pattern formation. *Dev Cell* 11, 289-300.

Reinhardt, D., Mandel, T., and Kuhlemeier, C. (2000). Auxin regulates the initiation and radial position of plant lateral organs. *Plant Cell* 12, 507-518.

Reinhardt, D., Pesce, E.R., Stieger, P., Mandel, T., Baltensperger, K., Bennett, M., Traas, J., Friml, J., and Kuhlemeier, C. (2003). Regulation of phyllotaxis by polar auxin transport. *Nature* 426, 255-260.

Ridley, A.J., and Hall, A. (1992). Distinct patterns of actin organization regulated by the small GTP-binding proteins Rac and Rho. *Cold Spring Harb Symp Quant Biol* 57, 661-671.

Ridley, A.J., Schwartz, M.A., Burridge, K., Firtel, R.A., Ginsberg, M.H., Borisy, G., Parsons, J.T., and Horwitz, A.R. (2003). Cell migration: integrating signals from front to back. *Science* 302, 1704-1709.

Robert, H.S., Grones, P., Stepanova, A.N., Robles, L.M., Lokerse, A.S., Alonso, J.M., Weijers, D., and Friml, J. (2013). Local auxin sources orient the apical-basal axis in *Arabidopsis* embryos. *Curr Biol* 23, 2506-2512.

Robert, S., Kleine-Vehn, J., Barbez, E., Sauer, M., Paciorek, T., Baster, P., Vanneste, S., Zhang, J., Simon, S., Covanova, M., *et al.* (2010). ABP1 mediates auxin inhibition of clathrin-dependent endocytosis in *Arabidopsis*. *Cell* 143, 111-121.

Rolland-Lagan, A.G., and Prusinkiewicz, P. (2005). Reviewing models of auxin canalization in the context of leaf vein pattern formation in *Arabidopsis*. *Plant J* 44, 854-865.

Rubery, P.H., and Sheldrake, A.R. (1973). Effect of pH and surface charge on cell uptake of auxin. *Nat New Biol* 244, 285-288.

Rubery, P.H., and Sheldrake, A.R. (1974). Carrier-mediated auxin transport. *Planta* 118, 101-121.

Sabatini, S., Beis, D., Wolkenfelt, H., Murfett, J., Guilfoyle, T., Malamy, J., Benfey, P., Leyser, O., Bechtold, N., Weisbeek, P., *et al.* (1999). An auxin-dependent distal organizer of pattern and polarity in the *Arabidopsis* root. *Cell* 99, 463-472.

Sachs, T. (1981). The controls of the patterned differentiation of vascular tissues. *Adv Bot Res* 9, 151-262.

Sagner, A., Merkel, M., Aigouy, B., Gaebel, J., Brankatschk, M., Julicher, F., and Eaton, S. (2012). Establishment of global patterns of planar polarity during growth of the *Drosophila* wing epithelium. *Curr Biol* 22, 1296-1301.

Sauer, M., Balla, J., Luschnig, C., Wisniewska, J., Reinohl, V., Friml, J., and Benkova, E. (2006). Canalization of auxin flow by Aux/IAA-ARF-dependent feedback regulation of PIN polarity. *Gene Dev* 20, 2902-2911.

Sauret-Gueto, S., Schiessl, K., Bangham, A., Sablowski, R., and Coen, E. (2013). JAGGED controls *Arabidopsis* petal growth and shape by interacting with a divergent polarity field. *PLoS Biol* 11, e1001550.

Scarpella, E., Marcos, D., Friml, J., and Berleth, T. (2006). Control of leaf vascular patterning by polar auxin transport. *Gene Dev* 20, 1015-1027.

Sessions, A., Burke, E., Presting, G., Aux, G., McElver, J., Patton, D., Dietrich, B., Ho, P., Bacwaden, J., Ko, C., et al. (2002). A high-throughput *Arabidopsis* reverse genetics system. *Plant Cell* 14, 2985-2994.

Sessions, A., Weigel, D., and Yanofsky, M.F. (1999). The *Arabidopsis thaliana* MERISTEM LAYER 1 promoter specifies epidermal expression in meristems and young primordia. *Plant Journal* 20, 259-263.

Shapiro, L., McAdams, H.H., and Losick, R. (2002). Generating and exploiting polarity in bacteria. *Science* 298, 1942-1946.

Sharpe, J., Ahlgren, U., Perry, P., Hill, B., Ross, A., Hecksher-Sorensen, J., Baldock, R., and Davidson, D. (2002). Optical projection tomography as a tool for 3D microscopy and gene expression studies. *Science* 296, 541-545.

Shi, J.H., and Yang, Z.B. (2011). Is ABP1 an auxin receptor yet? *Mol Plant* 4, 635-640.

Simon, M.A. (2004). Planar cell polarity in the *Drosophila* eye is directed by graded Four-jointed and Dachsous expression. *Development* 131, 6175-6184.

Simon, M.A., Xu, A., Ishikawa, H.O., and Irvine, K.D. (2010). Modulation of fat:dachsous binding by the cadherin domain kinase four-jointed. *Curr Biol* 20, 811-817.

Smith, C., Prusinkiewicz, P., and Samavati, F. (2003). Local specification of surface subdivision algorithms. *Applications of Graph Transformations with Industrial Relevance (AGTIVE 2003): Lecture Notes in Computer Science* 3062, 313-327.

Smith, R.S., Guyomarc'h, S., Mandel, T., Reinhardt, D., Kuhlemeier, C., and Prusinkiewicz, P. (2006). A plausible model of phyllotaxis. *Proc Natl Acad Sci U S A* 103, 1301-1306.

Spemann, H., and Mangold, H. (1924). Über Induktion von Embryonalanlagen durch Implantation artfremder Organisatoren. *Arch mikr Anat und Entw mech* 100, 599-638.

Steinacher, A., Leyser, O., and Clayton, R.H. (2012). A computational model of auxin and pH dynamics in a single plant cell. *J Theor Biol* 296, 84-94.

Stoma, S., Lucas, M., Chopard, J., Schaedel, M., Traas, J., and Godin, C. (2008). Flux-based transport enhancement as a plausible unifying mechanism for auxin transport in meristem development. *PLoS Comput Biol* 4, e1000207.

Strutt, D., and Strutt, H. (2007). Differential activities of the core planar polarity proteins during *Drosophila* wing patterning. *Dev Biol* 302, 181-194.

Strutt, D.I. (2001). Asymmetric localization of Frizzled and the establishment of cell polarity in the *Drosophila* wing. *Mol Cell* 7, 367-375.

Strutt, D.I. (2002). The asymmetric subcellular localisation of components of the planar polarity pathway. *Semin Cell Dev Biol* 13, 225-231.

Strutt, H., and Strutt, D. (2009). Asymmetric localisation of planar polarity proteins: Mechanisms and consequences. *Semin Cell Dev Biol* 20, 957-963.

Swarup, R., Kargul, J., Marchant, A., Zadik, D., Rahman, A., Mills, R., Yemm, A., May, S., Williams, L., Millner, P., et al. (2004). Structure-function analysis of the presumptive *Arabidopsis* auxin permease AUX1. *Plant Cell* 16, 3069-3083.

Takada, S., Hibara, K., Ishida, T., and Tasaka, M. (2001). The CUP-SHAPED COTYLEDON1 gene of *Arabidopsis* regulates shoot apical meristem formation. *Development* 128, 1127-1135.

Tepass, U. (2012). The apical polarity protein network in *Drosophila* epithelial cells: regulation of polarity, junctions, morphogenesis, cell growth, and survival. *Annu Rev Cell Dev Biol* 28, 655-685.

Terasaka, K., Blakeslee, J.J., Titapiwatanakun, B., Peer, W.A., Bandyopadhyay, A., Makam, S.N., Lee, O.R., Richards, E.L., Murphy, A.S., Sato, F., et al. (2005). PGP4, an ATP binding cassette P-glycoprotein, catalyzes auxin transport in *Arabidopsis thaliana* roots. *Plant Cell* 17, 2922-2939.

Usui, T., Shima, Y., Shimada, Y., Hirano, S., Burgess, R.W., Schwarz, T.L., Takeichi, M., and Uemura, T. (1999). Flamingo, a seven-pass transmembrane cadherin, regulates planar cell polarity under the control of Frizzled. *Cell* 98, 585-595.

van Berkel, K., de Boer, R.J., Scheres, B., and ten Tusscher, K. (2013). Polar auxin transport: models and mechanisms. *Development* 140, 2253-2268.

Venema, D.R., Zeev-Ben-Mordehai, T., and Auld, V.J. (2004). Transient apical polarization of Gliotactin and Coracle is required for parallel alignment of wing hairs in *Drosophila*. *Dev Biol* 275, 301-314.

Verkhovsky, A.B., Svitkina, T.M., and Borisy, G.G. (1999). Self-polarization and directional motility of cytoplasm. *Curr Biol* 9, 11-20.

Vernoux, T., Brunoud, G., Farcot, E., Morin, V., Van den Daele, H., Legrand, J., Oliva, M., Das, P., Larrieu, A., Wells, D., et al. (2011). The auxin signalling network translates dynamic input into robust patterning at the shoot apex. *Mol Syst Biol* 7, 508.

Vieten, A., Sauer, M., Brewer, P.B., and Friml, J. (2007). Molecular and cellular aspects of auxin-transport-mediated development. *Trends Plant Sci* 12, 160-168.

Vieten, A., Vanneste, S., Wiśniewska, J., Benková, E., Benjamins, R., Beeckman, T., Luschnig, C., and Friml, J. (2005). Functional redundancy of PIN proteins is accompanied by auxin-dependent cross-regulation of PIN expression. *Development* 132, 4521-4531.

Wabnik, K., Kleine-Vehn, J., Balla, J., Sauer, M., Naramoto, S., Reinohl, V., Merks, R.M.H., Govaerts, W., and Friml, J. (2010). Emergence of tissue polarization from synergy of intracellular and extracellular auxin signaling. *Mol Syst Biol* 6, 447

Wabnik, K., Robert, H.S., Smith, R.S., and Friml, J. (2013). Modeling framework for the establishment of the apical-basal embryonic axis in plants. *Curr Biol* 23, 2513-2518.

Waites, R., and Hudson, A. (1995). *phantastica*: a gene required for dorsoventrality of leaves in *Antirrhinum majus*. *Development* 121, 2143-2154.

Wang, W., Xu, B., Wang, H., Li, J., Huang, H., and Xu, L. (2011). YUCCA genes are expressed in response to leaf adaxial-abaxial juxtaposition and are required for leaf margin development. *Plant Physiol* 157, 1805-1819.

Wang, Y., and Nathans, J. (2007). Tissue/planar cell polarity in vertebrates: new insights and new questions. *Development* 134, 647-658.

Wedlich-Soldner, R., and Li, R. (2003). Spontaneous cell polarization: undermining determinism. *Nat Cell Biol* 5, 267-270.

Wenzel, C.L., Schuetz, M., Yu, Q., and Mattsson, J. (2007). Dynamics of MONOPTEROS and PIN-FORMED1 expression during leaf vein pattern formation in *Arabidopsis thaliana*. *Plant J* 49, 387-398.

Wisniewska, J., Xu, J., Seifertova, D., Brewer, P.B., Ruzicka, K., Blilou, I., Rouquie, D., Scheres, B., and Friml, J. (2006). Polar PIN localization directs auxin flow in plants. *Science* 312, 883-883.

Wong, L.L., and Adler, P.N. (1993). Tissue polarity genes of *Drosophila* regulate the subcellular location for prehair initiation in pupal wing cells. *J Cell Biol* 123, 209-221.

Xu, T., Wen, M., Nagawa, S., Fu, Y., Chen, J.G., Wu, M.J., Perrot-Rechenmann, C., Friml, J., Jones, A.M., and Yang, Z. (2010). Cell surface- and Rho GTPase-based auxin signaling controls cellular interdigitation in *Arabidopsis*. *Cell* 143, 99-110.

Yamaguchi, T., Nukazuka, A., and Tsukaya, H. (2012). Leaf adaxial-abaxial polarity specification and lamina outgrowth: evolution and development. *Plant Cell Physiol* 53, 1180-1194.

Yang, Y., Hammes, U.Z., Taylor, C.G., Schachtman, D.P., and Nielsen, E. (2006). High-affinity auxin transport by the AUX1 influx carrier protein. *Curr Biol* 16, 1123-1127.

Yang, Z., and Lavagi, I. (2012). Spatial control of plasma membrane domains: ROP GTPase-based symmetry breaking. *Curr Opin Plant Biol* 15, 601-607.

Yang, Z.B. (2008). Cell polarity signaling in *Arabidopsis*. *Annu Rev Cell Dev Biol* 24, 551-575.

Zhao, Y. (2010). Auxin biosynthesis and its role in plant development. *Annu Rev Plant Biol* 61, 49-64.